Etude du phénomène de bifurcation des écoulements vrillés par la Simulation aux Grandes Échelles et l'adaptation de maillage

Mario Falese

Université de Toulouse

THÈSE

En vue de l'obtention du

DOCTORAT DE L'UNIVERSITÉ DE TOULOUSE

Délivré par :
Institut National Polytechnique de Toulouse (INP Toulouse)

Discipline ou spécialité :
Dynamique des fluides

Présentée et soutenue par :
Mario FALESE

le : 07/10/2013

Titre :

A study of the effects of bifurcations in swirling flows using Large Eddy Simulation and mesh adaptation

---

Ecole doctorale :
Mécanique, Energétique, Génie civil et Procédés (MEGeP)

Unité de recherche :
CERFACS

Directeur(s) de Thèse :
Thierry Poinsot
Eleonore RIBER

Rapporteurs :
Stephan MOREAU
Patrick BONTOUX

Membre(s) du jury :

Pascal BRUEL
François GALLAIRE
Vincent MOUREAU
Cecile DOBRZYNSKI

A study of the effects of bifurcations in swirling flows using Large Eddy Simulation and mesh adaptation

Mario Falese

October 7, 2013

This manuscript is dedicated to the two masters I never knew:
Max Stirner who teached me grammar,
Ernst Junger who showed me how to make poetry out of it.

Abstract and *Résumeé en français*

Swirling flows, which are widely employed in gas turbines, are known to undergo bifurcation between different topologies (large reconfigurations of the flow field) affecting the engine performance and safety.
This work focuses on the study of such bifurcations using Large-Eddy Simulation (LES). It shows that a small change in the fluid dynamics conditions, induced by the different Sub-Grid Scale (SGS) models used in the simulations, can cause a transition between two, distinct, flow states when the swirling flow is close to transition conditions. The sensitivity of LES to SGS modeling is also identified as the result of a lack of mesh resolution at some critical locations, a problem which is analyzed using mesh adaptation. Mesh adaptation is tested on canonical and industrial flows. Here, by adjusting the mesh resolution based on the characteristics of the flow examined (refining and coarsening the grid keeping constant the numerical cost), substantial improvements of the LES predictions can be obtained.
This work can be considered as the first step toward the establishment of a standard (repeatable and user independent) meshing procedure for LES.

Les écoulements tourbillonnants, qui sont largement utilisés dans les turbines à gaz, sont connus pour etre subject a des bifurcationnes entre différentes topologies (grandes reconfigurations du champ d'écoulement) qui peuvent affecter les performances et la sécurité du moteur.
Ce travail se concentre sur l'étude de ces bifurcations en utilisant la simulation aux grandes échelles (LES). Ce travail montre qu'un petit changement dans les conditions dynamique du fluide, induite par les différentes modèles de sous-maille utilisés, peut provoquer une transition entre deux, distincts, régimes d'écoulement lorsque l'écoulement tourbillonnaire est proche des conditions de critiques et de transition. La sensibilité des la LES au modeles de sous-maille est également identifié comme le résultat d'un manque de résolution à certains endroits critiques, un problème qui est analysé en utilisant une methode d'adaptation du maillage. L' adaptation du maillage est testé sur des cas accademique et industrielle. Ici, par ajustement de la résolution du maillage sur la base des caractéristiques de l'écoulement étudié (affinage et le grossissement de la grille en maintenant constant le coût numérique), des améliorations substantielles des prédictions de la LES peuvent être obtenue.
Ce travail peut être considéré comme une des premières étapes vers la mise en place d'une procédure standard (reproductible et utilisateur indépendant) de maillage pour la LES.

Thanks

It was always a good place for working (...)
Some other places were not so good,
but maybe we were not so good when we were in them.
E. Hemingway

I would like to thanks the following people. Geoffroy (aka *J'ai frois* or *le tap*) and Mi, my good friends and fellow sailors in the mediterranean sea. Lukash Kuban (aka *Mastro Lindo* or *Monsieur Proper*) my fellow polish liberal, Dmitry Kolomenskiy, Guillame Le Coq (aka *Olivia*) and Matthias Kraushaar with whom I shared some weird months living in meteofrance (and a weird week in Poland). Javier Urzay, who showed me the power of pen-and-paper.
All my collegues at CERFACS: Gregory Hannebiq (aka *le Canard*) and Basti Hermerth (aka *l'allemande*), Remy Franzen, Emmanuel Motheau (a good example of "la france profonde"), Stephane Jaure (whose conversations about coding in C helped me a lot) et JP Rocchi, Anthony Ruiz (whose conversations about LOTAR helped me a lot), Ignacio Duran (see you in London), Pablo Salas (aka *the brandy guy*, who opened my eyes on "les vins du sud-ouest"), Pierre Quillarte (aka *le rouge*) and David (aka *le petit muscle*) who had the pleasure to play with a superior italian footballer (yes, I brought football knowdlege to you, frenchies), Jerome Dombard and Elza Gullaud and Sandrine Berger (fellow sailors) and Abdulla Ghani (who, the legend says, is doing my PhD at my place), and all the others who shared with me the last 3 years at CERFACS. Also, I would like to thank (in chronological order) Valentina and Marta, my sweets.

I want to thank the real Chief of CERFACS (Marie Labadens) and Nicole Boutet and all the people of CSG and administration, above all Michelle Campassens. Laurent Giquel, Gabriel Staffelbach and Jens Muller for all their help/supervision during my thesis. Cecile Dobrzynski from INRIA for MMG3D, then all the seniors of CERFACS: Eleonore, Benedicte, Antoine, Olivier and Frank Nicoud who were always available for a scientific chat: all of this was useful. Thanks to the reviewers of this manuscript and to all the members of the jury. Finally, I want to thank my supervisor Thierry Poinsot for his scientific guidance and supervision.

Contents

Chapter 1

Introduction

Aeronautical transportation is one of the few markets un-affected by the world economic crisis. For instance, the long-range forecasts of the two major aircraft builders, AIRBUS and Boeing, predict an agglomerate business of more than 7 trillions dollar (7×10^{10}\$) between now and 2030 thanks to a combination of both emerging-market and rich world growth.
The source of demand is driven by the rising numbers of urban middle-class people (a demand insensitive to any world crisis, see Fig. 1.1 left), but also, from the rich world, by the need to replace ageing and inefficient planes in order to fulfill new regulations on emissions [1]. For instance, new regulations (demanded by the Advisory Council for Aero-

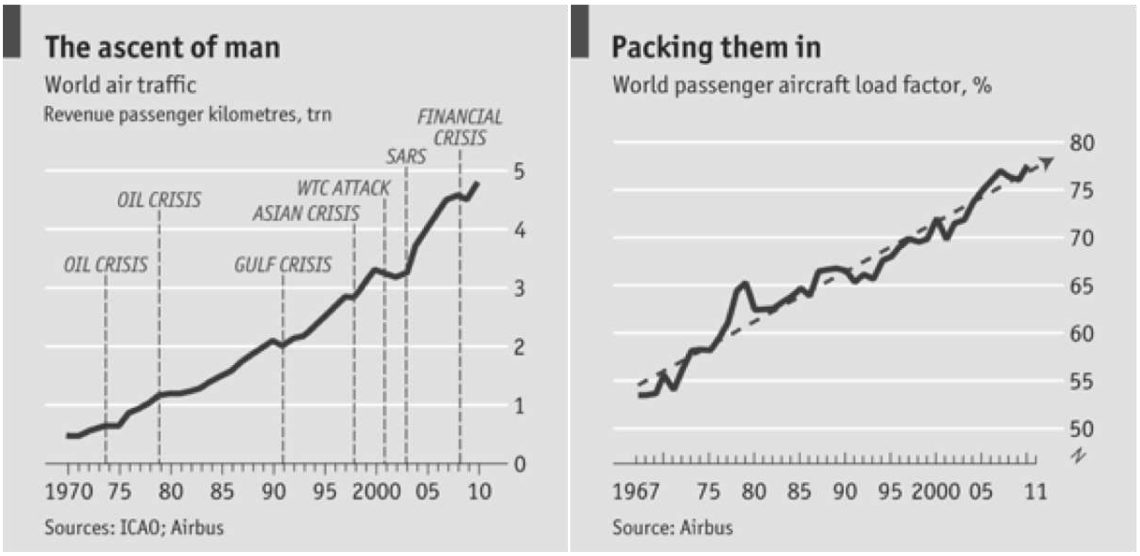

Figure 1.1: From [1]. Growth trend of aeronautical passengers and airplanes load factor.

nautics Research in Europe) will force a reduction of the exhaust greenhouse gases such as CO2 by 50% and of pollutant such as NOx by 80% in 2020 [55]. This context explains the need for new engine designs to gain in efficiency and reduce pollution[1].
Aeronautical propulsion relies heavily on combustion technology, therefore reducing green-

[1]Note that a large increase in efficiency is given by the growing airplane load factor [1] (Fig. 1.1 right).

house gases and pollutant consists mainly in improving combustion. Other propulsion systems (i.e. not involving combustion) are limited to small-scale unmanned or proof-of-concept research applications [47]. Fig. 1.2 shows a typical aircraft modern engine. In

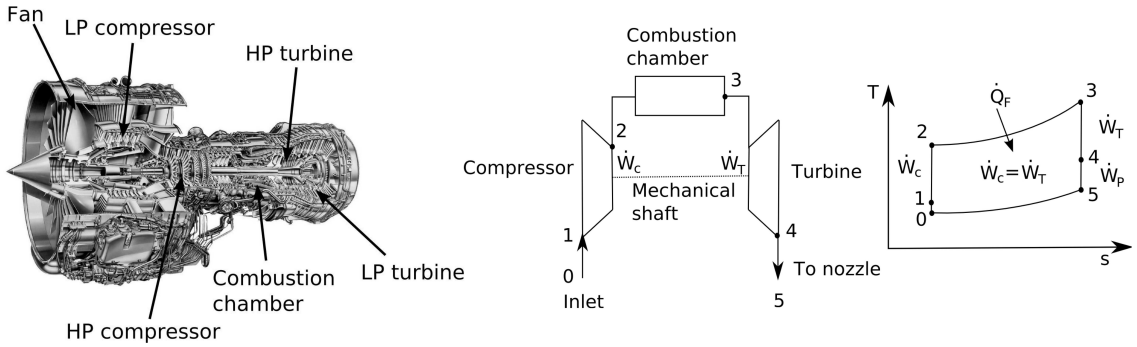

Figure 1.2: From [101]. Left: a typical aircraft modern engine, a turbogas (V 2500). Center: scheme of a simplified jet engine operation and the associated idealized Joule-Brayton cycle (right).

such combustion-based propulsion systems (Fig. 1.2) energy conversion, from the chemical energy of the fuel to internal energy of the gas, takes place in the combustion chamber which is therefore central in the engine performance. Almost all gas turbines combustion systems employ swirl flows whose dynamics are determined by the swirler geometry (Fig. 1.3). The swirler is a device which is mounted at the entry of the combustion chamber to generate a flow which helps to stabilize the flame, by the transport of burnt gases at the fuel injection point and to improve mixing via higher turbulence levels. This thesis focuses on the simulation of the complex flow field generated by such devices: the swirling injection system.

1.1 Swirling injection systems

Swirling injection systems used in most gas turbines lead to complex flows which control the fuel atomization, the shape of the recirculating zone produced in front of the swirler and ultimately a large part of the performances of the engine. Predicting these flows has been a major challenge for CFD for a long time. It did not take a long time to realize that RANS codes (predicting mean steady turbulent flows) had difficulties in these flows with strong rotation and LES has rapidly proved its superior potential, allowing to capture not only the mean flow velocity fields with precision but also the flow instabilities, such as the PVC (Precessing Vortex Core), with or without combustion, for gaseous or liquid fuels [42, 99, 11, 5].

Fig. 1.3 (left) displays a typical LES result performed in 2004 by S. Roux et al. on 2 million cells where the PVC is visualized using a low-pressure region [91]. Fig. 1.3 (right) shows one of the largest LES ever performed for a swirled flow in 2010, in the same geometry as Roux et al [91], but on a much finer mesh using 2.6 billion cells [76].

After a first period (until 2009) where LES seemed to deliver all expected results in swirlers, a few disturbing facts appeared: (1) despite the fact that the velocity fields produced by LES were accurate, the pressure losses through the swirlers were definitely not as good showing errors of the order of 30 to 100 percent and (2) LES results also seemed extremely

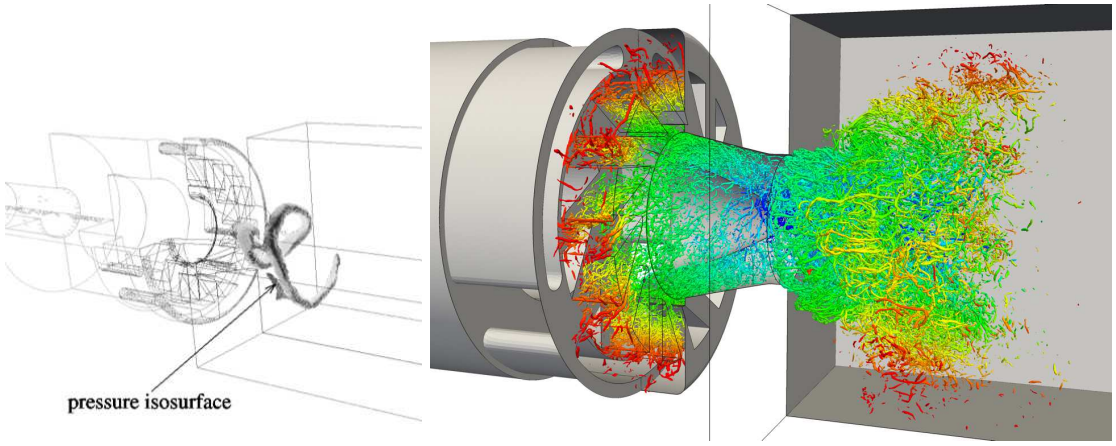

Figure 1.3: Examples of LES of swirled flows. Left: the LES of Roux et al [91]. Right: the LES of Moureau et al [76]

sensitive to parameters such as the SGS model or the boundary conditions. An additional difficulty arising with recent swirlers is that they use multiple passages while the injection system of Fig. 1.3 used in [91, 76] used a single swirling passage. For a single swirler, errors on pressure losses have no effect on the velocity field since the flow can use only one passage. As soon as a swirler with multiple passages is used, any error on pressure losses will directly impact the flow split between the passages, leading to significant flow variations. Finally, the impact of the mesh (quality and number of points) remains obviously a weak point for all LES where near-wall regions must be resolved and the impact of the wall model on the results is also certainly an issue in these swirlers.

The difficulties encountered to simulate swirling flows are less surprising when one considers the experimental literature on these flows [10, 32]. Experimentalists know that bifurcation is a common feature in many swirling flows where multiple instabilities take place. Even simple, academic flows shows multiple configurations: seven different types of vortex breakdown (vortex breakdown is the main structure of highly swirled flows) have been identified depending on the swirl and Reynolds number [23] and there are "numerous borderline ranges for which two forms or more can exist and transform spontaneously into each other" [64]. As a result, the combustion community today has clearly identified the fact that (1) swirl flows are important but pathological flows subject to violent bifurcations and that (2) even though LES seems to correctly capture these flows, as the output of LES codes depends strongly on external settings and modeling, the margin of reliability is low.

These observations share many common points with a more general field called UQ (Quantification of uncertainties) which has been growing rapidly in the CFD community in the last five years [65, 20]. Obviously, what the previous statements demonstrate is that swirling flows are highly dependent on multiple uncertain parameters and that since these flows are also submitted to bifurcations, these two phenomena (large UQ sensitivity and possible bifurcations) lead to a problem which becomes very difficult for simulation. We will not develop any element of the UQ methodology in the present work because we needed to identify which parameters are actually important before trying to vary them in a systematic fashion. At the present stage, there are too many important parameters

(mesh, SGS model, boundary conditions, inlet conditions, wall models, numerical dissipation) which affect the solution of swirling flow simulations in practical configurations to apply a UQ technique but we are aware that this will be the next logical step, once the controlling parameters will have been identified. A second reason why UQ was not used here is that we will be considering unsteady solutions and unsteady flows are still very difficult to handle with UQ tools.

1.2 Mesh adaptation, the way toward standardization

As underlined in section 1.1 and as will be shown in this thesis, simulating swirling flows presents major difficulties. Such difficulties have a trivial solution: resolving all turbulent length scales, which is also known as Direct Numerical Simulation (DNS). Despite the fact that computational power is constantly increasing (see Fig. 1.4) DNS is unaffordable at the present time for industrial configurations[2].

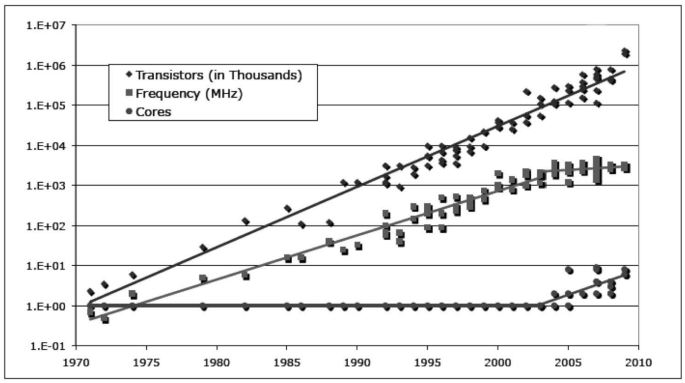

Figure 1.4: Frequency and number of transistors for CPU plotted against Moore's law from 1965 (continuos line on the top). A change occurred after year 2000, showing an increase of the number of cores per processor. From [55].

As a consequence of the cost of DNS in industrial configurations, LES is employed. LES requires modeling to close its formulation and modeling is, by construction, affected by the grid size. However, to choose the proper grid size presents some major difficulties because of the very wide range of length scales and phenomena involved in industrial flows. A very fine grid implies unaffordable numerical costs while a very coarse grid will lead to wrong predictions. A compromise solution between the two extrema, i.e. an homogeneous mesh as fine as possible but not as fine as a DNS mesh, does not represent the optimum solution: some turbulent length scales could be properly resolved in such grid, some others not. Since turbulent structures interact with each other in a non-linear manner, the outcome of such approximations is unknown and unpredictable a priori.
Non-homogeneous grids, which are used in most LES of industrial flows, represent a solution to take into account the different flow length scales. However, there is no general

[2]For instance, if only one of all simulations performed during this thesis would have employed a grid size in the order of the Kolmogorov length scales, i.e. $\Delta = O(\eta_k)$, such LES would have required 3.21×10^{11} CPU hours. (this approximation is obtained extrapolating the numerical cost of the LES performed) that makes, at a cost of 0.01 euro for CPU hour, a cost of 3 billions of euro in the best case scenario

criterion to design such grids. The mesh, which is the leading order parameter in LES, is most of the time created arbitrarily and its "quality" relies on the experience of the scientist (in the best case scenario) or of the first year phd student/engineer (as usually happens) who is generating it.
The most obvious solution to this problem is mesh convergence studies. However, such studies are not always affordable in industrial configurations since the numerical cost is usually pushed to its edge from the beginning. Since the scientific study of industrial flows is by default computing-time expensive, a factor 16 (which implies the use of a twice finer mesh) on its cost is most of the time unaffordable, especially when multiple configurations are tested. Also, the whole set of the flow statistics will never converge and the only option available is to hope low order statistics to converge with increasing mesh resolution [90], and that numerical and modeling errors do not compensate each other [72].
As a consequence, the most important LES parameter, the mesh, is chosen more or less arbitrarily. What should be the result of a scientific investigation (which requires standard parameters such as well established numerical methods, SGS models or boundary treatments), is often the outcome of an arbitrary choice made on the mesh. This disturbing truth contrasts a global trend, for instance in industry where it is becoming more and more common to certify (using international standards such as ISO9001 etc.) all procedures in order to ensure high quality standards.
For all these reasons, the second part of this thesis focuses on mesh adaptation, that is the ability of manipulating a grid based on a set of criteria. Mesh adaptation methods have been widely applied to improve mesh quality based on the mesh geometrical properties (which is also known as *a priori* adaptation) or coupled with a flow solver to adapt the mesh based on a given flow property (which is also known as *a posteriori* adaptation).
An example of *a priori* adaptation is shown in Fig. 1.5 which shows a "basic" mesh (left) with bad quality elements (highly stretched) which comes from two different domains and an "adapted" mesh (right) where such elements are replaced by more regular ones to obtain a smoother grid.

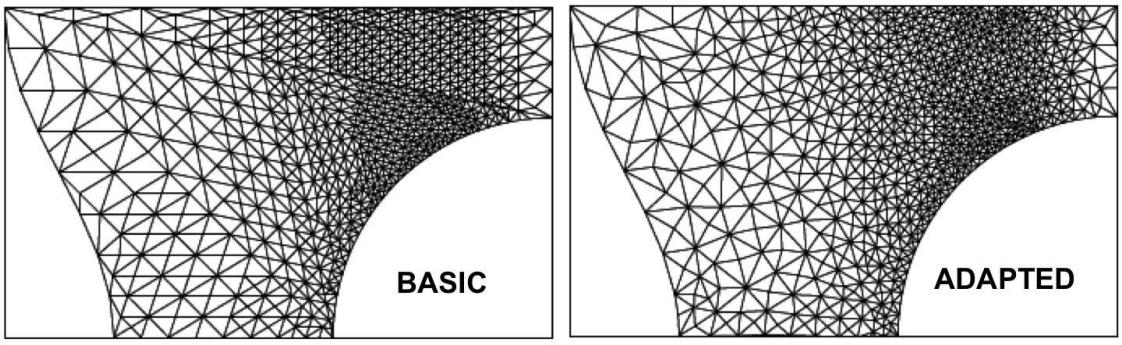

Figure 1.5: *A priori* mesh adaptation, from Freitag et al. [24]

An example of *a posteriori* mesh adaptation is shown in Fig. 1.6, in which the mesh is adapted to capture the shock interface (which is moving) caused by a blast: the grid resolution is increased where the shock is located, a type of refinement impossible to perform a priori (without knowing the shock location) or to be made by hand with a common commercial mesh generator.

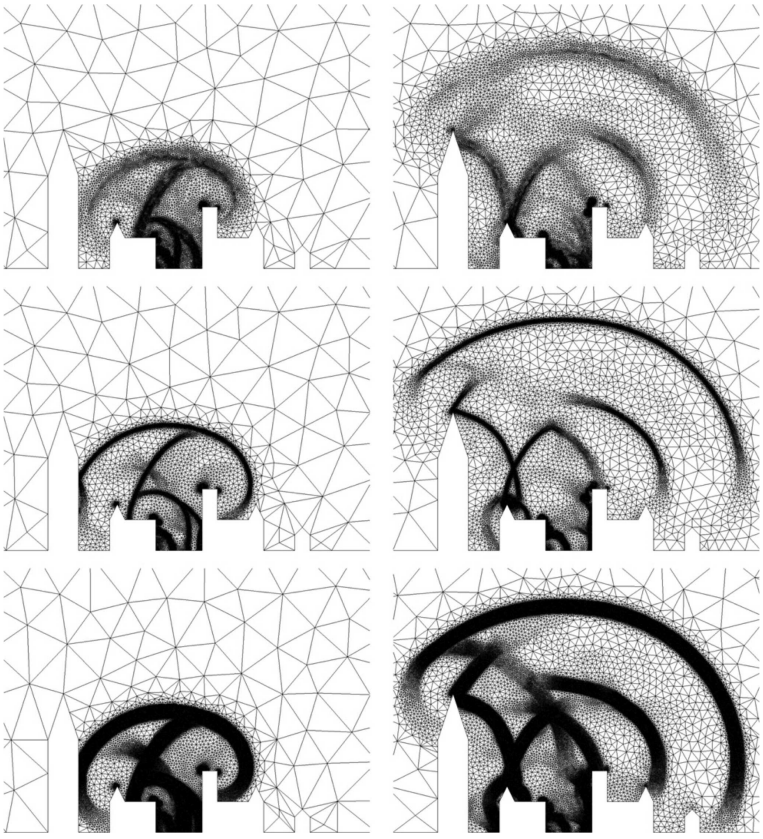

Figure 1.6: *A posteriori* mesh adaptation, from Alauzet et al. [3]. The mesh is adapted continuously in order to capture the moving shock wave caused by a blast (the different images corresponds to different instants).

Such mesh adaptation methods have been widely used in the context of the Euler equation (see for instance [25, 3, 2, 63]) while very few examples in LES can be found in the literature.
One example is the work of Hertel and Fröhlich [37], who used a self-adaptive method executed in parallel to the LES solver. Mesh adaptation, obtained by nodes displacement, is included in the LES equations via the ALE (Arbitrary Lagrangian Eulerian) formulation. The results of such a method [37], tested on the flow over a periodic hill, showed (for a sensor based on the velocity gradient) a quality comparable to a highly-resolved LES many times bigger in terms of the number of nodes.
Here, a metric based mesh adaptation method will be used (the same as [25, 3, 2, 63]) coupled with simple, empirical criteria for adaptation. It will be shown that mesh adaptation can improve results while keeping the numerical cost of the simulation constant, therefore optimizing the simulation outcome, and making the meshing process a repeatable procedure.
A clear distinction must be made between standardization/repeatability and optimization.

- Standardization/repeatability is the ability to use the same adaptation method on different flows and configurations and allows to transform meshing from an handicraft process to an "industrial" process.

- Optimization is the ability of the adapted mesh to improve results and is a function of the particular criterion chosen for adaptation and of the flow which is simulated.

All mesh adaptation results presented in this thesis show improvements with respect to the original, arbitrary mesh used for comparison[3]. What makes them useful is the possibility to apply them to similar configurations in an automatic fashion, i.e. without relying strongly on the experience of the person who is using them. Of course, there is large margin of improvement in all of them, but thanks to the repeatability property of mesh adaptation, an optimal criterion for a given flow can be easily extended to all similar flows. Note that mesh adaptation has been applied to a very limited number of canonical LES studies [37, 38, 39] and has never been tested in complex, industrial configurations such as the aeronautical swirler studied in the first part of this thesis. This work can be considered as one of the first efforts in such direction and is the first step toward establishing such a mesh adaptation framework.

1.3 Plan of the work

This thesis is organized as follows:

- The first part (Chapters 2-3-4) discusses the difficulties encountered in simulating a confined, industrial swirling jet. Such difficulties will be related to natural phenomena, such as violent bifurcations and hysteresis, present in the flow and which are investigated on a very fine mesh in chapter 5.

- In the second part (Chapter 5-6-7-8) the fundamental of mesh adaptation are presented and tested in simple cases.

- In chapter 9 the first two parts merge. Mesh adaptation methods presented in part II are tested on the industrial configuration studied in part I. In this last chapter a mesh adaptation criterion will be presented which improves significantly the flow prediction in terms of velocity profiles and pressure drop and can be extended to other similar industrial configurations without tuning.

[3]Note that only simulations at the same numerical cost are compared.

Part I

Bifurcations & hysteresis in LES of swirling flows

Chapter 2

LES of swirling flows

The objective of the first part of this thesis is to study mechanisms which control the accuracy of LES when it is used to compute strongly swirled flows in a real, industrial configuration. Here the LOTAR experiment, a high Reynolds number flow using multiple swirling jets installed at ONERA Fauga for the KIAI European Program, is chosen but we expect results to be fairly general.
In order to study leading order simulation parameters, a sensitivity analysis is performed by changing:

- subgrid scale models: ranging from SIGMA [80], to Dynamic Smagorinsky [29],
- the mesh,

while keeping constant all fluid dynamics and thermodynamics conditions. All variations artificially induced by simulation settings will be then analyzed and linked to local modifications in the computed flow field. As swirl jets are subject to bifurcation, **LES results will show that such small modifications can trigger large flow reconfigurations**. The various numerical and physical parameters have the capacity to modify the results: small, local, variations can lead to global bifurcation phenomena if the flow is close to critical conditions. The most obvious example is artificial viscosity: a small amount of numerical viscosity can be enough to decrease the effective Reynolds number seen by the flow and lead to another regime; if the flow is very Reynolds sensitive, this small variation in numerical parameters may trigger a large change in the results.
LES results are compared to experimental data obtained at ONERA. It is known that the main drawback of such a posteriori testing is that it characterizes whole codes and not only single parameters [51]. To overcome this problem two completely different LES codes are tested on the same numerical mesh and settings: an incompressible LES code, YALES2 [76], and AVBP, a compressible LES solver [93, 92]. Using two codes allows to identify the effects of a single parameter variation by isolating spurious, hidden effects of the numerical procedure. The configurations are itemized in table 2.1. A complete span of the parameter space would have required an excessive number of simulations but this reduced set is sufficient to obtain conclusions at a reasonable cost. Sensitivity analysis is then performed in a limited way and the use of two codes has been limited to the most significant cases.

NAME OF RUN	MESH USED	CODE MODEL	SGS
AVBP-SIGMA	basic (14M cells)	AVBP	SIGMA
YALES-SIGMA	basic (14M cells)	YALES2	SIGMA
AVBP-DSMAG.	basic (14M cells)	AVBP	DYN. SMAG.
YALES-DSMAG.	basic (14M cells)	YALES2	DYN. SMAG.
YALES-DSMAG._O	optimized (15M cells)	YALES2	DYN. SMAG.
YALES-SIGMA_O	optimized (15M cells)	YALES2	SIGMA
AVBP-SIGMA_O	optimized (15M cells)	AVBP	SIGMA

Table 2.1: List of LES performed in Chapter 3.

After the main flow features for the various configurations of table 2.1 (i.e. flow split, swirl numbers and ratio) were obtained, a new experiment was performed on a simplified geometry extracted from the complete configuration (Fig. 2.1) to be able to change the swirl level continuously.

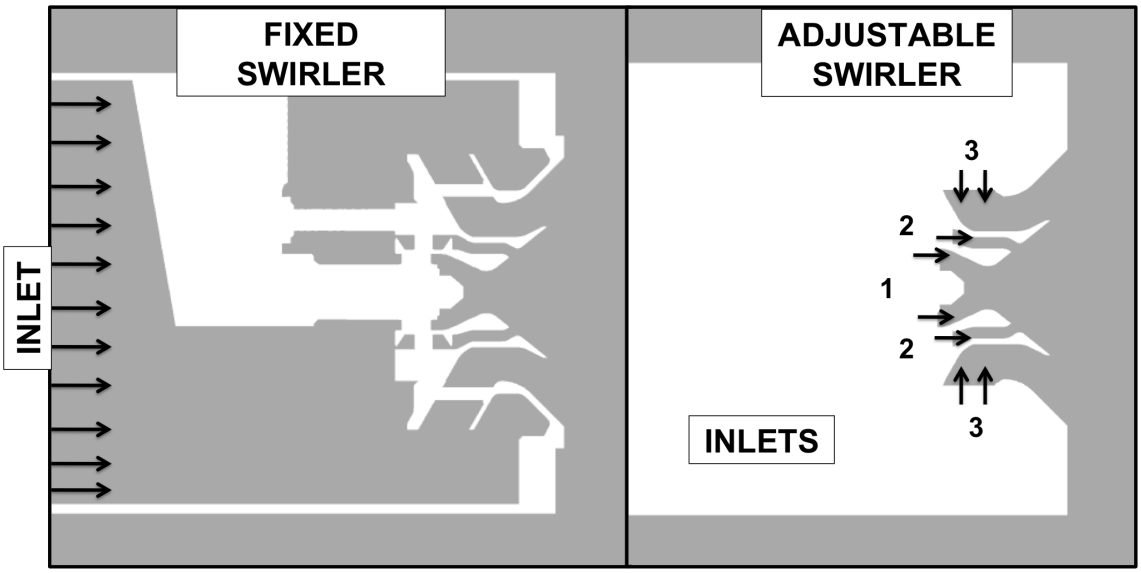

Figure 2.1: Fixed swirler, used for simulation in table 2.1, and adjustable swirler, used for the fluid dynamics analysis of chapter 4. Arrows represent inlet boundary conditions.

In this simplified domain, called "adjustable swirler" in Fig. 2.1 right, the inlet boundary condition has been shifted downstream at the exit of the swirler vanes in order to decouple the flow swirl and Reynolds numbers from the injector geometry: this geometry is therefore named adjustable swirler. Removing the small swirl passages, O(1) mm in size, present in the complete domain reduces the computational effort and resolution can be increased in the swirler bowls at a reasonable computational cost. It also allows to change the swirl level easily by changing the velocity angle on the boundary conditions 1-2-3 (Fig. 2.1 right), something that is more difficult in the full configuration (named therefore fixed swirler, Fig. 2.1) where any change of swirl would require a total change of the CAD/mesh.

In this second analysis numerical settings are kept constant while fluid dynamics conditions (which are controlled by swirl) are varied. Results agree with the first analysis, showing that a small variation of the leading order parameter (the swirl ratio) for a fixed geometry and Re, can cause a natural bifurcation. These numerical results are then compared to a similar study performed experimentally by Vanierschot and Van Den Bulck [105]. Even if the exact limits of the different states and the hysteresis patterns differ (as a consequence of the different geometries), both the present LES of an aeronautical swirler and the simpler configuration of Vanierschot et al. [105], exhibit similar bifurcations mainly controlled by the swirl level.

2.1 Organization

This first part of this thesis focuses on the simulation and the analysis of the swirled flow in the configurations of Fig. 2.1. It is organized as follows.

- **Chapter 2**

  In the following part of this chapter evidences of hysteresis, bifurcation and bistability in swirl flows will be given, based on the experimental literature on the subject. The main features of swirl flows, such as vortex breakdown and the Precessing Vortex Core (PVC), will be shown. A review of the state of the art of LES of industrial flow will be presented in order to clarify up-to-date requirements for such simulations and which level of complexity it has reached. The mathematical foundation of bifurcation will also be recalled briefly.

- **Chapter 3**

  In this chapter the LOTAR experiment of ONERA, the numerical setups used for AVBP and YALES2 and the characteristics of the SGS models and numerics used, will be clarified. The discussion of results will begin in Section 3.4 by presenting a baseline case where AVBP and YALES2 results are compared for a first mesh called *basic* (see Table 2.1). The two codes are using the same mesh and the same SGS model (SIGMA). Results are compared to experiment in terms of velocity fields and pressure losses: they show that the flow is badly predicted in both cases leading to a jet which expands too much and a level of accuracy very far from what usually observed in LES. The effect of the SGS model is discussed in Section 3.5 by replacing the SIGMA model by the Dynamic Smagorinsky model. Finally the effect of the mesh is determined using an *optimized* mesh (Section 3.7), which does not have significantly more cells (15 millions vs. 14 millions) but where nodes have been placed in critical zones, reducing the local mesh size where needed. Results show that the changes in the numerical settings can cause the flow solution to bifurcate leading to a jet which expands less rapidly and a comparison with experimental velocity fields which is much better.

- **Chapter 4**

  While chapter 3 shows evidences of bifurcation induced by numerical settings, chapter 4 proves that this strong non-linear response is due to the fact that the baseline case studied in LOTAR corresponds to a geometry and a swirl ratio (of the order of 0.8) close to critical conditions where a bifurcation takes place. For a fixed numerical setup, fluid dynamics conditions are varied in the configuration called "adjustable" thanks to a simplification (see Fig. 2.1) introduced in the geometry (which also allows to use a very fine mesh). Results confirm that the swirl ratio of the radial jet of LOTAR controls the flow states and allow to construct a bifurcation diagram where the flow state is determined by the swirl ratio and by the flow history.

2.2 General features of swirling flows

The aim of this section is to review the main features of free swirl flows and their different instabilities (Vortex breakdown, PVC, axial and azimuthal Kelvin-Helmholtz instabilities). Experimental evidences of bifurcation and hysteresis phenomena for confined swirling flows (such as the one that will be shown in chapter 3 and 4) will be presented and finally the mathematical basis of bifurcation will be exposed briefly.

2.2.1 Nondimensional parameters.

A swirling flow, or jet, is defined as one undergoing simultaneous axial and azimuthal motions. Swirl flows are characterized by the Reynolds number and the Swirl number S (or the swirl ratio S_r).
The Reynolds number is a measure of inertia force over viscous force and is used to characterize the transition from a laminar to a turbulent regime:

$$Re = \frac{U\ D}{\nu}, \tag{2.1}$$

where U and D are the characteristic speed and dimension of the flow respectively, while ν is the kinematic viscosity. Industrial flows are fully turbulent and "swirling flows in combustors are usually built to be insensitive to small Reynolds number modifications to avoid transition between vortex breakdown type, as this could cause large variations in the recirculation and mixing zones" [32].
The swirl number (S) is defined as the ratio of axial transport of angular momentum over axial transport of axial momentum: both are invariant for a jet in stagnant surroundings [32] (see also [83] for a rigorous derivation). There are several definitions in the literature of the swirl number that also include the axial thrust due to pressure difference and the Reynolds stresses representative of turbulence intensity. In this work these terms will not be included and the swirl number will be defined as:

$$S = \frac{\int_A \rho u_a u_\theta r dA}{R \int_A \rho u_a^2 dA} \tag{2.2}$$

where u_a is the axial velocity, ($u_\theta\ r$) is the angular momentum in the longitudinal direction, R is the characteristic radius of the jet[1]. When the swirl number is increased above a critical value $S \approx 0.6$ (that is an empirical criterion while Eq.(2.7) derives from analytical considerations) vortex breakdown is triggered.
In addition to the swirl number S, another non-dimensional number called swirl ratio (S_r) is also used in certain cases. The swirl ratio is defined as:

$$S_r = \frac{\int_A u_\theta dA}{\int_A u_a dA}. \tag{2.3}$$

[1]Since some of the flows here examined are made of multiple concentric and counter-rotating jets, R is chosen arbitrarily as the radius of the largest.

2.2.2 Main instabilities of free swirling flows

Experimentalists know that bifurcation is a common feature in many swirling flows where multiple instabilities take place [23]. The most common of them is vortex breakdown [10, 64], which occurs when reverse flow takes place along the jet axis [13]. As first proposed by Hall [35], vortex breakdown can be explained with the presence of an adverse pressure gradient induced by the conservation of circulation and the jet expansion [10]. The presence of azimuthal velocity (and therefore centrifugal force) induces a radial pressure gradient given by the simplified radial equilibrium relation (radial velocity is assumed to be zero):

$$\frac{dp}{dr} = \rho \frac{u_\theta^2}{r}. \tag{2.4}$$

For a stagnant fluid, the pressure field imposed by centrifugal force and local pressure (P_r) must balance pressure at infinity (P_∞). As a consequence, the presence of a zone with a strongly rotating flow results in a local subpressure (P_d),

$$P_d = P_\infty - P(r) = \int_0^r \rho \frac{u_\theta^2}{r} dr. \tag{2.5}$$

As the jet is spreading along the axial direction (x), the conservation of total circulation implies a decay of the tangential velocity and therefore a recover of $P(r)$ to P_∞. As a consequence, the flow senses an adverse pressure gradient along the axial direction,

$$\frac{dP(r)}{dx} > 0. \tag{2.6}$$

Above given critical conditions (when the swirl is larger than a critical threshold, see Eq.(2.7)), axial momentum is first balanced and then overwhelmed by this "secondary" axial pressure gradient (Eq.(2.6)). The result is the creation of a recirculation zone: vortex breakdown is taking place.
As stated by Liang and Maxworthy [60], vortex breakdown is commonly associated with a finite transition between a super-critical upstream and sub-critical downstream states in an axisymmetric flow, as first proposed by Benjamin [9]. The location of breakdown can be predicted by the non-dissipative transition from a super-critical to a sub-critical flow [60]. Using the assumptions of Escudier et al. [22], Billiant et al. [10] developed a criterion ($C_{Billant}$ in Eq.(2.7)) for the appearance of the vortex breakdown as:

$$C_{Billant} = \frac{(\int_0^r \rho \frac{u_\theta^2}{r} dr)^{\frac{1}{2}}}{u_a} = \frac{1}{\sqrt{2}}, \tag{2.7}$$

which shows a very good comparison with experimental data [10, 60]. The Rankine vortex of Billiant et al. [10] (Fig. 2.2) is of particular interest since it is prone to hysteresis between different flow states (as the open cone shown in Fig. 2.2 or as a closed bubble) and flow states can appear randomly (as they lie in the same parameter space).

In general, seven different types of vortex breakdown have been identified depending on the Reynolds (Eq. 2.1) and swirl (Eq. 2.2) numbers [23] but "there are numerous parameters ranges for which two forms (or more) can exist and transform spontaneously into each other" [64]. The seven different types of vortex breakdown found by Faler and

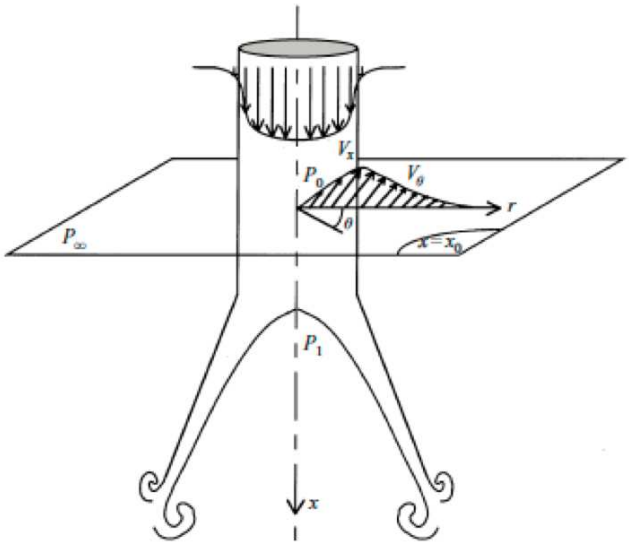

Figure 2.2: Cone vortex breakdown mode, from Billant et al. [10]

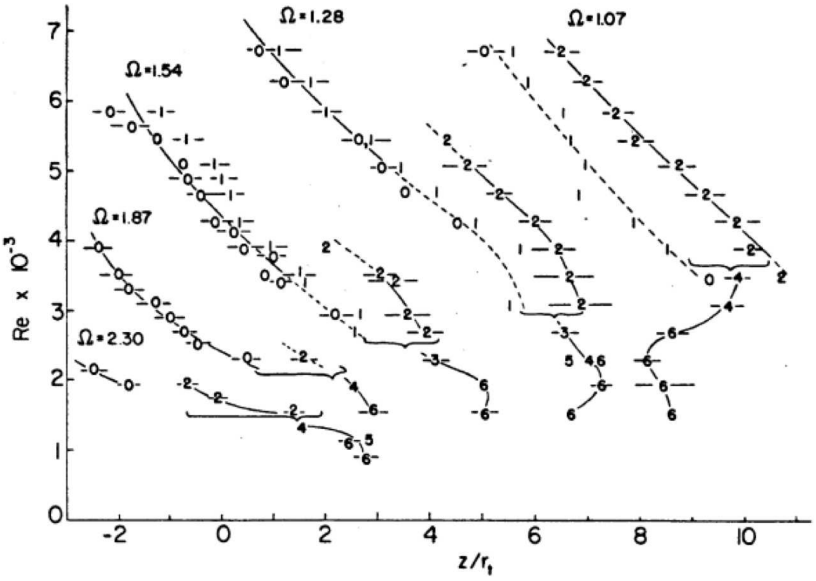

Figure 2.3: Vortex breakdown types (from zero to six) as a function of the Reynolds (in ordinate) and circulation number (in abscissa), from Faler and Leibovich [23]

Leibovich [23] are summarized in Fig. 2.3 where flow states are plotted in the Reynolds number (Re) - circulation number (Ω) space ($\Omega = \frac{\Gamma}{u_a D}$, with $\Gamma = 2\pi R_e u_\theta$).

Mode 3,4,5,6 in Fig. 2.3 are "less commonly observed than the others and occur only for low Re, while at high Reynolds number the only characteristic forms are the bubble (Fig. 2.4(a)) and spiral (Fig. 2.4(b))" [64], respectively modes zero and two in Fig. 2.3 (while mode one is a slightly asymmetric bubble).

The bubble mode is characterized by "a stagnation point on the swirl axis followed by an abrupt expansion of the centerline dye filament to form the envelope of a bubble of

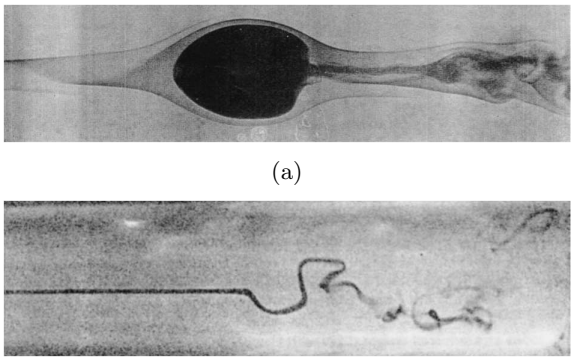

(a)

(b)

Figure 2.4: The bubble mode (a), from Sarpkaya [96], and the spiral mode (b), from Faler and Leibovich [23]

recirculating fluid" [64] (Fig. 2.4(a)). The spiral mode is characterized by "a rapid deceleration of the dye filament marking the swirl axis which causes stagnation and by an abrupt kink followed by a corkscrew-shaped twisting of the dye" [64] (Fig. 2.4(b)). The spiral mode is associated to the instability of the bubble: the development of disturbances in the flow is "responsible for the appearance of a breakdown dominated by spiral waves" [60]. However, this "two-modes" classification (bubble-spiral) is "by no means certain and is open to further interpretation" [60]. Discharge orifice geometry [32] as well as adverse pressure gradient, [96] (i.e. generated by a divergent nozzle) can modify the features of swirl flows; in general "the overall pressure and velocity fields are important as they are interrelated" [34].
A clear example of the large sensitivity of swirling flows to small variations in the flow fields is the delta wing of Lambourne [59] (Fig. 2.5) in which each side of the wing shows different breakdown types at the same time (so, in a first approximation if the flow is axisymmetric, under the same fluid dynamics conditions). Even though it is a physically complex mechanism, vortex breakdown is also a desirable property of high swirl flows as "the vast majority of gas turbine systems employ it to provide flame stabilization" [43].

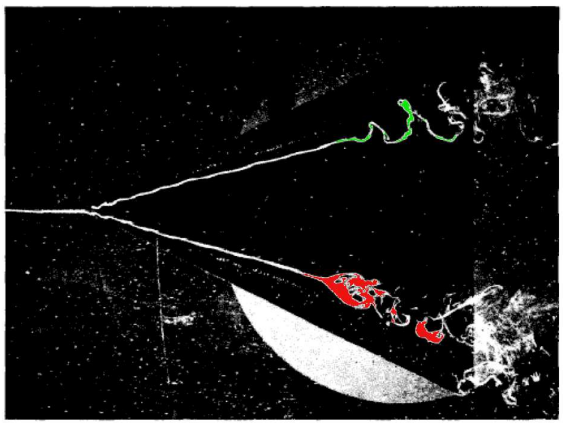

Figure 2.5: Delta wing of Lambourne [59]: upper side, spiral breakdown mode, bottom size, bubble mode. The picture has been colored.

A second important instability of swirling flows is PVC (Fig. 2.6): after vortex breakdown has occurred, "the central forced vortex region of the flow can become unstable and start to precess about the axis of symmetry" [64]. The frequency of the PVC can be characterized by the Strouhal number (which is a weak function of the Reynolds number) and by the swirl number [102]. However, its frequency and shape remain a function of the particular burner/swirler flow system configuration [102].

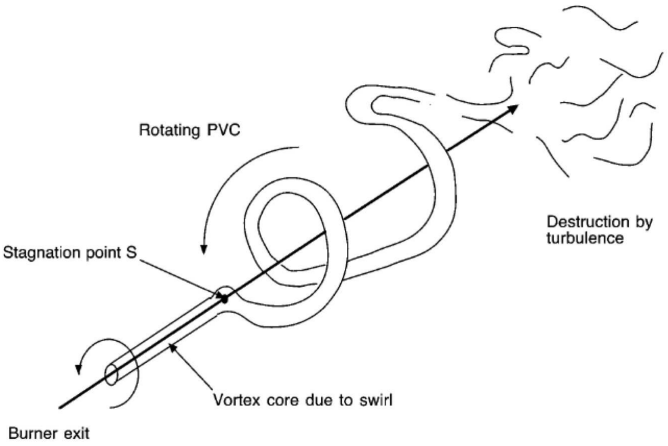

Figure 2.6: Schematic view of the PVC, from Selle et al. [100].

The PVC can be useful or detrimental for the engine performance, since, as stated by Huang [43], "the PVC may improve combustion efficiency through its enhancement of turbulence intensity and mixing, but it also represents a largely undesired characteristic because of the possible resonant coupling with low frequency acoustic oscillation in the gas turbine combustor".
Finally, two types of Kelvin-Helmholtz instabilities, related to the presence of an axial shear layer (which eventually degenerate in an external PVC, as shown by Villalba et al. [28]) and an azimuthal shear layer (which give birth to the helical instabilities shown in Fig. 2.7 which are related to a "stratification" of the angular momentum along the radial direction [60]) can be present in swirling flows depending on the swirl level and the jet configuration.

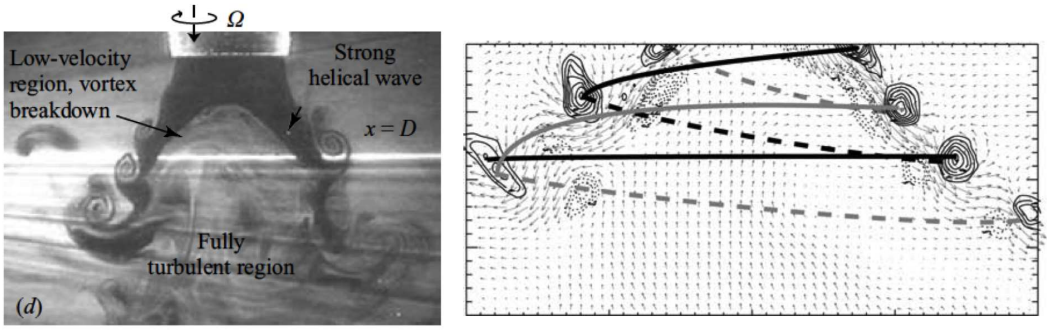

Figure 2.7: From Liang and Maxworthy [60], (left) picture of the free swirling jet and (right) a couple of vortex spirals (helical instabilities).

2.2.3 Bifurcation & hysteresis in confined swirling flows.

This section discusses flow states which can appear in confined swirling flows because of the proximity of solid boundaries. Without confinement walls, after vortex breakdown has occurred, the jet opening half-angle (α, expressed in degrees) varies linearly with the swirl number of the jet [32] as:

$$\alpha = 4.8 + 14 \;\; S. \tag{2.8}$$

Eq.(2.8) is obtained by regression of experimental data. One can imagine this condition as if a solid body is forced to rotate around an axis by a spring. As the solid body gets closer to the axis of rotation, centrifugal force ($F_c = \frac{\rho u_\theta^2}{r}$) gets higher and pushes it radially; moving away from the axis, centrifugal force weakens and the solid body is re-called by the spring. The resulting jet opening angle (in a first approximation) is linearly dependent on the introduced angular momentum (considering a constant streamwise velocity) as the radial position of the solid body would be in the system spring-rotating body.
Above a critical swirl strength (which is configuration dependent), confinement walls alter the expansion angle of the jet, which can attach to the sidewalls and behave like a radial jet, a phenomenon similar to the Coanda effect [32]. The Coanda effect is the tendency of a jet stream to adhere to a wall. Using the words of the first European colloquium on the subject (1965), the Coanda effect is "the rather spectacular phenomenon which can be observed by holding a finger against a jet of water running out of a tap: the jet will adhere to some extent to the finger and be deflected" [112].
The critical swirl number at which this transition takes place is dependent on the nozzle geometry: in Chedaille et al. [46], three different swirling jet configurations appear depending on the nozzle opening angle or on the expansion rate of the divergent nozzle. Similar jet configurations and recirculation zones are reported by Beer and Chigier [8], in a qualitative manner and more recently by Vanierschot and Van Den Bulck [105]. The experiment of Vanierschot et al. [105] (whose geometry is shown in Fig. 2.8) provides a quantitative analysis of a flow with variable swirl and will be used here as a reference example to classify flow states.

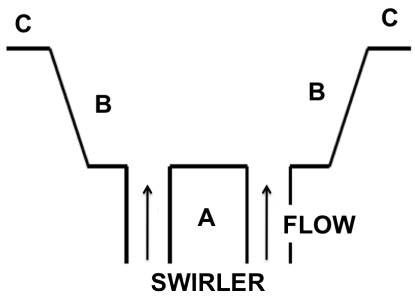

Figure 2.8: Geometry (nozzle) of Vanierschot and Van Den Bulck, [105]. A: central rod, B: nozzle walls, C: side walls. The swirler is upstream while arrows indicate the flow.

Vanierschot et al. [105], investigated the influence of swirl (Eq. 2.2) on an annular jet with a stepped-conical expansion (Fig. 2.8) at $Re = 11000$, identifying four, distinct flow states. The first two states identified by Vanierschot et al. [105], are named here, "Unbroken axial jet" (UJ) and "free Axial Jet" (AJ) (Fig.2.9). UJ states are obtained when $S < 0.4$ while AJ states appear for $S \geq 0.4$. At $S = 0.4$, vortex breakdown takes place

in this configuration. The transition between the "Axial Jet" and the "Weak axial Jet" (WJ), as named here, and the transition between the WJ and the "Blasted Breakdown jet" (BB), as named here, take place as follows (Fig. 2.10).

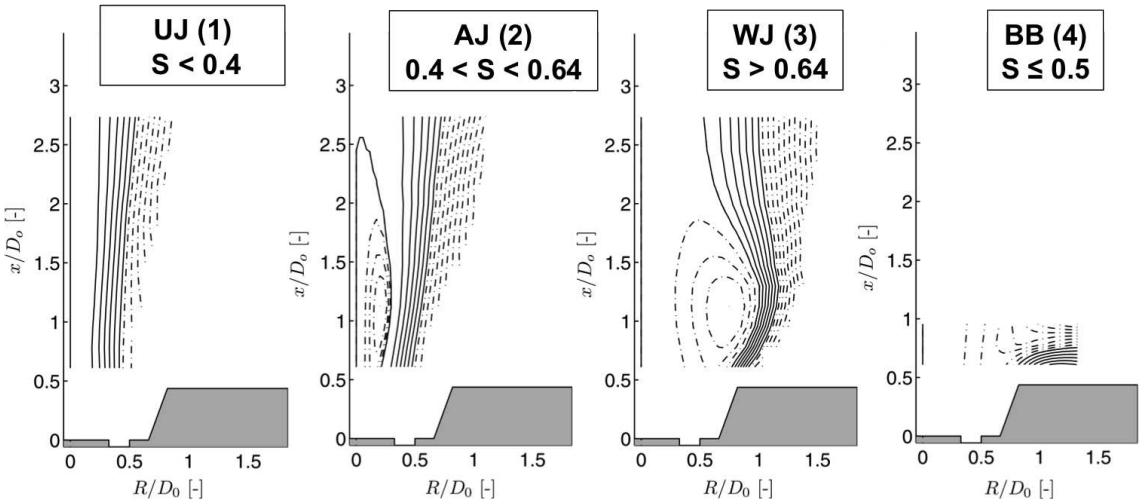

Figure 2.9: Experimental results of Vanierschot and Van Den Bulck, [105]: streamlines for four different flow states. Solid lines correspond to the jet boundaries and dashed-dotted lines are recirculation zones. Swirl number exact values are from left to right: $S = 0.335, 0.56, 0.69, 0.5$.

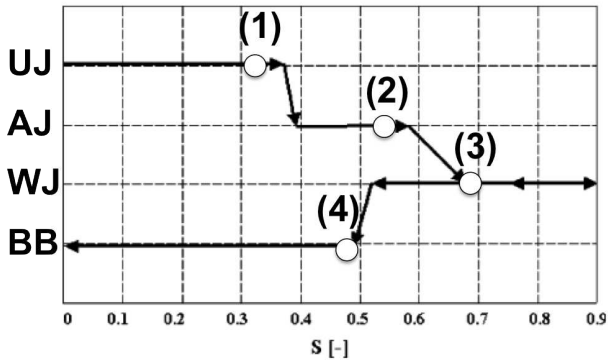

Figure 2.10: Transition map of Vanierschot and Van Den Bulck, [105]. The different flow states are plotted against the swirl number S. The four states of Fig. 2.9 (1 to 4) are added on the diagram.

First, increasing the swirl number up, from state AJ, to the second critical threshold of $S = 0.6$, the flow bifurcates to the WJ state. This bifurcation is characterized by an abrupt expansion of the Central Toroidal Recirculation Zone (CTRZ) which doubles its diameter (Fig. 2.9 & Fig. 2.11(a)). At the same time, the azimuthal velocity (Fig. 2.11(b)), turbulence levels (Fig. 2.11(c)) and the sub-pressure (Fig. 2.11(d)) in the CTRZ, decrease. The transition AJ-WJ is due to the appearance of a vortical structure close to the diffuser walls, named *Corner Recirculation Zone* (CRZ) in [107]. This structure is generated by the interaction of the jet shear layer, which, as the swirl number increases, gets closer to the solid boundary, and the inclined diffuser walls. Because of hysteresis, the WJ state remains stable even when swirl is decreased back to values which are lower than the transition point AJ-WJ ($S = 0.6$). At $S = 0.5$ (transition WJ-BB), a third bifurcation

takes place: the recirculation zone widens even more (its "eye" has disappeared from Fig. 2.9 & Fig. 2.11(a)); sub-pressure (Fig. 2.11(d)), tangential velocity (Fig. 2.11(b)) and turbulent intensity (Fig. 2.11(c)) drop to zero close to the flow centerline (where the vortex breakdown, in the WJ state, is located). Subpressure, or pressure deficit, is defined as:

$$P_D = (P_{atm} - P)/(0.5\ U_0^2\ \rho), \tag{2.9}$$

where P_{atm} is the far field atmospheric pressure, P is the local pressure, while $0.5\ U_0^2\ \rho$ is the kinetic energy of the jet[2]. In Vanierschot et al. [108] this counter-intuitive behavior (an expanding CTRZ with a decreasing swirl) is explained with a pressure balance between the CTRZ and the surroundings. In the author's opinion, this transition has to be explained with the CRZ dynamics (as for example explained in Vanierschot et al. [107] which seems to be in contradiction with itself [108]) and with the flow field close to the discharge orifice. However, the present work will not focus on this controversial and geometry dependent aspect. The characteristics of the three flow states of interest for the current study are summarized in table 2.2: after each transition (AJ-WJ-BB) CTRZ expands, tangential velocity and subpressure (which are inter-related) diminish, turbulence intensity reduces. For a swirl number of 0.3, for example, two very different states (UJ and BB) can be obtained (Fig. 2.10).

flow state	CTRZ size	normalized subpressure	CTRZ tangential velocity	CTRZ Reynolds Stresses
AJ	$R_v < 0.5$	$1.4 < P_D < 0.8$	high	high
WJ	$0.5 < R_v < 1$	$P_D < 0.4$	moderate	moderate
BB	$R_v >> 1$	$P_D = 0$	zero	zero

Table 2.2: Summary of the characteristics of the three different states (AJ-WJ-BB) documented in [105] after vortex breakdown. R_v indicates the approximate radial position of the "eye" of the CTRZ.

As mentioned before, similar results are present in the literature but no quantitative characterization of the flow (such as RMS profiles) are available. Fig. 2.12 shows the flow patterns described by Beer and Chigier [8] for a divergent nozzle (the figure is extracted from [83]). The swirl number increases from the flow of type A to type C. The type A flow, using the nomenclature used to classify [105], is a UJ, the type B is an AJ and the type C looks like a BB: no WJ was documented in [8].

Finally Fig. 2.13 shows the flow states documented in Chedaille et al. [46]. The flow configuration named B in Fig. 2.13 corresponds to an AJ state while configurations B' and C are more difficult to classify. Flows B' and C show a recirculation zone which is "open-ended and the annular character of the flow is preserved for the entire length of the chamber" [46]. Also, "the internal reverse flow is weak and the static pressure throughout the whole recirculation zone is close to atmospheric" [46] (see the WJ and BB states of table 2.2). States B' and C appear depending on the nozzle geometry.

[2]Pressure deficit is usually measured inside the recirculation zone where it is minimum. Therefore, the subpressure characterizes the strength of the recirculating flow.

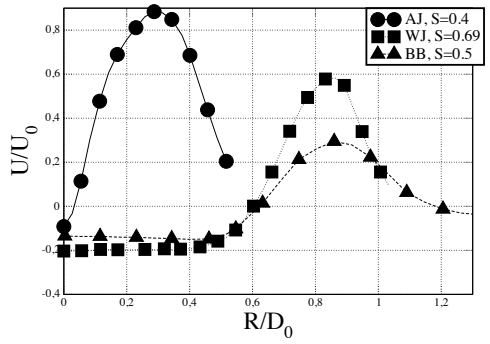

(a) Axial speed.

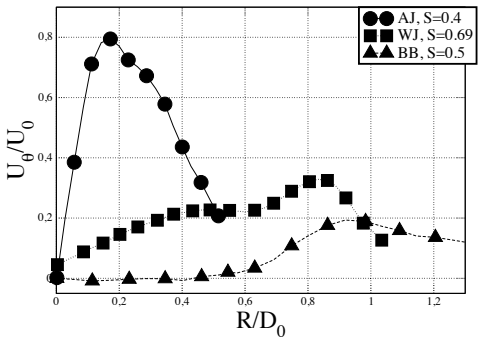

(b) Tangential speed.

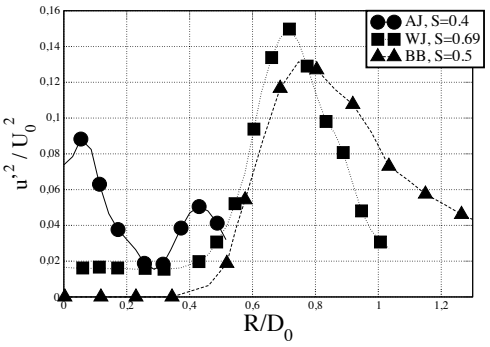

(c) Axial Reynolds stresses.

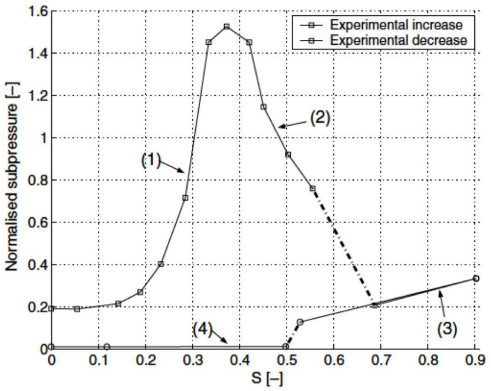

(d) Normalized subpressure.

Figure 2.11: (a)-(b)-(c) Flow measurement at an axial position of $x/D = 0.61$ plotted against the swirl number S, for the AJ, WJ and BB states. (d) Normalized subpressure ($P_D = \frac{P_{atm}-P}{0.5\rho U_0^2}$) where P is measured $3[mm]$ downstream of the injector orifice plotted against the swirl number S (rearranged from [105]).

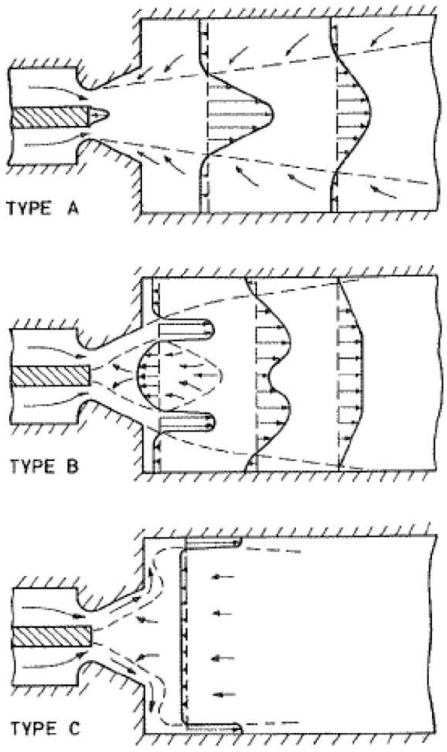

(a)

Figure 2.12: From[83] (rearranged from [8]): flow states issuing from a divergent nozzle, swirl intensity increases from type A to type C flows. Flow states show characteristics similar to Vanierschot et al.[105] (Fig. 2.9).

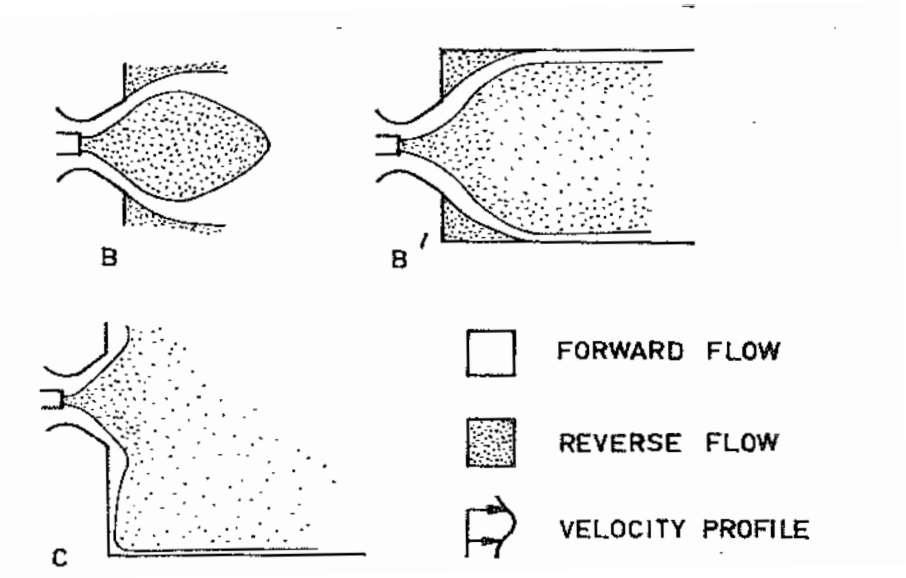

Figure 2.13: From[46] Flow states show characteristics similar to Vanierschot et al.[105] (Fig. 2.9).

2.3 Mathematical definition of bifurcation

This section, extracted from the book of Y.A. Kuznetsov "Elements of Applied Bifurcation Theory" [57], gives a very brief overview of dynamical systems and of bifurcation. A mathematically rigorous analysis of the phenomena described in this thesis would be too complicated because of the flow configuration complexity (such analytical efforts are commonly focused on much simpler-configuration, free swirling flows [60, 61]; already such type of canonical problems require complex analytical solutions).
A dynamical system is "the mathematical formalization of the general scientific concept of a deterministic process" [57]. "The future and past states of many physical, economical, chemical systems can be predicted knowing their present state and the laws (φ^t) governing their evolution" [57]. A dynamical system is defined as:

Definition 1 *A dynamical system is a triple* $\{T, X, \varphi^t\}$ *where* T *is a time set,* X *is a state space and* φ^t *is a family of evolution operators parametrized by* $t \in T$ *and satisfying* $\varphi^0 x = x$ *and* $\varphi^{t+s} x = \varphi^t(\varphi^s x)$

The properties of a dynamical system can be represented using geometrical images. The basic geometrical objects associated with a dynamical system $\{T, x, \varphi^t\}$ are its orbits in the state space ($Orbit(x_0) = \{x \in X : x = \varphi^t x_0, \forall \;\; t \in T$ such that $\varphi^t x_0$ is defined$\}$) and the phase portraits composed of these orbits. Orbits in continuous-time system with continuous evolution operator are curves in the state space X parametrized by the time t and oriented by its direction of increase (see Fig. 2.14). A phase portrait of a continuous-time dynamical system could be "interpreted as an image of the flow of some fluid, where the orbits show the path of the "fluid particles" as they follow the current" [57]. All possible orbits can be classified into equilibrium points (x^0 is an equilibrium point if $x^0 \in X \;\; \varphi^t x^0 = x^0 \;\; \forall t \in T$), cycles (see later for the definition of a periodic cycle) and "all others" [57].
Dynamical system can depend on parameters. Let us take a dynamical system of such type, in the continuous-time case it can be written as:

$$\dot{x} = f(x, \alpha), \tag{2.10}$$

where $x \in \mathbb{R}$ and $\alpha \in \mathbb{R}^m$ represent phase variables and parameters respectively. As the parameters vary, the phase portrait (the "flow field") also varies. There are two possibilities: **either the system remains topologically equivalent to the original one**[3], **or its topology changes**. This is taken as the definition of a bifurcation:

Definition 2 *The appearance of a topologically nonequivalent phase portrait under variation of parameters is called a* ***bifurcation****.*

Thus a bifurcation is a change of the topological type of the system as its parameters pass through a *bifurcation (critical) value*. In order to clarify this definition, an example of

[3] "Two topologically equivalent systems have the same number of equilibria and cycles of the same stability types. Formally two systems are topologically equivalent if there is an homeomorphis (an invertible map such that both the map and its inverse are continuous) mapping the orbits of the first system onto orbits of the second system preserving the direction of time" [57].

bifurcation is given. Consider a planar system in polar coordinates ($\rho = radius, \theta = angle$) as:

$$\begin{cases} \dot{\rho} = \rho(\alpha - \rho^2), \\ \dot{\theta} = 1. \end{cases} \tag{2.11}$$

Since α and θ are independent in Eq.(2.11), it is possible to easily draw phase portraits of the system in a fixed neighborhood of the origin (Fig. 2.14).

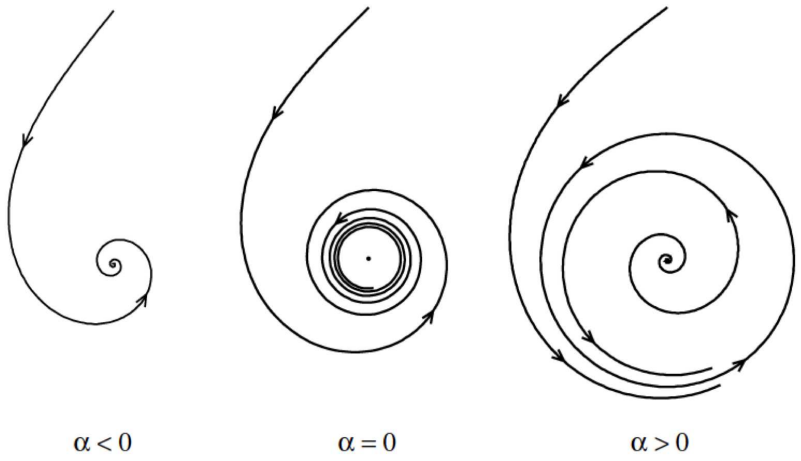

Figure 2.14: From [57], phase portraits of an Hopf bifurcation.

For $\alpha < 0$ the equilibrium is a stable focus (for which perturbations decay oscillatorily, the system always "falls" to $\rho = 0$), since $\dot{\rho} < 0$ and $\rho(t) \to 0$ if we start from any initial point. On the other hand, if $\alpha \geq 0$ it is easy to see that the system has a periodic orbit at $\rho_0 = \sqrt{\alpha}$ (a periodic orbit L_0 is defined as: $\varphi^{t+T_0} x_0 = \varphi^t x_0 \ \forall x_0 \in L_0$ with some $T_0 > 0$) and this periodic orbit is stable since $\dot{\rho} > 0$ if $\rho < \rho_0$ and $\dot{\rho} < 0$ if $\rho > \rho_0$. Therefore $\alpha = 0$ is a bifurcation parameter value since the topology of the system varies (compare the phase portraits of Fig. 2.14 for $\alpha < 0$ and $\alpha \geq 0$). This type of bifurcation is called the *Andronov-Hopf bifurcation*.
Swirl flows are subject to bifurcations, for instance the one shown in Liang and Maxworthy [60] is likely to be of the Andronov-Hopf type. Even turbulence can be explained with the evolution of a dynamical system. As stated by Jimenez [50], "one of the surprising discoveries of the last fifty years has been that deterministic systems with relatively few degrees of freedom can behave in very complex ways, and that as soon as the topological restriction of two-dimensional systems is removed (the system of Eq.(2.11) is two-dimensional), the generic behavior of an arbitrary system is to be chaotic". The key property of chaotic system is their sensitivity to initial conditions: "two orbits with initial conditions which differs only by a small amount diverge exponentially and soon become completely de-correlated" [50], as happens to "flow particles" in turbulent flows.

2.4 LES of realistic swirl injectors: state of the art

This section is dedicated to a brief review of LES of aeronautical swirling flows, results are analyzed with a particular focus on the similarities/differences with the LOTAR injector

that will be shown on chapters 3 & 4, and on useful tips in terms of numerics and mesh requirements. Swirl motion is usually generated in aeronautical engines by a swirler; the swirler is commonly mounted at the entry of the combustion chamber as vortex breakdown is used to stabilize the flame, to help ignition by the transport of burnt gases at the fuel injection point and to improve mixing via higher turbulence levels. Fig. 2.4 shows an example of such devices.

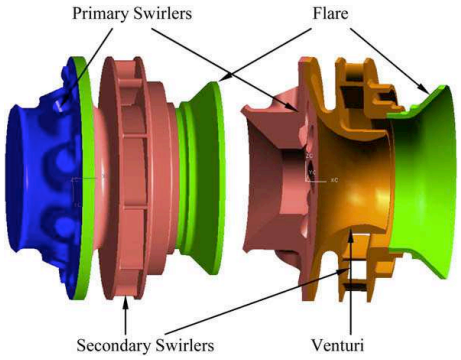

Figure 2.15: Swirler of Wang et al.[111].

The swirler of Fig. 2.4 consists of eight counter-clockwise elliptical primary jets and ten clockwise secondary vanes, a venturi section and a flare and it was numerically studied by Wang et al. [111] using a compressible LES solver (finite differences on a fully structured grid, 2^{nd} order accurate in space and time, employing static and dynamic [29] Smagorinsky SGS models and the Van Driest dumping function near the walls). The computational domain of Wang et al. [111] was restricted to the swirler and the downstream chamber, inlet boundary conditions were imposed inside the swirler vanes using average values obtained by a RANS simulation (a similar exercise will be done in this thesis in chapter 4). The "typical" flow structures of high swirl confined flows are present in this configuration: a Precessing Vortex Core (PVC), Central Toroidal Recirculation Zone (CTRZ) and Corner Recirculation Zones (CRZ) at the periphery of the chamber; proper-orthogonal-decomposition (POD) analysis reveals that the PVC is dictating flow dynamics, while standing acoustic waves play a minor role. A similar study was repeated by the same authors (Wang and Yang [109, 110]) for a twin-swirler injector. This study [109, 110] focuses on the different flow instabilities and their interaction for different swirl numbers and in forcing conditions and it can be used as a source of inspiration for a further analysis of the swirler studied here.
A realistic, complex Pratt & Whitney combustor (only a portion of the whole device), with a swirl injector device is the simulation domain of Moin and Apte [74]. Due to the complexity of the geometry, domain is triangulated via irregular polyhedra (hybrid mesh with tetrahedra, prisms, pyramids) and a compressible LES formulation equations is performed using an energy conserving, finite volume, numerical algorithm [67].

A specific aspect of this paper is the numerical scheme employed (energy conserving). Numerical dissipation has been shown to be detrimental in accurate prediction of turbulent flows, for instance in Mittal et al. [73] an up-wind biased high-order numerical methods is compared with a lower order central difference numerical scheme on flow past a cylinder at Re=3900: numerical dissipation inherent in the up-wind scheme removes substantial

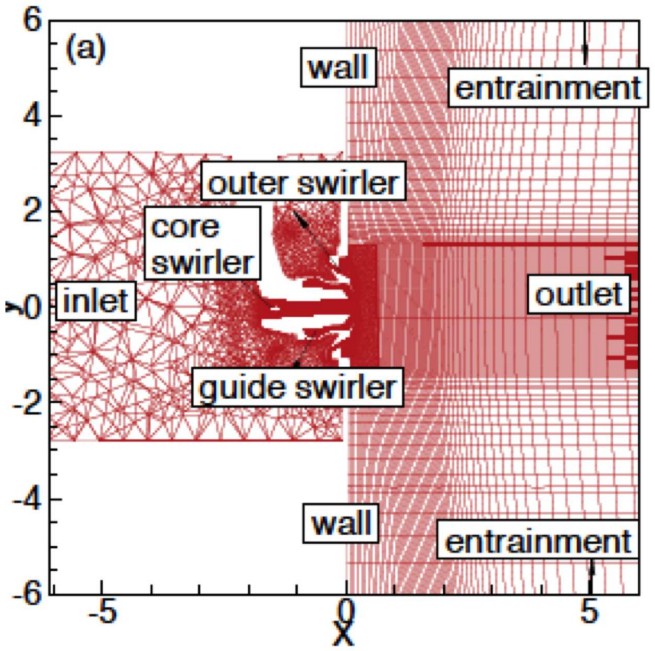

Figure 2.16: Pratt & Whitney combustor of Moin et al. [74]

energy from roughly three quarters of the resolved wave number range, while the non-dissipative, lower order central scheme shows much better agreement with experimental energy spectrum. The impact of the numerical scheme is clarified in Mahesh et al. [67]. The numerical algorithm is a kinetic energy conserving finite volume scheme with no artificial viscosity. Energy conservation assures that numerical instabilities due to non-dissipative central difference schemes remain bounded. With such a scheme a fully non-dissipative (switching off SGS modeling) HIT (Homogeneous Isotropic Turbulence) simulation at $Re = O(10^9)$ is obtained without any dissipation of kinetic energy (for such a Re, viscous scales lies outside the grid spacing and kinetic energy is transferred from the largest scale to smallest and remains there because, in absence of an eddy viscosity model, it can only be dissipated by laminar viscosity).

It is important to note that the criterion of kinetic energy conserving schemes is not globally accepted by the LES community. Many finite differences schemes and hybrid schemes [77, 93] do not try to conserve kinetic energy, as for a compressible flow it is not conserved. Moreover tests show that a 3^{rd} or 4^{th} order scheme (as the one used in the present work) which does not conserve kinetic energy still offers much better precision than a second order scheme conserving kinetic energy on simple tests such as the conservation of vorticity. Focusing on swirling flows, numerical dissipation gives a faster decay to swirl velocities and this has an impact on length of the recirculation region [104].

Swirl injectors are everyday bread of CERFACS researchers and some of their results will be summarized below. One of the classical applications of LES is to couple it with an acoustic solver [68, 91, 100]. LES is used to extract unsteady flame response to resolved acoustic oscillations (heat release). The obtained Flame Transfer Function (FTF) is fed to the acoustic solver, flame/acoustics interaction are then studied in order to optimize

combustion chamber design. In Selle et al. [100] this coupled LES- Helmoltz solver is performed on the geometry of Fig. 2.17.

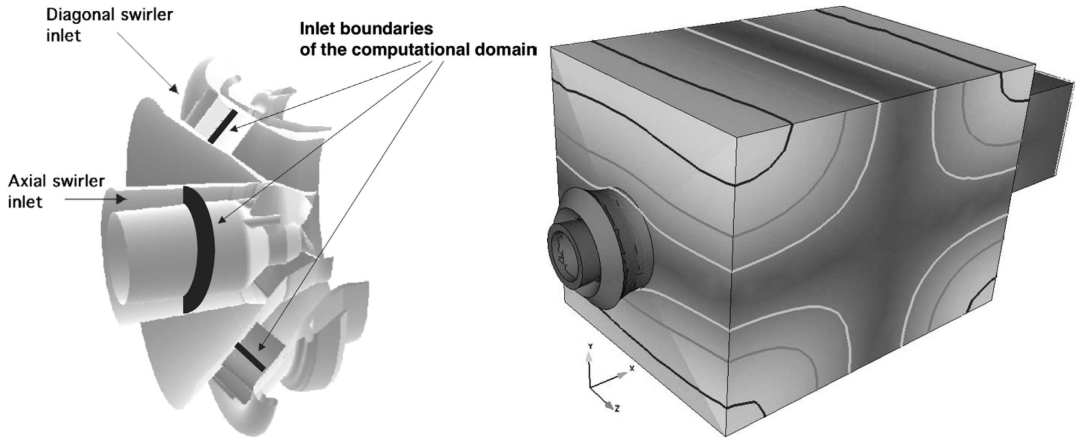

Figure 2.17: (a)Injector of and (b) pressure fluctuation modulo if on e transverse mode calculated by the Helmoltz solver from [100]

Results of Selle et al. [100] show that the flow field in the reacting configuration is dominated by a PVC at a Strouhal number $St = 0.62$ (typical of these swirl flows, see section 4.6.2), while the reacting case is fully dominated by acoustics and the PVC is not observed. Similar results were obtained recently by Oberleithner et al. [81] which shows how non-uniform density suppresses the PVC. A similar numerical experiment is repeated in Roux et al. [91], where the computational domain is enlarged in order to reduce BCs effects (which are placed inside the vanes in [100], see Fig. 2.17). A phenomenon similar to [100] is again experienced: cold flow is hydrodynamically dominated by a PVC (no acoustics eigenmodes around its frequency are identified) while reacting case is dominated by acoustics. Combustion, dilatation and increased viscosity induced in the burnt gases seem to damp the PVC, while the flame acts as a strong acoustic energy source. As for [100], LES prediction matches experimental data without tuning BCs.

A non-reacting, two-phase flow staged, injector was simulated by Sanjose et al. [95] and Jaegle et al. [48] (Fig. 2.18). The swirler design is basically the same as LOTAR and the injector is a good example of recent staged architectures: three counter-rotating jets are generated by a series of three different swirl vanes. Flow split in this configuration is 90% through the radial swirler (while for LOTAR is $\approx 86\%$) and 10% in the two co-axial swirlers but no comparison with the experimental permeability measurements is available. Results showed a good comparison with experimental data for the axial and the tangential velocity components for both single and multiphase approaches, while the radial velocity component is not shown.
To summarize the non exhaustive survey given in this section, several issues in simulating swirl flows of real injectors have been identified. The first limitation of real life LES is related to the grid used to discretize the domain: while structured grids can be generated to discretize simple geometries, their use is almost impossible when the level of geometrical detail is increased. Structured meshes are put aside and unstructured meshes within

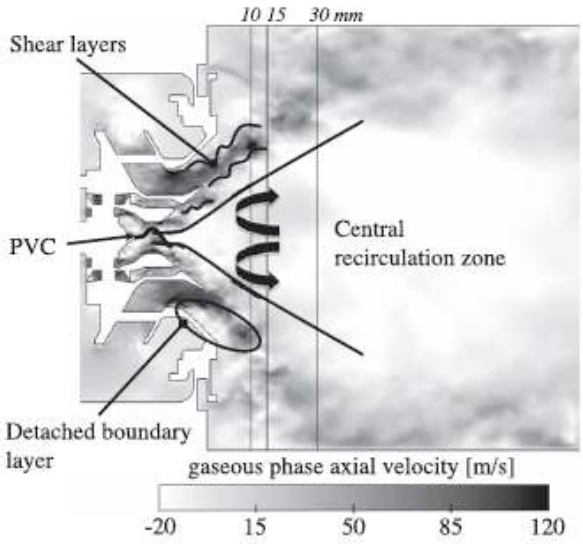

Figure 2.18: domain and flow structures of [48]

elements of any shape must be deployed; at the present time commercial programs are able to generate such unstructured meshes using tetrahedral elements, fast and accurately. Unstructured meshes imply that finite differences, so in general higher-order schemes, such as six or eight-order accurate, cannot be employed. Variational methods, such as Finite Volumes or Finite Elements must be used.

As for higher-order methods, it is difficult to perform explicit filtering LES on unstructured meshes. At the present time explicit filters have been used only on academic cases [12, 66, 30] and implicit filtering in LES is often the only practical solution for complex geometries (despite the numerical corruption of the highest wave number [31, 16]). However, from the theoretical point of view, implicit filtering in LES cannot be strictly derived from the Navier Stokes equations if the filter is not homogeneous in space [66]; from a more practical point of view, to define filter size (which determines the magnitude of the modeled term in LES) on highly anisotropic grids is an open research issue [98, 97]. Finally a properly resolved LES everywhere in the flow field is an expensive task, modeling is necessary and therefore remains a central issue; in particular cases, such as LOTAR, it will be shown that LES modeling can trigger strong variations in the simulated flow field. These three main issues, which impact accuracy for a single-phase, non-reacting flow, were already itemized by Selle et al. [100]:

1. dispersion and dissipation of numerical schemes,
2. filtering operation on unstructured grids,
3. modeling subfilter phenomena.

The impact of these issues grows with the level of complexity of the flow as multiple instabilities can arise depending on the LES setting (as will be shown in this work). Despite these drawbacks LES represent the future in this field as RANS, for such complex turbulent flows, fails in predicting the proper velocity profiles. In Moin et al. [74] RANS

velocity profiles are off experimental data by a large amount. In Wang et al. [111] RANS predicts the two jets to counter rotate while experiment shows a strong mixing with only clockwise velocity profiles. In Kim and Syed [52] LES and RANS are directly compared: RANS modeling fails in predicting spreading of a swirling jet in a confined aero rig or to properly simulate jet in cross flow. This suggests that LES is the only tool which is sufficiently accurate to simulate swirl injectors.

	STRUCTURED	UNSTRUCTURED
RANS	Wang et al. [111]	Moin et al. [74]
LES	Wang et al. [111]	Jaegle et al. [48], Selle et al. [100] Roux et al. [91], Moin et al. [74]

Table 2.3: LES analyzed in this section

Considering LES performed at CERFACS, there is a clear trend in increase the simulation domain in order to include all geometrical details of the combustion chamber and the plenum. Such an increase and an effort to extend the CFD domain is mainly motivated by the importance of acoustics which requires proper boundary conditions. Clearly it is easier to define a boundary condition at the plenum inlet and outlet from the acoustics and fluid dynamics point of view than inside the vanes of a swirler or in the middle of a chamber. In the case of a multiple passages injector, computing the whole domain, including the plenum, also avoids to guess the flow split.
Note also that in none of the simulations of industrial swirlers of this section, bifurcations or hysteresis as the one shown here in chapters 3 & 4 were identified. Even though these mechanisms may have been observed, they were not reported yet. This is why they are specifically discussed in the present thesis.

Chapter 3

Sensitivity analysis of swirling flows LES to numerical settings

3.1 The LOTAR experiment: description and working conditions

The fuel injector used on LOTAR set-up is a SNECMA aeronautical injector displayed in Fig. 3.1 & 3.2. This multipoint injection system was used during the TLC European program [36]. It consists of "a pilot injector, surrounded by two axial swirlers and a multipoint injection system, surrounded by a radial swirler with a perforated plate which let's air bypass the injection swirlers to create a cooling film on the periphery of the section" [82] (here it will be also referred to cooling film).

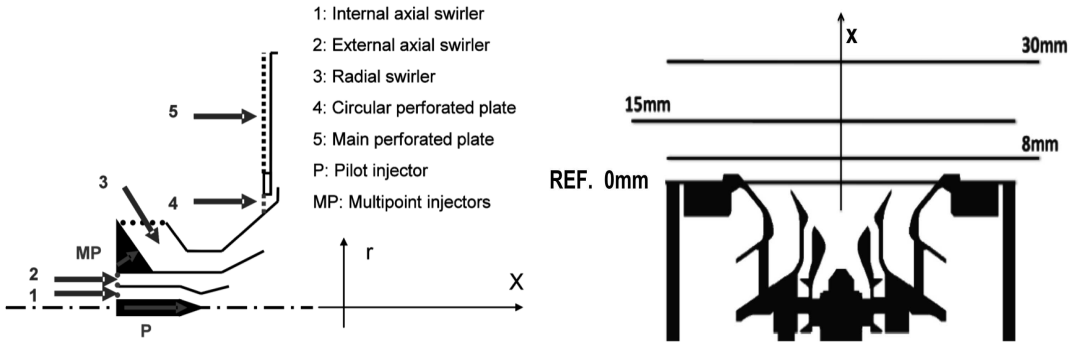

Figure 3.1: (a) Injector scheme from ONERA KIAI deliverables[82] and (b) measurement planes. The zero position (REF. in Fig.) corresponds to the end plate of the injector.

Each swirler stage generates a counter rotating jet, increasing shear and turbulence level and improving mixing in between the two phases. Experimental measurements are taken in open atmosphere: the injector is fed with air and the resulting free jet is analyzed in terms of the mean and root mean square (RMS) velocity field. The injection device is mounted downstream of a plenum. Measurements are taken at three different planes situated 8 [mm], 15 [mm] and 30 [mm] downstream of the injector end plate along two

perpendicular directions, Fig. 3.1b. Velocity profiles were measured with a Laser Doppler Anemometry (LDA) technique [82]. ONERA used zirconium dioxide (ZrO2) particles injected inside the plenum; the particles mean diameter was 3e-6 [m] [82].

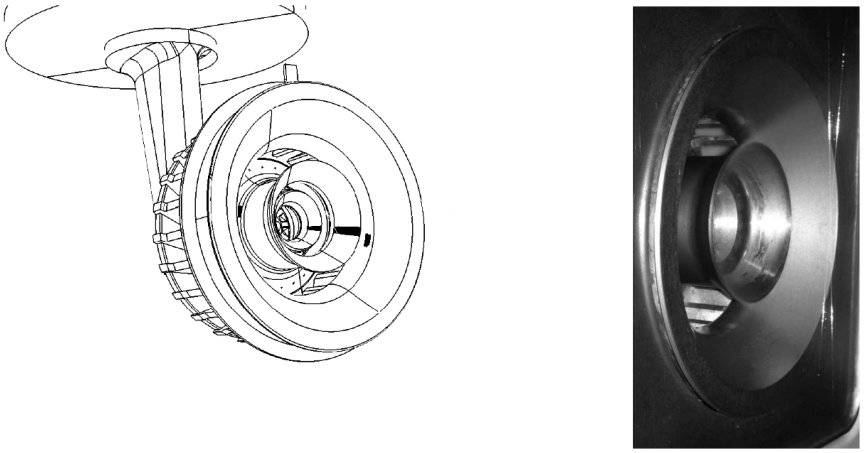

Figure 3.2: Injector device, CAD and real picture, from ONERA KIAI deliverables [82].

The injector is fed with a mass flow rate of 138 [g/s], with a confidence of 2.6 %, at 270 K. The atmospheric pressure of the chamber is 99000 [Pa]. Pressure is measured between the atmosphere and the plenum using a 0 to 10 kPa micro-manometer with an accuracy of 0.1 %. The pressure drop corresponding to this condition is **4.8 KPa**. Permeability measurements are also available with the corresponding flow split between the five different air passages of Fig. 3.1(three swirler stages + circular and main perforated plates). Globally 5 % of the mass flow rate pass through the innermost axial swirler (1 in Fig. 3.1a), 7 % through outermost axial swirler (2 in Fig. 3.1a) and 62 % through the radial stage (3 in Fig. 3.1a). The remaining 26 % is evacuated by the perforated plates (4 & 5 in Fig. 3.1a), used for cooling purposes.
Thanks to permeability measurements the flow split is, under a first approximation, known: it is therefore possible to avoid including these small passages in LES (as it will be done in chapter 4 *for all* flow passages of Fig. 3.1). Note that, even though bifurcations will be observed between the AJ and BB states (see the nomenclature of section 2.2) only the AJ state was observed experimentally. Studying bifurcation in LES was not the objective of the LOTAR experiment and no time was available to study this question experimentally at ONERA since it would have required substantial modifications of the experimental setup.

3.2 The LOTAR LES

The numerical settings are obtained by plugging the mesh obtained from the CAD of the swirler injector in an open atmosphere like cylinder. The swirler blows into open atmosphere where the domain is limited to a large cylinder with non reflecting boundary conditions [87] (Fig. 3.3 right). As in the experiment, the injector studied with these conditions in LES, generates an unconfined jet.

3.2.1 Boundary & initial conditions, numerical grid.

Fig. 3.3 shows a cut of the injector mounted inside the plenum and its boundary conditions ("swirler B.C.s"), the whole simulation domain and its boundary conditions ("far field B.C.s"). Boundary conditions are summarized in table 3.1.

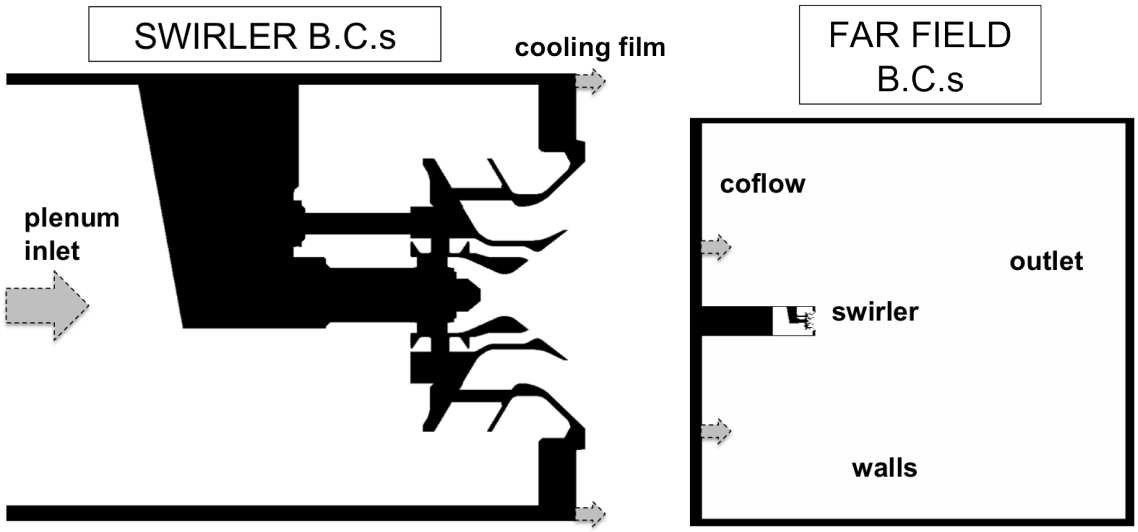

Figure 3.3: LOTAR boundary conditions. Arrows indicates inlets.

There are three inlets in the simulation domain, represented in Fig. 3.3 by arrows. The first inlet, named *coflow*[1], is introduced far upstream of the injector with an imposed velocity of 1 [m/s], (1.3 % of the jet characteristic speed). In the current analysis, the zone upstream of the injector is included (Fig. 3.3) and the largest flow structures generated by the jet in the cylindrical box are explicitly resolved. To test the effects of the coflow, a simulation was performed imposing a higher streamwise velocity (10 [m/s]) in section 4: the jet is not modified, confirming, as shown in [28], that the coflow speed has no major influence on the flow structure.
The second inlet, named *plenum inlet*, feeds only the two stages of the injector device, since the main and the circular perforated plates of Fig. 3.1(a), are not included in the geometry. The mass flow rate imposed at the *plenum inlet* is derived from the permeability measurement and equal to the supposed value passing through the swirler injector alone ($5\% + 7\% + 62\% = 74\%$ of 138 [g/s] so 102 [g/s]). This choice has been made to avoid meshing the extremely small details of the perforated plates.
The cooling film originated by the flow passing through the main perforated plate is not negligible in terms of top speed (from experimental results ≈ 40 [m/s]) and mass flow rate (from permeability measurement 22 % of 138 [g/s] so 30.36 [g/s]). Therefore a third inlet, named *cooling film*, representative of this flux, is directly introduced inside the atmosphere-like cylinder and the imposed target value is derived from the permeability measurement.

[1]The introduction of a coflow is a usual method to simplify the computation of jets, especially in terms of boundary conditions for compressible flows. It is justified only if the coflow has a limited effect on the results. This was verified in our setup for the configuration studied in Chapter 4, while these results are shown in Appendix B.

Fig. 3.4 clarifies this setup.

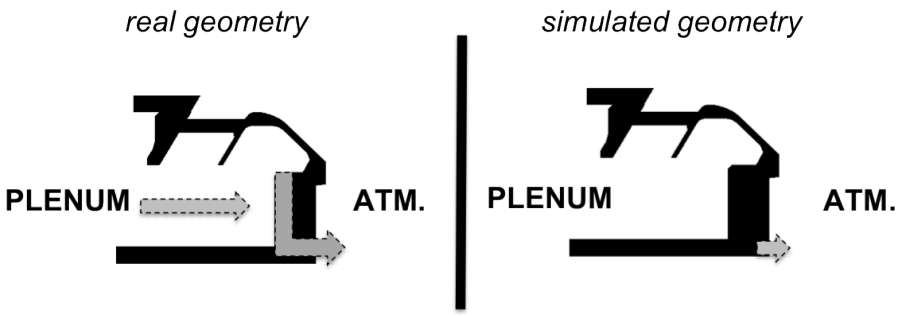

Figure 3.4: Real geometry scheme: a perforated plate connects the plenum and the open atmosphere (left). Simulated geometry, the perforated plate has been erased and an inlet is directly introduced in open atmosphere (right). The corresponding flow rate is deducted from the flow rate injected in the plenum by B.C. "plenum inlet" of Fig. 3.3.

At the periphery of the cylinder, solid walls are setup. The simulation outlet is located at the end of the cylinder. Boundary conditions at the periphery of the cylindrical box have been pushed as far as possible from the injector nozzle and the mesh size increases in their proximity to damp numerical oscillations. The bounding cylinder was sufficiently wide to totally contain the recirculation zone created by the jet, as will be shown later on. Because a bigger cylindrical box would have increased the computational cost without improving accuracy, its dimensions have been limited.

Reference temperature = 270 [K]		
BC NAME	IMPOSED PROPERTY	TARGET VALUE
coflow	velocity	1 $[m/s]$
plenum inlet	mass flow rate	102 $[g/s]$
cooling film	mass flow rate	30.3 $[g/s]$
outlet	pressure	99000 $[Pa]$
walls	adherence, impermeability, adiabaticity	

Table 3.1: Imposed values for boundary conditions sketched in Fig. 3.3.

In AVBP, as acoustics are directly simulated, each BCs target value is reached in a relaxation time (imposing a relaxation coefficient) to avoid reflexion of sound wave or their generation. In YALES2, thanks to the incompressibility assumption, boundary values are imposed in an hard way. Quantitatively, in terms of target values, the same set of boundary condition is used in YALES2 & AVBP. At the plenum inlet a volumetric mass flow rate is imposed and at the outlet, a reference pressure (in YALES2 outlet BC is based on the so-called *convective boundary condition* [85]). In both codes the imposed mass flow rates are the same. The mesh named *basic* in table 2.1 is presented in Fig. 3.5(a). The *basic* mesh has 2499443 nodes and 14081708 elements. It is a fully unstructured tetrahedral mesh. The minimum element volume is $\approx 3 \times 10^{-4}\,[\mathrm{mm}^3] < 0.1^3\,[\mathrm{mm}^3]$ and it is located inside the innermost axial swirler. The mesh wall resolution (Fig. 3.5(b)) expressed in terms of walls units:

$$y^+ = y\frac{u_\tau}{\nu}, \tag{3.1}$$

where u_τ is the friction velocity and y is the wall distance in [m], is in the range[2] $y^+ \in [30, 100]$.

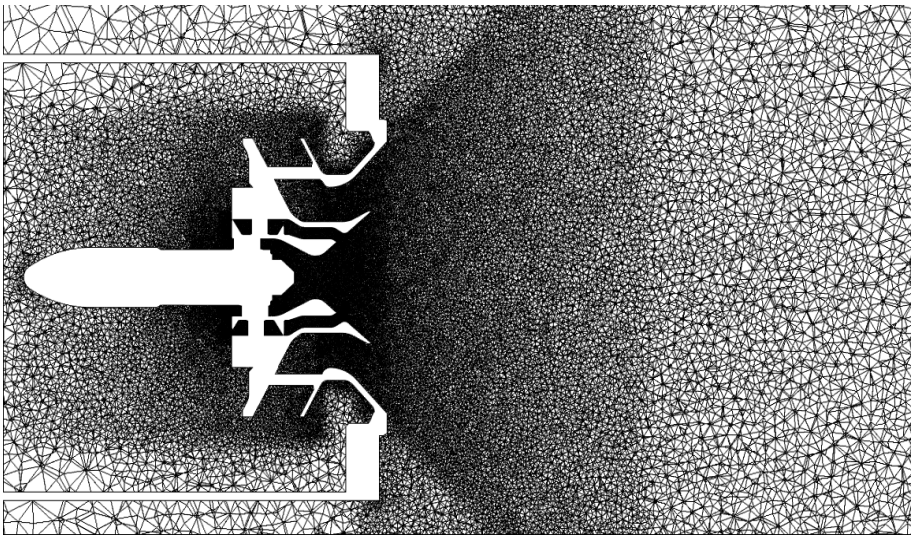

(a) Mesh, bulk of the jet.

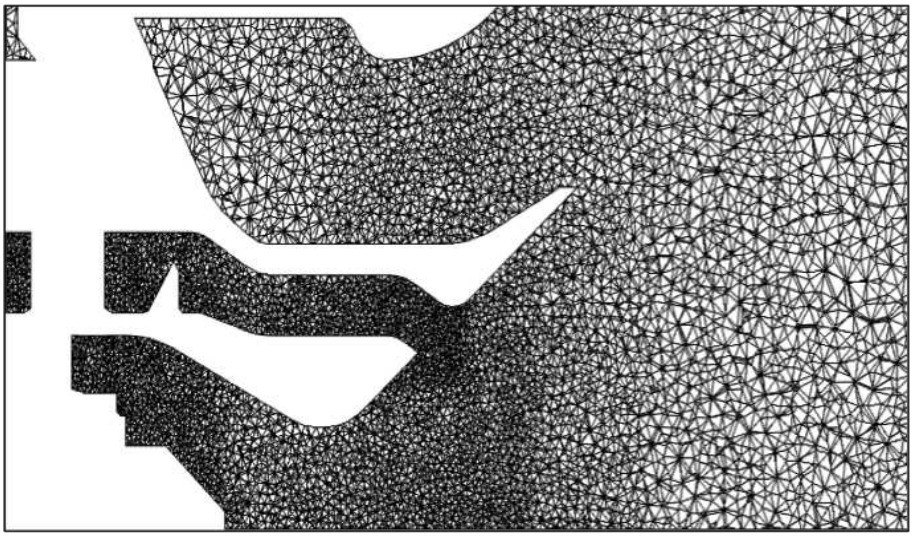

(b) Mesh, zoom at the walls.

Figure 3.5: Numerical grid named *basic* mesh.

Most simulations start from a zero velocity[3] solution except when bifurcation diagrams are studied for which LES are initialized using the final state of the previous run, as it will be done in chapter 4. All simulations run for at least 0.050 [s] equivalent to 5 flow through times, considering the plenum length, O(0.1) [m] and imposed velocity, O(10) [m/s].

[2]In Chapter 9 the y^+ distribution in the domain is shown.

[3]In AVBP the initial velocity field was imposed to be 1 [m/s] to avoid the generation of acoustic waves by the *coflow* inlet.

3.2.2 LES solvers & settings.

All simulations of the present work are performed using the compressible LES solver named AVBP [93, 92] or the incompressible LES solver named YALES2 [76].
AVBP is a finite-volume/elements solver, cell-vertex (i.e. variables are stored at nodes while conservation laws are integrated inside the elements).
YALES2 is a finite-volume solver, vertex centered (equations are solved at the element vertex), 4th-order accurate in space.
The numerical scheme chosen for time advancement is Lax Wendroff for AVBP while is TRK4 [55], for YALES2. TRK4 (or TFV4A) is a fourth order time integration scheme providing a large region of stability (in terms of the Courant-Friedrichs-Lewy, CFL, number) which gives the possibility to adjust the incorporated numerical diffusion [55]. The CFL number chosen for the current study is 0.9 for YALES2 and 0.7 (acoustic CFL number) for AVBP.
Both solvers use classical LES models. "The Large-Eddy Simulation derivation of governing equations is obtained by introducing operators to be applied to the set of compressible or incompressible Navier-Stokes equations. Unclosed terms arise from these manipulations and models need to be supplied for the problem to be solved. The peculiarity of LES comes from the operator employed in the derivation. In LES, the operator is a spatially localized time independent filter of given size, Δ, to be applied to a single realization of the studied flow. This spatial average creates a separation between the large (greater than the filter size) and small (smaller than the filter size) scales. The unclosed terms are representative of the physics associated with the small, high frequency, structures present in the flow" [6].
The filtered incompressible NS equations (which are chosen to be presented here for their simpler formulation) reduce to (using the implicit summation rule):

$$\frac{\partial \tilde{u}_i}{\partial x_i} = 0, \tag{3.2}$$

$$\frac{\partial \tilde{u}_j}{\partial t} + \frac{\partial \widetilde{u_i u_j}}{\partial x_i} = \nu \frac{\partial^2 \tilde{u}_j}{\partial x_i \partial x_j} - \frac{1}{\rho}\frac{\partial \tilde{p}}{\partial x_j}. \tag{3.3}$$

which are the mass and the momentum conservation equations respectively. The symbol $\tilde{f}$ defines the mass weighted filter $\tilde{f} = \overline{f\rho}/\overline{\rho}$ where $\overline{f}$ is the spatial filter applied to the property f. The second term on the left-hand side of equation 3.3 is split in two parts: one part that is explicitly resolved and a second part, representative of the smallest flow scales, that is modeled. This second part is the so-called sub-filter (or sub-grid), stress tensor:

$$\frac{\partial \widetilde{u_i u_j}}{\partial x_i} = \frac{\partial (\tilde{u}_i\ \tilde{u}_j)}{\partial x_i} - \frac{\partial \tau_{ij}^{SGS}}{\partial x_i}. \tag{3.4}$$

For implicit filtering LES (i.e. the grid size corresponds to the filter size), the terms sub-filter scale and sub-grid scale (SGS) have the same meaning. The isotropic part of the SGS tensor is included in the modified filtered pressure term $\tilde{p}$ [89], while the anisotropic part is modeled as:

$$\tau_{ij}^{SGS} - \frac{1}{3}\delta_{ij}\tau_{kk} = 2\tilde{\rho}\nu_{SGS}(\tilde{S}_{ij} - \frac{1}{3}\delta_{ij}\tilde{S}_{kk}). \tag{3.5}$$

Equation 3.5 assumes that the SGS term is aligned with the rate-of-strain tensor S_{ij}: this assumption is also known as the eddy viscosity assumption originally applied to the time-averaged NS equations (Boussinesq, 1877). However, in many Direct Numerical Simulation

(DNS), S_{ij} and τ_{ij}^{SGS} are found to be poorly correlated [70]. The proportionality coefficient between these two tensors is the turbulent viscosity, ν_{SGS}. Turbulent viscosity is expressed as:

$$\nu_{SGS} = (C_m\Delta)^2 D_m(\tilde{u}), \tag{3.6}$$

so that ν_{SGS} is "proportional to the square of the grid size per an ad-hoc coefficient multiplied by a differential operator associated with the model $D_m(\tilde{u})$" [80]. Two SGS models are chosen for the current study. The first is SIGMA [80], "whose differential operator (i.e. turbulent viscosity coefficient) goes to zero in near-wall regions in order to mimic the turbulence damping due to the no-slip condition (turbulent stress should decay as the distance to the solid boundary to the third power [15]) and vanishes in the case of a flow in solid rotation and in the case of a pure shear" [80]. These properties are of importance since the flow under examination in the present study is both confined and swirled.
The second is Dynamic Smagorinsky, "whose ad-hoc coefficient is computed dynamically as the calculation progresses rather than input a priori" [29]. The model is constructed "to generate an effective viscosity which is proportional to some measure of the turbulent energy at the high wavenumber end of the spectrum" [49] which evidently vanishes in the case of laminar flows and therefore is suited, for instance, to simulate transition to turbulence [49]. However, this model shows a very good performance even when its basic hypothesis (i.e. scale similarity) is not satisfied and it is argued [49] that the reason why it works so well is that it contains a sensor "which responds to the energy in the high wavenumber of the spectrum before it contaminates the energy containing range" [49].

3.3 Terminology.

Here the different jets definitions and the measurement locations of some fluid dynamics properties, are clarified. These definitions will be used later on during the sensitivity analysis. In all the table and figures, the experimental data are named *EXP*. For clarity, the different swirlers, stages and jets are summarized in Fig. 3.6A. Each swirler device is made of different vanes. The two coaxial swirlers, forming the axial swirler stage, will be referred to the **innermost** (or the inner) and the **outermost** (or the outer) axial swirlers. The flow passing through these swirlers (or simply passages) generates the **innermost** respectively **outermost axial jets** which together are called the **central jet**. On the contrary, the radial swirler, or the radial stage, generates the **radial jet**.

3.3.1 Non-dimensional numbers

For all simulations of this sensitivity analysis, the swirl (Eq.(2.2)) and Reynolds (Eq.(2.1)) numbers have been monitored at three different locations (S_1, S_2 and S_3, Fig. 3.6B), in order to be representative of the three different jets before they merge in common structures. It has to be noticed that:

- the swirl number (defined by Eq. (2.2)) of the outermost axial jet (measured on surface S2 in Fig. 3.6B), shows no dependence on the particular sampling location (as the axial momentum flux and angular momentum are invariant of the free jet, even if in this case it is a wall bounded jet);

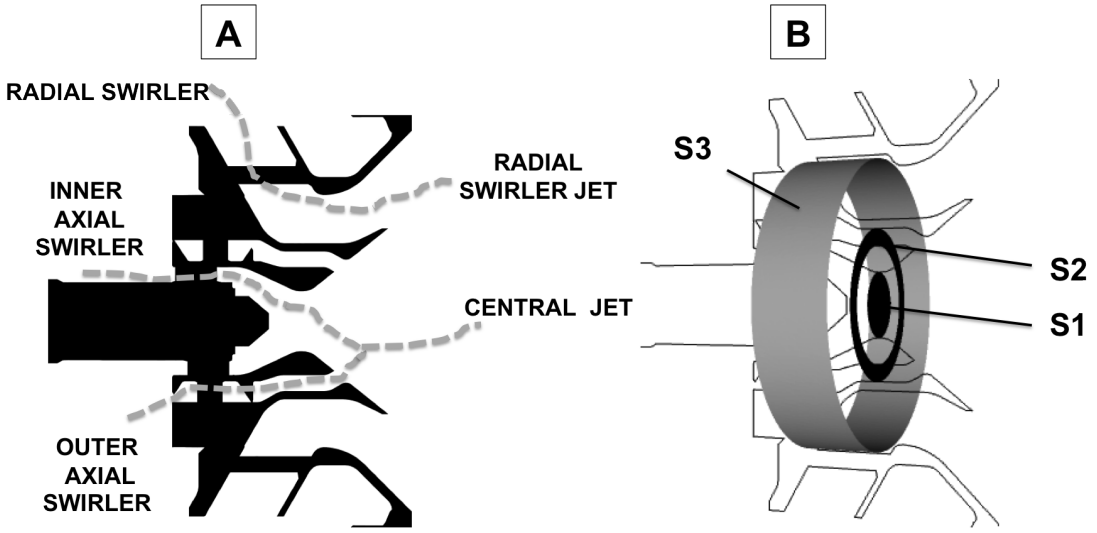

Figure 3.6: Different swirlers, stages and jets of LOTAR.

- the swirl number of the innermost axial jet (measured on surface S1 in Fig. 3.6B) has been measured at the minimum section. It varies because of the curvature of the injector and of the recirculation zones present in the innermost bowl; at the location chosen in Fig. 3.6B it is exactly equal to the swirl measured inside the vanes;

- the swirl number of the radial jet varies too because of the strong flow curvature (which turns from radial to axial direction). For this reason, the swirl number of the radial jet, evaluated using formula 2.2, does not properly represent the flow and the swirl ratio (defined by Eq.(2.3)) has been monitored instead.

The swirl ratio is measured on a cylindrical surface ($R = const.$) downstream of the radial swirler boundary condition (surface S3 in Fig. 3.6). Here, introducing the approximation of constant jet velocity and density, the two definitions, Eq.(2.2) & Eq.(2.3), are equivalent:

$$S = \frac{\int_A \rho u_d u_\theta r dA}{R \int_A \rho u_d^2 dA} \approx \frac{\int_A u_\theta dA}{\int_A u_d dA} = S_r, \tag{3.7}$$

where u_d is the discharge speed ($u_d = u_r$ on $S3$ in Fig. 3.6). The monitored quantities of the different jets are summarized in table 3.2. Note that the value of R is the same for all jets and equal to $R = 0.018\,[\mathrm{m}]$. The Reynolds number results of each jet are close to $O(40000)$ for the outer axial jet and $O(75000)$ for the inner and for the radial jets, independently of the flow configuration.

	Reynolds	Swirl ratio	Swirl number
Formula	Eq.(2.1)	Eq.(2.3)	Eq.(2.2)
Symbol	Re	S_r	S

Table 3.2: Non-dimensional numbers monitored for the different jets of Fig. 3.6B

3.3.2 Jet opening half-angle.

LES results and experimental data are presented in cylindrical coordinates. Experimental data, extracted for each of the three planes of Fig. 3.1, along two lines normal to each other, are averaged into a single curve using the axisymmetry of the results. The same procedure is repeated for the LES results in order to use the same approach for both, the simulation and the experiment. LES and experimental data are then compared along the radial direction. The jet opening half-angle has been measured at the 30 [mm] plane (Fig. 3.1b) and it is defined as the angle subtended at the apparent origin by the axis and a line to the half-velocity radial location, so: $\frac{u(r)}{u_{max}(r)} = \frac{1}{2}$ [32]. The definition of the jet opening half-angle is explained in Fig. 3.7.

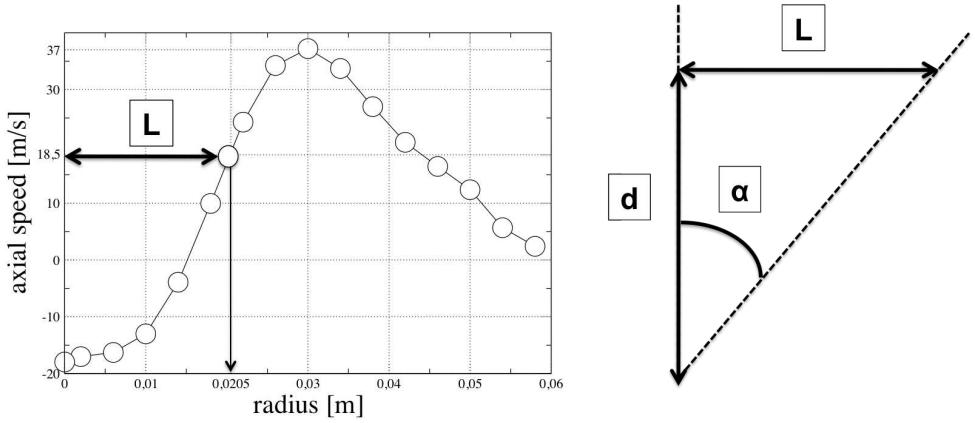

Figure 3.7: Evaluation of the jet opening half-angle for experimental data at the last measurement plane of Fig. 3.1. L = radial location of the half velocity, $d = 30[mm]$ (distance from the injector ending plate), α is the jet opening half-angle.

For all the BB states shown in the next sections (with a jet that stick to the diffuser walls and expands radially), α is set to 90 deg. For experimental data (circles in Fig. 3.7) the radial location at which axial velocity is half of the jet top speed is $L = 20.5[mm]$, therefore for $d = 30[mm]$ it corresponds to a jet opening half-angle of $\alpha = arctan(\frac{L}{d}) \approx 34 \ \ deg$. **Note that throughout this thesis $R_0 = 30[mm]$ is taken as the injector reference radius**.

3.4 Baseline simulation of the LOTAR swirler

The baseline LOTAR simulation has been first performed using the SIGMA model [80] coupled with no-slip boundary conditions at the solid boundaries on both codes while the other boundaries are shown in table 3.1. The simulations settings are summarized in table 3.3.

name	mesh	code	SGS	Wall
AVBP-SIGMA	basic	AVBP	SIGMA	NO SLIP
YALES-SIGMA	basic	YALES2	SIGMA	NO SLIP

Table 3.3: Baseline LES

3.4.1 Global flow field

Both codes show the same general behavior and only minor discrepancies are present. Despite the fact that the two LES codes are very different, they provide similar results. This result is quite encouraging considering that RANS solvers usually exhibit much larger variability for such flows. Opening half-angles of the jets are 90 deg (as evident from Fig. 3.8) in LES results of both codes. The jet arising from the radial swirler first separates in the diffuser then soon reattaches following the geometrical curvature of the device. The central jet, generated by the two inner coaxial swirlers, sticks to the wall until it merges with the outermost flow (Fig. 3.8).

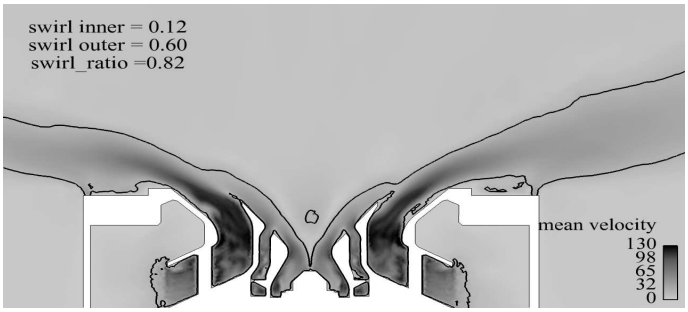

(a) AVBP-SIGMA

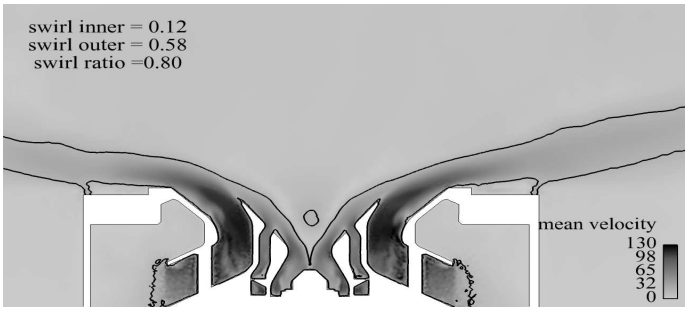

(b) YALES-SIGMA

Figure 3.8: Mean velocity magnitude [m/s] and mean velocity isoline ($u_{mean} = 10$ [m/s]) for simulations of table 3.3. The swirl values indicated on the figures correspond to the swirl number (S, Eq.(2.2)) for the inner and outer jets and to the swirl ratio (S_r, Eq.(2.3)) for the radial jet.

3.4.2 Flow split and pressure drop

Both codes provide a similar flow split in the two different stages. The small discrepancy in the total mass flow rate is due to the AVBP target oriented BC (target values are not imposed in a hard way but reached in a relaxation time to limit acoustic oscillations). Most of the flow is passing through the radial swirler, because of its bigger section, table 3.4. Computed pressure drops are similar within the two codes, table 3.5.

Flow repartition			
	axial stage	radial stage	total
EXP	16.5 [g/s]	85.5 [g/s]	102 [g/s]
AVBP-SIGMA	13.8 [g/s]	88.6 [g/s]	102.4 [g/s]
YALES-SIGMA	14.2 [g/s]	87.6 [g/s]	102.0 [g/s]

Table 3.4: flow repartition in the baseline configuration

Pressure drop		
	LES	reference
EXP	4800 Pa	+0%
AVBP-SIGMA	8248 Pa	+72%
YALES-SIGMA	7945 Pa	+66%

Table 3.5: pressure drop in the baseline configuration

3.4.3 Swirl numbers and ratio

The swirl numbers and the swirl ratios computed by the two codes are similar, table 3.6 & table 3.7.

Swirl number		
	AVBP-SIGMA	YALES-SIGMA
INNER	0.12	0.12
OUTER	0.60	0.58

Table 3.6: Swirl numbers, S Eq.(2.2), for the baseline configuration

Swirl ratio		
	AVBP-SIGMA	YALES-SIGMA
mean axial velocity	32.5 [m/s]	33.50[m/s]
mean radial velocity	-41.77 [m/s]	-41.34[m/s]
mean tangential velocity	-33.45 [m/s]	-34.08[m/s]
Swirl ratio, Eq.(2.3)	0.8	0.82

Table 3.7: Mean velocities and swirl ratios, S_r Eq.(2.3), for the baseline configuration

3.4.4 Recirculation zone

The recirculation zone extends several diameters downstream of the injector orifice along the streamwise and radial directions (Fig. 3.9). The recirculation zone slightly differs in the two codes because of different running times of the two simulations related to the cheaper numerical cost of YALES2. Note that the far field, i.e. the flow inside the cylindrical box, keeps on slowly evolving while the jet remains, unaffected, in the same flow state.

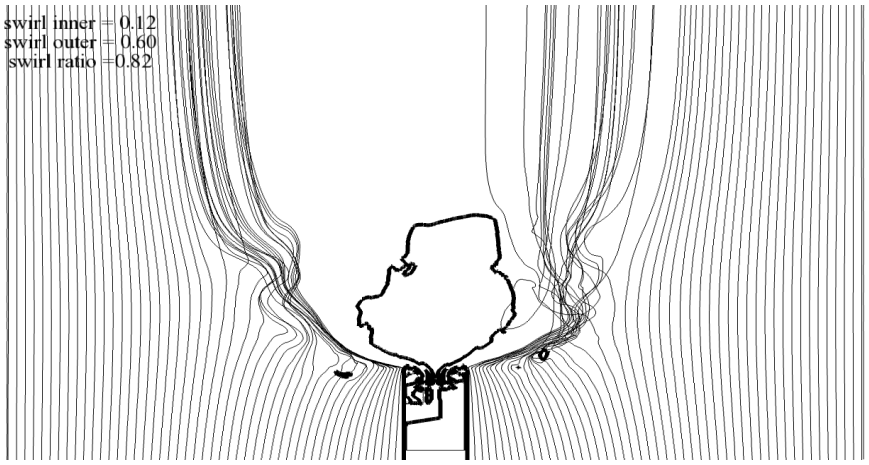

(a) AVBP-SIGMA

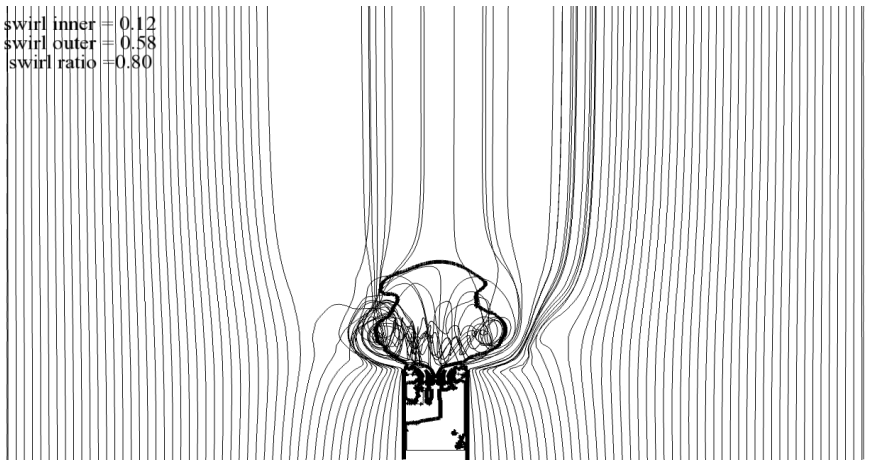

(b) YALES-SIGMA

Figure 3.9: Recirculation bubble. Zero axial velocity (thicker black line) and streamlines for simulations of table 3.3. The seeding used is a line upstream of the injector and is the same for both simulations.

3.4.5 Comparison with experimental data

LES results show a poor comparison with experimental measurements, the two LES codes simply predict the wrong flow topology. The swirling jet obtained experimentally at ONERA is a free Axial Jet (see section 2.2.3) as shown by the size of the recirculation zone (Fig. 3.10), the high tangential velocity (Fig. 3.10) and high turbulence intensity

inside the CTRZ[4] (as it will be shown later in Fig. 3.15). On the contrary, LES using the settings of table 3.3 predicts in both codes a flow that looks like a Blasted Breakdown jet (BB) of section 2.2.3. The wrong LES prediction is evident from Fig. 3.10 which shows profiles of axial, radial and tangential velocity at three axial positions.

3.4.6 Summary of the main features of the "baseline" run

The baseline LOTAR simulation was performed on both codes using SIGMA as SGS model coupled with no-slip boundary conditions at the solid walls. In both codes the opening angle is large ($\approx 90\,\text{deg}$). Both codes predict, in the axial swirlers, a similar swirl number, table 3.6, flow split, table 3.4, and swirl ratio of the radial jet, table 3.7. The recirculation zone established by the jet is wide and spans several injector diameters in both radial and axial directions (Fig. 3.9). The pressure drop through the device estimated by both codes is higher than experimental results, table 3.5. Comparisons with velocity profiles of experimental data are poor (Fig. 3.10). Obviously the two LES codes have a major difficulty to predict this case: the two LES codes predict a jet in the BB state[5] (using the nomenclature of section 2.2.3) while the experiment corresponds to an AJ state. LES prediction and experimental measurements do not match because they corresponds to two totally different flow states.

[4]Note that no pressure signal from the inside of the jet was taken experimentally.

[5]This classification will be proven and clarified in section 3.6.

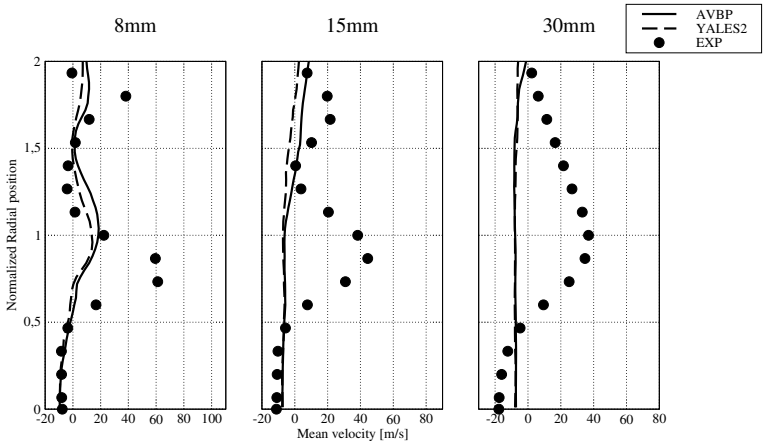

(a) Axial

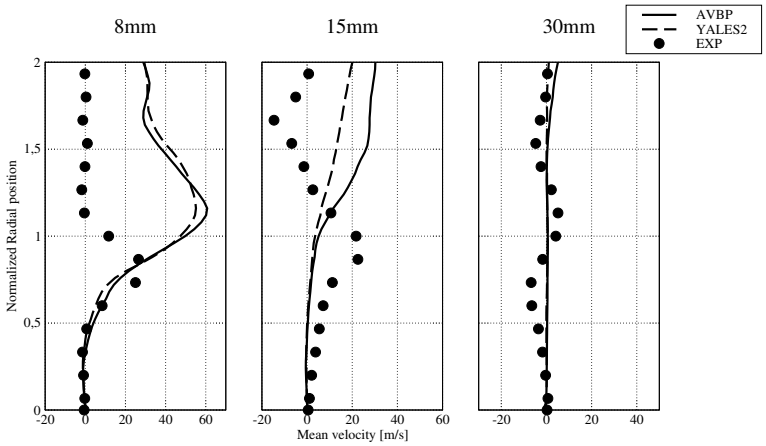

(b) Radial

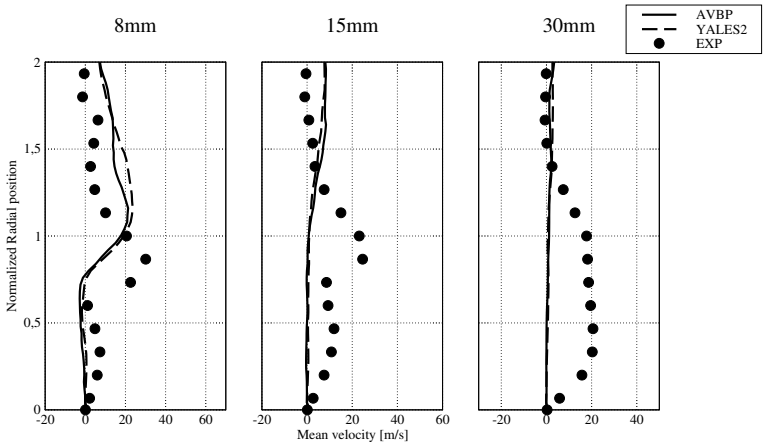

(c) Tangential

Figure 3.10: Velocity profiles for AVBP-SIGMA and YALES-SIGMA, the normalization radius is $R_0 = 30[mm]$.

3.5 Sensitivity to SGS modeling

The previous section has shown that both YALES2 and AVBP failed to give proper results for the first two runs of Table 2.1, apparently capturing the wrong flow state (BB instead of AJ). In this section the effect of the SGS term is investigated by replacing the SIGMA model [80] used in section 3.4 by the Dynamic Smagorinsky model [29] in both codes, keeping constant all other numerical parameters.

3.5.1 Global flow field

name	mesh	code	SGS	Wall
AVBP-DSMAG.	basic	AVBP	DYN. SMAGO.	NO SLIP
YALES-DSMAG.	basic	YALES2	DYN. SMAGO.	NO SLIP

Table 3.8: Influence of the SGS model tests

The first result obtained when changing the SGS model is that the flow state changes: a strong flow reconfiguration is induced in both codes. Jet opening half-angle is now reduced to $\approx 23 - 33\,\text{deg}$ from $\approx 90\,\text{deg}$. The BB jet experienced in the previous simulations has disappeared (Fig. 3.11). Despite the fact that the two codes give a similar jet opening half-angle (showing a net improvement with respect to the run of section 3.4), the flow fields slightly differ.

3.5.2 Flow split and pressure drop

Flow split changes with the jet configuration but both codes compute a similar flow split, which is now closer to permeability measurements, table 3.9.

Flow repartition			
	axial stage	radial stage	total
EXP	16.5 [g/s]	85.5 [g/s]	102 [g/s]
AVBP-DSMAG.	15.7 [g/s]	86 [g/s]	101.7 [g/s]
YALES-DSMAG.	16.1 [g/s]	85.9 [g/s]	102.0 [g/s]

Table 3.9: Flow split for simulations of table 3.8.

While flow split results (table 3.9) are closer to experimental data, pressure drop predictions (table 3.10) deteriorate with the Dynamic Smagorinsky model. This phenomenon is explained by the higher levels of turbulent viscosity generated at the solid boundaries (with a $y+$ in the range [30,100]) by the Dynamic Smagorinsky model compared to SIGMA. Higher turbulent viscosity levels create:

- an increase of the dissipation rate of kinetic energy,
- a reduction of the hydraulic section of the vanes, since the velocity at the solid boundary is damped.

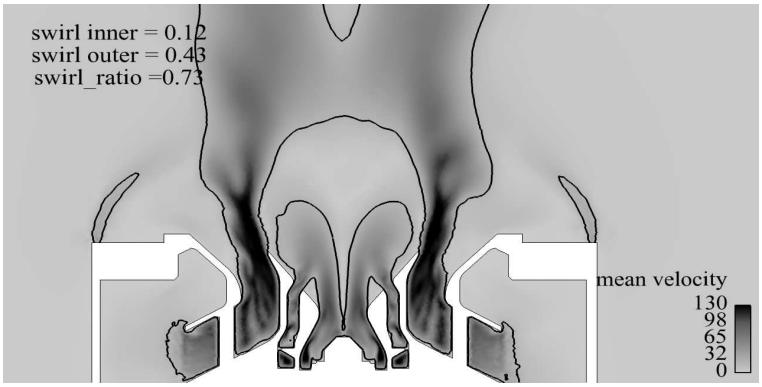

(a) AVBP-DSMAG.

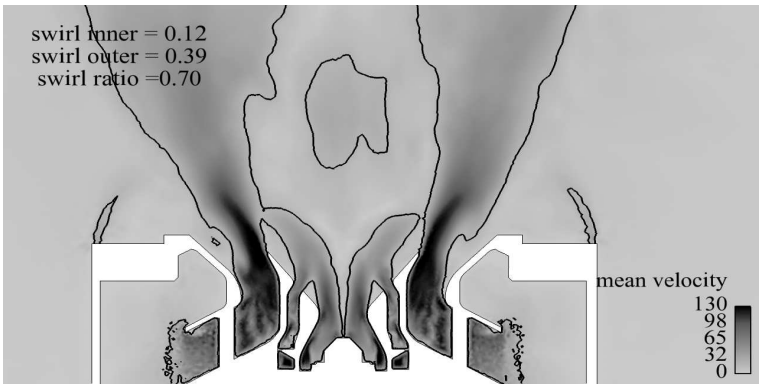

(b) YALES-DSMAG

Figure 3.11: Mean velocity for simulations of table 3.8.

Both effects increase pressure losses through the injector device. The fact that pressure drop predictions deteriorate while comparison of other quantity with experimental data improves (Fig. 3.14) may suggests that pressure drop prediction could be an issue decoupled from velocity prediction. With respect to the simulations of section 3.4, the mass flow rate passing through the radial stage has decreased (tables 3.4 & 3.9). This is an evidence of the dissipation distribution between the passages: as the level of turbulent viscosity increases, the mass flux decreases in the less resolved passage for a given hydraulic diameter, that is for the *basic* mesh, the radial one. However, the effects of the strong curvature of the radial jet, present in the results obtained with SIGMA, can also impact the flow split. It is therefore difficult to separate the dissipative effect of an increased viscosity in the swirler vanes from the different amount of dissipation related to the flow configuration.

3.5.3 Swirl numbers and ratio

The most important difference between the SIGMA computations of section 3.4 and the Dynamic Smagorisnky simulations of table 3.8, is the substantial decrease of the swirl number of the outer jet (from 0.6 to 0.43) and of the swirl ratio of the radial jet (from 0.8 to 0.7). Tables 3.11 and 3.12 show these quantities. Both codes give similar results.

Pressure drop		
code	LES	reference
EXP	4.8 [Kpa]	+0%
AVBP-DSMAG.	12930 Pa	+166%
YALES-DSMAG.	12272 Pa	+155%

Table 3.10: Pressure drop for simulations of table 3.8.

Swirl number		
	AVBP-DSMAG.	YALES-DSMAG.
INNER	0.12	0.12
OUTER	0.43	0.39

Table 3.11: Swirl number, Eq.(2.2), for simulations of table 3.8. To be compared with table 3.6.

Swirl ratio		
	YALES-DSMAG.	AVBP-DSMAG.
mean axial velocity	30.14 [m/s]	29.4[m/s]
mean radial velocity	-41.3 [m/s]	-39.84[m/s]
mean tangential velocity	-29 [m/s]	-29 [m/s]
swirl ratio	0.7	0.73

Table 3.12: Swirl ratio, Eq.(2.3), for simulations of table 3.8. To be compared with table 3.7.

3.5.4 Recirculation zone

The recirculation zone is different in the two codes (Fig. 3.12) even though the overall topology is the same. While the CTRZ is well defined in YALES2, this structure is narrower in AVBP. The narrow central recirculation bubble in AVBP (Fig. 3.12) is related to the behavior of the central jet. Vortex breakdown is triggered by the pressure gradient (induced by the rotational motion) which overwhelms the jet inertia along the axial direction. The central jet in AVBP has a higher inertia along the axial direction (Fig. 3.11) therefore a higher penetration than the jet simulated by YALES2. As a consequence, the size of the recirculation bubble is reduced. Also, the dynamics of the detachment of the jet from the diffuser wall changes with SGS modeling (see the different lip close to the diffuser on Fig. 3.12) and this can affect the jet opening half angle and therefore the shape of the recirculation zone. Peripherical recirculation zones, equivalent to corner recirculation zones, are induced in the flow field (Fig. 3.13). These structures disappear for longer simulation times. It is very likely that the differences observed in Fig. 3.13 are due to the very long time required to converge and to the sensitivity of the recirculation zone to the details of the boundary condition. The asymmetry in the far field flow, visible from Fig. 3.13, can be related to mesh effects (small asymmetry in the azimuthal direction in the far field mesh) as suggested by Moreau [75].

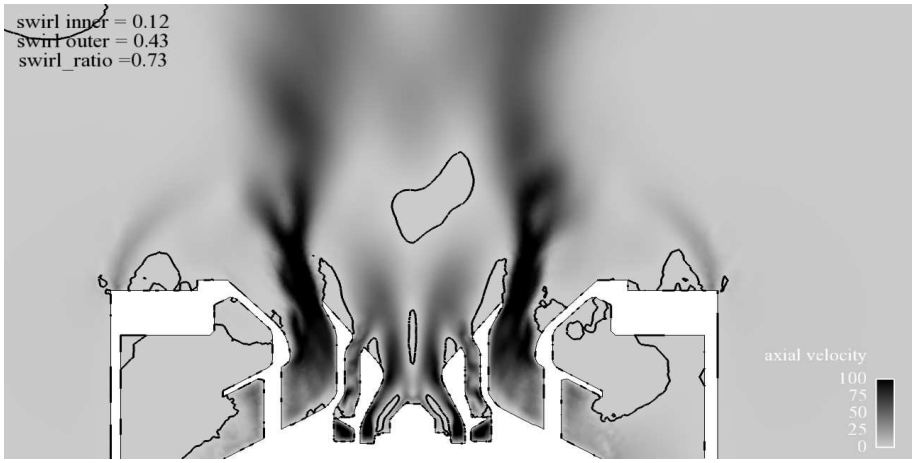

(a) AVBP-DSMAG.

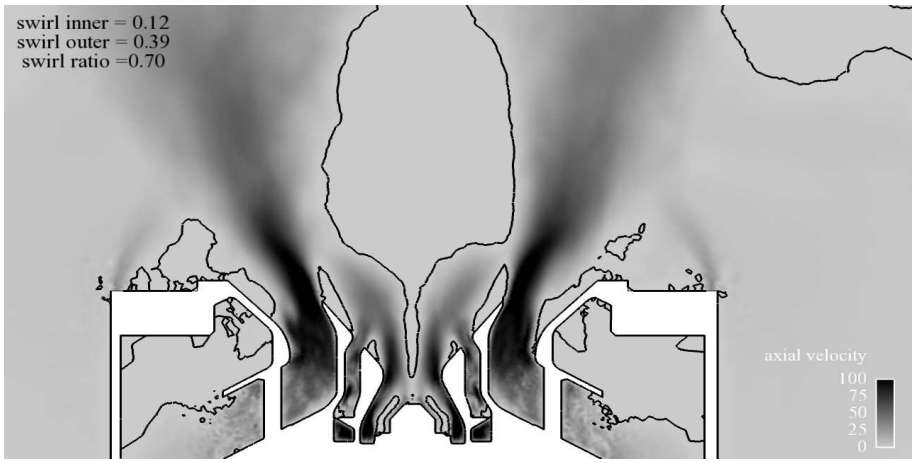

(b) YALES-DSMAG.

Figure 3.12: Recirculation bubble, mean axial velocity component and zero velocity isoline for simulations of table 3.8.

3.5.5 Comparison with experimental data

The smaller recirculation bubble in AVBP is confirmed also by the comparison with experimental data (Fig. 3.14) which is not fully satisfactory but much better than in section 3.4. With respect to the previous configuration both codes show a better comparison with measurement, because the wrong flow topology, the BB state, has been replaced in both solvers by a different state: AJ which is coherent with the experimental data.

3.5.6 Summary of the main features of the run

The SGS model has a deep impact on the flow behavior: the flow state changes radically depending on this parameter. The flow split also changes with an increase of the mass flow rate in the axial stage (table 3.9). A net decrease of the swirl number in all passages and of the swirl ratio of the radial jet is also experienced (tables 3.11 and 3.12). Similarly to the previous case, the two codes predict similar flow split and swirl but in this case the

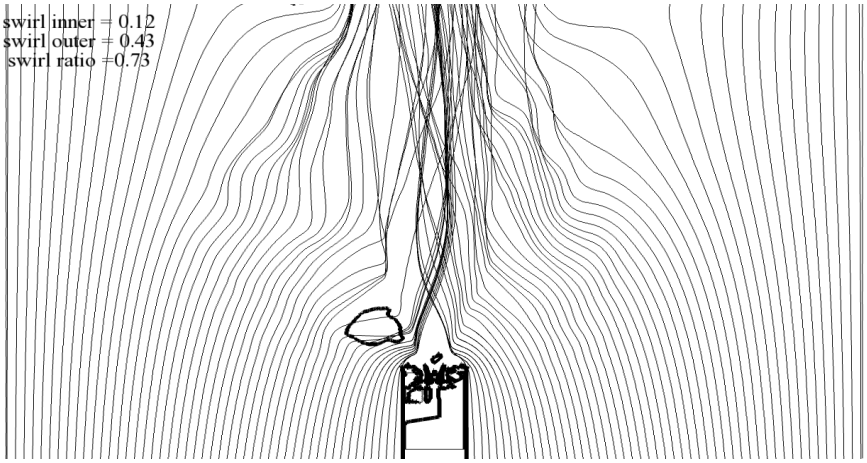

(a) AVBP-DSMAG.

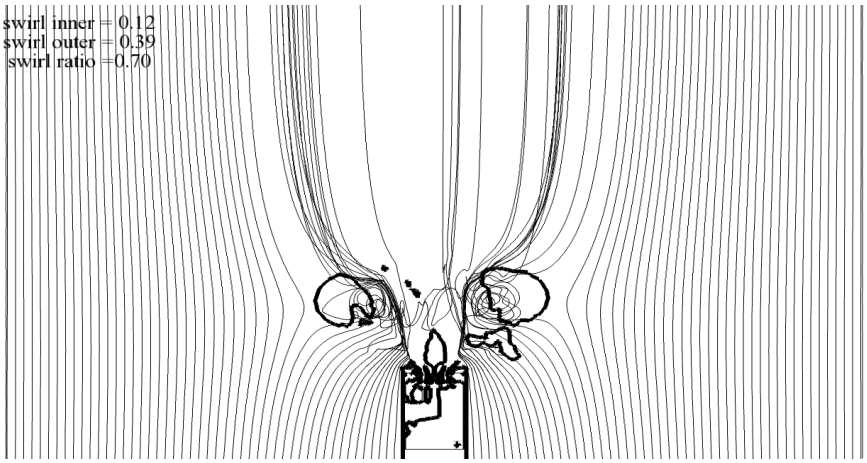

(b) YALES-DSMAG.

Figure 3.13: Recirculation bubble zoom out, zero axial velocity line (thicker black line) and streamlines for simulations of table 3.8.

recirculation zone shape changes (Fig. 3.12): YALES2 shows a well defined CTRZ while AVBP produces a much narrower one. This difference could be related to the central jet, which in AVBP has (Fig. 3.11 or plot 3.14) a higher axial penetration. Comparison with experimental data is sufficient for both codes if compared with the results obtained in section 3.4.

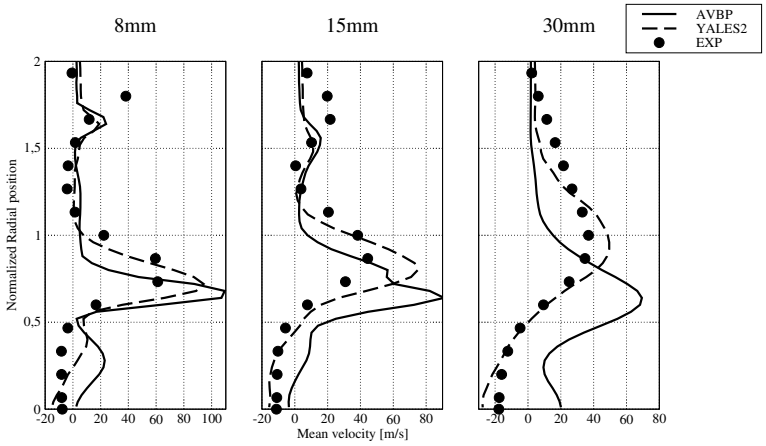

(a) Axial

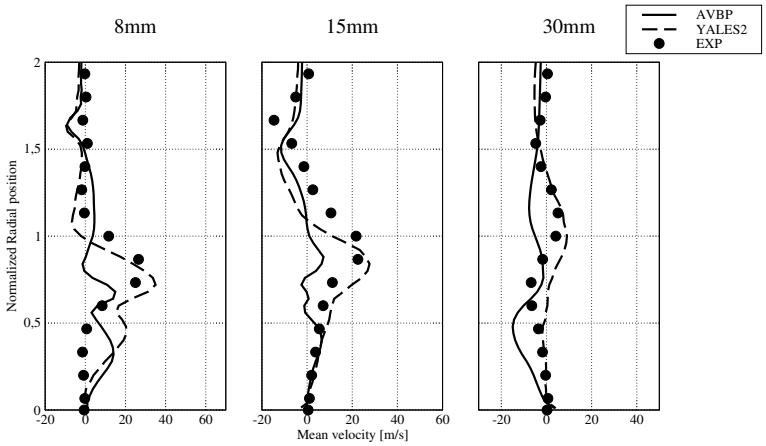

(b) Radial

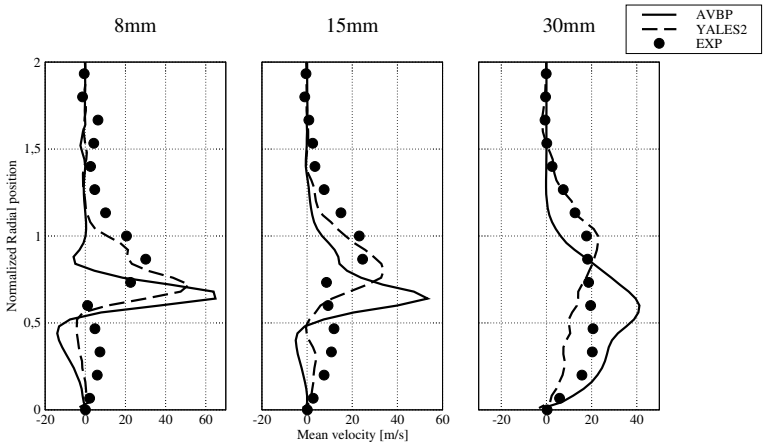

(c) Tangential

Figure 3.14: Velocity profiles for AVBP-DSMAG. and YALES-DSMAG, the normalization radius is $R_0 = 30[mm]$.

3.6 Classification & analysis of the flow states.

The previous sections show that two flow configurations appear depending on the SGS model. The first configuration is obtained with the SIGMA model and corresponds to a jet opening half-angle $\alpha \approx 90\,\text{deg}$ and a BB state. The second configuration is obtained with Dynamic Smagorinsky and corresponds to a jet opening half-angle of $\alpha \approx 20-30\,\text{deg}$ and an AJ state. The first configuration ($\alpha \approx 90\,\text{deg}$) is characterized by a wider recirculation zone (Fig. 3.10) and by (inside the CTRZ) a zero tangential velocity (Fig. 3.10), a negligible turbulent activity and sub-pressure (Fig. 3.15). The second configuration is characterized by a recirculation zone smaller than one injector diameter (Fig. 3.14) and a high tangential velocity (Fig. 3.14), a high level of turbulent activity and a high subpressure coefficient ($P_D = \frac{P_{atm}-P}{0.5\rho U_0^2} \approx 0.7$) close to the injector orifice (Fig. 3.15). The comparison of these flow states with Vanierschot's jets [105] is shown in Appendix D.

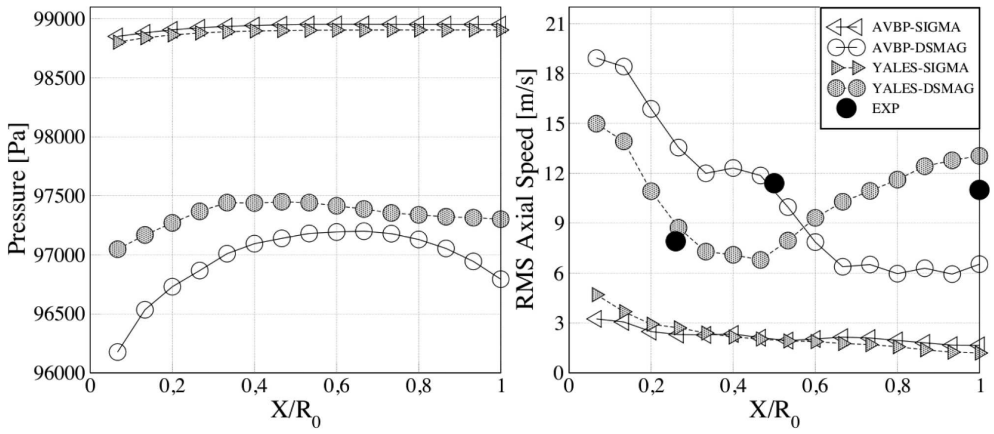

Figure 3.15: Axial velocity RMS and pressure distribution measured along the centerline of the geometry for simulations of tables 3.3-3.8. Results are plotted against normalized axial distance (X/R_0) from the swirler end plate. Experimental data are available only for RMS values.

Considering also results shown in Fig. 3.15, and using the nomenclature introduced in section 2.2.3, the $\alpha \approx 90\,\text{deg}$ state can be classified as a Blasted Breakdown Jet (BB) since it shows flow properties similar to the BB state described by Vanierschot et al. [105]. Similarly, the $\alpha \approx 20-30\,\text{deg}$ configuration can be classified as a free Axial Jet (AJ). The BB state is not observed experimentally while the AJ state shows a good comparison with experimental data. Both BB & AJ states appear independently of the LES solver used, i.e. AVBP or YALES2, even if some discrepancies in prediction between the two codes are present.
Obviously, the two LES codes predict two very different states for this flow depending on small changes (LES sub-model). In the next sections these results will be analyzed and it will be demonstrated that they are not due to numerical artifacts but to the fact that the present flow is very close to a bifurcation and therefore very sensitive to all parameters (physical or numerical).

3.7 Sensitivity to the mesh

An interesting observation from tables 3.7 & 3.12 is that the AJ state is characterized by a lower swirl ratio ($S_r \approx 0.7$) in the radial jet (measured on surface S3 of Fig. 3.6) while the BB state is characterized by a higher swirl ratio ($S_r \approx 0.81$) in the radial jet. This variation of the swirl ratio can be justified only by an *effective geometry* variation or by a variation of the fluid dynamics conditions, both due to SGS modeling. As it will clarified in appendix A, SGS modeling in the wakes of the radial swirler vanes and inside the vane itself is able to modify the amount of swirl in the flow. **A low resolution in this zone of high shear can create numerical noise that modifies the jet velocity**[6]. The Dynamic Smagorinsky model damps the velocity gradient because of its higher turbulent viscosity that smoothes the velocity field. The SIGMA model does not: therefore numerical noise can modify the solution. **In order to reduce this noise, the mesh has been refined in the wake of the radial swirler passages, upstream inside the vanes and downstream, inside the swirler bowl**. This new mesh is named *optimized*. The *basic* and the *optimized* meshes (optimization based on the macro flow analysis of section 3.6) are shown side by side in Fig. 3.16. The optimized mesh has 15873485 cells. Typically, the basic mesh had $6-7$ nodes in the flow passages while the optimized mesh has roughly twice this number at the same location[7].

[6]The same issue is happening at all the nozzle lips but is more evident for the radial swirler because its vanes are closer to each others with respect to the inner and outer swirler vanes.

[7]Note that it was not possible to generate a mesh with a prismatic layer at the wall for this configuration because of the complexity of the geometry.

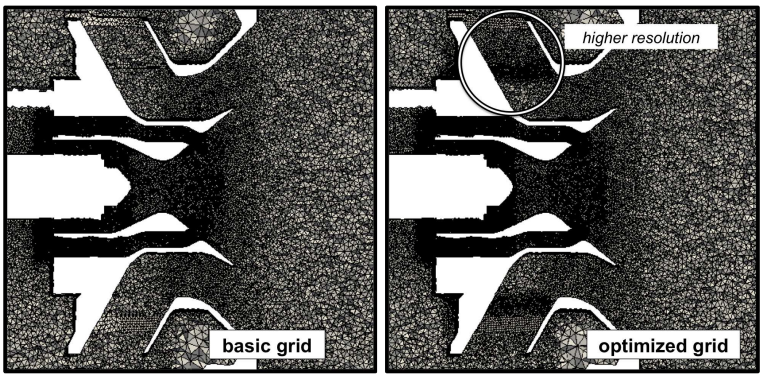

(a) axial-radial directions cut

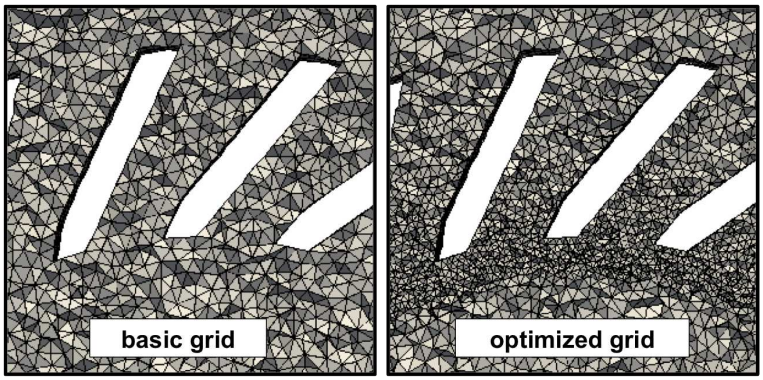

(b) tangential-radial directions cut

Figure 3.16: Optimized vs. basic mesh.

3.7.1 Global flow field

The first remarkable result of the computations performed on the locally refined mesh shown in Fig. 3.16 is that, on the optimized mesh, the flow topology observed for the baseline case (section 3.4) changes again: a strong modification of the jet opening half-angle is observed for the BB state, characteristic of the LES with the SIGMA model, with a net improvement of predictions. The simulations of this section are itemized in table 3.13. LES outputs are still code independent and the AJ state is now predicted by both SGS models as evident from the high subpressure and turbulence intensity fields (Fig. 3.17) or simply from the jet direction (Fig. 3.18).

name	mesh	code	SGS	Wall
YALES-DSMAG_O	optimized	YALES2	DYN.SMAG.	NO SLIP
YALES-SIGMA_O	optimized	YALES2	SIGMA	NO SLIP
AVBP-SIGMA_O	optimized	AVBP	SIGMA	NOSLIP

Table 3.13: simulation table, effects of the mesh

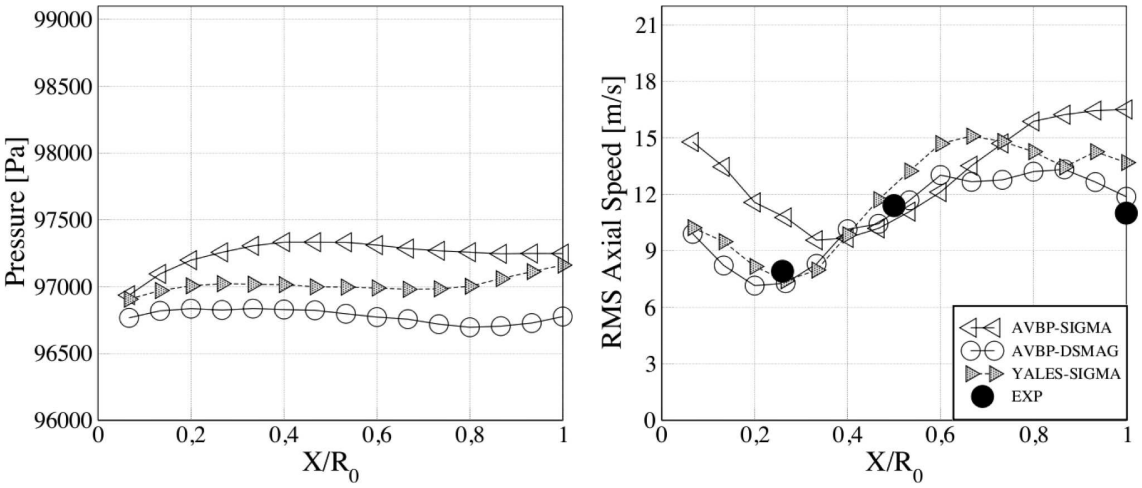

Figure 3.17: Axial velocity RMS and pressure distribution measured along the centerline of the geometry for simulations of table 3.13. Results are plotted against normalized axial distance (X/R_0) from the swirler end plate. Experimental data are available only for RMS values.

3.7.2 Flow split and pressure drop

Flow split and pressure loss predictions are in line with the previous simulations: Dynamic Smagorinsky LES predict a higher pressure drop, table 3.15, and a higher mass flow rate through the axial stage, table 3.14. Pressure drop predictions are similar in both codes.

3.7.3 Swirl numbers and ratio

The scatter of the swirl number of the outer jet for the various simulations already experienced in the previous sections (tables 3.6-3.11), is present also with the optimized mesh (table 3.16). This result is expected since it is related to the mesh resolution along the

Flow repartition			
	axial swirlers	radial swirler	total
EXP	16.5 [g/s]	85.5 [g/s]	102 [g/s]
YALES-DSMAG_O	15.9 [g/s]	86.1 [g/s]	102.0 [g/s]
YALES-SIGMA_O	15 [g/s]	87 [g/s]	102.0 [g/s]
AVBP-SIGMA_O	15.7 [g/s]	85.8 [g/s]	101.5 [g/s]

Table 3.14: Flow repartition for simulations of table 3.13.

Pressure drop		
RUN	LES	reference
YALES-DSMAG_O	10657 Pa	+122%
YALES-SIGMA_O	8535 Pa	+77%
AVBP-SIGMA_O	8647 Pa	+80%

Table 3.15: Pressure drop for simulations of table 3.13.

outer jet streamlines: since the mesh was not modified in this zone, this scatter (related to SGS modeling) had to appear also with the *optimized* mesh. On the contrary, the swirl ratio of the radial jet is lower than 0.8 for all the simulations of table 3.13 (table 3.17) and mesh refinement has reduced the variability due to SGS modeling shown by LES on the basic mesh (tables 3.7 & 3.12) .

Swirl number			
	YALES-SIGMA_O	YALES-DSMAG_O	AVBP-SIGMA_O
INNER	0.12	0.12	0.12
OUTER	0.58	0.4	0.52

Table 3.16: Swirl number, Eq.(2.2), for simulations of table 3.13.

3.7.4 Recirculation zone

Recirculation zones differ in the different simulations because of the different swirl number and because of the central jet detachment dynamics (with Dynamic Smagorinsky the central jet detaches, see section A). YALES2 and AVBP give similar results (Fig. 3.19).

3.7.5 Comparison with experimental data, *optimized* mesh

Comparison with experimental data is sufficient for the Dynamic Smagorinsky simulations while the best agreement is obtained using SIGMA (Fig. 3.20). AVBP and YALES2 give extremely similar curves using the SIGMA model and results are close to experimental data.

3.7.6 Summary of the main features of the run

This section shows how a small refinement, localized in the wake of the tiny jets in the radial swirler bowl, is sufficient to eliminate most of the limitations due to the SGS model

Swirl ratio			
	YALES-SIGMA_O	YALES-DSMAG_O	AVBP-SIGMA_O
axial	34.6	32.8[m/s]	-34.5
radial	-41.45	-41.3 [m/s]	-40.96
tangential	-30.58	-29 [m/s]	-30.71
swirl ratio	0.74	0.72	0.76

Table 3.17: Swirl ratio, Eq.(2.3), for the *optimized* mesh.

effects. Comparison with experimental data is now reasonable for all the simulations using the SIGMA model, independently of the code.

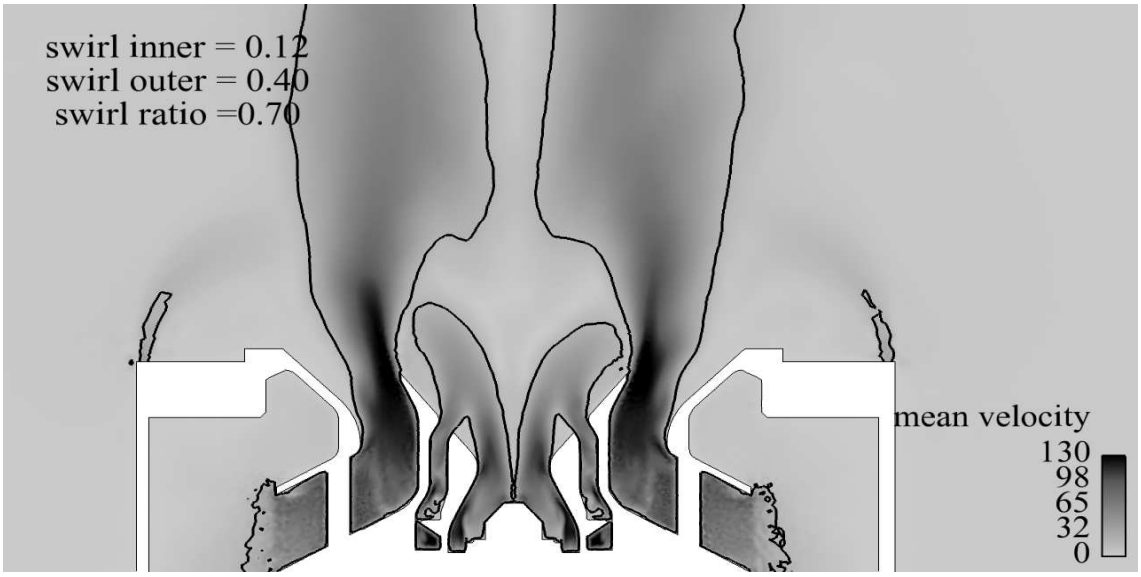

(a) YALES-DSMAG_O

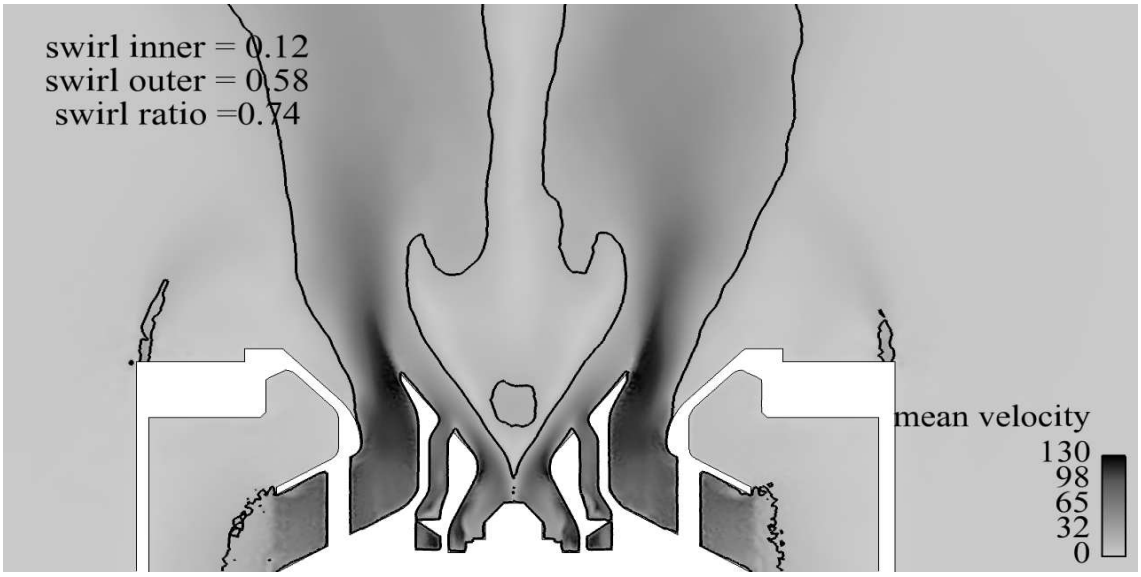

(b) YALES-SIGMA_O

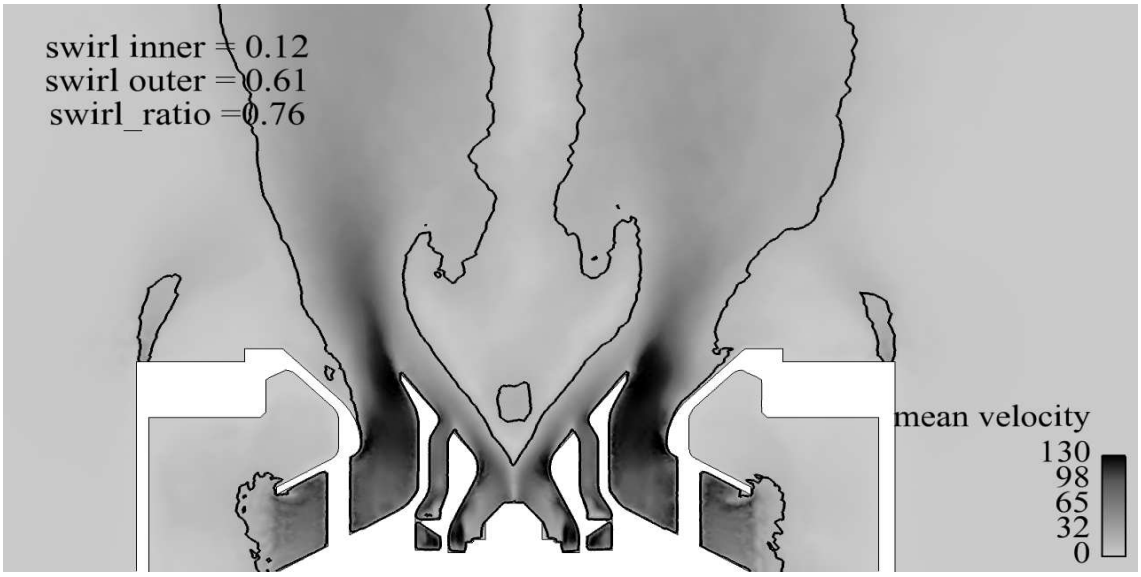

(c) AVBP-SIGMA_O

Figure 3.18: Mean velocity for LES of table 3.13

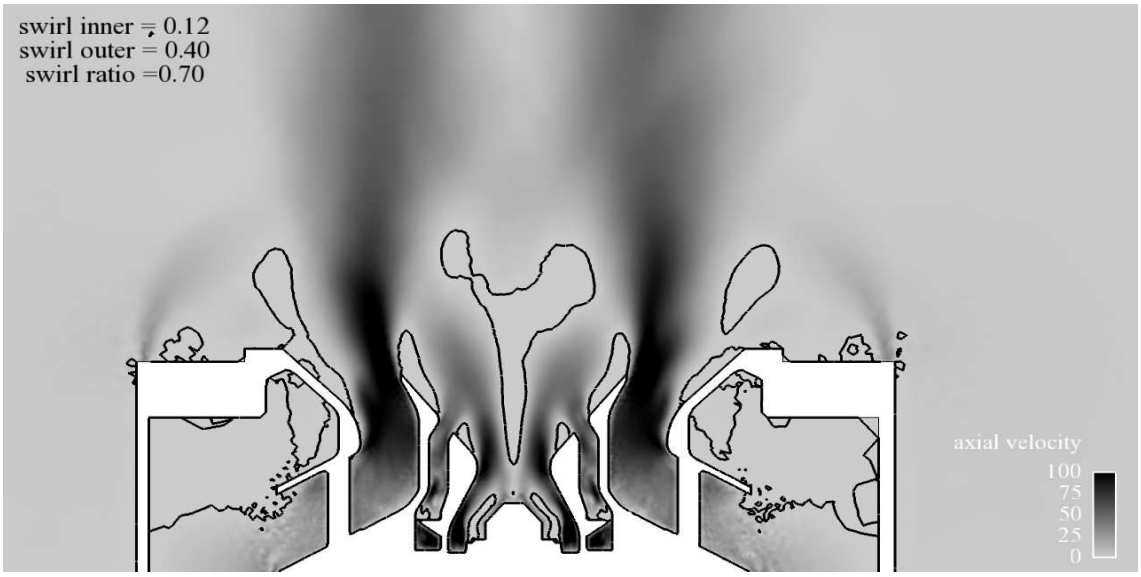

(a) YALES-DSMAG_O, the central jet detaches because of high turbulent viscosity, see section A.

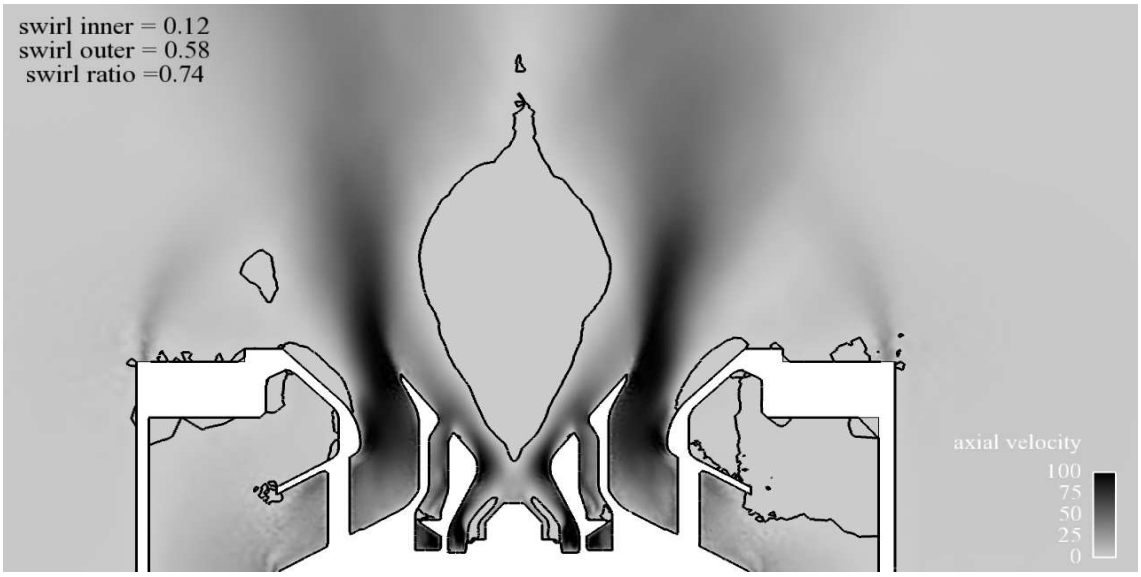

(b) YALES-SIGMA_O

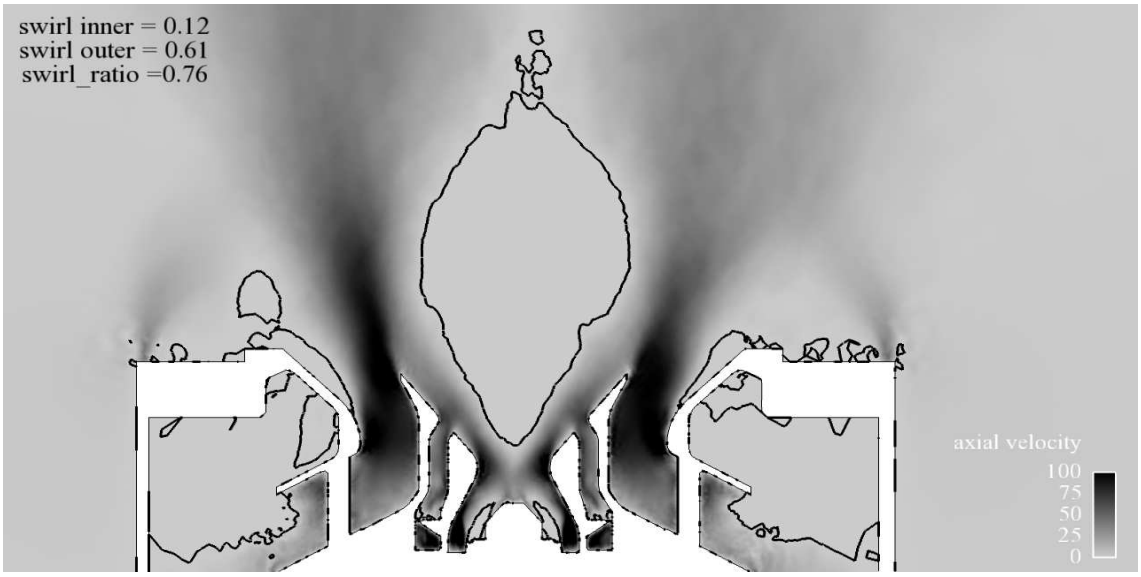

(c) AVBP-SIGMA_O

Figure 3.19: Recirculation bubble, velocity isolines and zero isosurface.

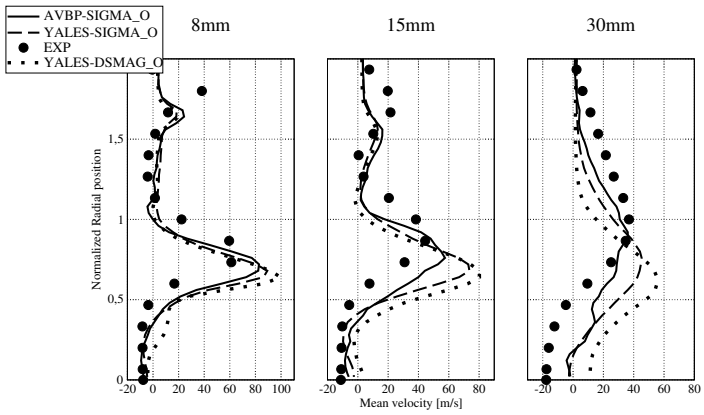

(a) Axial

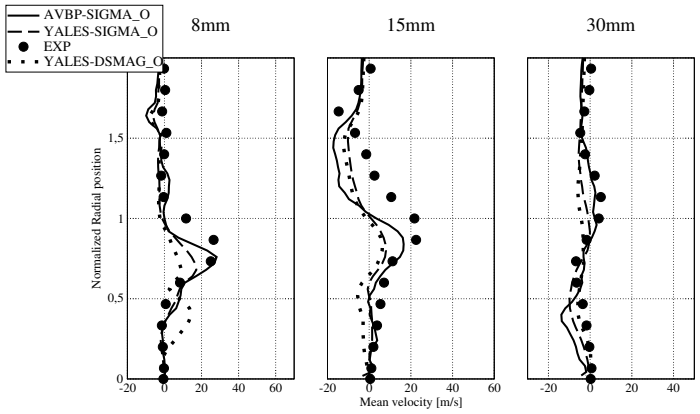

(b) Radial

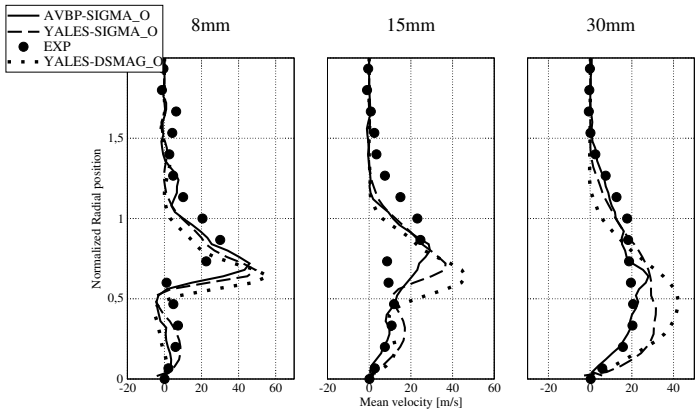

(c) Tangential

Figure 3.20: Velocity profiles, YALES-SIGMA_O, YALES-DSMAG._O, AVBP-SIGMA_O, the normalization radius is $R_0 = 30[mm]$.

3.8 Synthesis of results and explanation scenario

The sensitivity analysis of the LOTAR LES described in sections 3.4 to 3.7 shows that:

1. the swirl ratio (Eq. 2.3) variation of the radial jet is related to numerical noise/error which can be damped or not by turbulent viscosity and reduced by mesh refinement (as explained in appendix A),

2. flow split & pressure loss and the detachment dynamics of the central jet are dependent on the SGS model used (as explained in sections 3.10 and clarified in appendix A: these variations are related to the different amount of turbulent viscosity generated by the SGS model at the solid walls),

3. the mesh quality plays an important role and only the optimized grid allows to obtain coherent conclusions even though the optimized mesh has a $y^+ \in [30, 100]$.

The previous simulations require further analysis and can be used to propose an explanation for the observed results.

3.8.1 An hypothesis on the source of bifurcation.

The jet opening half-angle and the swirl ratio of the radial swirler are plotted for all simulations of table 2.1 in Fig. 3.21. Independently of the code used, the jet-opening half angle shows a small linear dependence on the swirl ratio (S_r) as long as the flow is in the AJ state ($S_r \leq 0.76$). This result is consistent with the correlation between S and α proposed by Gupta et al. [32] (Eq.(2.8)) which is also displayed[8] in Fig. 3.21.
Above $S_r \approx 0.76$, the linear dependence is lost because the flow undergoes a transition to the BB state: the jet opening half-angle becomes $\alpha \approx 90\,\text{deg}$.

A possible interpretation of Fig. 3.21 is that the state BB is obtained in both codes for a swirl ratio of $S_r = 0.8 - 0.82$ (measured on section S3 of Fig. 3.7), while AJ states are obtained for a smaller swirl ratio ($S_r \approx 0.76$). This suggests a possible explanation for the sensitivity of the flow to the numerical settings: in some cases numerical parameters or mesh (or their coupling) lead to a higher swirl ratio and this change leads to a BB state while, in other cases, numerical parameters lead to a smaller swirl ratio and this change leads to an AJ state. This explanation makes sense only if a small variation of swirl can trigger a large jet re-configuration, something that is possible only if the flow conditions are close to critical. **However, too many flow properties change depending on the mesh resolution or on the SGS model employed** (see tables 3.4-3.6-3.9-3.11-3.14-3.16 which show a high scatter of the flow split and of the swirl number of the inner and outer jets).
If the proposed explanation is valid, i.e. if the flow state is mainly controlled by one parameter only, the swirl ratio S_r, this can be checked by using another set of simulations where only S_r would be changed in a controlled manner. In the fixed geometry setup, S_r was not controlled: it was the result of the numerical setup and, as shown in Fig. 3.21, it was changing over a wide range because the flow within the swirler was changing.

[8] Note that Eq.(2.8) shows the dependence of the jet opening half-angle (α) on the swirl number (S) while Fig. 3.21 is a $S_r - \alpha$ diagram. However, Eq.(3.7) shows that the swirl number and the swirl ratio are equivalent if measured on surface S_3 of Fig. 3.6.

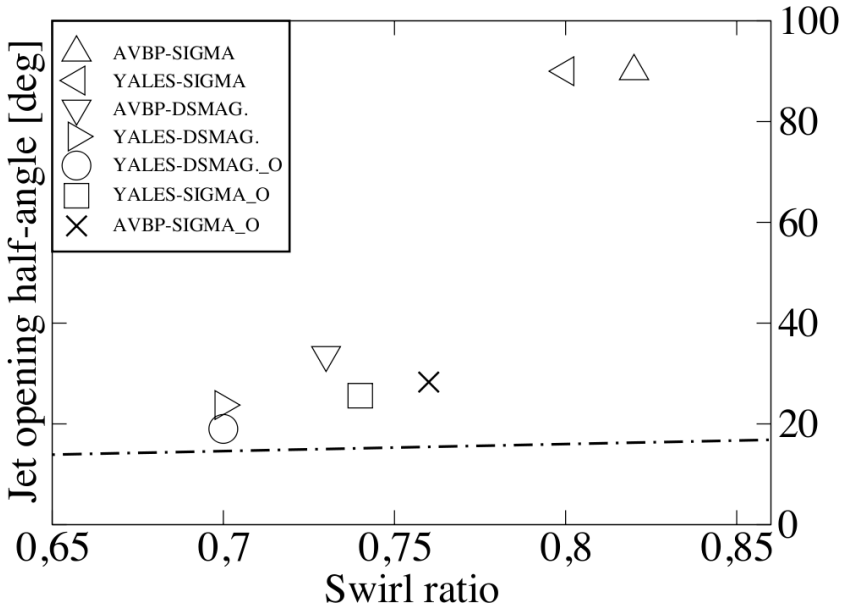

Figure 3.21: Jet opening half-angle (Fig. 3.7), vs. swirl ratio measured on surface S3 of Fig. 3.6 of all LES of table 2.1 performed in this chapter. Dashed lines group the AJ and BB states while the dot-dashed line is the correlation (Eq.(2.8)) proposed by Gupta et al.[32]. The correlation of Eq.(2.8) and LES results do not match very well. This was expected since Eq.(2.8) is obtained by regression of single free-swirling jets, a condition far from the LOTAR experiment.

To clarify this issue, a modified swirler geometry (Fig. 2.1 right) will be tested in LES (chapter 4) where the simplification of the geometry allows to change the swirl levels easily and to decouple each jet from the others while keeping all numerical parameters constant.

3.8.2 Pressure drop

Fig. 3.22 shows the predicted pressure drops measured in all LES of the previous sections. First, the pressure drop is weakly dependent of the particular flow state (AJ-BB) while it is strongly dependent of the SGS model used (turbulent viscosity level modifies the effective hydraulic section of the flow). Second, mesh refinement localized at a position of high numerical error (Fig. 3.16) improves pressure drop, compare[9] YALES-DSMAG. and YALES-DSMAG._O in Fig. 3.22. This is consistent with basic hydraulic concepts: pressure drop is a function of distributed and localized losses. Finally the error level on pressure drop remains too high for all cases shown here and the y^+ (Eq. 3.1) is in the range[10] $[30, 100]$ for all LES performed in this Chapter. Note that the wall resolution in terms of y^+ is also very inhomogeneous in the various swirler vanes, a phenomenon which could affect flow split direclty and pressure drop indirectly.
However, the pressure drop results computed here are in line with previous results obtained on similar geometries (at least when the SIGMA model is used). For instance the LES computations of Jaegle on a very similar injector [47] predict a pressure loss error of +54% despite the use of a dedicated wall function. Similarly Barre et al.[7] mismatched pressure

[9]Note that this comparison makes sense only for the Dynamic Smagorinsky LES which show the same flow state independently of the mesh resolution

[10]In Chapter 9 the y^+ distribution in the domain is shown.

losses from +105% to +52% with respect to experimental data (depending on the grid resolution, from a y^+ of $O(60)$ to O(15) respectively) on a much simpler swirler geometry using both YALES2 and AVBP.

Finally flow split between the swirler and the cooling films is an additional source of uncertainty which could influence pressure drop. The pressure drop issue is not further investigated here but it remains an open question for such type of confined flows and requires further work.

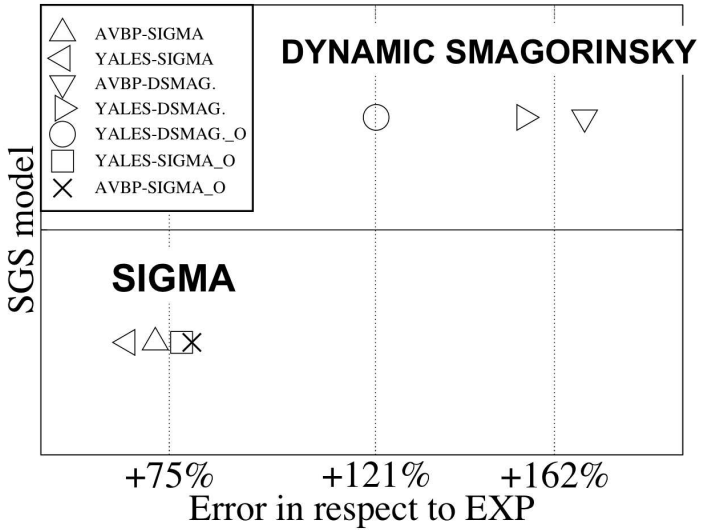

Figure 3.22: Pressure drop of all LES of table 2.1 performed in this chapter.

3.8.3 Numerical considerations

The sensitivity analysis of the LOTAR LES shows that:

- Numerical error is an important issue. The most important (because of its supposed effect on the overall flow behavior, see section 3.8.1) numerical error is generated by the strong velocity gradient soon at the exit of the radial swirler vanes, between the solid boundary and the multiple jets cores.

- High levels of turbulent viscosity can damp numerical error: turbulent viscosity smoothes the velocity gradients and indirectly reduces it.

- A LES with a SGS model which generates low turbulent viscosity, as SIGMA does, can be contamined by numerical noise. Such LES is more demanding in terms of mesh quality, but it can give very good results if the grid is sufficiently refined.

- A LES with a SGS model which generates high levels of turbulent viscosity, as Dynamic Smagorinsky does, is less contamined by numerical noise on under-resolved

meshes. The quality of such a simulation is low, since this viscosity level is not physically justified. The outcome is a **poorer prediction of pressure loss, flow split** and of the velocity profile (on a proper mesh) with respect to SIGMA and the generation of non-physical flow behavior (like the detachment of the central jet, see appendix A).

- A reduced, localized mesh refinement, can have a deep impact on the velocity profiles. In figure 3.23 turbulent kinetic energy, just downstream of the exit of the radial swirler vanes, is shown for two SIGMA simulations on the *basic* vs. *optimized* meshes. A low resolution in this critical area makes the distribution of turbulent kinetic energy fuzzy and undefined, while a higher resolution leads to a flow field of kinetic energy organized along the recirculation bubbles.

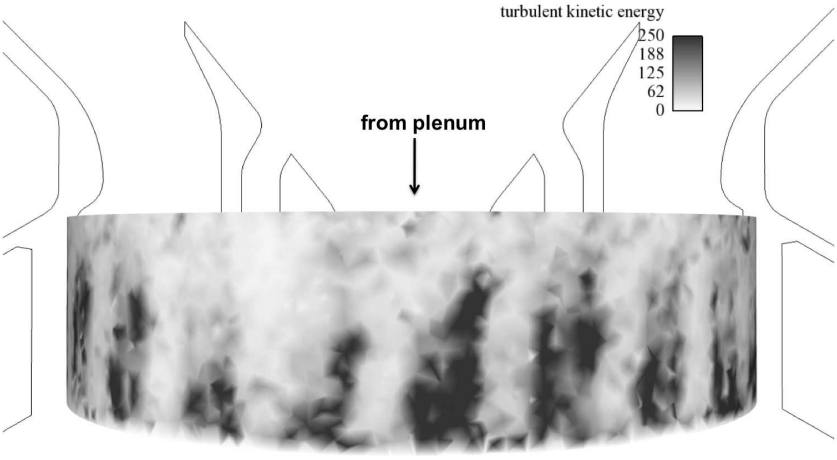

(a) YALES-SIGMA

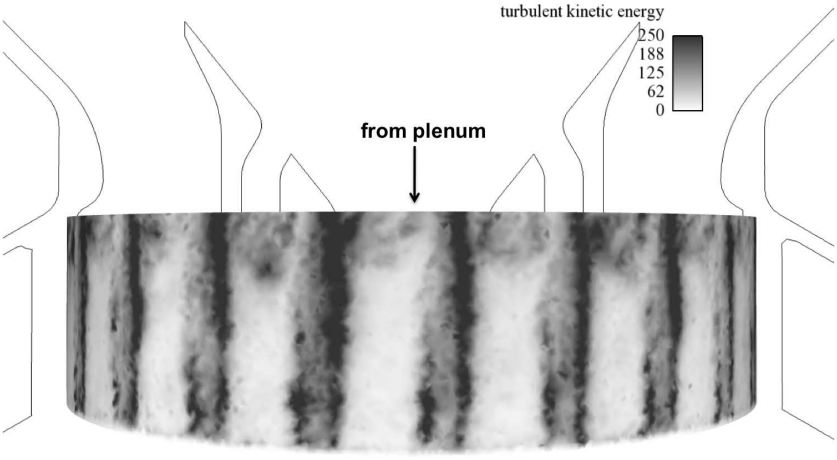

(b) YALES-SIGMA_O

Figure 3.23: Turbulent kinetic energy levels on a cylindrical surface inside the radial swirler bowl, just downstream of the exit of the swirler vanes, (a) *basic* mesh, vs. (b) *optimized* mesh.

Chapter 4

Sensitivity analysis of swirling flows LES to fluid dynamics conditions

4.1 Motivation and methodology

Chapter 3 shows that the two LES codes used in this work predict that the unconfined swirling jet, generated by the LOTAR injector, undergoes bifurcation between two states (AJ-BB) which leads to different flow fields and different jet expansion angles. This bifurcation seems to depend on multiple numerical parameters (mesh, SGS model) but the analysis of results of chapter 3 has suggested that the parameter governing the flow response is the swirl ratio of the radial jet (Eq.(2.3)). The swirl ratio of the radial jet is representative of the total angular momentum of the radial jet for a given mass flow rate. This dependency is made clear by Fig. 3.21 in which the jet opening half-angle is plotted against the swirl ratio: for a swirl ratio above $S_r \approx 0.8$ the jet is in the BB state, while for S_r below ≈ 0.76 is in the AJ state.
This variation of the swirl ratio was related to the different numerical settings employed in the various simulations, which modified the mean velocity profile downstream of the radial swirler vanes. Numerical settings influenced the swirl numbers of the various jet as well as the flow split and the detachment dynamics of the central jet. The effects of such modifications are unknown and cannot be identified clearly from the analysis of chapter 3 because they all act on the flow at the same time.
The assumption that the AJ-BB bifurcation is related to the amount of swirl in the radial jet requires a further verification in a controlled environment: an additional numerical experiment is setup in this chapter, keeping all numerical settings constant and variating simply the fluid dynamics conditions of the jet. The target of this chapter is therefore to prove that it is possible to cause bifurcation in the LOTAR configuration by modifying the swirl ratio of the radial jet only, keeping all numerical parameters constant.
The existence of confined swirling flows exhibiting two or more possible states as a function of the swirl intensity, characterized by a different jet expansion angle, has already been studied experimentally in the past (see Chedaille et al. [46] or Beer and Chigier [8]) and recently (2007) by Vanierschot et al. [105] (as shown in chapter 3, the flow states of LOTAR

and of Vanierschot [105] show common, peculiar properties). Here the same experiment will be repeated numerically for LOTAR. The analysis is conducted as follows:

- In order to remove the dependence on the numerical settings, these are kept constant: YALES2 is used for all tests with SIGMA as SGS model and no slip walls.
- In order to better capture turbulence and the wall phenomena, the resolution is increased at the solid walls and in the whole simulation domain.
- In order to impose the desired fluid dynamics conditions for each of the jets of Fig. 3.6, the simulation domain is modified (Fig. 4.1) making possible to decouple swirl intensity from the swirler geometry. This allows to vary the swirl number continuously.
- In order to study hysteresis, the initial conditions are varied.

Results will confirm the assumption reached in chapter 3: a variation of O(10%) of the swirl ratio is able to cause the bifurcation that distinguishes the AJ from the BB states. Evidences of hysteresis are also included. All simulations performed in this chapter are itemized in table 4.1: the two basic simulations are named "basic" and "high" and they start with a zero velocity flow field while the hysteresis LES are named P"X"_"U" (where "X" is the simulation number and "U" or "D" stands for the Up or Down part of the hysteresis loop respectively).

LES name	S (eq. 2.2) inner/outer jet	S_r (eq. 2.3) radial jet	initial condition	jet configuration
basic	0.12/ 0.4	0.75	zero velocity	AJ
high	0.12/ 0.4	0.84	zero velocity	BB
P1_U	0.12/ 0.4	0.84	basic	AJ
P1_D	0.12/ 0.4	0.75	high	BB
P2_D	0.12/ 0.4	0.60	P1_D	AJ
P3_D	0.12/ 0.4	0.75	P2_D	AJ

Table 4.1: First set of LES of the adjustable swirler case.

4.2 Mesh, boundary conditions and numerical settings

The original LOTAR CAD was modified to decouple the flow properties from the geometry of the device. This is achieved by removing the plenum and the swirlers from the domain (Fig. 3.3) keeping un-modified the diffusers and the bowls. This geometry is named *adjustable swirler* (Fig. 2.1 right). Instead of feeding the injector via the *plenum inlet* of Fig. 3.3, three inlets (corresponding to the inner, outer and radial jets) are placed downstream, just at the exit of the swirler vanes (Fig. 4.1). In Fig. 4.2 it is possible to see the various inlets corresponding to each vane (darker parts, clustered together in single boundary conditions) for the three different jets. This geometrical detail is kept since the presence/absence of the end walls had an impact on the bifurcation diagram (this test is not shown here).

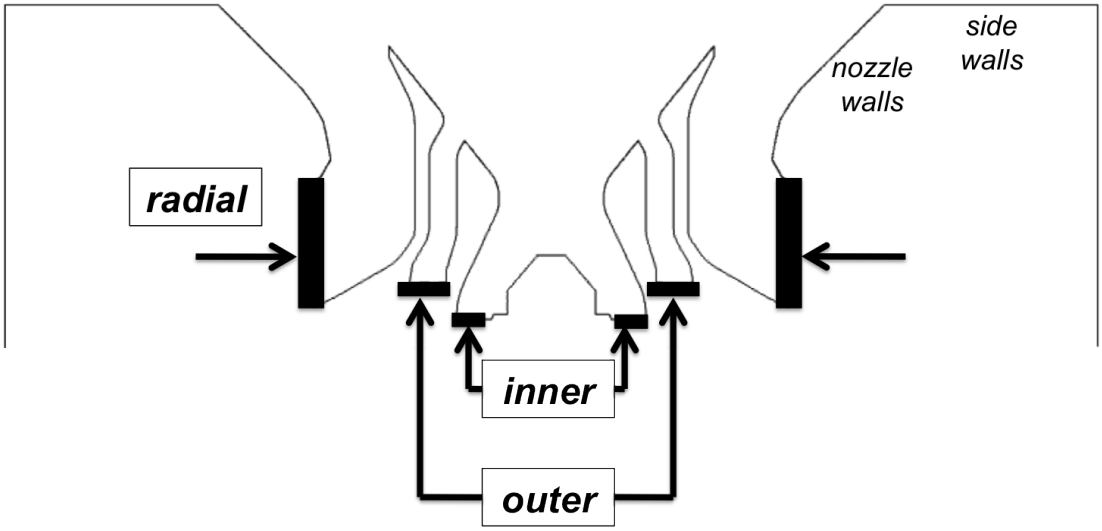

Figure 4.1: Inlet boundary conditions of the LOTAR adjustable swirler case, inside the swirler. Boundary conditions are imposed on the shaded sectors visible in figure and not at the inlet of the plenum which is not resolved anymore.

Geometry simplifications of swirlers are quite common in the literature because they make LES simpler and often allow to tune results since inlet velocity profiles can be adjusted as needed. At CERFACS, this practice is avoided since it requires to implement *ad-hoc* boundary conditions inside the swirler, something that is a different and somewhat *ad-hoc* exercise. In the present case, however, it has a clear intent: it allows to impose the desired swirl number, ratio and Reynolds number (i.e. mass flow rate) for each jet by changing the velocity profiles on the black lines of Fig. 4.1 which corresponds to the inlet sections of the adjustable swirler geometry.
The mesh is shown in Fig. 4.3-4.4. To ensure that the resolution is sufficient, the minimum cell size is 50 times smaller than the smallest element of the *basic* or *optimized* meshes employed in chapter 3. The smallest cells are located at the solid boundaries where a minimum cell size of $50\mu m$ is imposed, while, inside the swirler, elements size varies between $300\mu m$ and $400\mu m$ (Fig. 4.3). The mesh is then smoothly coarsened away from the swirler (Fig. 4.4), the cell size gradation (variation of the cell size in neighbor elements) has been limited to 1.3 and the cell aspect ratio to 2.

4.2.1 Boundary conditions

As in chapter 3, the swirler is mounted on a cylindrical box to mimic open atmosphere. Boundary conditions used in this chapter are the same shown in Fig. 3.3 ("far field B.C.s") including the cooling film (Fig. 3.3 "swirler B.C.s" and Fig. 3.4). A coflow is added like in Fig. 3.3. Annex B shows that this coflow has a very limited effect on the results. Evidently, the plenum inlet in Fig. 3.3 is removed and replaced by three inlets (inner, outer and radial in Fig. 4.1). Boundary conditions are summarized in tables 4.2 and 4.3.

Target values of the new inlets introduced inside the swirler are summarized in table 4.3, the mass flow rate and a specific velocity profile (in terms of mean values), are imposed. The velocity profile is flat (a turbulent velocity profile), but no turbulence is injected. The no-slip boundary condition naturally damps the speed at the solid walls. A

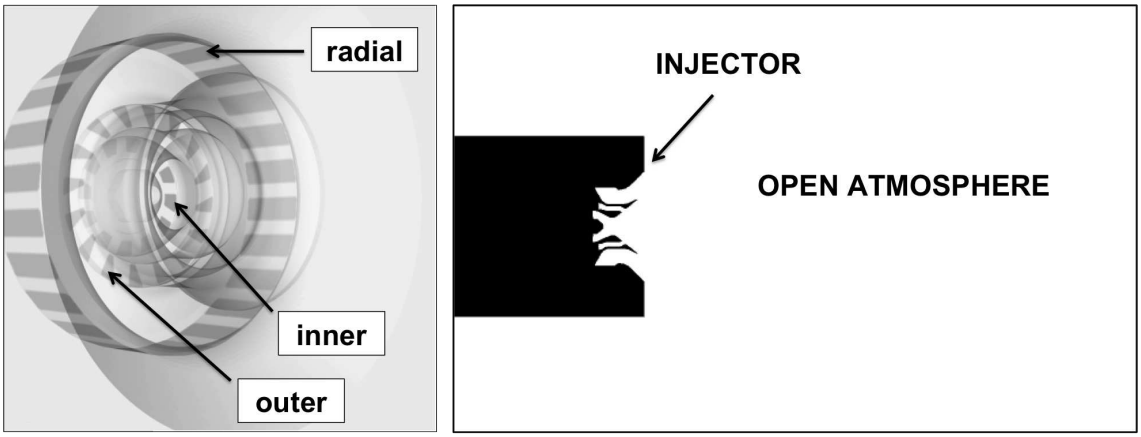

Figure 4.2: Left, Inlet boundary conditions of the LOTAR adjustable swirler case. The different vanes (darker parts) forming the inlet boundary conditions in the swirler, are visible. Right, sketch of the whole configuration of the adjustable swirler case. The jet generated by the swirler expands in the open atmosphere. Only the part in white is simulated.

Reference temperature = 270 [K]		
BC NAME	IMPOSED PROPERTY	TARGET VALUE
coflow	velocity	1 $[m/s]$
cooling film	mass flow rate	30.3 $[g/s]$
outlet	pressure	99000 $[Pa]$
walls	adherence, impermeability, adiabaticity	

Table 4.2: Imposed values for boundary conditions sketched in Fig. 3.3 (with the exception of *plenum inlet* which has been removed).

systematic study of the effects of the injected turbulence (which in the real configuration is generated inside the swirler vanes, a set of turbulent channels) goes behind the scope of this numerical experiment. However this small scale turbulence is supposed to have a limited influence on the large flow structures generated downstream by the swirler because of the different length scales involved. For each INLET of Fig. 4.1:

- the normal velocity component is imposed through the mass flow rate.
- The tangential velocity component is adjusted in order to get the desired swirl number or ratio: this component is the only one that is varied in the various simulations of table 4.1.
- The remaining velocity component is obtained by post-processing simulation YALES-SIGMA_O (this component is ≈ 0 for the inner and outer jets, while for the radial jet is $\approx 31[m/s]$). The choice of this third component is arbitrary since it is supposed to have only a second order effect on the overall jet response.

The swirl ratio (S_r) and the swirl number are evaluated at the same locations (S1, S2, S3) used in chapter 3 (Fig. 3.6). Note that the swirl ratio (S_r, Eq. 2.3) is used to measure the amount of swirl in the radial jet while the swirl number (S, Eq. 2.2) is used for the inner and outer jets, as described in section 3.3.1. The measured mass flow rates are in line

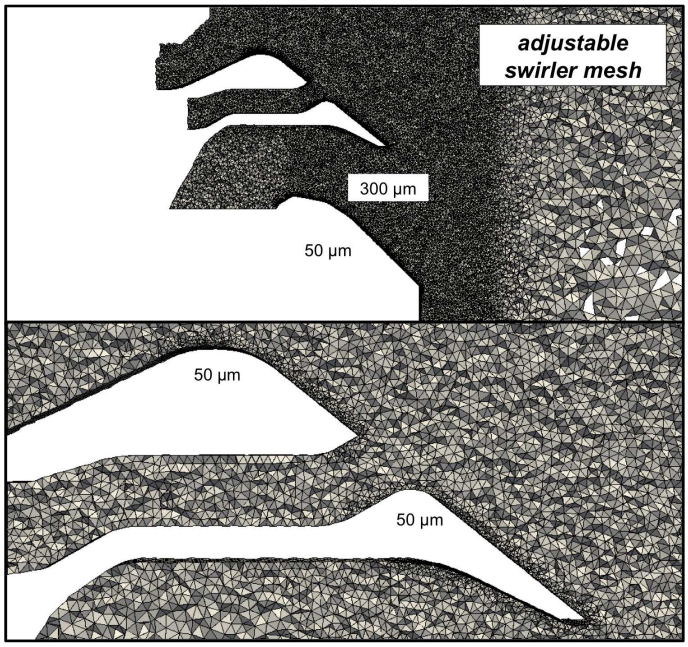

Figure 4.3: Adjustable swirler case mesh, zoom at the swirler.

SWIRLER Boundary Conditions, imposed velocity			
B.C. NAME	axial	tangential	radial
INNER	66.7 [m/s]	-21.5 [m/s]	1[m/s]
OUTER	64[m/s]	38.6 [m/s]	0.9[m/s]
RADIAL	31.6 [m/s]	simulation dependent	-57.9[m/s]

Table 4.3: Imposed boundary values inside the swirler, Fig. 4.1. The only passage that is changed for the simulations is the radial one (with the exception of LES "outer" as it will be shown later on), which is used to vary swirl intensity.

with the predicted values (error is O(4%) for the axial stage and O(0.5%) for the radial, see table 3.14). The measured swirl ratio of the radial jet and the tangential velocity imposed at the corresponding B.C. are in linear proportion in the whole range tested (Fig. 4.5). This is linear correspondence is a clear result of the high mesh resolution in the radial swirler, a too coarse mesh would have cause a different swirl ratio for the same incoming tangential velocity (determined by the swirler vane angle) as already experienced in chapter 3.

4.2.2 Numerical Settings

The simulations of table 4.1, use the same code (YALES2), SGS model (SIGMA), numerical settings and wall treatment (no-slip solid boundaries). The simulations differ only because of the fluid dynamic properties imposed at the three inlets of the swirler (table 4.3) and of the initial conditions.

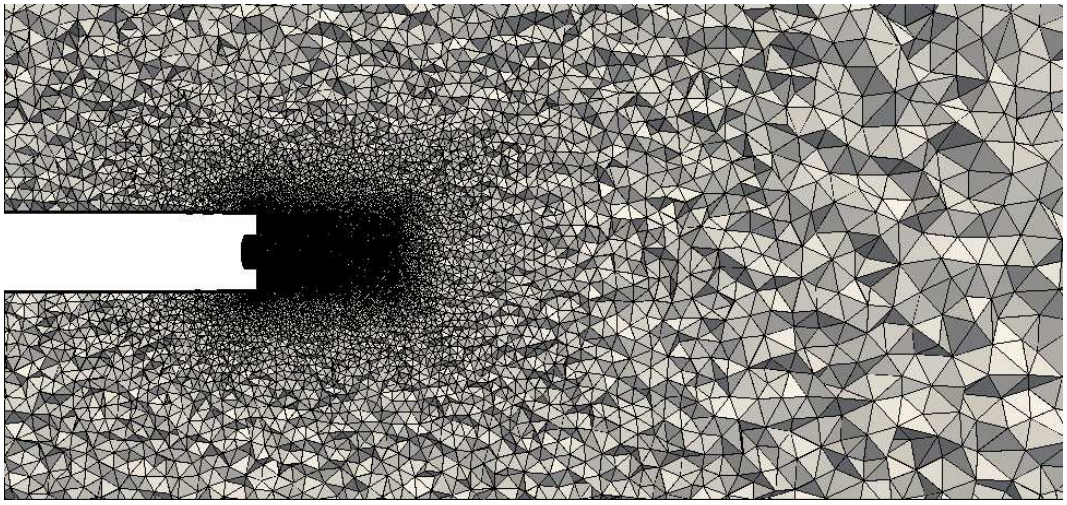

Figure 4.4: Adjustable swirler case mesh, far field.

JET	mass flow rate	swirl number or ratio
INNER	6.5 [g/s]	0.12 (Eq.2.2)
OUTER	9.1 [g/s]	0.4 (Eq.2.2)
RADIAL	86.4 [g/s]	simulation dependent (Eq.2.3)

Table 4.4: Measured mass flow rate and swirl ratio for LES of table 4.1.

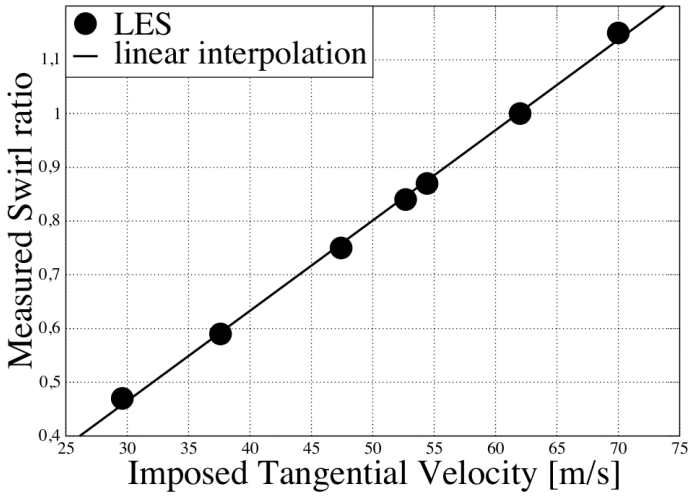

Figure 4.5: Swirl ratio (Eq. 2.3) of the radial jet plotted against boundary tangential velocity imposed at the radial B.C. in Fig. 4.1. The continuous line is the linear interpolation of the points.

4.3 Simulations Quality

LES quality is assured by monitoring multiple sensors: the wall distance nondimensionalized by the boundary layer thickness, the y^+ values, the ratio between laminar and turbulent viscosity and the Pope criterion [89] (ratio of resolved turbulent kinetic energy to resolved plus SGS turbulent kinetic energy, Eq. (4.1)). The values of y^+ (evaluated

at the cell baricentrum) are below 10 everywhere except downstream of the swirler vanes because of the high jet velocity (Fig. 4.6).

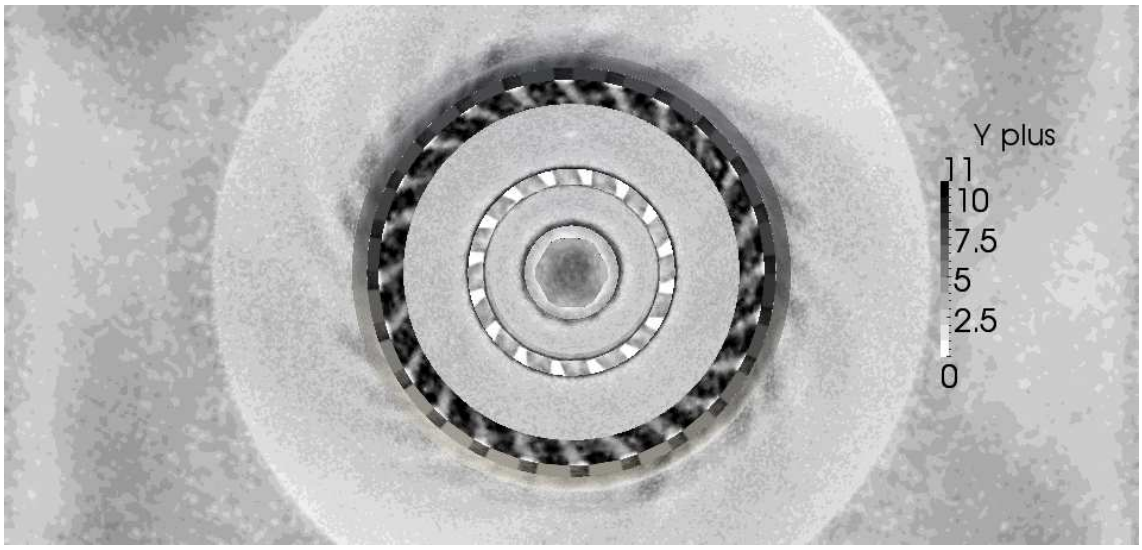

Figure 4.6: Mean y^+ values for LES basic of table 4.1. The swirler surface is seen from the open atmosphere.

The ratio of turbulent to laminar viscosity is low (Fig. 4.7 right and Fig. 4.8), while the Pope criterion [89]:

$$Pope = \frac{k_{res}}{k_{res} + k_{sgs}}, \tag{4.1}$$

is everywhere higher than 0.9 in the proximity of the swirler and equal to 1 inside the well resolved jet (Fig. 4.7 left). Resolved turbulence, k_{res}, is evaluated as $\frac{1}{2}\sum_{i=1}^{3}(u_i'^2)$ where u_i' is the Reynolds decomposition of the velocity component u_i. Subgrid scale turbulence is evaluated as [94]:

$$k_{sgs} = (\frac{\nu_t}{C_M \Delta})^2 \tag{4.2}$$

where $C_M = 0.069$ and Δ is estimated as the cubic root of the elements volume.

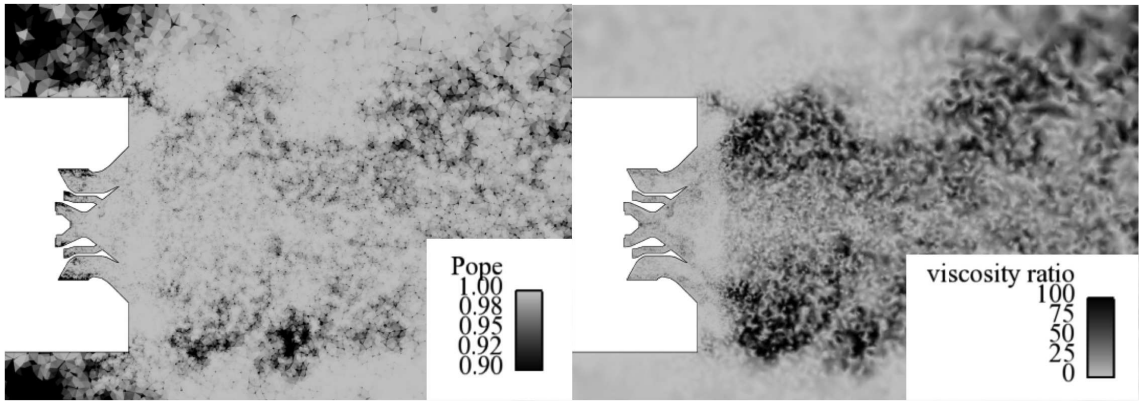

Figure 4.7: Snapshots of ratio of turbulent over laminar viscosity and Pope criterion, Eq. (4.1), for LES basic of table 4.1.

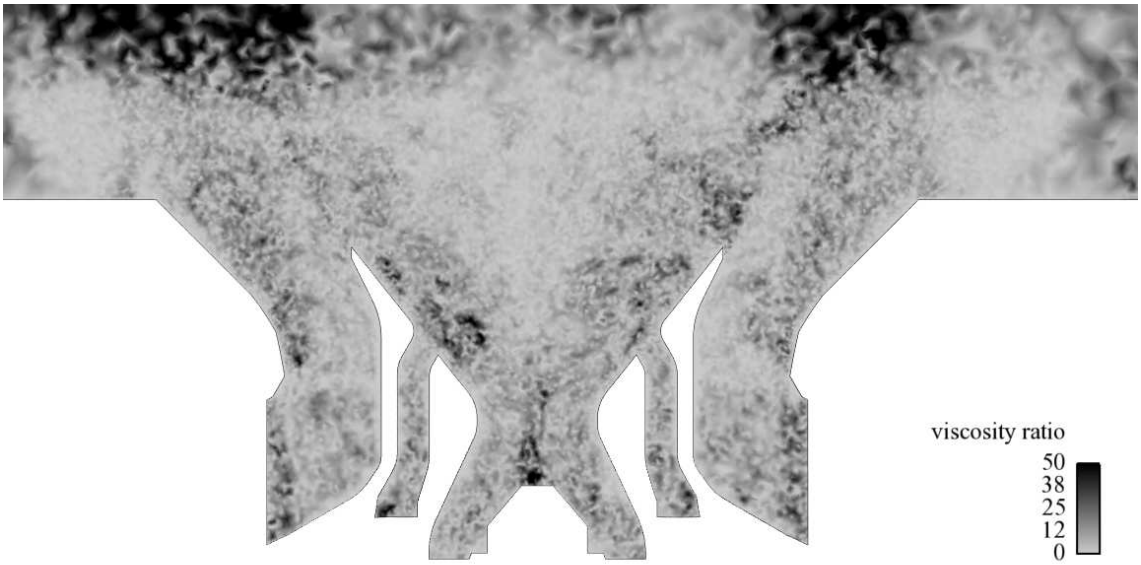

Figure 4.8: Ratio of turbulent over laminar viscosity of LES basic of table 4.1.

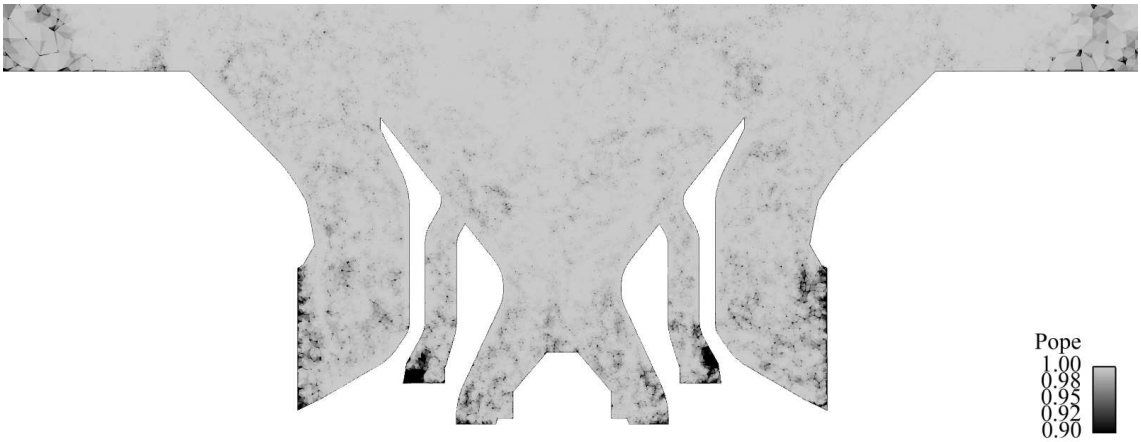

Figure 4.9: Pope criterion of LES basic of table 4.1.

All simulations show a P over ≈ 0.9 in the swirler, with the exception of some localized zone at the swirler inlets, since turbulence is not injected in the simulation domain and it does not have time to be produced by the flow (so $k_{res} \approx 0$, Fig. 4.9).

4.4 Simulation times and convergence

All statistics of LES of table 4.1 were collected after a period of 0.030 [s] and averaged for at least 0.004 [s] equivalent to ≈ 4 flight through times (considering a length scale of twice the injector diameter, $\approx 2D \approx 0.1[m]$, and a convective velocity of $\approx 100[m/s]$). Fig. 4.10 shows the time evolution of volume-average kinetic energy of the **basic & high** simulations of table 4.1. The kinetic energy is evaluated on a box big enough to fully

contain the recirculation bubble of the **high** case (Fig. 4.11) which is the largest observed. This choice is motivated by the fact that to obtain the convergence of kinetic energy in the whole simulation domain (inside the whole cylindrical box used to mimic open atmosphere) it requires a simulation time of $\approx 0.3[s]$ (so 300 simulations for each configuration) and by the fact that the far field has little influence on the jet, as shown in appendix B.

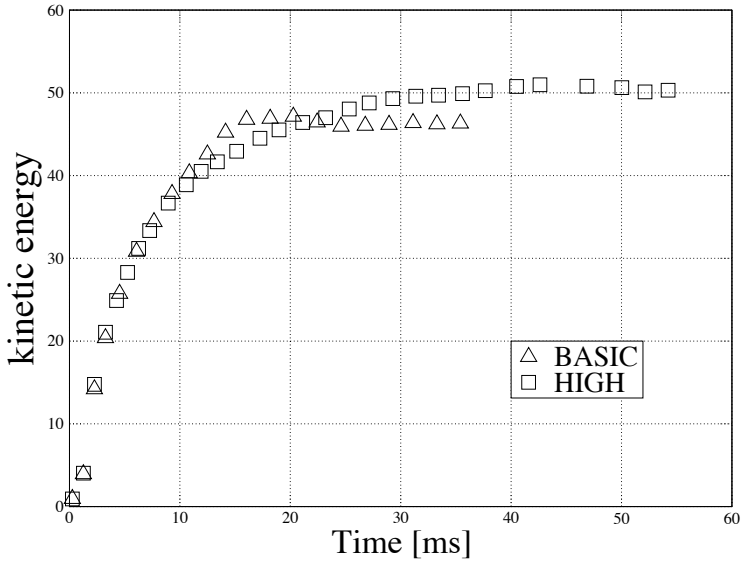

Figure 4.10: Kinetic energy evolution for simulations **basic, high & outer** of table 4.1.

To go from one of the LES of table 4.1 to another one (with a different set of B.C.s), the swirl ratio imposed at the radial boundary condition is varied continuously (unless LES is re-initialized). The acceleration rate of the tangential velocity used for these transition phases is $O(1000)[m/s^2]$. Even if this value is $O(100)$ times the gravitational acceleration, a slower acceleration/deceleration rate would cause a slower convergence to the desired target value. However, two things should be underlined. First, this type of injector is susceptible to acoustics. The characteristic frequency of these waves is $O(100)[Hz]$ with a oscillation in terms of flow speed that could reach $O(10)[m/s]$ [88], which leads to an acceleration rate of $O(1000)[m/s^2]$. Second, stiff transitions are not un-common in LES: a switch from an SGS model to another would cause an even stiffer change in the flow field. Therefore such acceleration rate can be considered as consistent with the common fluid dynamics and/or numerical conditions.

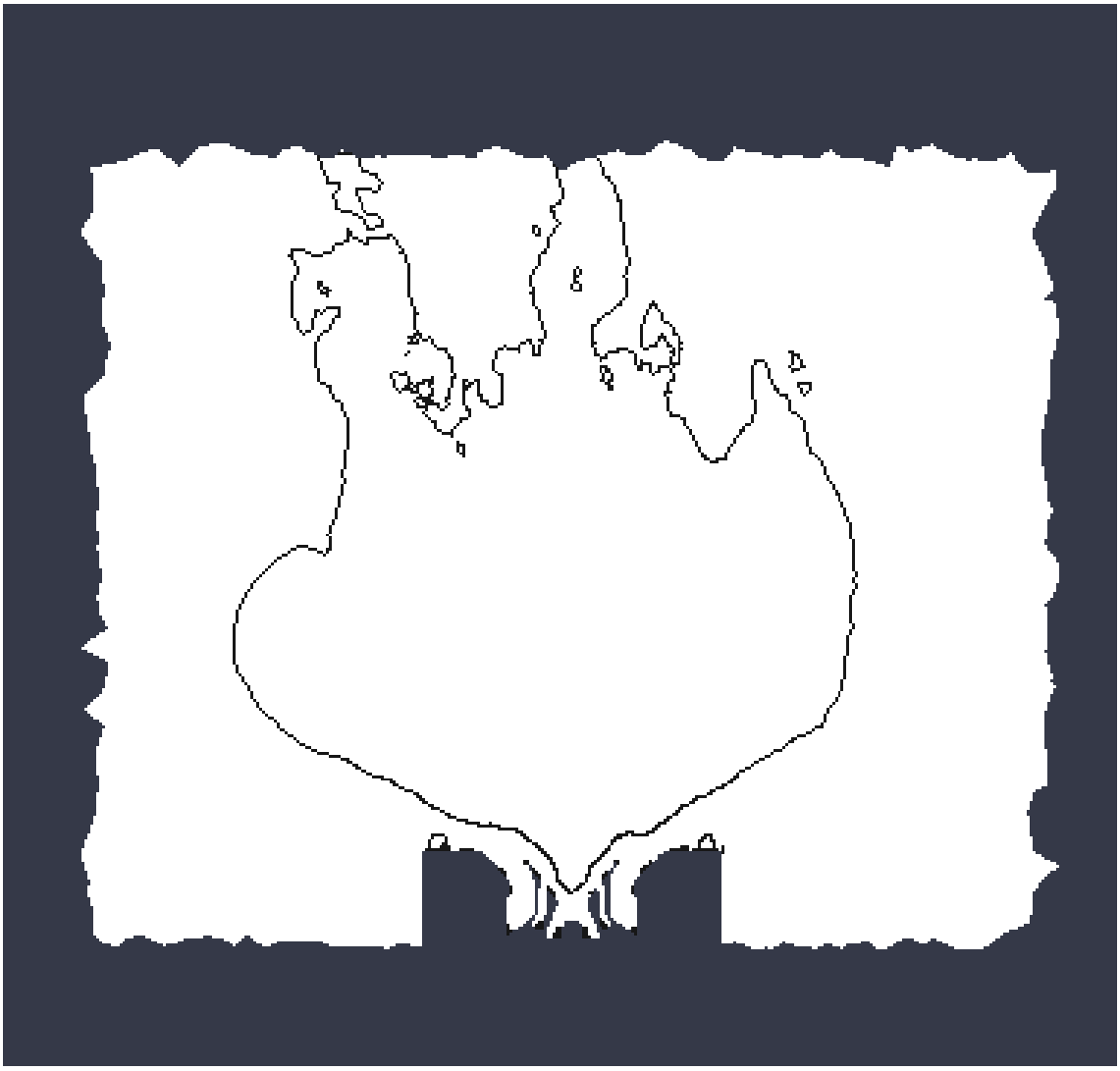

Figure 4.11: White zone: box used to evaluate the jet's kinetic energy. The black line is the zero axial velocity isoline for simulation high of table 4.1.

4.5 Basic configurations

Two simulations are first tested for two different radial jet swirl ratios. The swirl introduced by the inner and outer jets is kept constant ($S = 0.12$ and $S = 0.4$ respectively, the swirl number S, Eq. 2.2, is always used for the two co-axial jets). The first simulation (basic) uses a swirl ratio (the swirl ratio S_r, Eq.2.3, is always used for the radial jet) of the radial jet similar to simulation YALES-SIGMA_O; the second (high), uses a swirl ratio 10% higher ($S_r = 0.84$). The characteristics of these two simulations are summarized in table 4.5, while their flow fields and CTRZs are shown in Fig. 4.12.

LES name	S (eq. 2.2) inner/outer jet	S_r (Eq. 2.3) radial jet	jet configuration
basic	0.12/ 0.4	0.75	AJ
high	0.12/ 0.4	0.84	BB

Table 4.5: First set of LES of the adjustable swirler case.

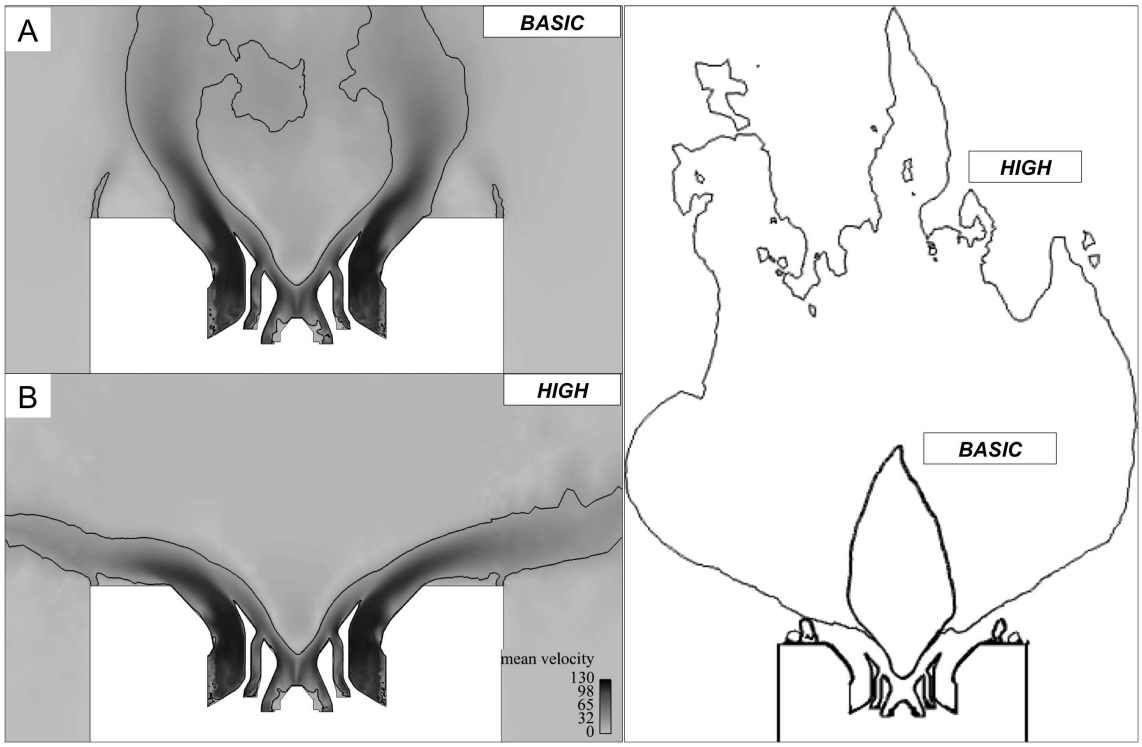

Figure 4.12: A-B: flow fields and velocity isoline ($U = 20[m/s]$) of simulations *basic* & *high* of table 4.5. CTRZs (zero axial velocity isoline) of these simulations are shown in the picture on the right.

The flow configuration of the *basic* case is characterized by a CTRZ smaller than one injector diameter (Fig. 4.12), a high tangential velocity (Fig. 4.13), a high sub-pressure ($P_D \approx 0.44$) and high turbulence intensity inside the CTRZ (Fig. 4.14). On the contrary, the flow configuration of the *high* case is characterized by a CTRZ which is several injector diameters wide (Fig. 4.12), a strong reduction of tangential velocity inside the CTRZ (Fig. 4.13) and a reduced sub-pressure ($P_D \approx 0$) as well as a negligible turbulence intensity inside

the CTRZ (Fig. 4.14). The jet of *basic* LES is therefore in the AJ state while the jet of the *high* case is in the BB state: an increase of 10% of the swirl ratio of the radial swirler jet (from $S_r = 0.75$ to $S_r = 0.84$) is enough to induce a bifurcation of the flow from AJ to BB states. Note also that the flows in the fixed swirler case of chapter 3 (i.e. Figs. 3.10-3.15 & Figs. 3.17-3.20) are similar to the flows in the adjustable swirler case (Figs. 4.13 and 4.14), showing that replacing the full swirler computation by an equivalent set of boundary conditions has a limited impact on the flow organization, as long as both jets are in the same state (AJ or BB).

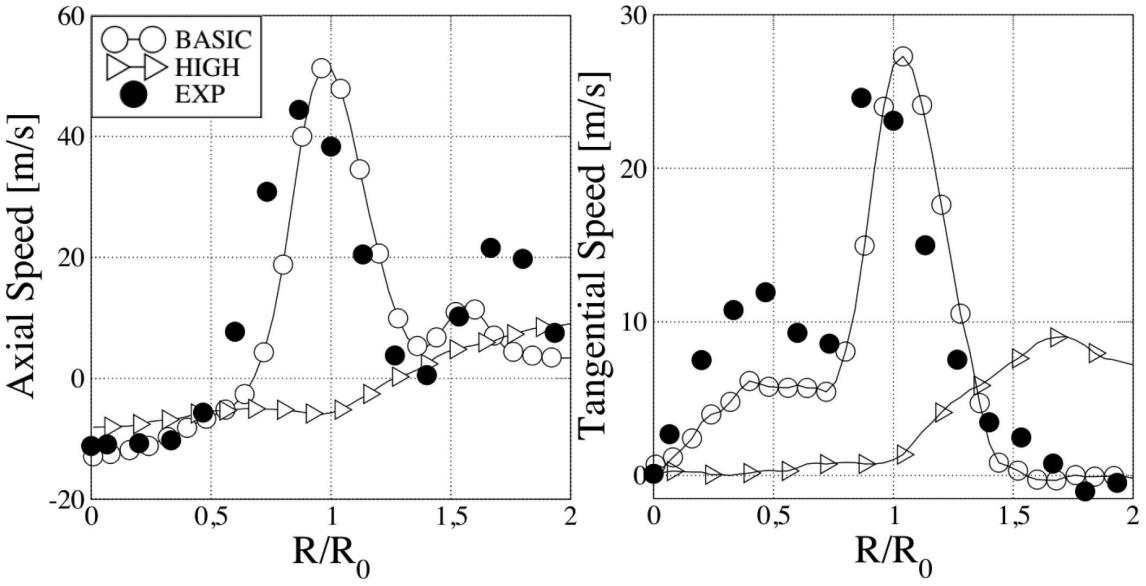

Figure 4.13: Flow velocities plotted against normalized radial positions for simulations of table 4.5. Measurements are taken $0.5R_0$ ($15[mm]$) downstream of the swirler end plate.

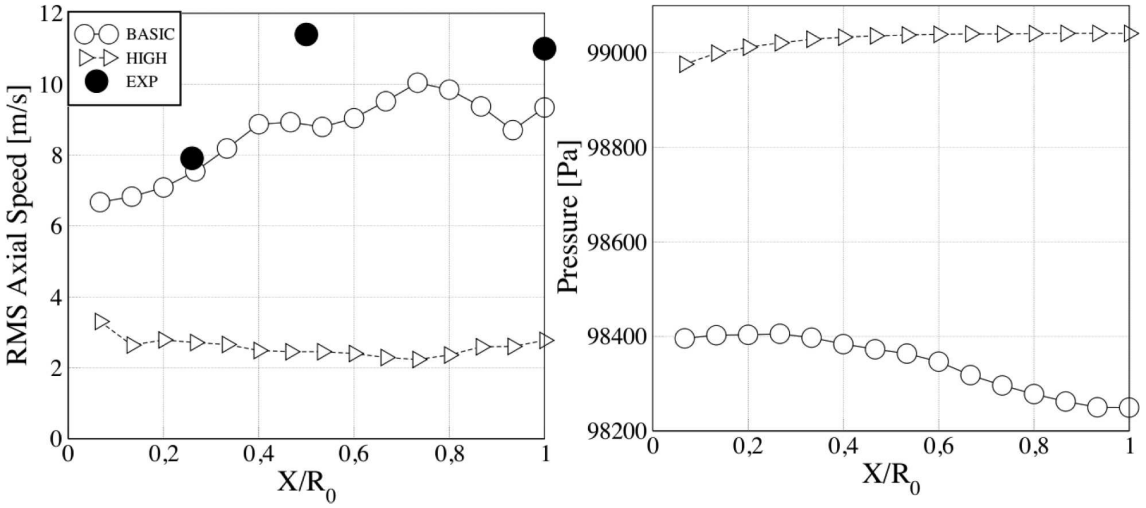

Figure 4.14: Axial velocity RMS and pressure distribution measured along the centerline of the geometry. Results are plotted against normalized axial distance (X/R_0) from the swirler end plate for simulations of table 4.5.

4.6 Pressure fields and flow patterns

Fig. 4.15 shows the pressure fields of simulations of table 4.5 where the different flow states are visualized by the mean pressure distribution. The jet attachment to the side walls (see Fig. 4.1) of simulation *high* is made evident by a localized subpressure in that zone, a phenomenon not observed for LES *basic* (in which a negative pressure gradient is present from the side wall toward the CTRZ core).

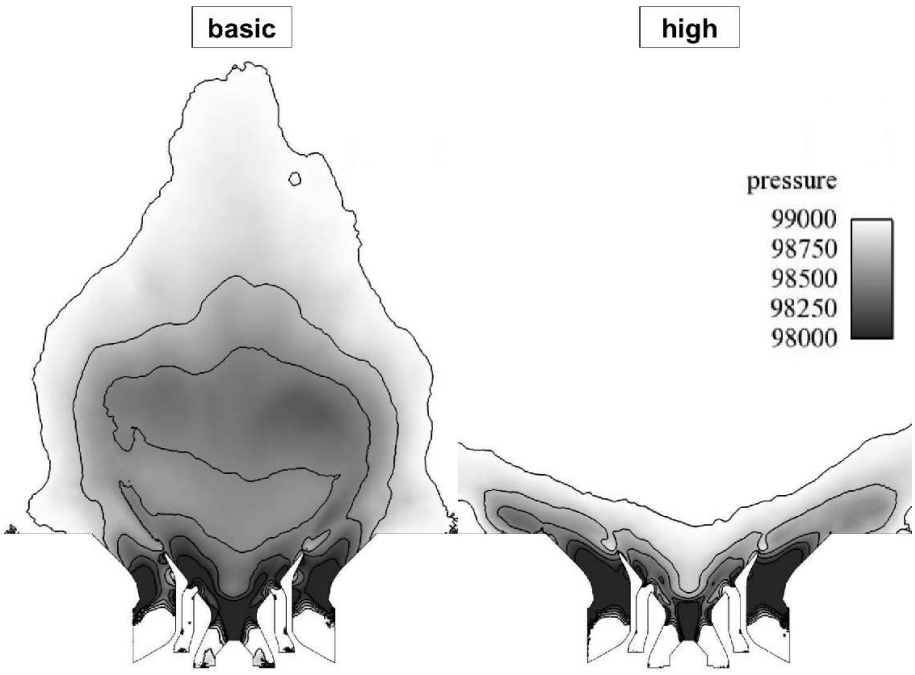

Figure 4.15: Mean pressure field for simulations of table 4.1.

An interesting feature of the *basic* simulation is the dynamics of the central jet, which remains attached. Comparing Fig. 4.16 and Fig. A.1, it is evident that an attached central jet can be obtained despite a low swirl number in the inner and outer jets, see tables 4.3 and 3.11: the detachment dynamics of the central jets are related to the SGS model and to a locally poor mesh resolution, as explained in appendix A, and not to the swirl numbers of the central jet.

To visualize the flow pattern, a passive scalar (the numerical equivalent of the smoke or dye used in the experimental literature on the subject) is injected at the radial inlet. Fig. 4.17 shows the instantaneous distribution of a passive scalar (named R) for simulations *basic* & *high*: the jet direction is made evident by the convection of R.

4.6.1 Comparison with experimental data

Comparison with experimental data is shown here just as a reference for simulations *basic* and *high*, Figs. 4.18, 4.19, 4.20. The *basic* LES shows a very good comparison with experimental data, with the jet opening half-angle matched by LES. The length of the recirculation zone, see Fig. 4.18 third plane, is well predicted by LES.

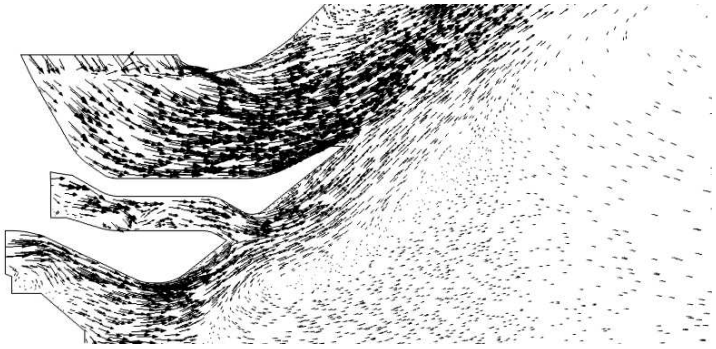

Figure 4.16: Velocity vectors, simulation **basic**.

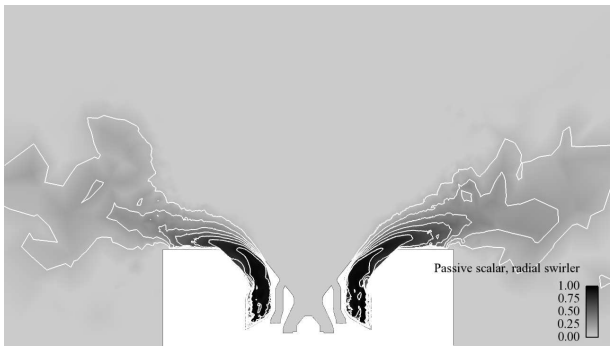

(a)

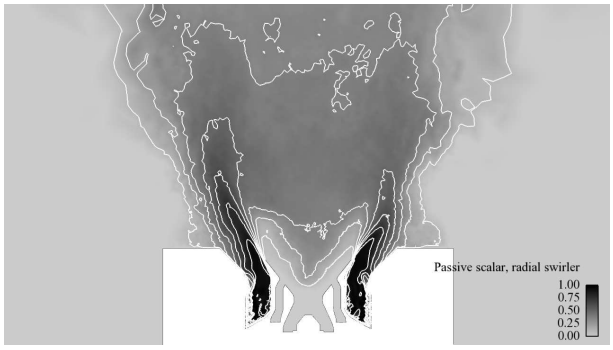

(b)

Figure 4.17: Distribution of the passive scalar R (injected at the radial inlet of Fig. 4.1) **high** (a) vs. **basic** (b).

Differently from the *basic* LES, the *high* simulation forecasts a BB state: results are bad. Note that the true value of the swirl ratio in the experiment is unknown. When setting up this simulation, using a low ($S_r = 0.75$) or an high ($S_r = 0.84$) swirl value is clearly an "uncertain" parameter. The results of Fig. 4.18 to 4.20 show that this uncertain parameter actually controls a very strong bifurcation and that only the *basic* case corresponds to the experimental data since the flow is in the same state (AJ).

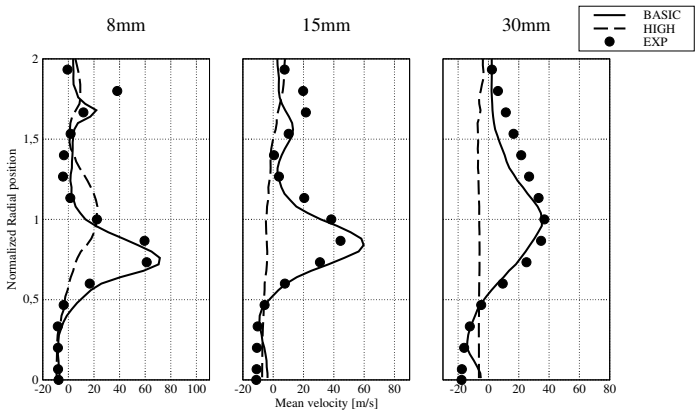

Figure 4.18: Axial velocity for simulations *basic* and *high* of table 4.1, radius for normalization $R_0 = 30[mm]$.

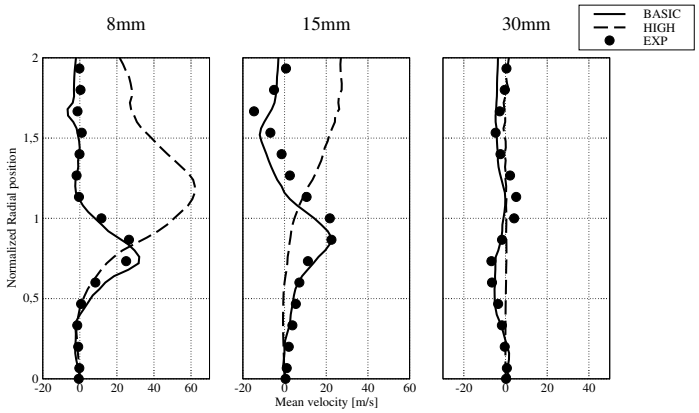

Figure 4.19: Radial velocity for simulations *basic* and *high* of table 4.1, radius for normalization $R_0 = 30[mm]$.

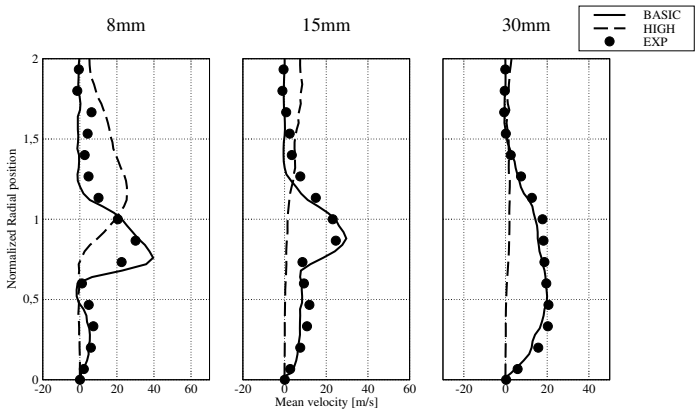

Figure 4.20: Tangential velocity for simulations *basic* and *high* of table 4.1, normalization radius $R_0 = 30[mm]$.

4.6.2 PVC

The PVC can be identified in simulations *basic* and *high* by injecting a second passive scalar (named C) at the pilot injector, in a central position inside the innermost bowl (Fig.4.21a). By monitoring the pressure signal at three different locations (Fig.4.21b), it is possible to identify the frequency of the PVC, which is $\approx 2500Hz$ for both simulations.

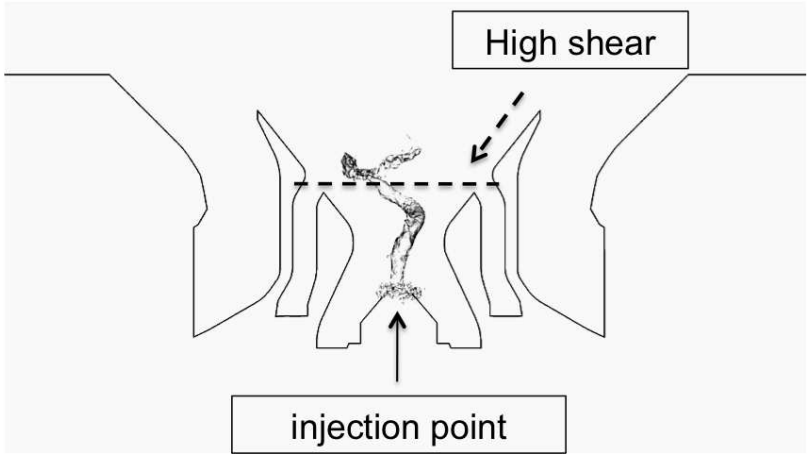

(a) PVC

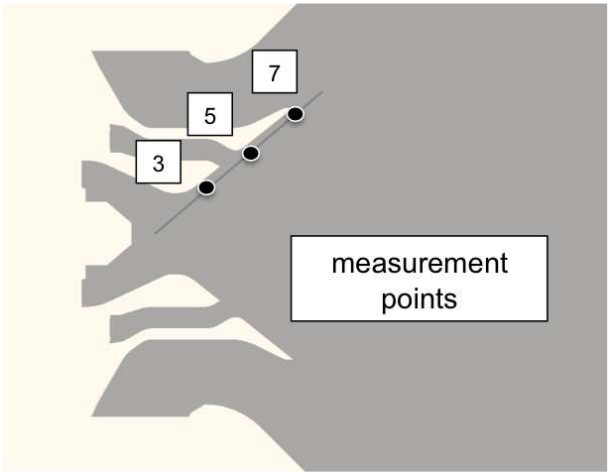

(b) Measurement location of the the pressure signal of Fig. 4.22.

Figure 4.21: (a) Passive scalar C injection point and PVC (made evident by a passive scalar isosurface) of simulations *basic* and *high* of table 4.1.

Fig. 4.22 shows the Discrete Fourier Transform of the pressure signal taken at the different points.

The PVC extends until the position where the inner and outer counter-rotating jets merge (Fig. 4.23). Visually (Fig. 4.24) and from the spectrum of the pressure signal at three different locations (Fig. 4.22) is possible to determine the size of the PVC which ends where the inner and outer counter-rotating jets merge in a single stream (Fig. 4.23). Here, because of the high shear, the *numerical smoke* (the passive scalar C, which evidently can

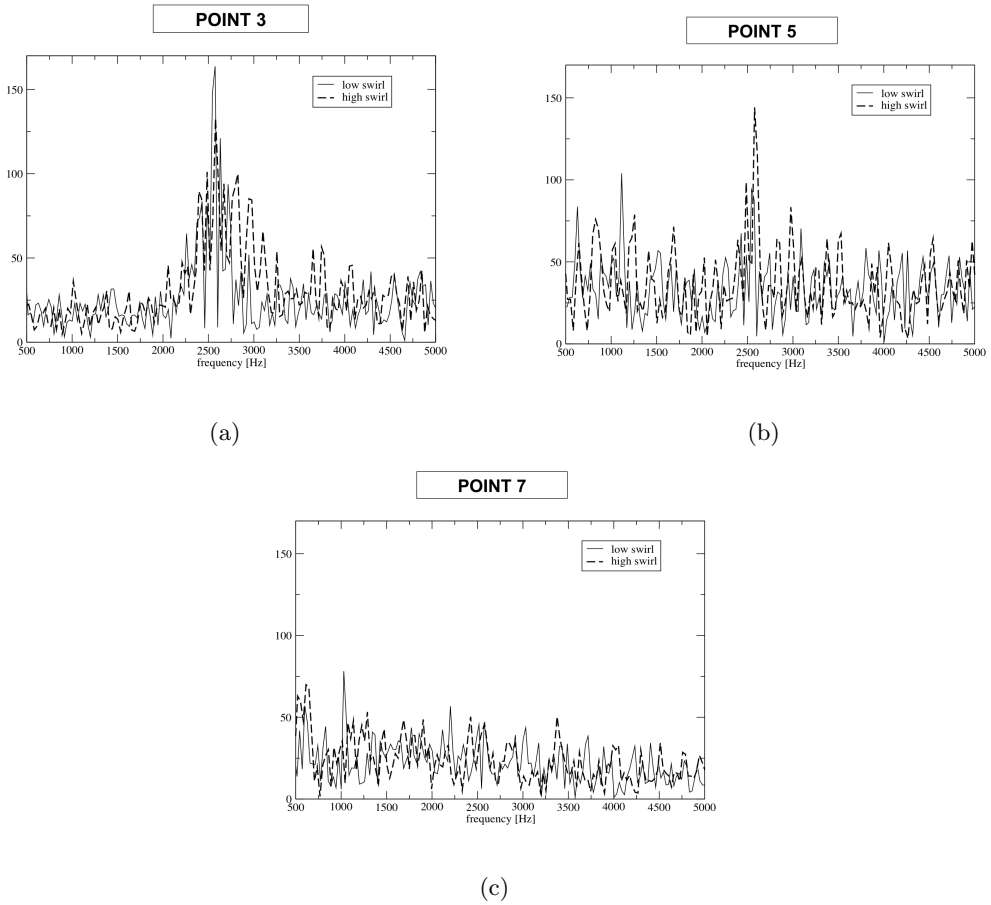

Figure 4.22: Discrete Fourier transform of the pressure signal of simulations *basic* and *high* of table 4.1.

only be spread by the flow) is diffused by turbulence everywhere and the *small tornado* is destroyed. Fig. 4.25 and Fig. 4.26 show the axial cut equivalent to points of Fig. 4.21, at the same time instant: the PVC is clearly destroyed at point 7 (Fig. 4.25c and Fig. 4.26c) with the turbulent diffusion of the passive scalar. As shown in this section, the dynamics of the PVC are similar in the *basic* and the *high* simulations: in this configuration the PVC is somehow independent of the CTRZ (which changes significantly with the jet configurations). This phenomenon can be explained with the fact that the PVC is confined inside the innermost bowl of the swirler. As a consequence, its dynamics are controlled only by the inner axial jet which does not change in the two configurations considered. The Strouhal number (S_t) of the PVC corresponding to a precession frequency of $f = 2500Hz$ is:

$$St = \frac{f\ D^3}{Q} = 0.49 \tag{4.3}$$

where Q = flow rate $= 0.005[m^3/s]$ and D = flow diameter $= 0.01[m]$.

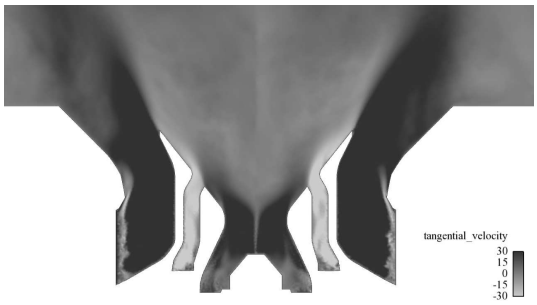

Figure 4.23: Tangential velocity of simulation *basic* of table 4.1.

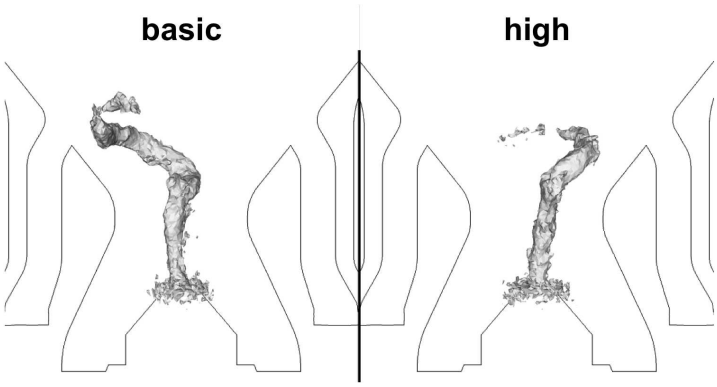

(a)

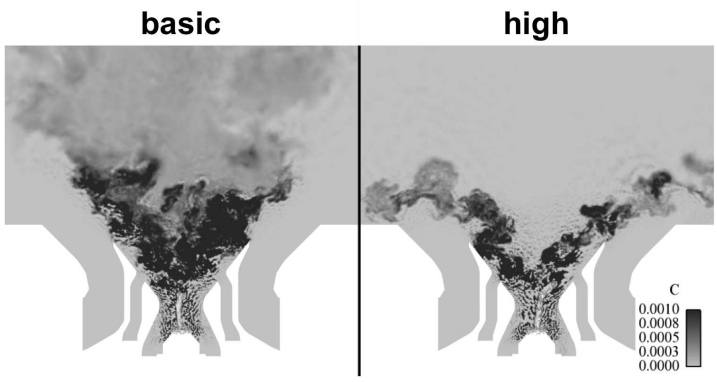

(b)

Figure 4.24: PVC in simulations *basic* and *high* of table 4.1 visualized by a passive scalar C isosurface (a). Passive scalar C field (b).

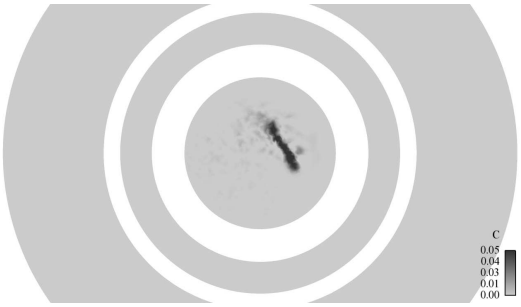

(a) Point 3 (Fig. 4.21) plane

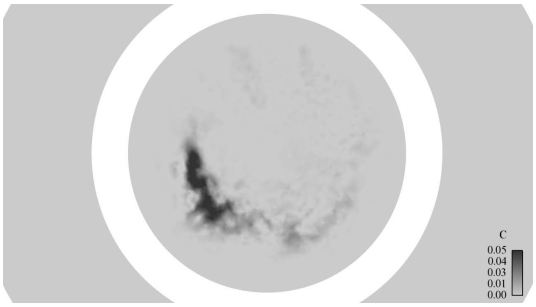

(b) Point 5 (Fig. 4.21) plane

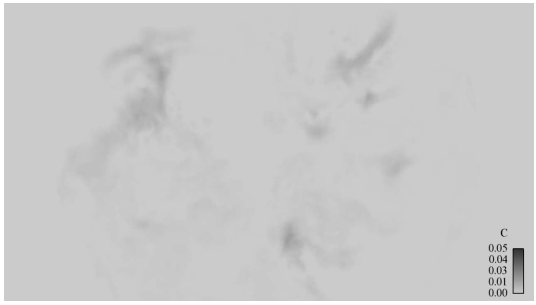

(c) Point 7 (Fig. 4.21) plane

Figure 4.25: PVC, made clear by the passive scalar C, at three planes equivalent to points of Fig.4.21, for simulation *high* of table 4.1.

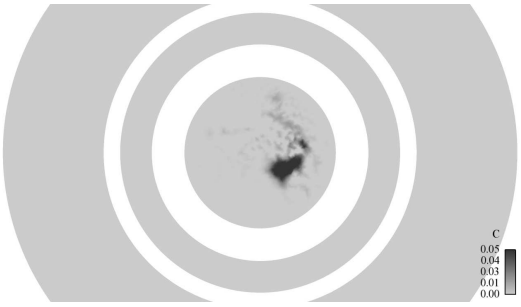

(a) Point 3 (Fig. 4.21) plane

(b) Point 5 (Fig. 4.21) plane

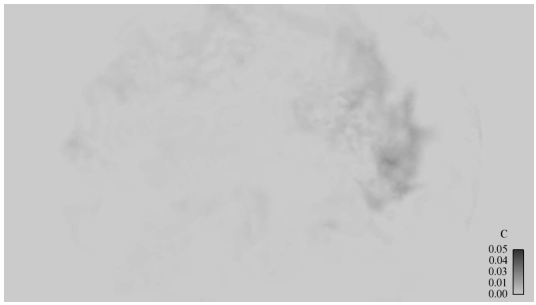

(c) Point 7 (Fig. 4.21) plane

Figure 4.26: PVC, made clear by the passive scalar C, at three planes equivalent to points of Fig.4.21, for simulation *basic* of table 4.1.

4.7 Evidences of hysteresis

In order to verify if hysteresis is also present in the adjustable swirler case and if it is controlled by the swirl level, a second set of tests is performed by changing continuously the swirl ratio of the radial jet while the amount of swirl of the remaining co-axial jets is kept constant at $S = 0.12$ and $S = 0.4$ respectively.
LES are cast in two groups named path A & B. Each path corresponds to a succession of simulations performed with increasing or decreasing values of swirl.

- Path A begins with LES *basic* and the following simulation is obtained by increasing the swirl ratio of the radial swirler jet to the swirl level of LES *high*.
- Path B begins with LES *high* and the successive simulations are obtained by decreasing the swirl ratio of the radial swirler jet except for the final simulation ($P3\_D$) in which the swirl level is brought back to LES *basic* ($S_r = 0.75$).

The investigation is limited to the range $0.6 < S_r < 0.84$, around the working condition of $S_r \approx 0.75$, which is of interest for the present study and which is sufficient to close the hysteresis loop. Above $S_r = 0.84$ no flow change is expected anymore and this zone is not explored. Below $S_r = 0.6$ a transition to an UJ state similar to the one shown in Fig. 2.9 is expected, however such zone corresponds to a very a low swirl level, far from the working condition of the device.
Paths A & B are summarized in table 4.6, while the swirler transition map is shown in Fig. 4.27. The swirler bifurcation diagram (Fig. 4.27) differs from the one of Vanierschot et al. [105] (Fig. 2.10): this does not come as surprise since each transition map is dependent on the particular flow and geometry examined (as made evident in Vanierschot and Van Den Bulck [106], who analyzed the influence of the nozzle geometry on the bifurcation diagram of their original experiment [105], presented in section 2.2.3).

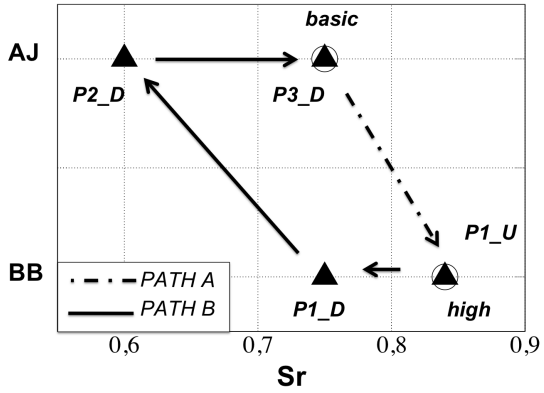

Figure 4.27: Transition map of the aeronautical swirler, adjustable swirler case, where the various simulations and flow states are plotted against the swirl ratio (Eq. 2.3). Circles are LES of path A (which starts with LES *basic*) while black triangles are LES of path B (which starts with LES *high*). The hysteresis loop is closed.

LES name	S_r (eq. 2.3) radial jet	initial condition	jet configuration
P1_U	0.84	basic	AJ
P1_D	0.75	high	BB
P2_D	0.60	P1_D	AJ
P3_D	0.75	P2_D	AJ

Table 4.6: Characteristics of LES of Path A & B.

LES along path A are characterized by multiple bifurcations. At a swirl ratio of the radial swirler jet of 0.84 (simulation P1_U) the jet bifurcates from AJ to a state which is not AJ or BB. All flow properties are in an intermediate level between the AJ and BB states and the central vortex core which characterizes the AJ state is still present but weaker, exactly as described in the Vanierschot case [105] of section 2.2.3. The flow can be therefore classified as a "Weak axial Jet" (WJ). However, this flow state is unstable and transitory: after a period of $0.05[s]$ the flow bifurcates to the BB state. Transitions change pressure and turbulence intensity distributions (Fig. 4.28) as well as the shape of the CTRZ (Fig. 4.29) which expands both radially and axially after each bifurcation.

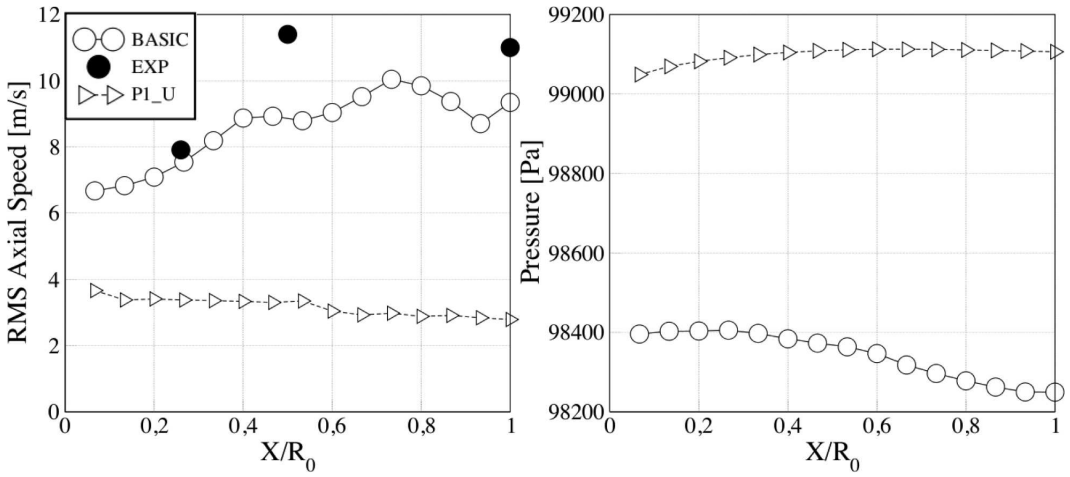

Figure 4.28: Axial velocity RMS and pressure deficit (Eq.(2.9)) measured along the centerline of the geometry. Results are plotted against normalized axial distance (X/R_0) from the swirler end plate, for simulations of path A, table 4.6.

On the contrary, a decrease of the swirl ratio of the radial swirler jet from the value of 0.84 triggers a transition in LES of path B only at $S_r = 0.60$ (simulation $P2\_D$): at this swirl level the jet detaches from the external side walls and bifurcates back to the AJ state (Fig. 4.29-4.30).

The adjustable swirler case results, summarized in Fig. 4.27, show that the aeronautical swirler flow field (with a swirl ratio of the radial jet close to 0.8, see section 3.3) is close to multiple bifurcations (AJ-WJ, WJ-BB, BB-AJ) and this confirms the assumptions proposed in chapter 3.

Two stable flow states (AJ-BB) can appear as a function of the swirl level of the jet and of the initial conditions. Results obtained in the adjustable swirler case are consistent with results of the fixed swirler configuration. They show that the swirl ratio of the radial jet

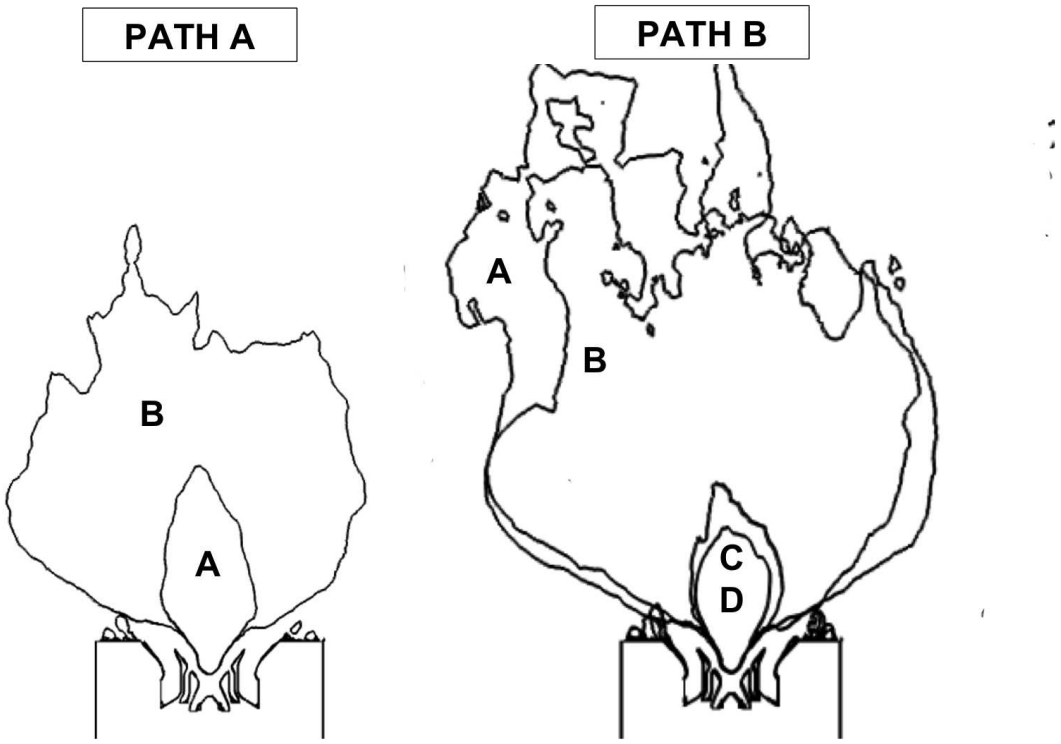

Figure 4.29: Path A: CTRZs of LES *basic* (A), $P1\_U$ (B). Path B: CTRZs of LES *high* (A), $P1\_D$ (B), $P2\_D$ (C), $P3\_D$ (D).

of the fixed swirler case $(0.74 - 0.82)$ studied in chapter 3 is very close to the bifurcation threshold obtained in the adjustable swirler case: between $0.75 < S_r < 0.84$, the flow is bistable. LES senses this property and becomes sensitive to multiple parameters such as grid refinement or SGS model. As a result, characterizing swirling flows using LES can become difficult when the flow is in such conditions. Obviously, performing LES for $S_r < 0.75$ or $S_r > 0.84$ would have been much simpler because the flow is not bistable in these regions. Around $S_r = 0.8$ much more caution must be used since LES becomes much more "sensitive", like the real flow does.

4.8 Conclusions

The first part of this thesis has shown that LES of industrial swirling jets can be an extremely difficult task since small flow modifications can trigger large flow re-configurations near critical flow conditions and small changes in the numerical setup of LES are sufficient to induce violent changes of flow state.
In the case examined here, for an adjustable swirler case, LES results demonstrate that the main parameter controlling the flow state is the swirl level of the radial jet. Bifurcations occur when swirl is changed by modifying inlet conditions or when it is changed by a modification of the LES grid or SGS model. This hypothesis was verified in chapter 4 by using a high-fidelity LES to simulate an adjustable swirl device where the amount of swirl in the flow can be controlled and modified easily. These bifurcations, which appeared to be due to uncontrollable errors in LES, were reproduced in a controlled environment where swirl

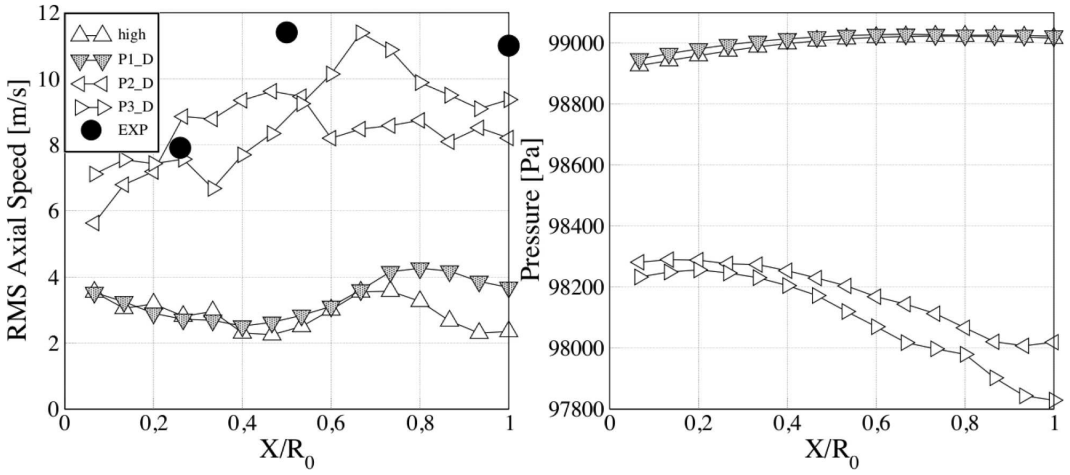

Figure 4.30: Axial velocity RMS and pressure distribution measured along the centerline of the geometry. Results are plotted against normalized axial distance (X/R_0) from the swirler ending plate, for simulations of path B, table 4.6.

was varied continuously. Two flow states were obtained and characterized based on the strength of the central, coherent, turbulent, vortex core associated with vortex breakdown. They are:

- a "free Axial Jet" (AJ) in which the central vortex core is not (or only weakly, like in simulation *basic* of table 4.1) influenced by the presence of confinement and behave like a free swirling jet,
- a "Blasted Breakdown jet" (BB), in which the central vortex core, made evident by *high* tangential velocity and turbulence intensity, has disappeared (or "blasted").

A third flow state, a "Weak axial Jet" (WJ) in which the central vortex core is weaker because of a jet expansion angle higher than the one of a free Axial Jet under the same amount of swirl, appeared as an unstable, transient state with the flow bifurcating to the BB state (or to the AJ state in some different conditions) for long simulation times.
These flow states obtained in LOTAR have many features in common with the reference case of Vanierschot et al. [105]. A second useful consideration is that, because of hysteresis, a change in the simulation parameters (in the case of "sensitive" LES of swirling flows), should be accompanied by a re-initialization of the flow field. More generally, LES for swirled flows with combustion are also very likely to exhibit bifurcating behaviors. Since combustion can act as a triggering mechanism for bifurcations and instabilities, LES codes used to study turbulent swirled confined flames should be expected to exhibit a sensitivity to numerical "details" (similarly to what shown in this thesis) which is much larger than what has been observed in non-swirling free flames and this might raise significant difficulties.

Part II

Mesh adaptation methods for LES of swirling flows

Chapter 5

Introduction to solution based mesh adaptation

Since Part I demonstrated that one of the most important parameters controlling the quality of LES in a swirler is the mesh, the natural following question is to know how to ensure that the best mesh is used. Of course, using extremely fine meshes everywhere could be a solution [76] but it is not always possible, practical or economical especially for optimization where multiple configurations must be tested. A possible strategy is to use mesh refinement/coarsening to relocate points only where they are needed, keeping constant the overall numerical cost of the simulation (if it is not otherwise desired to further increase the simulation accuracy).
In general, as already mentioned in the introduction of this work (see section 1.2 and which is reported here), a second issue concerning meshing in the LES context arises. At present time there is no standard procedure to generate a LES-suited grid. The mesh, which is the most important LES parameter since it determines the filter size in implicit filtering LES, see section 3.2.2, and influences modeling in a non-trivial way[1], is chosen more or less arbitrarily.
Because of the importance of the numerical grid in LES and because of the lack of standard meshing procedures, the second part of this thesis focuses on mesh adaptation, that is the ability of manipulating a grid based on a set of criteria. This methodology, which has been applied to a very limited number of LES of canonical flows [37, 38, 39], it has never been applied to complex industrial configurations.
This chapter provides: a description of mesh adaptation and the main definitions used, the mesh adaptation methods (here referred as *INRIA* [25, 3, 2, 63]) and the numerical tool (MMG3D) which performs the so-called metric based adaptation. Then, a review of the error analysis in the LES context and the mutual interaction/compensation of the various error sources (see [31, 71, 53]) are presented.
The presented tools and the error analysis are then re-arranged in Chapter 6 in order to build a set of mesh adaptation criteria suitable for LES. The mesh adaptation strategy and the constraints used to build the adapted mesh are discussed there.

[1] All models used in the LES solvers employed here, rely on the Boussinesq hypothesis, or eddy viscosity hypothesis, which links the kinetic energy dissipation rate to the resolved velocity field strain rate (as for molecular diffusion in a Newtonian fluid, see also section 3.2.2). The resolved flow field is the input for modeling and modeling modifies the resolved flow field in a circle.

Finally, in Chapters 7-9, mesh adaptation is tested on low Reynolds number turbulent jets in order to study the efficiency of the developed sensors and the validity of mesh adaptation strategy. Chapter 7 is dedicated to the Dellenback experiment [17] in the case of a purely axial jet, Chapter 8 is dedicated to the same experiment [17] but in the case of a swirled jet, Chapter 9 is dedicated to the LOTAR experiment shown in the first part of this thesis.

5.1 Mesh adaptation: basic definitions.

The aim of mesh adaptation is to improve "the accuracy of the numerical solution of a given problem, by modifying the domain discretization according to size and directional constraints" [3]. Such constraints are determined by the adaptation criterion used (for instance in [25, 3, 2, 63] the criterion is based on the linear interpolation error). Criteria can be casted in two different families depending on the fact that they rely:

- on the **geometrical properties** of the mesh elements (for instance a measure of the element stretching such as equivolume skewness), and which therefore requires only the grid to be evaluated, or,
- on the **numerical solution** of the problem (and therefore on the discretized equations).

The first family of methods relies on the fact that the shape of the elements of the mesh will affect the numerical resolution of the problem. As reported in [69], "as the element's dihedral angles become too large, the discretization error in the finite element solution increases [45]; as angles become too small the condition of the element stiffness matrix increases [26]". These algebraic constraints need to be satisfied to avoid errors generated by the numerical scheme. Such methods can be named *a priori* since they do not rely on the computed numerical solution but on the mesh only.
The second family of methods aims to adapt the mesh based on the numerical solution, as there is a correlation between the error on the numerical solution and the local mesh size [25], as for instance happens to be the case for LES.
Independently of the error estimate chosen (which is clearly dependent on the problem to be solved and which may not always be derived analytically), such methods can be defined as *a posteriori* since they rely on the computed numerical solution.
The techniques employed to manipulate the mesh, relocate nodes, inserting etc., are the same for the two families. They are [37]:

- the h technique, that consists in node insertion or deletion
- the r technique, that consists in relocating grid points
- edge swapping, local reconnection of grid points modifying element faces

Another technique, not discussed here, is the p technique which consists in increasing the order of the basis function (for Finite Element methods, which implies a local increase of accuracy). Many mesh adaptation programs exist, for instance [62]: Yams,

Forge3d, Fun3d, Gamic, MeshAdap, Mmg3d, Mom3d, Tango, and even a direct CAD mesher as CENTAUR has a mesh adaptation module (which however does not allow mesh coarsening).

5.2 Metric-based mesh adaptation methods

As stated in [3], the aim of mesh adaptation is to improve the accuracy of a numerical solution by modifying the grid based on a given criterion. This criterion can be derived from the numerical solution of the problem which is used to generate an estimate of the approximation error (difference between the exact and the numerical solution of the problem).
In the work of Frey and Alauzet [25], Alauzet et al. [3], Dobrzynski and Frey [2], Loseille et al. [63], the approximation error is estimated via the linear interpolation error as for elliptic problems the approximation error is bounded by the linear interpolation error (according to the Cea's lemma [14]). The interpolation error is the error arising from approximating a continuous solution with a discrete one using a finite number of degrees of freedom.
For the variational formulation of a set of partial differential equations (finite volumes or finite elements), the exact and the numerical solution (that is the one to be *really* interpolated) do not necessarily coincide anywhere in the domain [4]. Because of this limitation, the linear interpolation error in the context of finite elements/volumes can be only estimated as the departure of a quadratic interpolation of the real solution from a linear one [33, 21].
This implies the departure of the solution obtained with a linear basis function from a quadratic basis function [33] (that will give a better or at least equal, representation of the real solution). In a 1D case the point-wise linear interpolation error is the difference between the two curves shown in Fig. 5.1, the parabola and the piecewise linear function used to interpolate it.

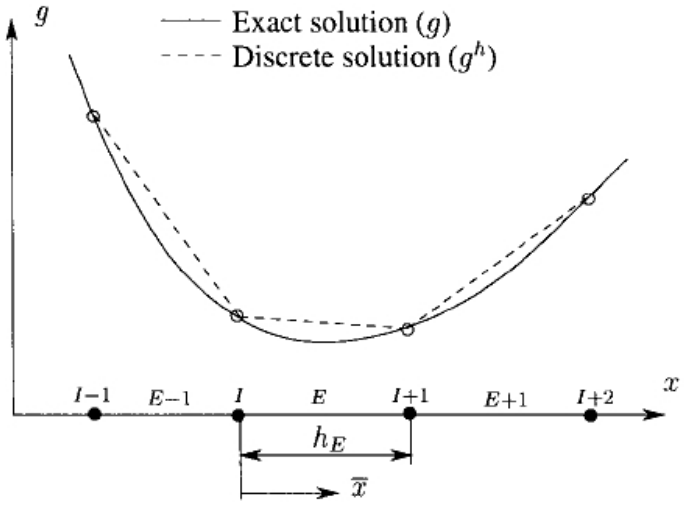

Figure 5.1: Approximate solution by a discrete method, from [33]

In 1D this error is bounded by the second order derivative of the real solution [33, 21] as by interpolating a linear function with linear basis function, the interpolation error is

zero (obvious). In a 2D or 3D case the second order partial derivatives of the solution are casted in the Hessian tensor (H). The linear interpolation error can be expressed analytically as a function of the element size and orientation with respect to the Hessian matrix (Loseille and Alauzet [62]) as,

$$||u - \Pi_h u||_{L^1(K)} \leq \frac{|K|}{40} \sum_{i=1}^{6} \vec{e_i}^T |H| \vec{e_i}, \tag{5.1}$$

(the inequality becomes an equality when u is elliptic or parabolic) and where:

- u is a quadratic function (as the interpolation error is estimated using a quadratic interpolation of the function),
- $\Pi_h u$ is the linear interpolation of u,
- $||\cdot||_{L^1(K)}$ is the L^1 norm evaluated on a tetrahedra K,
- $|K|$ is the volume of the tetrahedra,
- $\vec{e_i}$ are the set of edges of the tetrahedron K taken in a particular order,
- H is the Hessian matrix of the solution.

The linear interpolation error can be evaluated exactly using Eq.(5.1) or it can be estimated by substituting the Hessian matrix with a *"bounding"* metric (M_b), in the sense that $\exists\ M_b$:

$$\vec{e_i}^T |H| \vec{e_i} \leq \vec{e_i}^T M_b \vec{e_i} \quad \forall \vec{e_i} \in K, \tag{5.2}$$

where $|H|$ denotes the positive symmetric matrix deduced from H by taking the absolute values of its eigenvalues [62] (i.e. the eigenvalues of $|H|$ are equal to the absolute value of the eigenvalues of H, $\lambda^i_{|H|} = |\lambda^i_H|$ with $i = 1, 2, 3$).
The interpolation error of Eq.(5.1) will be bounded by the quantity obtained by replacing $|H|$ with M_b in Eq.(5.1)[2].
A metric is a symmetric definite-positive form expressed as a matrix M. Metrics are used to define the dot product in Euclidean *metric* spaces (therefore the notion of distance d_M between points):

$$(\vec{u}, \vec{v})_M = \vec{u}^T M \vec{v}, \tag{5.3}$$

where $()_M$ is the dot product defined for the Euclidean space with a metric M. In the 2D-3D space of classical mechanics, metrics are the identity matrices I_2 and I_3.
Metrics can be easily visualized by transformation of geometric entities (Fig. 5.2). The unit ball in the metric space defined by the identity matrix (which is the locus of points whose distance from the ball center is lower-equal than $r = \lambda^{-1/2} = 1$, where $\lambda = 1$ is the eigenvalue of the identity matrix) is transformed into an ellipsoid with its axis aligned with the principal direction of M [62]. The metric defines distance d_M between points and therefore "deforms" the locus of points (such as the unit ball) which requires the notion of distance to be defined.
If a metric is defined continuously, so that, at each point of the space $M = M(x)$, a **Riemannian space** is defined: the unit ball becomes a different ellipsoid at each location

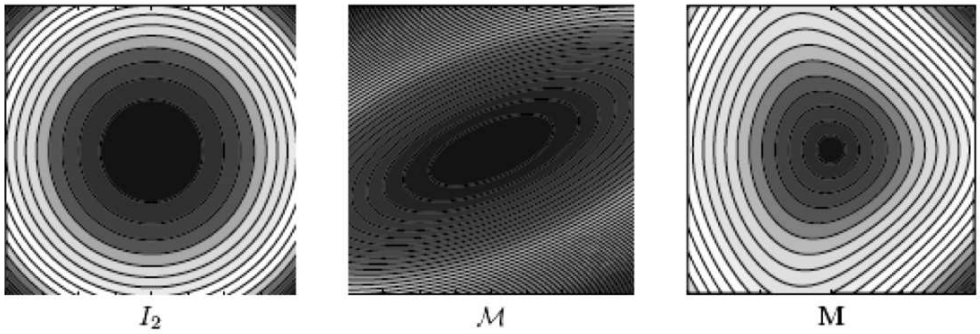

Figure 5.2: Isolines of $l_M = const.$ (evaluated via equation 5.4) in I_2, left, Euclidean space with a constant metric, center, Riemannian space, right. From Loseille and Alauzet [62]

and the isolines in Fig. 5.2 become complex curves. Since Riemannian spaces are curved, the length of a vector $\overline{ab}$ in a Riemannian space is calculated using the straight line parametrization $\gamma(t) = \overline{ao} + t\overline{ab}$ with $t \in [0, 1]$:

$$l_M(\overline{ab}) = \int_0^1 \sqrt{\overline{ab}^T M(a + t\overline{ab})\overline{ab}} \; dt, \tag{5.4}$$

Once the linear interpolation error is evaluated using the *bounding* metric M_b of Eq.(5.2) coupled with Eq.(5.1), the mesh can be adapted in order to minimize it[3]. The minimization of the overall interpolation error is achieved adapting the mesh in order to get all the tetrahedra which compose the mesh of the same length (Eq.(5.4)).
To summarize, the steps followed by the mesh adaptation method here named as *INRIA* are:

1. to **build a metric** (M) based on the Hessian of the solution (Eq.(5.2)),
2. to **evaluate the length of the edges** of each element of the original mesh in the metric space M (Eq.(5.4),
3. to **create a tetrahedra with sides of unit length** in the *metric* space defined by M.

[2]Note that in [25, 2, 3, 4] formulations different from Eq.(5.1) are used. Only Eq.(5.1) is reported here since it is the latest developed by Loseille and Alauzet[62].

[3]An exact evaluation of the linear interpolation error is proposed by Loseille and Alauzet[62] and it will be briefly reported here. Because for each tetrahedron K $\exists$ only one metric for which its edges are unit with respect to the metric:

Definition 3 *for K $\exists$ only one M : $l_M(\vec{e_i}) = 1$ for i=1,.,6 ,*

it is possible to define a Riemannian space using the mesh elements [62]. Based on this continuous metric definition is possible to evaluate the linear interpolation error continuously and express it as a function of the Hessian of the solution and of the local metric M of definition 3. So Eq.(5.1) becomes [62]:

$$||u - \Pi_h u||_{L^1(K)} \leq \frac{|K|}{40} \sum_{i=1}^{6} \vec{e_i}^T |H| \vec{e_i} = \frac{\sqrt{2}}{240} det M^{-\frac{1}{2}} trace(M^{-\frac{1}{2}} H M^{-\frac{1}{2}}). \tag{5.5}$$

where $M = R\lambda R^T$ is the spectral decomposition of the metric and $M^{-\frac{1}{2}} = R\lambda^{-\frac{1}{2}} R^T$.

Step 1 (evaluation of the linear interpolation error) is peculiar to the INRIA mesh adaptation method [25, 2, 3, 4] while step 2-3 can be used for any mesh adaptation method since they deal with grid manipulation only and not with an error estimate.
Fig. 5.3 shows an example of a mesh adapted using the linear interpolation error estimate (step 1) and the metric concept (steps 2-3).

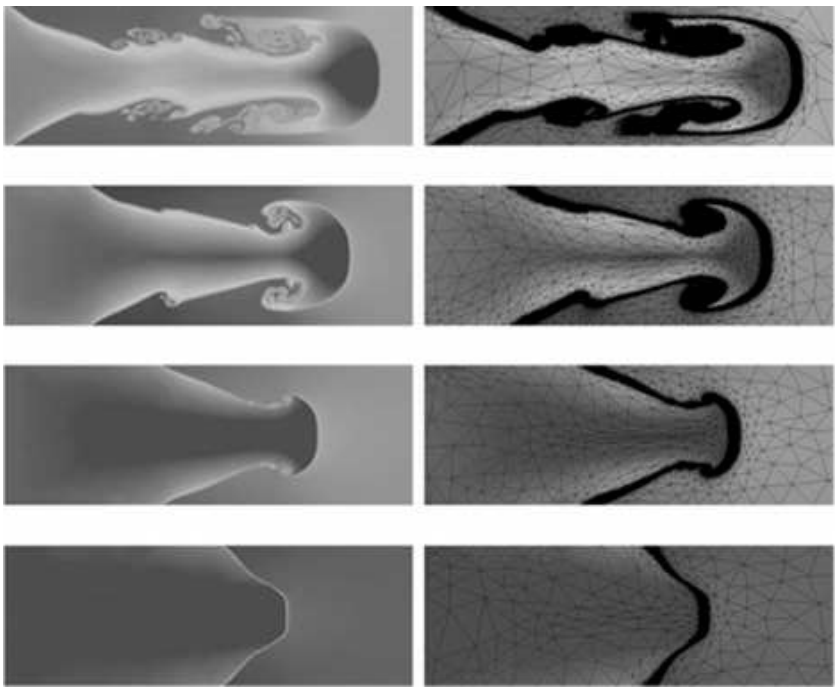

Figure 5.3: Mesh (right) adapted to capture miscible fluids interface (solution, left), from [3]

To conclude, since it is impossible to tessellate the 3D space only with the regular tetrahedron, the unit mesh (a mesh of tetrahedra with sides of unit length, see also definition 3), can only be approached by an adaptation program [62].

5.3 MMG3D

MMG3D is a program developed by C. Dobrzynski and P. Frey to adapt the mesh based on a given metric field. It performs the second and the third steps defined at the end of section 5.2.
The metric field (M) is only an input of the program and it is not evaluated or modified by MMG3D. The re-meshing is performed using an algorithm based on a modified Delaunay criterion by evaluating the length of the elements edges in the given metric space (Eq. 5.4). The Delaunay criterion is clarified by Fig. 5.4: the couple of triangles on the left does not respect the Delaunay criterion since the vertex P lies inside the circle circumsfere of triangle K while the couple of triangles on the right does. MMG3D simply tries to generate elements (in 3D) of the type of Fig. 5.4 right, i.e. it generates tetrahedra which respect the modified Delaunay criterion. The only difference with the classic Delaunay approach is that the circle circumsfere (or the circumsfere in 3D) is evaluated in the metric space

given by the user as input using Eq.(5.4).

Together with the h technique (**node insertion/deletion**) MMG3D is able **to displace**

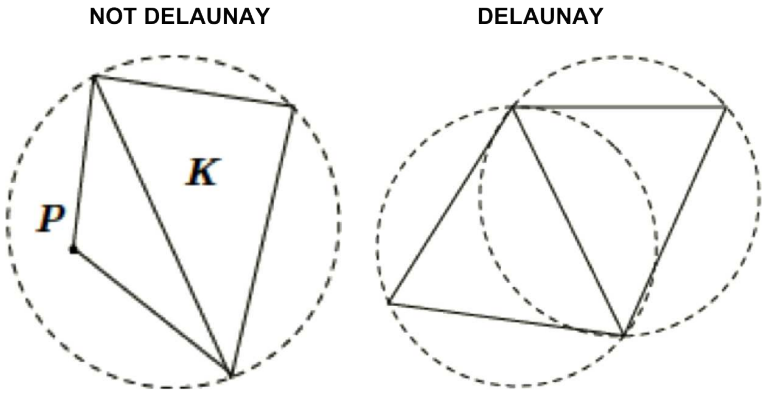

Figure 5.4: From [18]. Left: 2D example of two triangles which do not respect the Delaunay criterion: the point P is inside the circle circumference of triangle K. Right: two triangles respecting the Delaunay criterion.

the grid nodes (r technique) and **to perform edge swapping**, i.e. all techniques itemized at the end of section 5.1. A more detailed description of the algorithm used by MMG3D to manipulate the grid is given in reference [18] and it is not discussed here since the program is used as a "black box".

Fig. 5.5 gives an example of a mesh adapted with MMG3D (using a Hessian based metric). From Fig. 5.5 it is evident that the mesh, adapted to capture shocks, is as anisotropic as the Hessian of the pressure field is (pressure changes strongly across the shock). MMG3D

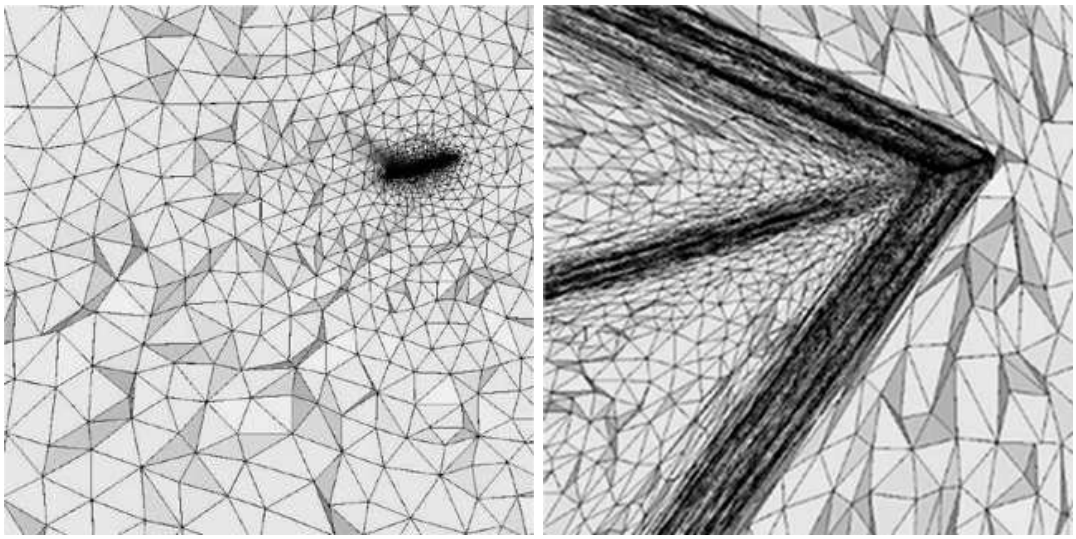

(a) (b)

Figure 5.5: Original mesh (left) and mesh adapted to capture shocks (right), from [19]

can handle only tetrahedral elements in a 3D space, hexahedral and pentahedral elements are decomposed by the program in tetrahedra to be adapted. A 2D version of the code,

MMG2D, is available but is not used here.
The number of mesh nodes can be trivially kept constant by deactivating node insertion/deletion.
The quality of each tetrahedron K is evaluated as:

$$Q_K = \frac{e_s^3}{|K|}, \tag{5.6}$$

with $e_s = \sqrt{\sum_{i=1}^{6} (l_i)^2}$ and l_i is the length of the edge i evaluated using Eq.(5.4) and $|K|$ is the element volume. The quality index is equal to one for equilateral tetrahedra (in the metric space M). The quality index is dependent on the metric imposed: if a constant, isotropic metric is defined everywhere in the domain, the program will try to generate equilateral tetrahedra everywhere. The size of the elements is directly controlled via the metric as it will be explained in chapter 6.

5.4 Error estimate in the LES context

As mentioned in section 5.1, the *a posteriori* mesh adaptation strategy relies on a quality measure or error estimate. Such an estimate does not exist in mathematical form for LES and in general for the Navier-Stokes equations. Concerning LES, the most famous effort in such direction (a study of the main error components in LES) was made by Ghosal [31, 94] and his analysis is briefly presented here.
The "overall" error in LES cannot be lower than the error arising from the approximation of a continuous solution (u) with a discrete one using a finite number of degrees of freedom. This error is called the projection (or interpolation) error and it is intrinsic, since it is derived by using a finite number of degrees of freedom to represent a solution with an higher number of degrees of freedom. This error is minimal when:

$$e \equiv P(u) - u_d = 0, \tag{5.7}$$

where $P()$ is the best projection operator of the space of continuous solutions to that of the discrete solutions and u_d is the numerical solution. Eq.(5.7) simply states that the numerical solution can only approach the best projection $P()$ of the exact solution u. The Navier-Stokes equations can be written in the symbolic form:

$$\partial_t u = N(u) \tag{5.8}$$

where $\partial_t u$ is the time derivative of u and $N()$ is the nonlinear Navier-Stokes operator. By applying the projection operator $P()$ to Eq.(5.8), we obtain:

$$\partial_t P(u) = P(N(u)). \tag{5.9}$$

The discrete form of the Navier-Stokes equation can be written as:

$$\partial_t u_d = N_d(u_d). \tag{5.10}$$

where $\partial_t u_d$ is the time derivative of u_d and $N_d()$ is the discrete Navier-Stokes operator. By subtracting Eq.(5.10) from Eq.(5.9) and adding and subtracting $N_d(P(u))$ to the right-hand side, we obtain:

$$\partial_t(P(u) - u_d) = P(N(u)) - N_d(u_d) + N_d(P(u)) - N_d(P(u)), \tag{5.11}$$

$$\partial_t e - (N_d(P(u)) - N_d(u_d)) = P(N(u)) - N_d(P(u)), \tag{5.12}$$

which can be written, using the composition operator "$\circ$" which is not distributive, as:

$$\partial_t e - N_d \circ e = P(N(u)) - N_d(P(u)). \tag{5.13}$$

Error e is zero at the boundary and in the initial condition (since it u and u_d satisfy the same initial and boundary conditions), therefore the necessary and sufficient condition for it to remain zero is the right-hand side source term of Eq.(5.13) to be zero. In Ghosal's analysis, error in LES is therefore defined as this source term:

$$P(N(u)) - N_d(P(u)), \tag{5.14}$$

that is, the extent of the departure of the numerical solution from the best possible on a given grid. Eq.(5.14) includes all the error sources apart from the projection error (or interpolation error which is implicit in Ghosal's analysis) that are:

- modeling error due to the inaccuracy of the subgrid model,
- discretization error because of the discrete differentiation operator,
- aliasing error due to the computation of non-linear terms.

Note that all SGS models used in this thesis rely on the eddy viscosity assumption which approximates the residual stress tensor as a function of the resolved velocity field (Eq.(3.5)). Turbulent viscosity (ν_t in Eq.(3.5)), is usually taken as $\nu_t > 0$ to ensure a purely dissipative SGS model avoiding the backscatter of kinetic energy from the smallest to the biggest scales of motion. This assumption is found to be unrealistic [86] but avoids numerical instabilities.
Focusing on Ghosal's [31] theory, in order to simplify the analysis, the modeling error is erased by using an "ideal subgrid model" (obtained by imagining to filter instant by instant a DNS solution and giving this output to LES), while the solution (u) is chosen with an energy spectrum in the form proposed by Von Karman and the quasi-normality hypothesis is employed to evaluate certain non linear terms.
Under these simplifications the main result of Ghosal [31] is that "the finite-differencing operator error remains larger than the subgrid force over most of the wavenumber range for a second order operator while the situation is improved for higher-order schemes but even for an eighth-order scheme the numerical error is smaller than the subgrid term only about half of the wavenumber range" (Fig. 5.6). The aliasing error has the opposite behavior, being higher for higher-order schemes. Indeed aliasing error was found to be of minor importance and only relevant for very high-order discretization methods [84], so that most of the numerical analysis concentrates on the discretization error [71].

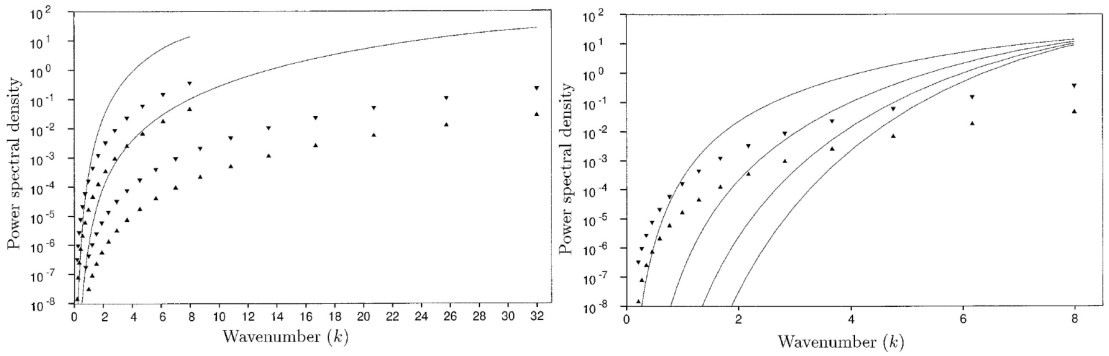

Figure 5.6: Results of Ghosal[31]. (a) The finite differencing error of a second order scheme, continuous line, compared to lower and upper bounds for the subgrid force (black triangles) at a different wavelength cut-off (8 vs. 32). (b) Idem for several numerical schemes, higher curve, eighth-order, lower curve, second-order.

The main consequence of Ghosal's analysis is that an increase of the resolution (mesh refinement) does not improve the ratio of numerical error over subgrid term as the subgrid scale term drops faster than the numerical error. However, mesh refinement reduces the size of the corrupted eddies so that their effect on the overall flow behavior could vanish or being negligible [66] and this is the path followed in this thesis.
In general, the only option able to modify the ratio of numerical error over SGS force is to increase the SGS contribution. To obtain this for a given mesh resolution, it is required to decrease the ratio grid spacing over filter width:

$$r = \frac{h}{\Delta}. \tag{5.15}$$

Decreasing r means to perform explicit filtering LES. Apart from the analytic and numerical difficulties in performing explicit filtering LES, such a strategy would imply an increase of the numerical cost without adding resolution: the mesh would not be used optimally [66, 12].

5.4.1 Verification of Ghosal's analysis

The theoretical results of Ghosal were verified numerically by Chow and Moin [16] for a HIT, showing that a filter ratio of at least $\frac{1}{4}$ is required (for a second order numerical scheme) to avoid numerical corruption of the results. However, a filter ratio of $\frac{1}{4}$ would require, for the same resolution, a simulation $4^4 = 256$ times more expensive than a simulation with a filter ratio of one (under the CFL condition). Kravchenko and Moin [56] verified the effects of the aliasing error on the turbulent channel flow, showing that "different (but analytically equivalent) formulations of the nonlinear terms give different results because of finite differences and aliasing errors" [16].
Using explicit filtering LES, Geurts and Fröhlich [30], were able to separate the numerical error contribution from the modeling error. For an HIT simulation, the a posteriori error indicator $\delta_E(\Delta, r)$ proposed in Geurts and Fröhlich [30] is:

$$\delta_E(\Delta, r) = \left|\left| \frac{E_{LES}(\Delta, r) - E_{\overline{DNS}}(\Delta, r)}{E_{\overline{DNS}}(\Delta, r)} \right|\right|; \tag{5.16}$$

where E is the volume averaged kinetic energy for LES (E_{LES}) and for a filtered DNS ($E_{\overline{DNS}}(\Delta, r)$) evaluated at the same instant, while the norm $||f||^2 = \int_{t_0}^{t_1} f^2(t)dt/(t_1 - t_0)$ represents time averaging. Since in a decaying HIT kinetic energy can only be dissipated, the parameter chosen to be compared with the exact error of Eq.(5.16) is the subgrid activity:

$$s = \frac{< \epsilon_t >}{< \epsilon_t > + < \epsilon_\mu >}; \tag{5.17}$$

where <> represents the ensemble average operator and ϵ_t and ϵ_μ are the turbulent and molecular dissipation of kinetic energy. If $s \to 0$ the simulation is a DNS, if $s \to 1$ is a LES with an infinite Reynolds number (a poorly resolved LES). The subgrid activity parameter s is the ratio of the dissipation related to the modeled turbulence over the total dissipation rate (modeled + viscous).
In Fig. 5.7 the total error of Eq.(5.16) is plotted against the subgrid activity (Eq.(5.17)) for different mesh resolutions. For $s > 0.5$ and $r > \frac{1}{2}$ (so a LES in which the SGS term is of importance, $s > 0.5$, and not contamined by numerical error $r > \frac{1}{2}$) all simulations fall on the same curve. In such as dissipation dominated simulation, the subgrid activity is a good estimate of the total error. However a decaying HIT LES has some peculiarities which are hard to find in the flows examined in this thesis and global, "one number", estimates such as Eq.(5.17) are unlikely be accurate.

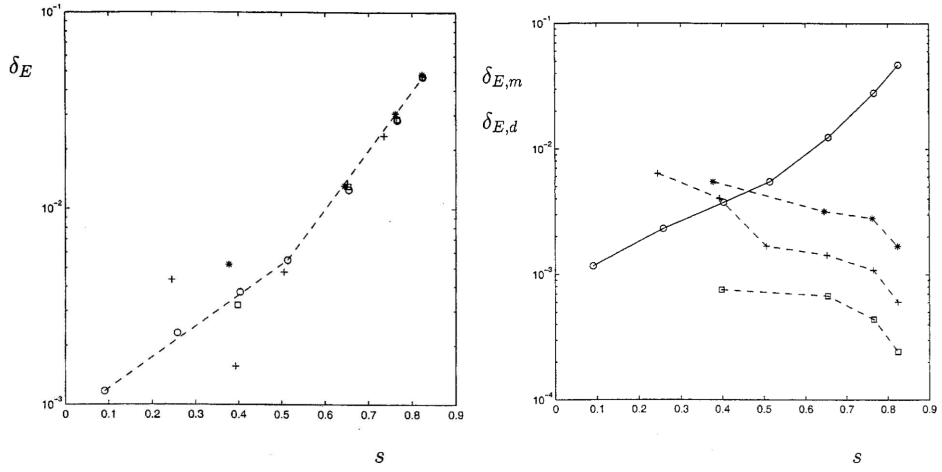

(a) (b)

Figure 5.7: (a) Relation between relative total error, Eq.(5.16), and subgrid activity s. Markers correspond to different resolution, dashed lines approximates the data of the highest resolution. (b) Modeling error, $\delta_{E,m}$ (solid ∘), and discretization error, $\delta_{E,d}$ (dashed lines), correspond to discretization error for different resolution. From 5.16.

The discretization error ($\delta_{E,d}$) of Fig. 5.7 (b) is evaluated variating the filter size, changing in Eq.(5.16) $E_{\overline{DNS}}(\Delta, r)$ with $E_{\overline{LES}}(\Delta, r)$ with $r \to 0$. The magnitude of the numerical error increases with increasing value of r and dominates for $r = 1$, a further verification of Ghosal's analysis.

5.4.2 Mutual error compensation

Decaying HIT simulations can be used to build the so-called *error landscapes*, [71]. By systematically varying the Smagorinsky parameter C_s (the Smagorinsky constant), the spatial resolution N and the Reynolds number, Meyers et al. [71] find the optimal refinement strategy (grid size-model constant) for which the prediction of a given flow property (such as total kinetic energy or enstrophy, see Fig. 5.8) is improved because of the mutual compensation of numerical and modeling error.

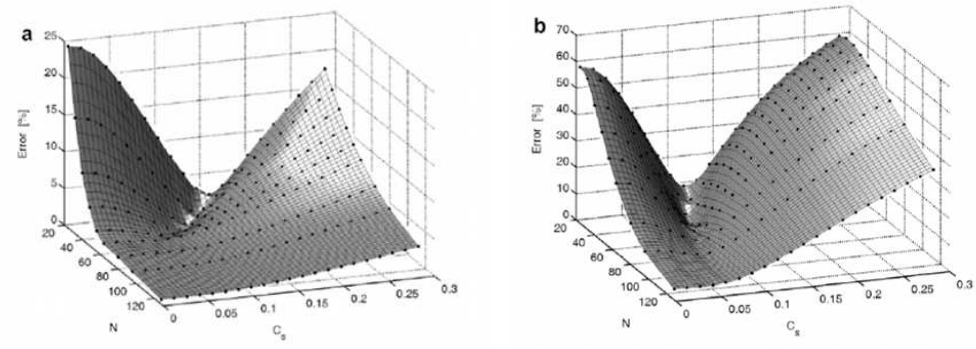

(a) (b)

Figure 5.8: Error landscapes, from [71]. Error similar to Eq.(5.16) is plotted against C_s and the number of discretization point. (a) error on the total kinetic energy, (b) error on the total enstrophy $\varepsilon =< \overline{\omega}_i\overline{\omega}_i/2 >$ with $\overline{\omega}_i = \nabla \times \overline{u}$

A similar non-monotone behavior was experienced in the work of Meyers and Sagaut [72]. The *classic* turbulent channel was simulated in DNS (but with a LES like resolution). The resulting zero error isosurfaces of the skin friction coefficient (Fig. 5.9) and the mean velocity profile correspond. However, the zero error isoline for the skin friction corresponds to a strong error on the Reynolds stresses, showing as the error on velocity fluctuations compensates with the lack of wall resolution therefore obtaining the proper skin friction coefficient.

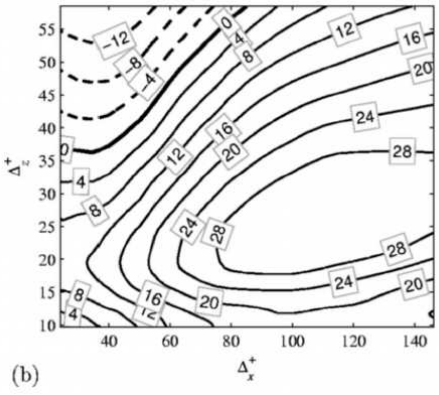

Figure 5.9: Turbulent channel of Meyers and Sagaut [72]: contour plot of the skin-friction error as function of the mesh size in the streamwise and spanwise directions (Δ_x^+ and Δ_z^+).

Note that all these studies were performed for academic turbulent flows (typically homogeneous turbulence or channel flows) and that we should not expect them to be directly applicable to complex swirled flows for which these simple and intuitive methods cannot hold because of the flow complexity.

5.5 Mesh adaptation in the LES context

Very few works dealing with mesh adaptation in LES can be found in the literature and none in the context of complex, industrial configurations as the one studied in this thesis. Here are briefly reported the results of Hertel et al. [37], who uses a methodology and criteria similar to the one developed in this thesis, and some of the results of Hoffman [38, 39]. In the work of Hertel et al. [37], a self-adaptive method is presented. The adaptation technique employed is the r (nodes displacement) which keeps the mesh connectivity untouched[4] allowing the mesh adaptation process to be executed in parallel to the LES solver. Mesh movement is included in the LES equations via the ALE (Arbitrary Lagrangian Eulerian) formulation, an approach first proposed by Huang and Russel [40]. Nodes density is determined by the monitor function, G, that is a symmetric definite-positive matrix. The objective of such method is to achieve uniformity of nodes distribution with respect to G, i.e. to obtain an error distribution homogeneous in space.
This target is achieved by minimizing a functional derived from G and from the nodes coordinates. If G is chosen to be the Hessian, H, of the solution, the linear interpolation used by *INRIA* (see section 5.2) can be recovered [41]. The monitor functions tested in [37] are:

1. the gradient of the mean streamwise velocity,
2. turbulent viscosity ratio, $\frac{<\nu_t>}{<\nu_t>+<\nu>}$,
3. turbulent kinetic energy ratio, $TKE = \frac{<k_{sgs}>}{<k_{res}>+<k_{sgs}>}$,
4. shear stress ratio, $\frac{<\tau_{12}^{mod}>}{<\tau_{12}^{mod}>+|<\overline{u}'\overline{v}'>|}$, with $\tau_{12}^{mod} = \nu_t(\frac{\partial \overline{u}}{\partial y} + \frac{\partial \overline{v}}{\partial x})$.

Adaptation is tested [37] on the flow over a periodic hill (Fig. 5.10) for which highly resolved LES data were available [27].

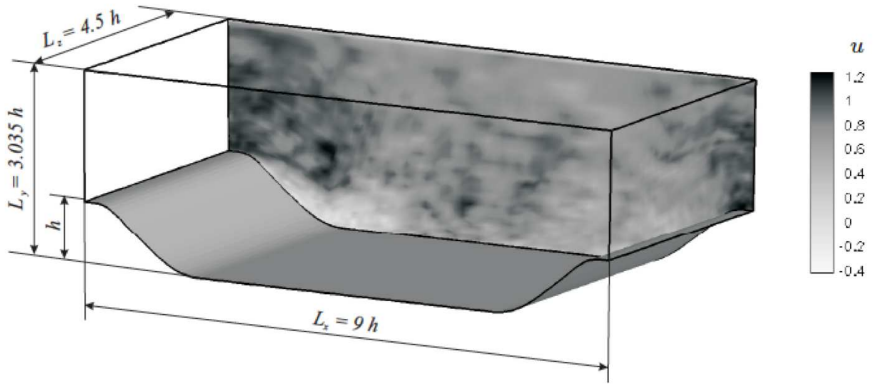

Figure 5.10: Geometry of Hertel et al. [37] and Fröhlich et al. [27] and flow field cut (u=streamwise flow speed).

Results obtained with the adapted meshes ($\approx$ 135000 nodes), are compared with the highly-resolved LES of 4.7M points, in terms of mean flow velocity profiles (Fig. 5.11).

[4]Note that the grid is fully hexahedral and structured.

Not all sensor fields, or criteria for adapting the mesh, were able to improve comparison with the highly resolved LES (Fig. 5.11). The gradient of mean velocity was the most successful in this respect because the structured grid was refined "near the windward side near the hill crest where a strong acceleration takes place" [37], yielding to a wall resolved mesh in the wall normal direction ($\Delta y^+ \approx 6$), and at the reattachment position. Results of [37] show no dependency on the initial grid used.

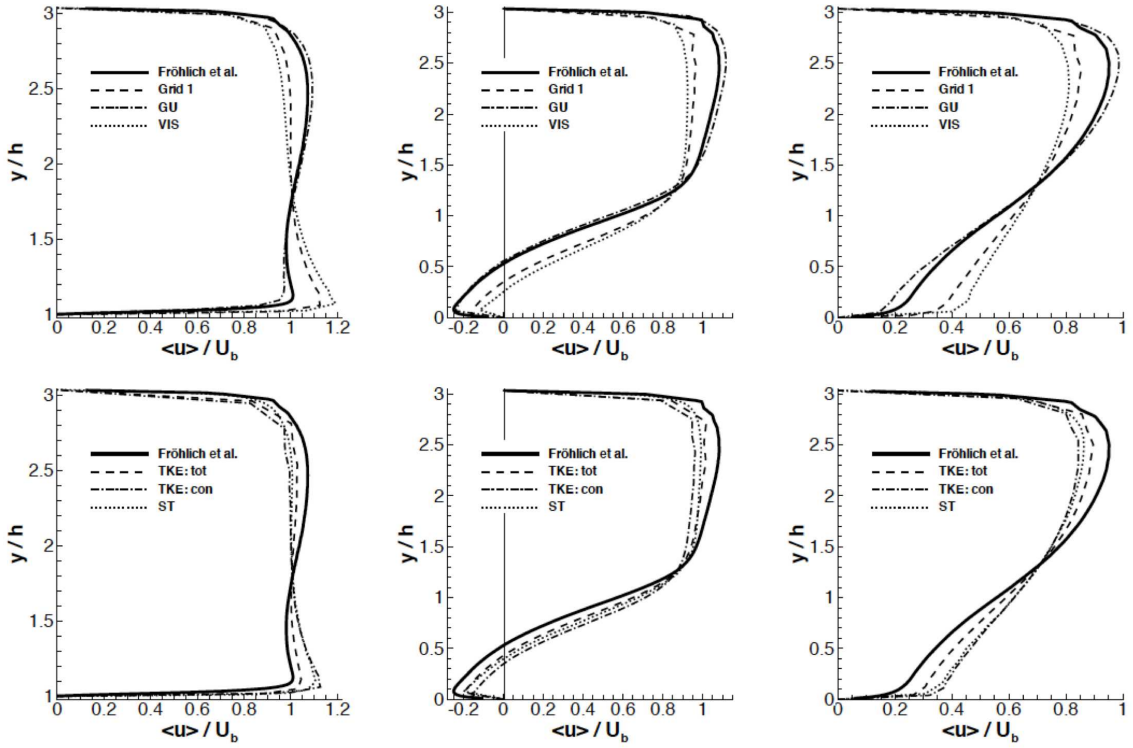

Figure 5.11: Comparison of the streamwise speed (normalized by the bulk flow speed) between results of Hertel et al. [37] and Fröhlich et al. [27] at three different measurement planes: GU=gradient of the mean velocity, VIS=turbulent viscosity (figures on top), TKE=turbulent kinetic energy, TKE con=turbulent kinetic energy using a constant denominator, ST=shear stress (figures on bottom). Results obtained using the gradient of the mean streamwise velocity (GU) compares very well with the highly resolved LES of [27], see figures on top.

A totally different approach is studied by Hoffman [38, 39]. Hoffman introduces a linearized dual problem in order to improve the prediction of a given quantity of interest (lift, drag, etc.). Based on that, he evaluates the various error sources [94] (coming from discretization and modeling) obtaining good result in drag or lift prediction in simple configuration as the one shown in Fig. 5.12. However, as shown in section 5.4 where results of Meyers and Sagaut [72] are reported, good results on a single flow quantity do not imply that the whole flow is better resolved because of the so-called mutual error compensation.

5.6 Summary

In section 5.1 errors in the LES context have been reviewed. In general all error components act on a LES flow whose solution (u_d) will differ from the exact solution of the Navier-

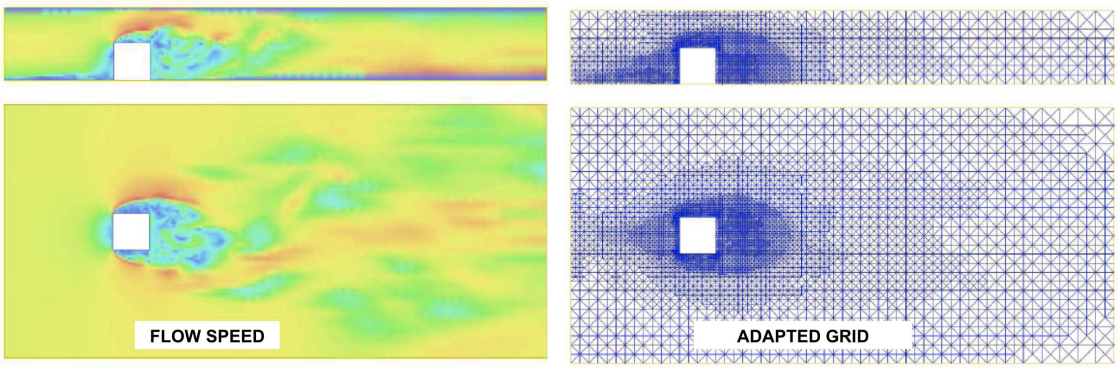

Figure 5.12: From [39], flow field and adapted mesh for flow behind a cubic bluff-body.

Stokes equations (u) introducing the so-called approximation error:

$$e_a = |u - u_d|. \tag{5.18}$$

By definition $e_a \neq 0$ in LES (since the number of degrees of freedom of LES is lower than the number of degrees of freedom of the flow). The approximation error is a function of three different components[5],

$$e_a = f(e_m, e_n, e), \tag{5.19}$$

where: e_m is the modeling error, e_n is the numerical error (therefore dispersion and diffusion), e is the interpolation (or projection) error (Eq.(5.7)). From the literature it has emerged that:

1. finite differences and finite volumes operators have large numerical errors (larger than the SGS term) concentrated at the highest wave numbers (smallest structures) [12, 31],

2. the combined effects of the three error components of Eq.(5.19) are unknown and could compensate each others [16, 71, 72],

3. mesh refinement reduces the size of the corrupted eddies so that their effect on the overall flow behavior could vanish or being negligible [66] (that is a different way of saying that LES is consistent with the Navier-Stokes equations).

The last property (localized mesh refinement) is used in this thesis to improve the accuracy of LES results (since explicit filtering LES or even higher order numerical schemes are not investigated). A possible refinement strategy is to refine everywhere the mesh (Moureau et al. [76]) but such an approach is evidently expensive. The strategy used here is to use a flow property (such as the velocity gradient as in Hertel et al. [37]) to increase the resolution only where needed. The mesh adaptation method used can therefore be defined as an *a posteriori* method since the mesh is adapted based on the computed flow. The manipulation of the mesh is performed using the program MMG3D, presented in section 5.3, which requires as input a metric field. The flow property chosen to adapt

[5]Eq.(5.19) puts together all error sources while Ghosal's [31] analysis does not consider interpolation error since it cannot be erased, $e_a \neq 0$.

the mesh is therefore transformed in a metric field to be read by the mesh manipulator. MMG3D performs the second and third steps shown in section 5.2 which are in common with the mesh adaptation method here used and the "INRIA" approach (Frey and Alauzet [25], Alauzet et al. [3], Dobrzynski and Frey [2], Loseille et al. [63]). While in the INRIA method the metric field derives directly from the Hessian of the solution, here it the metric field is constructed based on flow properties.

Chapter 6

Suitable sensors for LES

This chapter presents the criteria used for the *a posteriori* mesh adaptation method developed during this thesis and that will be validated in the test cases of chapters 7-9. Since *a posteriori* mesh adaptation requires a computed flow field, this chapter shows how to generate a set of criteria/sensors using a LES solution.
Generating an adaptation criterion is the intermediate step between the LES solver and the mesh adapter (Fig. 6.1). The mesh adapter (that is the program that moves, insert or delete nodes, elements, etc.) requires as input a metric field (see section 5.3). Therefore, creating an adaptation criterion consists in generating a metric field (see section 5.2) which can be read by the mesh adapter. Fig. 6.1 sketches the three mesh adaptation steps. The

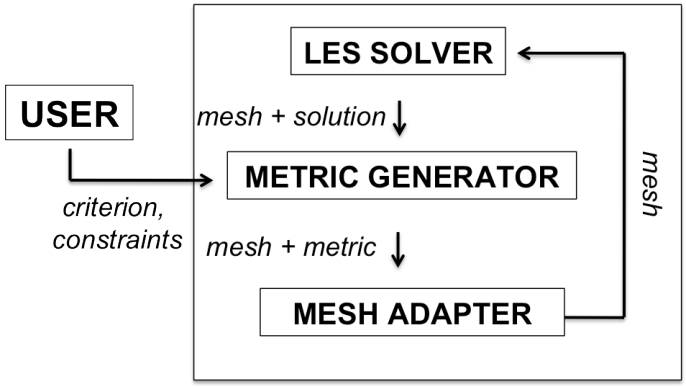

Figure 6.1: Mesh adaptation loop.

first step of Fig. 6.1 consists in performing a LES. The mesh and the solution of LES are the inputs of the metric generator. The metric generator analyses the flow field and generates as output a metric field depending on which criterion and constraints the user choses.
The mesh and the metric field are given to the mesh adapter which modifies the mesh based on the size and directional constraints prescribed by the metric. The LES solver used in this thesis (AVBP and YALES2) have been described in section 3.2.2 while the mesh adapter (MMG3D) has been described in section 5.3.
This chapter focuses on the metric generator that is the "decision maker" of the whole process: based on its analysis of the LES flow field it prescribes how the adapter has to ma-

nipulate the grid. The metric generator was developed by the author of this manuscript. It is written in **C** and it is named ADDA (which stands for nothing). Part of the metric generator tasks consists in translating the mesh from the LES format (in hdf5) to a format which can be read by MMG3D: it basically works as a link between the LES solver and the mesh adapter.

6.1 How to build a metric

We start our description by introducing some basic concepts that will be used in this chapter. A metric is a symmetric definite-positive form expressed as a matrix M. Metrics are used to define the dot product in Euclidean *metric* spaces (therefore the notion of distance d_M between points, Eq.(5.3)). A metric M in $\mathbf{R}^3$ can be diagonalized as follows:

$$M = R \begin{pmatrix} \lambda_1 & 0 & 0 \\ 0 & \lambda_2 & 0 \\ 0 & 0 & \lambda_3 \end{pmatrix} R^T, \tag{6.1}$$

where $\lambda_1, \lambda_2, \lambda_3$ are its three eigenvalues and R is an orthonormal matrix composed of the eigenvectors of M which verifies $RR^T = R^T R = I_3$ where I_3 is the identity matrix [63]. The three eigenvalues have to be strictly positive (a metric "deforms" the Euclidean space, if one of the eigenvalues is zero, it means that a dimension has disappeared) and symmetric (a metric defines distance; if the metric is not symmetric, distance would depend on orientation $\overline{AB} \neq \overline{BA}$).
There are two possible conditions: either the three eigenvalues are equal ($\lambda_1 = \lambda_2 = \lambda_3$) therefore the metric is isotropic in all directions or one of the eigenvalues is different from the others ($\lambda_1 \neq \lambda_2$) therefore the metric is anisotropic. An isotropic metric will force the mesh adapter to create isotropic elements while an anisotropic metric will result in anisotropic elements. In this thesis only the first path (isotropic metric) will be investigated since for implicit filtering LES the mesh has to be isotropic for LES to be consistent with the Navier-Stokes equations [66]. Also, the use of an isotropic metric reduces the number of parameters of the study performed here.
Since all metrics used here are isotropic in all directions ($\lambda_1 = \lambda_2 = \lambda_3 = \lambda$), they can be expressed as:

$$M = \lambda \; I_3, \tag{6.2}$$

simply. The main task of the metric generator of Fig. 6.1 is to generate a metric field, so to determine at each node n of the mesh a metric $M(n)$. Generating a metric field corresponds to evaluate the function:

$$M(n) = \lambda(n) \; I_3 = \begin{pmatrix} \lambda(n) & 0 & 0 \\ 0 & \lambda(n) & 0 \\ 0 & 0 & \lambda(n) \end{pmatrix}. \tag{6.3}$$

6.1.1 Metric based on a flow property

The simplest metric fields developed are based on a flow property Φ. The time-averaged value of a flow property (Φ_{mean}) is used to generate the metric as follows. First the mean

length $L(n)$ of the side of the tetrahedra sharing a node (n) is evaluated. Then a factor of scaling $s(n)$ is evaluated as:

$$s(n) = \frac{\Phi_{mean}}{\Phi(n)}, \tag{6.4}$$

where $\Phi(n)$ is the flow property Φ evaluated at the node n. The metric eigenvalue at the node n based on the flow property Φ (i.e. $\lambda_\Phi(n)$) is evaluated as:

$$\lambda_\Phi(n) = \frac{1}{(L(n) \times s(n))^2}, \tag{6.5}$$

and used is Eq.(6.3) instead of λ.
The resulting mesh size (Δ) of Eq.(6.5) is $\Delta = L(n) \times s(n)$ which is also the radius of the unit ball in the metric space defined by the metric (see section 5.2).
If $\Phi(n)$ is higher than the mean $(s(n) < 1)$, the size of the tetrahedron[1] will be reduced according to Eq.(6.4-6.5), vice-versa the size of the tetrahedron will be increased.
Φ can be any of the flow properties: fluctuation of the mean velocity or sub-grid dissipation, ratio of turbulent over laminar viscosity, etc. .

6.1.2 Metric based on the velocity gradient tensor

Building a metric using the gradient of the mean[2] velocity (∇u_{mean}) requires a different method to be applied. Since the mean velocity gradient tensor (∇u_{mean}) is not necessarily symmetric or definite positive it cannot be directly used as a metric field and some algebraic manipulations are required. These algebraic manipulations are the same proposed in Nicoud et al. [80] to build the SIGMA SGS model, see section 3.2.2, and a metric field based on the singular values of the velocity gradient is built.
Singular values are defined as the square root of the eigenvalues of the matrix $A^T A$ where A is a matrix with real entries and A^T is its transpose. Singular values are chosen because they are by definition nonnegative [80] and this simplifies their use to create a metric. Singular values of the gradient of the mean velocity are evaluated as follows. First the matrix:

$$G = \nabla u_{mean}^T \nabla u_{mean}, \tag{6.6}$$

is evaluated at each node n (the dependency on n is dropped for clarity). G is by construction symmetric and semi-definite positive. Then the eigenvalues of G (G_1, G_2, G_3) are used to evaluate the singular values (η_1, η_2, η_3) of ∇u_{mean} as $\eta_i = \sqrt{G_i}$ for $i = 1, 2, 3$. Singular values are not necessarily equal to each other, $\eta_i \neq \eta_j$, and some of them can be zero. Therefore the mean singular value $\eta_M = \sum_{i=1}^{3} \eta_i/3$ is used instead to build a metric field $M_{\nabla u}(n)$ as:

$$M_{\nabla u}(n) = \eta_M(n)\ I_3 = \begin{pmatrix} \lambda_{\nabla u}(n) & 0 & 0 \\ 0 & \lambda_{\nabla u}(n) & 0 \\ 0 & 0 & \lambda_{\nabla u}(n) \end{pmatrix}. \tag{6.7}$$

[1] The size of a tetrahedron depends on the scaling factor (Eq.(6.4)) of all nodes belonging to that tetrahedron.

[2] We assume that the mean and the gradient operator commute so $\nabla(u_{mean}) = (\nabla u)_{mean}$.

where $\lambda_{\nabla u}(n) = \eta_M(n)$ is by definition the eigenvalue of the metric $M_{\nabla u}(n)$. The peculiarity of the metric field of Eq.(6.7) is that the bigger the velocity gradient is, the smaller the element size is.

6.1.3 Metric intersection

Along with a metric field based on a flow property (Eqs. (6.4-6.5)) or based on the velocity gradient (Eq.(6.7)) a third method is used here. This method consists in mixing the previous two using the principle of metric intersection as explained by Alauzet and Frey [4].
For instance, if it is desired to adapt the mesh based on a criterion relying on both a flow property Φ and on the velocity gradient, two metric fields are evaluated:

- $M_\Phi(n) = \lambda_\Phi(n)\ I_3$, using Eqs. (6.4-6.5),
- $M_{\nabla u} = \lambda_{\nabla u}(n)\ I_3$, using Eq.(6.7) and the algorithm explained in section 6.1.2.

The intersection of $M_\Phi(n)$ and $M_{\nabla u}(n)$ is evaluated as:

$$INT(n) = M_\Phi(n) \cap M_{\nabla u}(n) = \lambda_\Phi(n)\ I_3 \cap \lambda_{\nabla u}(n)\ I_3. \tag{6.8}$$

Eq.(6.9) expresses formally that $INT(n)$ is the intersection of two concentric balls of different radii (any isotropic metric can be visualized by a circle in 2D or by a ball in 3D, see section 5.2). The ball of intersection $INT(n)$ obviously corresponds to the smallest ball between $\lambda_\Phi(n)\ I_3$ and $\lambda_{\nabla u}(n)\ I_3$, ergo:

$$INT(n) = M_\Phi(n) \cap M_{\nabla u}(n) = max[\lambda_\Phi(n), \lambda_{\nabla u}(n)]\ I_3, \tag{6.9}$$

since the square of the radius of the ball is inversely proportional to its characteristic eigenvalue λ.

6.2 Constraints

The mesh needs to satisfy some constraints to be used by a LES solver. Element shape, gradation (variation of the volume of neighbor elements), minimum and maximum cell size, total number of nodes are important properties which can influence the quality, the efficiency and even the possibility of doing a LES of a given flow. In this section are presented all manipulations performed on the metric field in order to match the external constraints additional to the *a posteriori* adaptation criterion.

6.2.1 Anisotropy

As mentioned in section 5.1, element shape cannot be arbitrary. Tetrahedra with an excessive equivolume skewness (or aspect ratio etc.) can cause numerical difficulties causing the simulation to crash. Equivolume skewness is defined as:

$$E_{Qv} = \frac{V_c - V}{V_c}, \tag{6.10}$$

where V_c is the volume of an equilateral tetrahedron with the same circumsphere of the current tetrahedron and V is the volume of the current tetrahedron. Fig. 6.2 clarifies Eq.(6.10) for a 2D tetrahedron, i.e. a triangle. Elements which are too stretched in one direction have a large equivolume skewness and cannot be used: a constraint on the element shape is imposed.

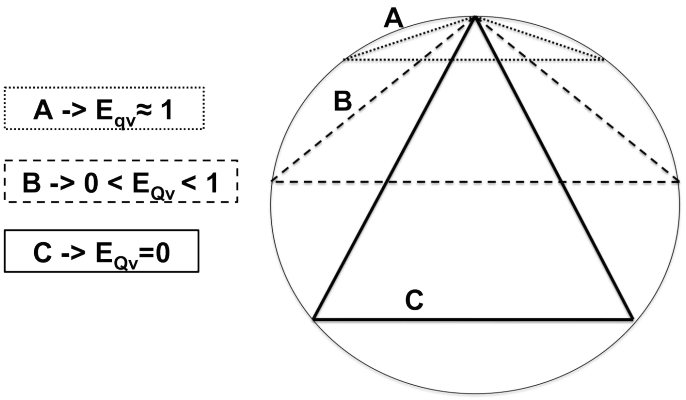

Figure 6.2: Equivolume skewness for 2D tetrahedra (i.e. equisurface skewness for different triangles). Triangle A has a high equisurface element, triangle B has a low equisurface skewness while triangle C, which is the equilateral triangle inscribed in the same circle circumference of A & B, has obviously an equisurface skewness of zero. The same concept is applicable to tetrahedra considering the circumsphere instead of the circle circumference.

This constraint is trivially satisfied for the isotropic metrics of section 6.1 (since the mesh adapter should generate only isotropic elements if the metric is purely isotropic). However, since it is impossible to tesselate the 3D space only with the regular tetrahedron [62], and because of the difficulties arising by not deteriorating the original CAD surface during the re-meshing procedure, the mesh adapter could generate highly stretched elements. For this reason the *a priori* optimization based algorithm of Freitag et al. [24] (employing only nodes displacement) was used to improve the quality of the worst elements in terms of equivolume skewness in the case that LES had numerical stability problems.

6.2.2 Minimum & maximum cell size

The time step of a LES under the Courant-Friedrichs-Lewy (CFL) condition is determined (the 1D case is used here for simplicity) by:

$$dt = min\left(\frac{dx}{c}\right)\ CFL, \tag{6.11}$$

where dx the grid spacing, c is the wave speed (which is $c = |u| + c_{sound}$ for compressible solvers or $c = |u|$ for incompressible solvers where $|u|$ is the absolute value of largest between the convective and the diffusive flow speeds and c_{sound} is the speed of sound) and CFL is the CFL number chosen. If the wave speed is approximately constant everywhere in the domain it is evident that, for a given CFL, the minimum cell size (dx_{min}) determines the simulation time advancement and therefore efficiency.
The maximum cell size (dx_{max}) has to be fixed since any criterion could lead to a metric field which has an eigenvalue close to zero locally (for instance a metric field based on the velocity gradient is zero for a parallel flow).

Based on these constraints (dx_{max} and dx_{min} defined by the user) if any eigenvalue ($\lambda(n)$) of the metric field exceeds the boundaries[3] imposed by dx_{max}/dx_{min}, i.e. $\lambda(n) > (1/dx_{min})^2$ or $\lambda(n) < (1/dx_{max})^2$, an artificial clipping is employed:

$$\lambda(n) = \left(\frac{1}{dx_{max}}\right)^2, \tag{6.12}$$

or,

$$\lambda(n) = \left(\frac{1}{dx_{min}}\right)^2. \tag{6.13}$$

if it exceeds the minimum/maximum bounds respectively.

6.2.3 Gradation

The cell size gradation is the variation of the size of the edges of neighbor elements.
Gradation is here computed as the ratio of the maximum eigenvalue between all nodes of a tetrahedron to the minimum eigenvalue between all nodes of the same tetrahedron. Formally, $\lambda^T_{min} = min(\lambda^i_{min})$ is the smallest eigenvalue of the tetrahedron, $\lambda^T_{max} = max(\lambda^i_{max})$ is the largest eigenvalue (where $i = 1, 2, 3, 4$ are the nodes of the tetrahedron). In case that the ratio

$$g_\lambda = \sqrt{\lambda^T_{max}/\lambda^T_{min}}, \tag{6.14}$$

is higher[4] then the desired level of gradation (β) the eigenvalues λ_{max} and λ_{min} are modified as follows.
First the mean eigenvalue is evaluated as $\lambda^T_{mean} = (\lambda^T_{max} + \lambda^T_{min})/2$. Then λ^T_{max} and λ^T_{min} are modified accordingly to the gradation level imposed by the user (β):

$$\lambda^T_{max} = \beta\ \lambda^T_{mean}, \tag{6.15}$$

$$\lambda^T_{min} = \frac{\lambda^T_{mean}}{\beta}. \tag{6.16}$$

The result is that their ratio g_λ becomes:

$$g_\lambda = \sqrt{\lambda^T_{max}/\lambda^T_{min}} = \beta. \tag{6.17}$$

Every non-boundary node belongs to two tetrahedra at least. Therefore, imposing a maximum gradation β for a tetrahedron corresponds, even if indirectly, to impose a gradation level between the size of the tetrahedron and its neighbour tetrahedra which share the same nodes.

6.2.4 Number of nodes

The cardinality of the grid nodes (the "number of nodes") obviously determines the computational cost of a simulation (in the best case scenario the computational cost increases

[3]The element size of the adapted mesh (Δ) is inverse proportional to $\lambda^{\frac{1}{2}}$, $\Delta = \lambda^{-\frac{1}{2}}$.
[4]The square root is chosen since the mesh size is proportional to $1/\lambda^2$.

linearly with the number of nodes). The number of nodes of the adapted mesh is determined as a function of the metric field as follows.
Let us consider a metric $M(n)$ evaluated at a point n of the mesh. The volume of the equilateral tetrahedra that is of unit length (i.e. the equilater tetrahedron whose edges are of unit length in the metric space defined by $M(n)$) with respect to the metric is:

$$V^M(n) = det(M(n))^{-\frac{1}{2}}\ V^{REF} = (\lambda(n)^3)^{-\frac{1}{2}}\ V^{REF}. \tag{6.18}$$

V^{REF} is the volume of an equilateral tetrahedron of unit length inscribed in a sphere of unit radius:

$$V^{REF} = \left(\frac{2}{3}\ \sqrt{6}\right)^3 \frac{\sqrt{2}}{12} = 0.5132[m^3]. \tag{6.19}$$

The ratio of the nodal volume $V^{OLD}(n)$ of the original mesh and the volume estimated by Eq.(6.18) is named $\gamma(n)$:

$$\gamma(n) = \frac{V^{OLD}(n)}{V^M(n)}. \tag{6.20}$$

The resulting total number of nodes on the adapted mesh can be approximated as:

$$N^{NEW} \approx \sum_{n=1}^{N^{OLD}} \gamma(n), \tag{6.21}$$

where N^{OLD} is the number of nodes of the original mesh to be adapted.
Suppose that N^{NEW} is different from the desired number of nodes on the adapted mesh (N^{TARGET}), we introduce a scale factor s between these two terms:

$$s = \frac{N^{NEW}}{N^{TARGET}}. \tag{6.22}$$

By multiplying each eigenvalue $\lambda(n)$ of $M(n)$ by a parameter α equal to:

$$\alpha = \left(\frac{N^{NEW}}{N^{TARGET}}\right)^{-\frac{2}{3}} = s^{-\frac{2}{3}}, \tag{6.23}$$

we obtain that,

$$V^M(n,\alpha) = (\alpha^3\lambda(n)^3)^{-\frac{1}{2}}\ V^{REF} = \alpha^{-\frac{3}{2}} V^M(n) = s\ V^M(n), \tag{6.24}$$

therefore,

$$\gamma(n,\alpha) = \frac{V^{OLD}}{V^M(n,\alpha)} = s^{-1}\gamma(n), \tag{6.25}$$

giving,

$$N^{NEW}(\alpha) = \sum_{n=1}^{N^{OLD}} \gamma(n,\alpha) = s^{-1} \sum_{n=1}^{N^{OLD}} \gamma(n) = s^{-1} N^{NEW} = N^{TARGET}. \tag{6.26}$$

Is therefore possible to estimate the number of nodes of the adapted mesh a priori (before the mesh adapter generates it). Obviously, any gradation present in the original metric

and any anisotropy will be left untouched by the scaling procedure (α of Eq.(6.23) is applied to the whole metric field). This method allows to determine the numerical size of the problem without modifying the properties of the original metric. Using the definition of Loseille and Alauzet [62], whose analysis inspired the method used here to impose the number of nodes of the mesh, the original and the "scaled" metric field (and therefore adapted mesh) are "embedded", since they have the same anisotropic ratios (in this case is trivially satisfied since the metric is isotropic) and orientations and they only differ from the number of nodes.

6.3 Simulation efficiency

In the final section of this chapter is introduced the definition of the simulation efficiency that will be used later on.

Definition 4 *The simulation efficiency is defined as the ratio of the simulation physical time (t_{simu}) over the computational time (t_{CPU}, the computational time) using a given solver, machine and number of processors:*

$$Eff = \frac{t_{simu}}{t_{CPU}}. \tag{6.27}$$

Considering a constant t_{simu}, for instance $t_{simu} = 5$ convective flow through times, in order to reach a converged statistic for a given *flow*, the simulation efficiency will be inversely proportional to t_{CPU}: the faster is the computation for a given solver, machine and number of processors, the more efficient is the simulation.

Chapter 7

Test case A: the Dellenback experiment, axial case

7.1 Description of the experiment

Dellenback's experiment [17] studied a confined jet at moderate Reynolds number and produced a detailed set of measurements. Measurements were taken at different swirl (S, Eq.(2.2)) and Reynolds numbers (note that the measurement position differs for the axial and swirled case) and a number of LES studies have been performed for this flow [103, 104]. In this thesis two cases will be examined:

- the first case corresponds to the fluid dynamics condition of $Re = 30000$ and $S = 0.0$ and it is named here "axial"case,
- the second case corresponds to the condition of $Re = 30000$ and $S = 0.6$ and it is named here "swirled" case (Chapter 8).

As explained in the first part of this thesis (see Chapter 2) the introduction of a swirl velocity component highly modifies the flow topology: the axial and swirled flows examined here have few common features except the geometry. The axial case is chosen for its simplicity which allows to easily understand the effects of mesh adaptation while the swirled case (closer the the topic of this manuscript) is the logical next step before analyzing more complex geometries. This chapter focuses on the axial case while chapter 8 focuses on the swirled case.
The LES solver chosen to test adaptation techniques is YALES2 (see section 3.2.2) since it gives reliable results at low numerical cost for such low Mach number flow ($Ma = 0.025$). In Fig. 7.1 the geometry of the Dellenback case is shown: it consists in two coaxial cylinders with the flow streaming from the smaller (with a diameter of $D_1 = 0.0508$[m]) expanding in the larger one (with a diameter twice larger, $D_2 = 0.1016$[m]). The simulation domain expands along the streamwise direction for $L = 0.7112$[m]$= 14D_1$, allowing to analyze numerical results down to the measurement position $12D_1$ downstream of the inlet (or $10D_1$ downstream of step expansion).

Three boundary conditions are used:

- an inlet where the experimental velocity profile obtained at the first measurement

plane is imposed ($2D_1$ upstream of the step expansion) as the same approach was used for this flow in [103, 104],

- an outlet (a so-called *convective boundary condition*[85]),
- solid, adherent and adiabatic walls everywhere else.

The average jet speed over the upstream section[1] is 9.13[m/s] which corresponds to the experimental Reynolds number chosen (considering a kinematic viscosity $\nu = 1.517 \times 10^{-5}[\mathrm{m}^2/\mathrm{s}]$ and $D_1 = 0.0508[\mathrm{m}]$). Note that no turbulence is injected at the inlet since the proper amount of synthetic turbulence would depend on the particular mesh resolution (considering the effects of dissipation) even tough the experimental conditions correspond to a fully developed turbulent flow in the upstream pipe. This investigation focuses mainly on the downstream part of the domain where the effects of such an approximation are negligible ($5D_1$ downstream of the inlet turbulence intensity reaches the experimental level) as will be shown in appendix C. Table 7.1 summarizes the B.C.s used.

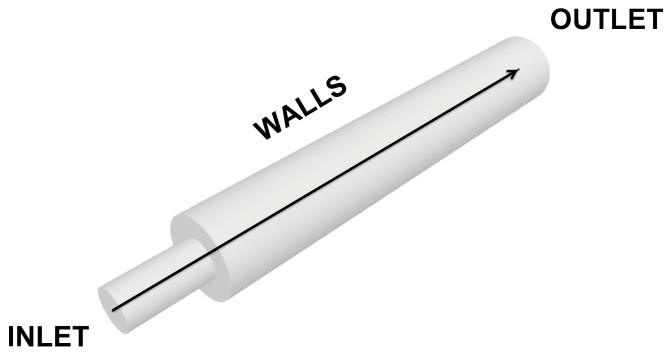

Figure 7.1: Geometry of the Dellenback LES (two coaxial cylinders), the arrow indicates the streamwise direction. The swirl generator, positioned upstream of the smaller cylinder, is not simulated.

BC NAME	IMPOSED PROPERTY	TARGET VALUE
inlet	EXP velocity profile	$U_{ref} = 8.9[m/s]$
outlet	pressure	101300 $[Pa]$
walls	adherence, impermeability, adiabaticity	

Table 7.1: Imposed values for boundary conditions sketched in Fig. 7.1.

The SGS model chosen for all LES of this chapter is $WALE$ [79] whose properties near the wall are similar to the SIGMA SGS model (i.e. the turbulent viscosity generated by the model is proportional to the cube of the wall distance, see section 3.2.2). All simulations are initialized with a zero velocity flow.

[1] In Dellenback et al.[17] the Reynolds number is evaluated using "the average velocity in the upstream tube". However, as shown in the experimental results[17] for the "axial" case, the mean velocity profiles normalized by the centerline jet speed shows absolutely no dependence on the Reynolds number.

7.2 Axial case, homogeneous meshes

In a first step, the effects of a non-adaptative mesh refinement strategy are compared by using four meshes (H1 to H4). This is done for the axial case which corresponds to a confined, unswirled jet at $Re = 30\ 000$ ($Re = U \times D_1/\nu$). Results are compared with experimental data taken at 8 measurement position (Fig. 7.2). Four different meshes are used for the basic LES (basic means without adaptation) ranging from mesh H1 to H4 (where "H" stands for homogeneous and the number for the refinement level). Results obtained with the homogeneous meshes are used as reference together with experimental data. This choice is motivated by the lack of a reliable error estimate which would justify an increase or a reduction of the mesh resolution. Therefore mesh adaptation is used here to re-distribute grid nodes based on a given criterion and comparison will be performed between homogeneous and adapted meshes of the same efficiency level (Eq.(6.27)).

The set of meshes of the basic case are isotropic, homogeneous and with a cell size that smoothly increases from the inlet to the outlet by a factor of 2 (elements close to the outlet are twice as large as elements close to the inlet). Meshes are fully composed of tetrahedra with a maximum equivolume skewness limited to $E_q = 0.9$ and a stretching ratio of 1.3, both imposed as input of the commercial mesh generator used to create them (CENTAUR).

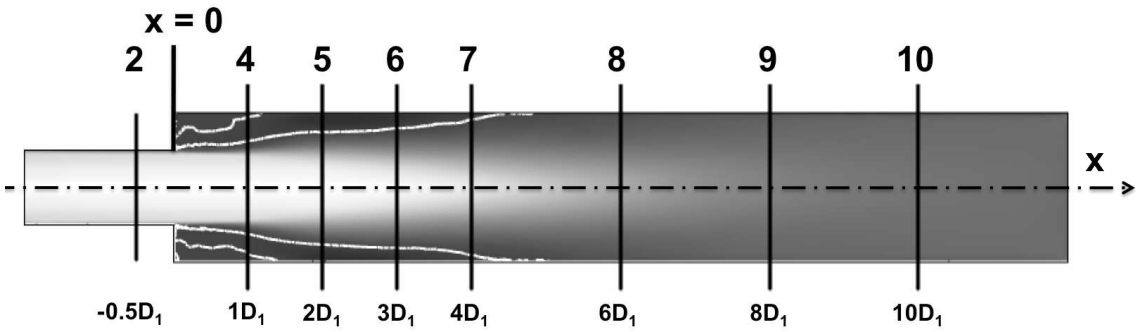

Figure 7.2: Measurement planes names (above) and axial position with respect to the expansion for the axial case of Dellenback[17]. The white line is zero mean axial velocity of LES H3, the picture is colored by the mean axial velocity just as a reference.

The set of basic LES and the characteristics of the meshes used are summarized in table 7.2 while $H1$ and $H4$ are shown in Fig. 7.3. Note that meshes H1 and H2 are finer at the inlet than inside the domain in order to improve the interpolation of the experimental velocity profile (a mesh size of $1[mm]$ is imposed at the inlet to get 50 nodes in the diameter). This refinement, which is necessary to match the mean velocity profile downstream at the first measurement plane (plane 2), introduces an additional cost which is zero for the fine meshes H3 and H4 (which are finer than $1[mm]$ at the inlet). When the inlet refinement is removed the efficiency of the simulation (E defined by Eq.(6.27)) scales roughly as the fourth power of the mesh size[2], i.e. $E_{H4} = 0.009 \approx E_{H3}(\frac{\Delta_{H4}}{\Delta_{H3}})^4 = 0.013$, see table 7.2. The inlet refinement causes a decrease of the efficiency, for instance LES H2 is just 1.48 times more efficient then LES H3 while it should be ≈ 2.3.

[2]Considering that the numerical cost scale as Δ^{-3} and cost of time advancement as Δ^{-1}.

mesh LES name	number of nodes	number of tetra	numerical efficiency Eq.(6.27)	Δ/η_K
H1	0.3M	1.6M	1	130
H2	1.3M	7.5M	0.31	82
H3	2.3M	13.4M	0.21	68
H4	25M	111M	0.009	34

Table 7.2: table of simulations performed. The numerical efficiency (Eq.(6.27)) is normalized by the efficiency of LES H1 while the average mesh size Δ is adimensionalized by the Kolmogorov length scale for a HIT at the same Reynolds number ($\eta_K = Re^{-\frac{3}{4}}\ D_1 = 2.24 \times 10^{-5}[m]$)

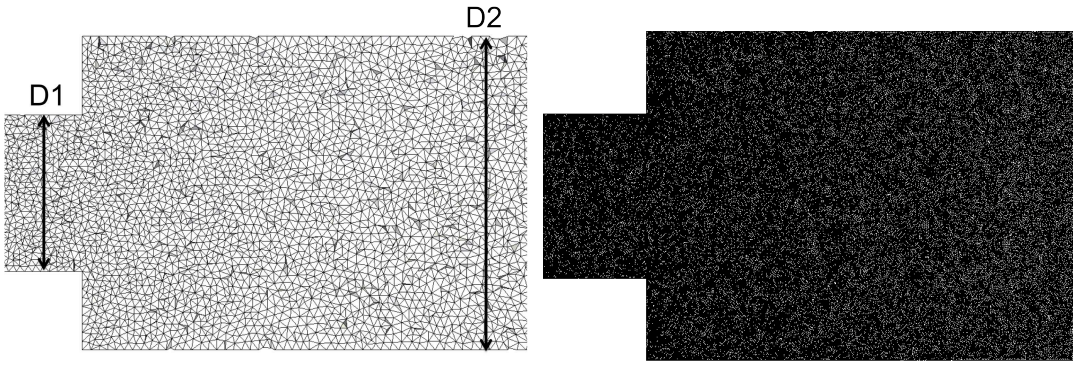

(a) H1 of table 7.2 (b) H4 of table 7.2

Figure 7.3: Meshes H1 and H4. H1 has $\approx$ 26-52 nodes for diameters D_1-D_2 respectively, while H4 has $\approx$ 84-168 nodes for diameters D_1-D_2 respectively (from the figure it is almost impossible to distiguinsh elements of mesh H4 which are 4 times smaller than the one of H1).

7.2.1 Flow field of the homogeneous meshes LES

First, the accuracy of LES is tested by increasing the mesh density everywhere as shown in table 7.2. The flow field changes significantly with this homogeneous refinement. When increasing the mesh resolution the turbulent structures generated in the shear layer of the jet get smaller and stronger, a larger amount of the flow turbulence is directly resolved (as evidenced by the snapshot of the Q criterion in Fig. 7.4). The Q criterion [44] is:

$$Q = \frac{1}{2}(\Omega_{ij}\Omega_{ij} - S_{ij}S_{ij}), \tag{7.1}$$

where Ω_{ij} and S_{ij} are the anti-symmetric and the symmetric part of the velocity gradient tensor. Where Q is positive (rotation dominates strain) a vortex core is present. The turbulent structures generated in the shear layer move toward the centerline of the flow while they are convected downstream by the mean flow as evident in Fig. 7.4.

Mesh resolution modifies these dynamics. With a low resolution these structures reach the centerline sooner (Fig. 7.4) causing an increase in the turbulence intensity ($TI = u^{'}/U_{ref}$ where $u^{'}$ is the root mean square of the velocity considered) in the axial (streamwise) direction along the centerline of the flow (Fig. 7.5). With a higher mesh resolution these structures reach the centerline later (Fig. 7.4) causing the peak of turbulence intensity to be shifted downstream (see H3 in Fig. 7.5). The distribution of axial

and radial turbulence intensities ($TI = \frac{u'}{u_{ref}} = \frac{u'}{8.92[m/s]}$) shown in Fig. 7.5 shows that turbulence along the flow centerline becomes more isotropic as the flow develops.
The mean axial velocity fields of Fig. 7.7 show that the jet reattachment position (at the end of the potential core of the jet where the two shear layer merges) moves downstream from H1 to H3 and that the jet penetration increases with the mesh resolution (compare the zero and the top speed isolines in Fig. 7.7).
The rms fields of Fig. 7.7 show that the shear layer instability grows faster in LES H1 and H2 than in H3 and H4 (compare the isolines of the rms of the axial velocity in Fig. 7.7).
Comparison of the mean axial velocity with experimental measurements is good for all LES (Fig. 7.8) up to plane 6, then the prediction of LES H1 and H2 rapidly deteriorate while H3 and H4 provide a good agreement with experimental data. Note that H4 results has to be taken with care since statistics are collected for a shorter time.
Comparison of the rms of the axial velocity is less accurate in all planes. One observation arises from the rms velocity profiles. Turbulence intensity at plane 4 is higher (and it compares better with experimental data) for the low resolution LES than for the higher resolution (Fig. 7.8(b)) as the shear layer instability grows faster. The dependency of the instability growth rate on the mesh resolution can be explained as an effect of the numerical noise generated close to the wall in LES H1 (see Fig. 7.9). This numerical noise (which remains undamped because the SGS model produces no turbulent viscosity at the wall and laminar viscosity is not sufficient to damp it) triggers the instability upstream and helps it to grow faster. Turbulence affects the mean velocity profile with H1 giving the best prediction at plane 4 (the only exception between all measurement positions). Appendix C shows results of LES H3 with turbulence injection at the inlet of the domain. Injected turbulence ameliorates prediction in this case, labelled $H3_{TJ}$, at plane 4 without being negatively affecting the velocity profiles downstream, obtaining therefore a good comparison with experimental data in the whole domain.
The transition from a laminar (as no turbulence is injected at the inlet) to a fully turbulent jet ends approximately at plane 5 (Fig. 7.9c) where a strong vortex pairing is made evident by the peak of turbulence intensity at a radial position corresponding to the upstream radius.

Finally, Fig. 7.6 shows the jet kinetic energy: all simulations reach convergence after $\approx 0.7[s]$ except LES H4 where the solution is initialized from a mesh of the same resolution as H3 and then refined isotropically. A further transient period is required for LES H4 to start oscillating around a mean value that is higher than LES H1-H2-H3 (as obvious since more flow structures are explicitly resolved in H4). As evident from Fig. 7.6, H4 statistics are collected for a shorter time.

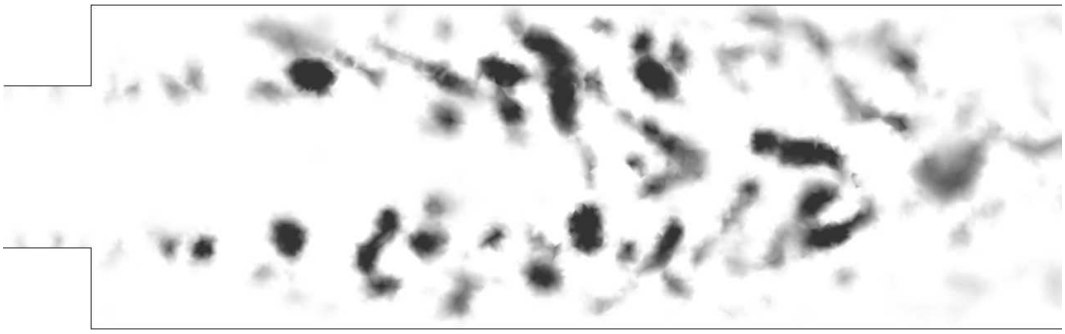

(a) H1 of table 7.2

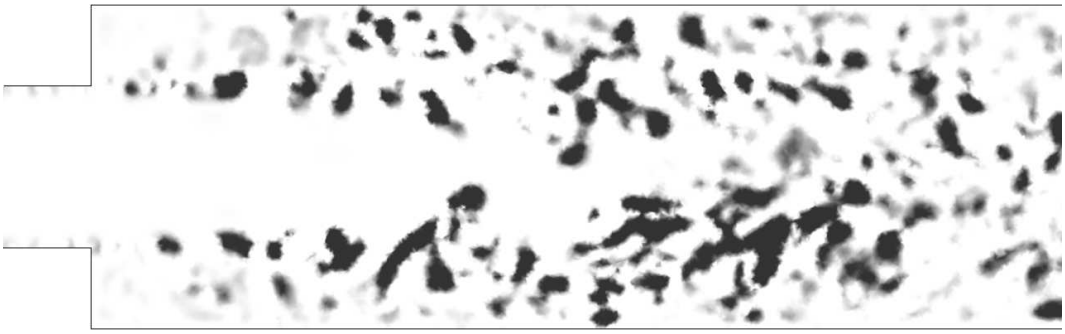

(b) H2 of table 7.2

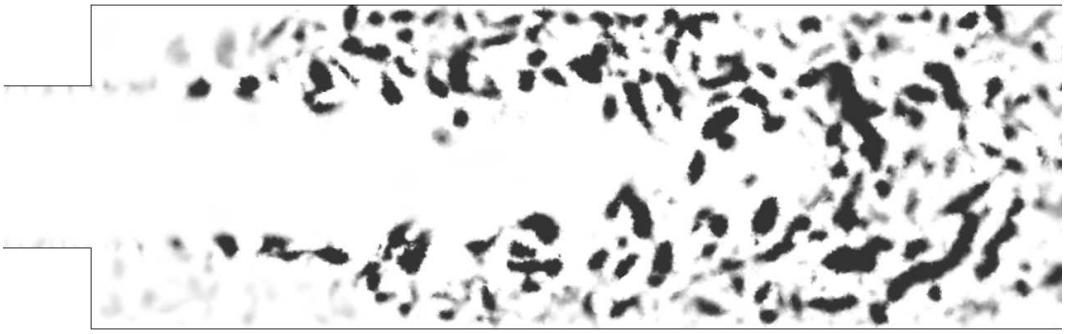

(c) H3 of table 7.2

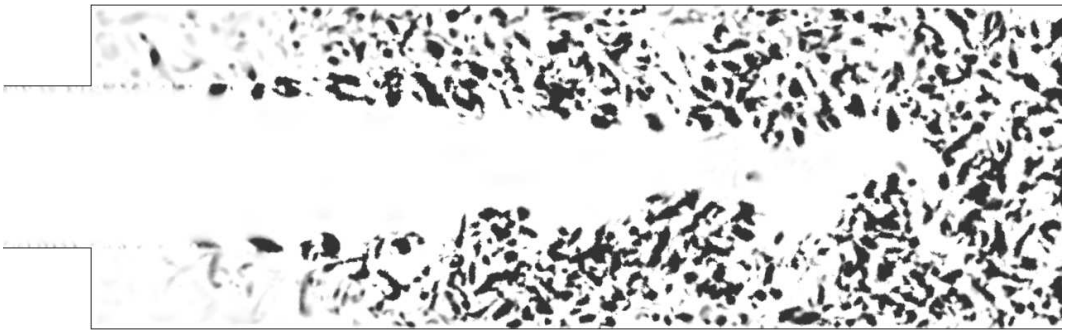

(d) H4 of table 7.2

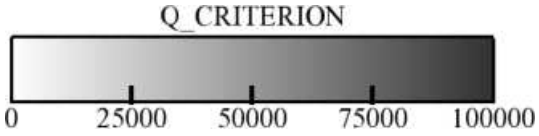

(e) legend

Figure 7.4: Snapshots of Q criterion for simulations of table 7.2.

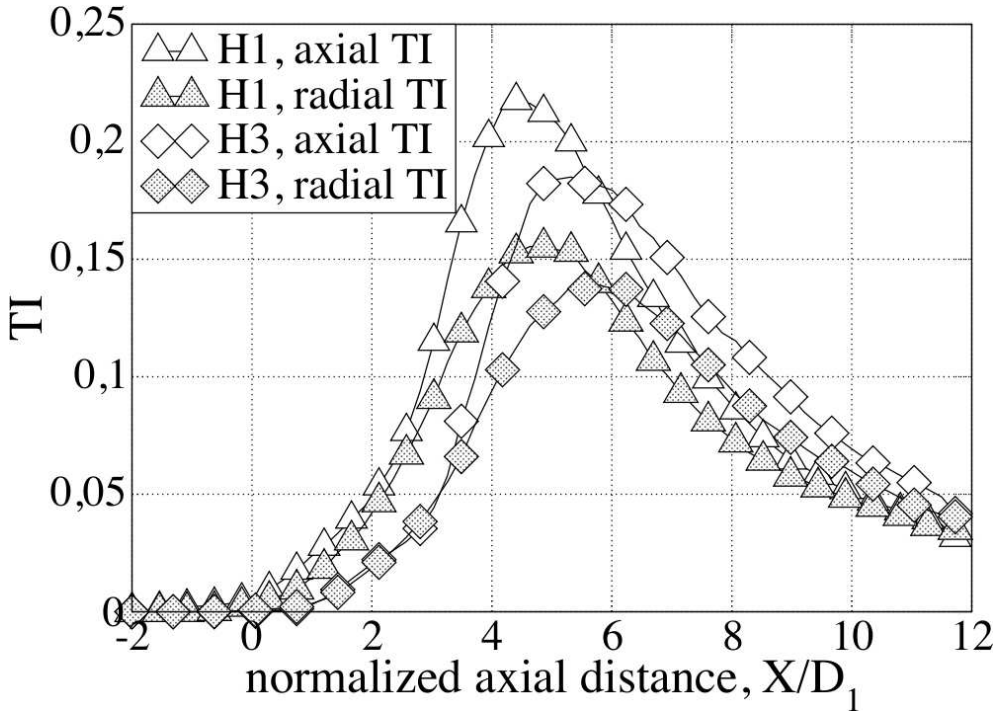

Figure 7.5: Distribution along the centerline of axial and radial (along the centerline radial and tangential TI overlaps) turbulence intensity ($TI = u^{'}/U_{ref}$) for LES H1 and H4 of table 7.2.

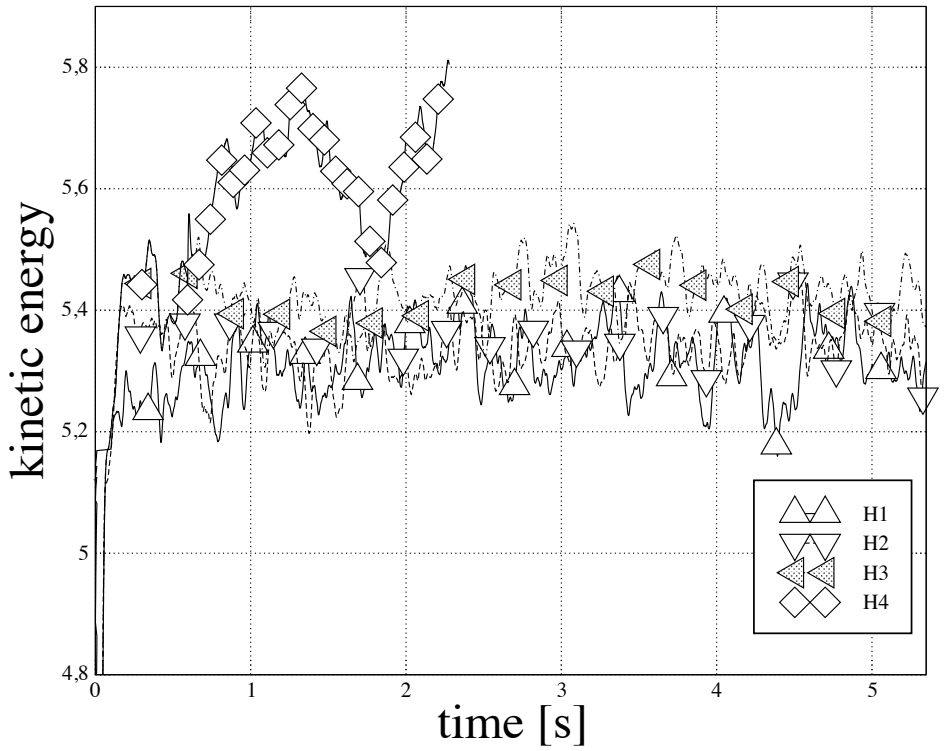

Figure 7.6: Time evolution of the L2 norm of U over the whole computational domain for LES of table 7.2. Note that H4 results has to be taken with care since statistics are collected for a shorter time.

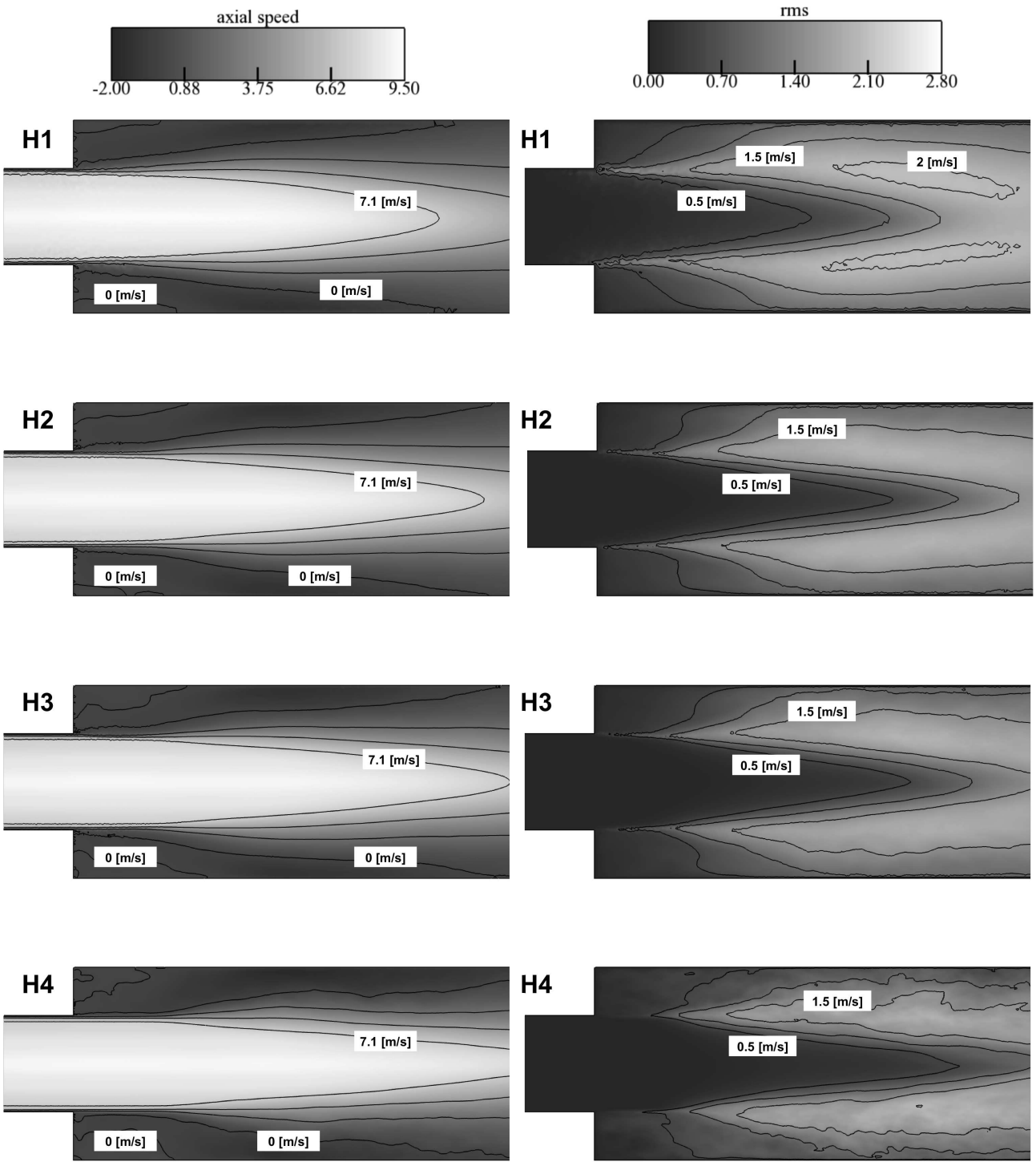

Figure 7.7: Mean flow & RMS for LES of table 7.2

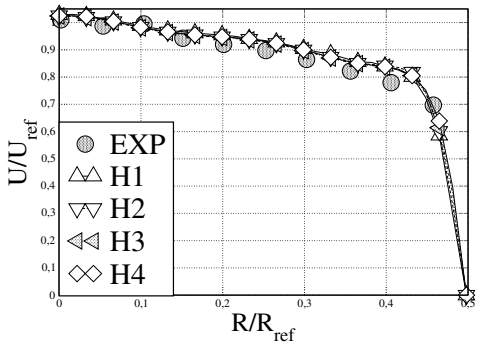

(a) Mean axial velocity profile at plane 2

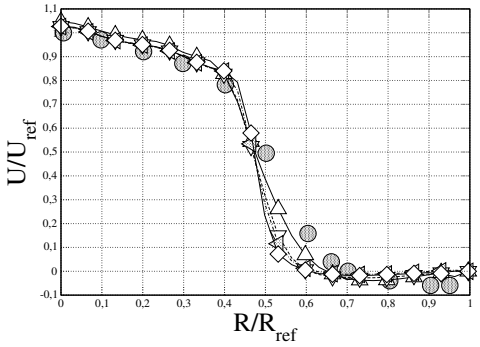

(b) Mean axial velocity profile at plane 4

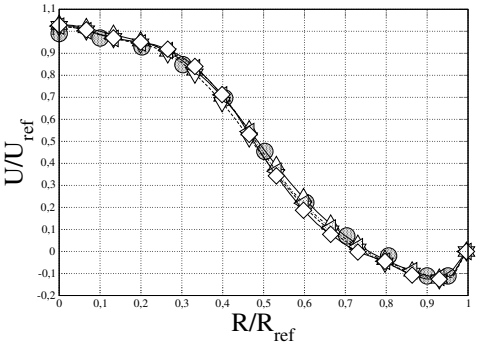

(c) Mean axial velocity profile at plane 5

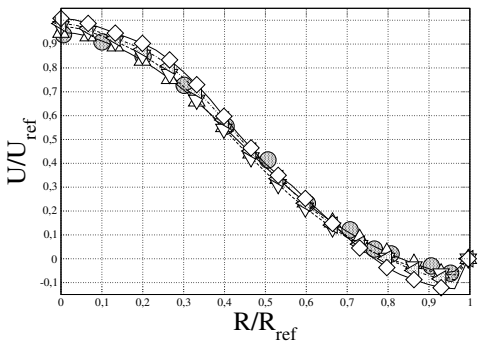

(d) Mean axial velocity profile at plane 6

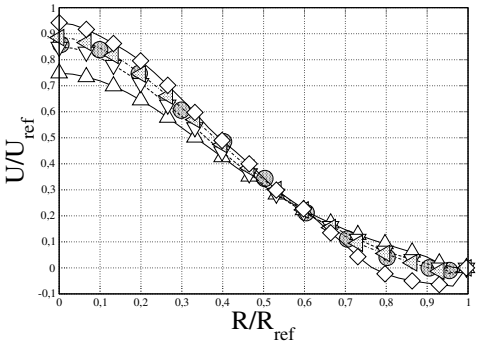

(e) Mean axial velocity profile at plane 7

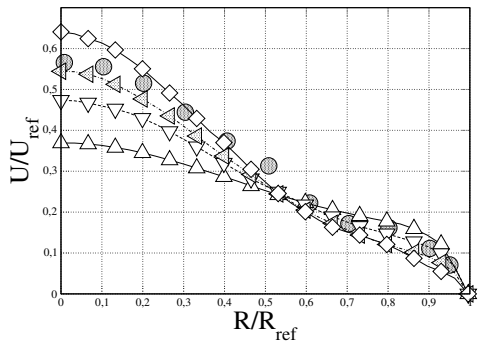

(f) Mean axial velocity profile at plane 8

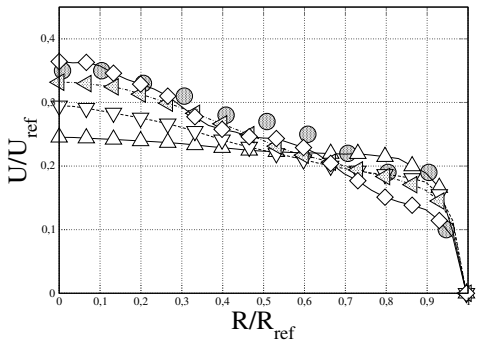

(g) Mean axial velocity profile at plane 9

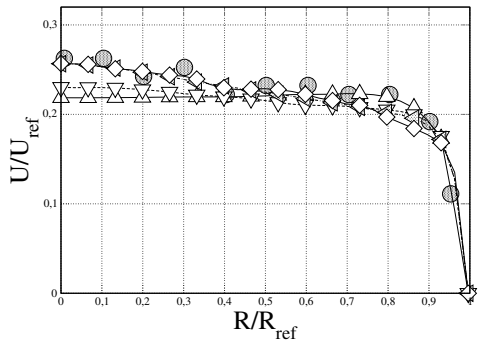

(h) Mean axial velocity profile at plane 10

Figure 7.8: Mean axial velocity profiles at the measurement planes of Fig. 7.2 for simulations of table 7.2.

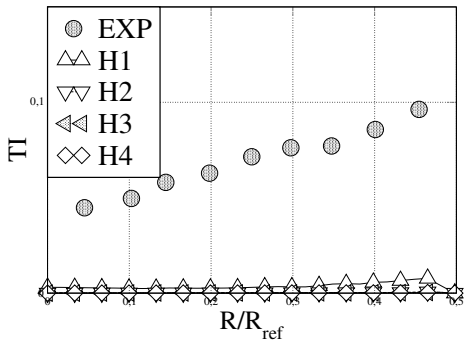

(a) TI axial velocity at plane 2

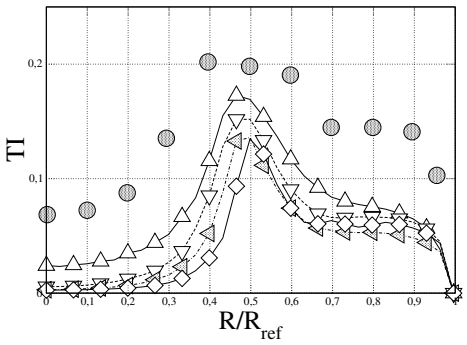

(b) TI axial profile at plane 4

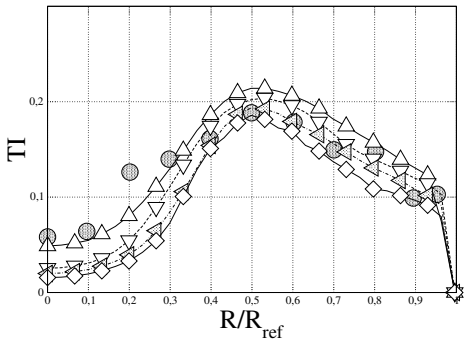

(c) TI axial profile at plane 5

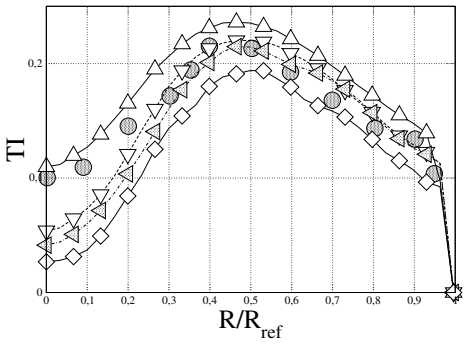

(d) TI axial profile at plane 6

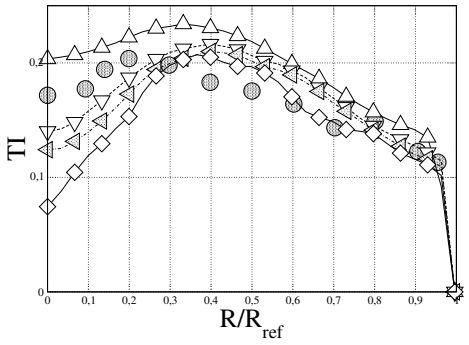

(e) TI axial profile at plane 7

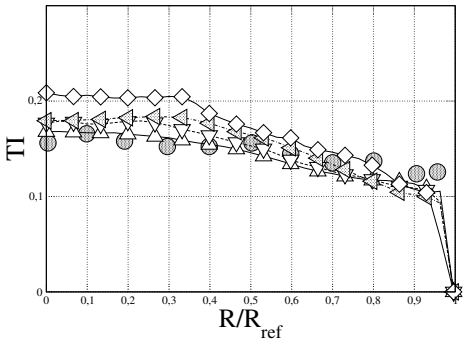

(f) TI axial profile at plane 8

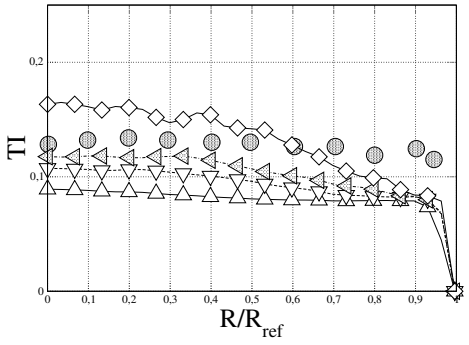

(g) TI axial profile at plane 9

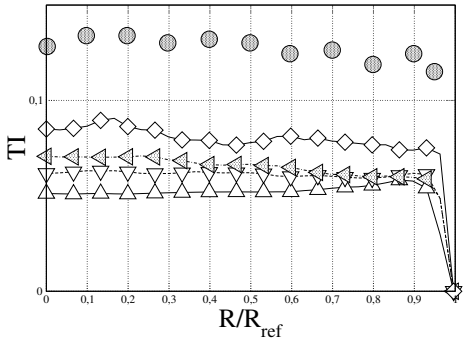

(h) TI axial profile at plane 10

Figure 7.9: TI axial profiles ($TI = \frac{u_{RMS}}{u_{ref}} = \frac{u_{RMS}}{8.92[m/s]}$) at the measurement planes of Fig. 7.2 for simulations of table 7.2.

7.2.2 Pressure drop and LES quality estimates

The prediction of pressure drop, i.e. the difference between total pressure measured at the INLET and total pressure measured at the OUTLET of the domain[3], does not change significantly with the mesh resolution, see table 7.3. Note that pressure drop was not measured experimentally.

mesh/LES name	Total pressure drop	y^+_{mean}	$\frac{\int_V <\frac{\nu_t}{\nu}> dV}{\int_V dV}$	$< max(\frac{\nu_t}{\nu}) >$	Pope criterion Eq.(4.1)
H1	40.8 [Pa]	10.6	6.3	149.0	0.56
H2	39.6 [Pa]	8.1	3.0	87.1	0.63
H3	39.1 [Pa]	7.1	2.3	69.6	0.66
H4	38.8 [Pa]	4.4	0.82	33.3	0.79

Table 7.3: Pressure drop, surface averaged y_+ and time-volume average of turbulent viscosity (normalized by laminar viscosity), time average of the max value of turbulent viscosity (normalized by laminar viscosity), time-volume average Pope criterion.

The comparison of Fig. 7.10 (which shows the variation of total pressure against the axial position) and Fig. 7.5 shows that the jump in total pressure corresponds to the position where turbulence intensity is the highest, i.e. where the turbulent structures generated in the shear layer reach the centerline of the flow, at the end of the potential core of the jet.

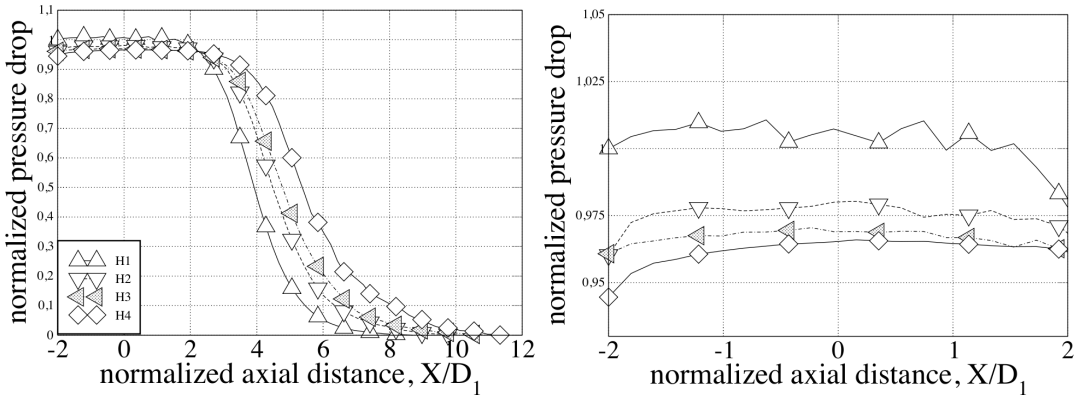

Figure 7.10: Normalized pressure drop (normalized by pressure drop of LES H1) for simulations of table 7.2.

Fig. 7.11 shows the time evolution of the turbulent viscosity normalized by laminar viscosity while table 7.3 shows the time and space average of the same quantity.

The trend of turbulent viscosity of table 7.3 and Fig. 7.11 with the mesh resolution can be explained as follows. Let us take an Homogeneous and Isotropic Turbulence (HIT). Based on the well-known [89] Kolmogorov dimensional analysis [54], for an HIT the char-

[3]Note that $\Delta P/P$, as usually pressure drop is presented, is in the order of 0.04% ($\Delta P/P \approx 40/101300 = 4 \times 10^{-4}$), therefore it is preferred to present results in terms of ΔP simply.

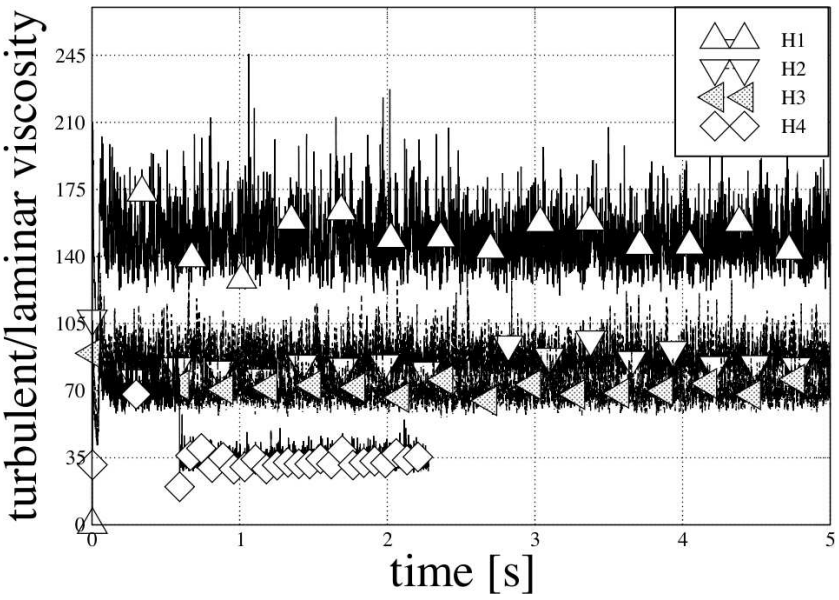

Figure 7.11: Time evolution of the maximum ratio of laminar over turbulent viscosity.

acteristic time scale τ of an eddy of size l in the *inertial subrange* is:

$$\tau = (l^2\epsilon^{-1})^{\frac{1}{3}} \approx (l_0^2\epsilon_0^{-1})^{\frac{1}{3}}, \tag{7.2}$$

where l is the characteristic length scale of the eddy, ϵ is the dissipation rate of kinetic energy at a length scale l, ϵ_0 is the dissipation rate of kinetic energy imposed by the largest eddies of size l_0 and characteristic velocity u_0,

$$\epsilon_0 = \frac{u_0^3}{l_0}. \tag{7.3}$$

Using Eq.(7.2) the velocity gradient can be approximated as:

$$\nabla u = \frac{u}{l} = \frac{1}{\tau} \approx l^{-\frac{2}{3}}\epsilon_0^{\frac{1}{3}}, \tag{7.4}$$

Using Eq.(3.6), turbulent viscosity can be expressed (assuming that the differential operator $D_m(\tilde{u})$ of Eq.(3.6) and the velocity gradient are in a linear proportion, as for the Smagorinky model) as:

$$\nu_{SGS} \propto \Delta^2 \ \nabla u. \tag{7.5}$$

Coupling Eq.(7.6) and Eq.(7.4) with $l = \Delta$ we obtain:

$$\nu_{SGS} \propto \Delta^2 \ \nabla u \propto \Delta^{\frac{4}{3}}\epsilon_0^{\frac{1}{3}}. \tag{7.6}$$

Let us consider two different HIT at a different mesh resolution. Using Eq.(7.6) and considering a large amount of samplings, turbulent viscosity in the two HIT should be in a proportion:

$$\frac{\nu_{SGS}^a}{\nu_{SGS}^b} \propto (\frac{\Delta^a}{\Delta^b})^{\frac{4}{3}} = r_\Delta^{\frac{4}{3}}. \tag{7.7}$$

This simple scaling factor ($r_{\Delta}^{\frac{4}{3}}$) is valid for a filtered DNS. Results of table 7.3 recast in Fig.(7.12) show that Eq.(7.7) approximates very well the trend of turbulent viscosity plotted against the average cell size (where ν_t is averaged in time and space) even though the assumptions are not entirely satisfied.

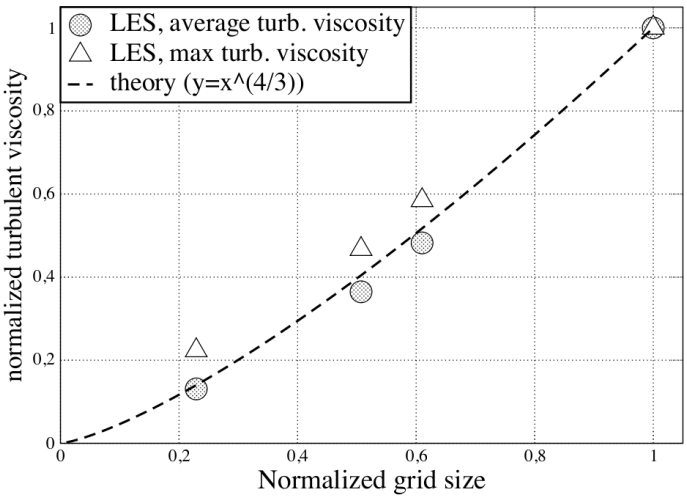

Figure 7.12:

Finally, Fig. 7.13 shows the Pope criterion (Eq.(4.1)) for simulations H1 and H4 using time-averaged turbulent viscosity. From Fig. 7.13 it appears that not even the 111 million of elements mesh H4 (with an average mesh size just 34 times larger than the Kolmogorov length scale for an HIT at the same Re) is able to reach the minimum, arbitrary, requirement of 0.8 set by Pope [89] (see also table 7.3) everywhere.

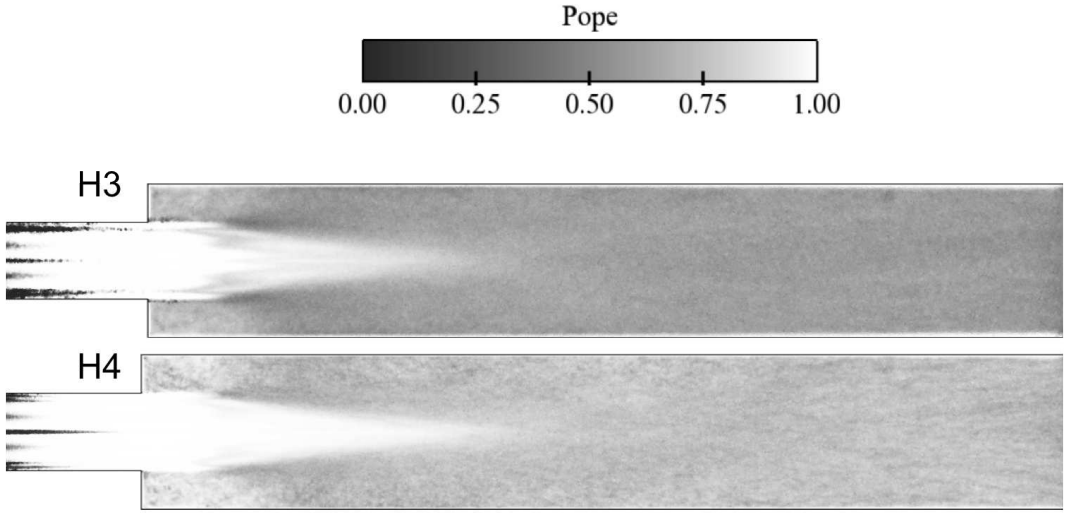

Figure 7.13: Pope criterion (Eq.(4.1)) for simulations H1 and H4 of table 7.2.

7.3 Axial case, adapted meshes

The previous section has shown what the effects of a homogeneous mesh refinement method (from H1 to H4) could be. We begin now to see how an adaptive mesh strategy can improve the results and which sensor should be used for refinement. In this section mesh adaptation is tested using three different sensors:

- the first sensor is named "GRAD" and is based on the mean velocity gradient (see section 6.1.2). Using the "GRAD" sensor the local mesh size is inversely proportional to the magnitude of the velocity gradient;
- the second sensor is named "RMS" and is based on a flow property Φ (Eq.(6.3-6.4-6.5)) where $\Phi = RMS = (u_{ii}^2)^{\frac{1}{2}}$; grid nodes are equi-distributed with respect to the intensity of the resolved turbulence and this sensor is chosen because the jet dynamics are driven by turbulence as explained in section 7.2.1;
- the third sensor is named "MIX" and it combines the previous two using the concept of metric intersection (see section 6.1.3).

All metrics are isotropic (see Chapter 6) and the mesh size gradation, set to 1.3, is based on experience as this value is commonly used at CERFACS for LES, even though a lower value would have been more appropriate for the simulation of jets, as suggested by Moreau [75].
Meshes adapted using the solution of LES H2 of table 7.2 are named A2 ("A" stands for adapted and "2" since sensors are based on the flow field of LES H2) and they have approximately the same numerical efficiency (Eq.(6.27)) as LES H2. Mesh $A1_{MIX}$ is obtained based on mesh and solution of LES H1 of table 7.2 instead. This test is set up to evaluate the effects of the flow field used to build the sensor. In order to compare different sensors/meshes, mesh $A1_{MIX}$ is built to have the efficiency (Eq.(6.27)) of the other adapted grids (this target is obtained by keeping constant the number of nodes and the minimum cell size in the domain). The characteristics of the meshes are summarized in table 7.4 while grids are shown in Fig. 7.14.

mesh/LES name	number of nodes	number of tetra	numerical efficiency (normalized by H1)	Δ/η_K
$A2_{GRAD}$	1.26M	7.2M	0.33	68.75
$A2_{RMS}$	1.3M	7.48M	0.23	71.42
$A2_{MIX}$	1.18M	6.78M	0.30	77
$A1_{MIX}$	1.17M	6.9M	0.34	76.5

Table 7.4: Table of simulations.

Mesh $A2_{GRAD}$ is refined at the location where the velocity gradient is higher, i.e. at the solid boundaries and in the shear layer (Fig. 7.14). Mesh $A2_{RMS}$ is refined downstream of the step expansion, along the centerline of the flow while it is coarsened everywhere else (Fig. 7.14). Refinement/coarsening zones correspond to the locations where resolved turbulence is higher/lower respectively (see Fig. 7.7-7.9). Meshes $A2_{MIX}$ and $A1_{MIX}$ are a compromise solution between $A2_{GRAD}$ and $A2_{RMS}$. Meshes $A2_{MIX}$ and $A1_{MIX}$

are refined both in the shear layer and along the centerline of the flow (Fig. 7.14). Note that $A2_{MIX}$ differs from $A1_{MIX}$ because of the different solution used to generate the metric field (H2 vs. H1). Obviously, since the number of nodes is kept constant, a mesh refinement somewhere implies a coarsening somewhere else (as shown by comparing Fig. 7.3 and Fig. 7.14).

Boundary nodes are not modified by adaptation in order to avoid deteriorating the ability of the mesh to match the CAD geometry. Note that this choice of not modifying the boundary nodes on the CAD surface is a disadvantage in certain cases, for example if the initial mesh is coarse, this would limit the capacities of adaptation to improve its quality. At the same time, this is also an advantage because it allows to use the mesh generator only once and never have to come back to the CAD data in the subsequent re-meshing phases. However, if the initial mesh is sufficiently resolved at the walls, it is a reasonable method.

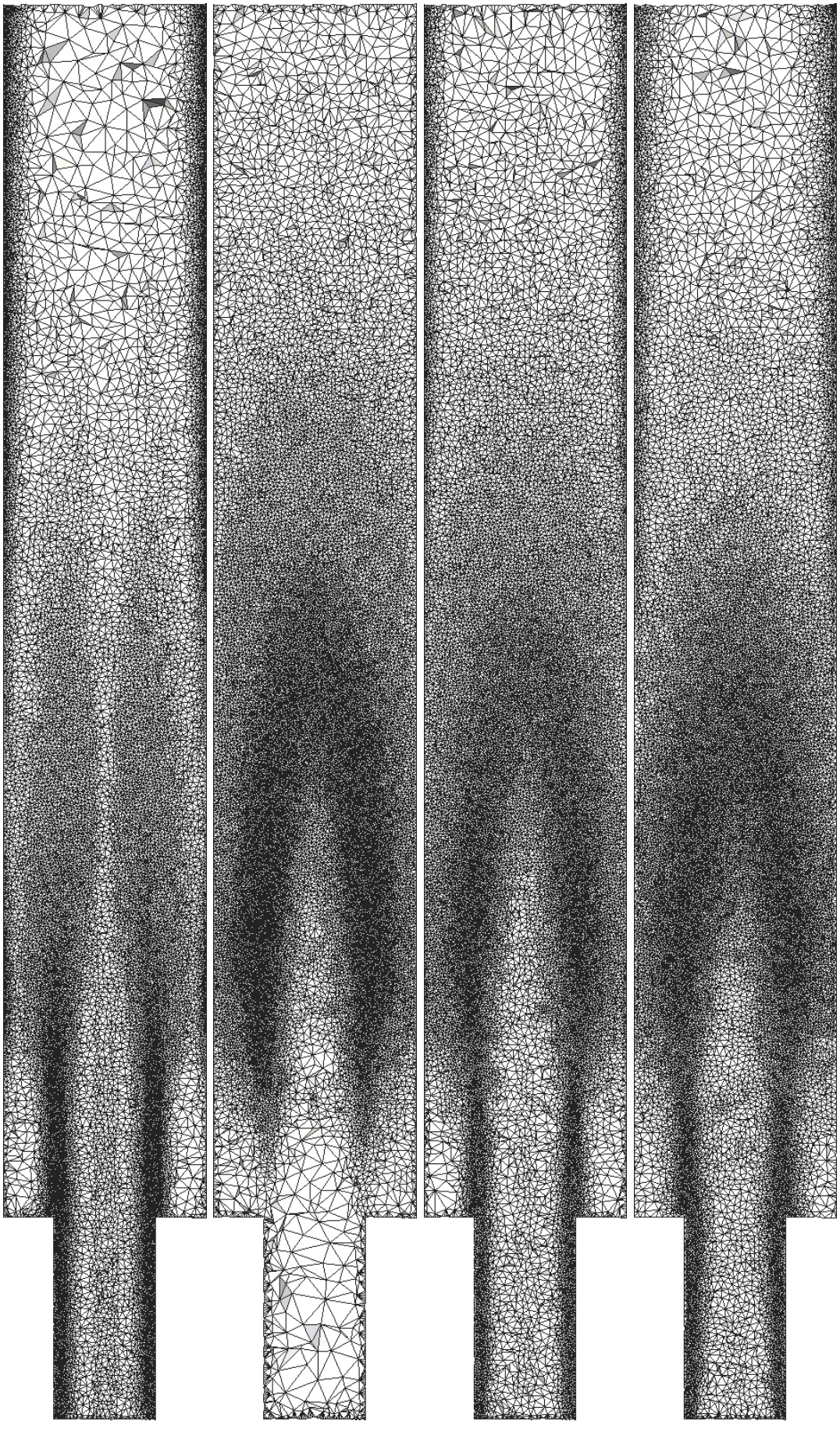

(a) $A2_{GRAD}$ (b) $A2_{RMS}$ (c) $A2_{MIX}$ (d) $A1_{MIX}$

Figure 7.14: Meshes of table 7.4

Flow fields of LES obtained using the meshes of table 7.4 are shown in Fig. 7.15. LES $A2_{RMS}$ is characterized by a very short jet penetration and by a high turbulence intensity a few diameters downstream of the jet expansion. On the other hand, LES $A2_{GRAD}$, $A2_{MIX}$ and $A1_{MIX}$ show a higher jet penetration and lower turbulence levels. The flows of LES $A2_{MIX}$ and $A1_{MIX}$ are barely distinguishable in Fig. 7.15.

Not all sensors improve LES prediction and only the "mixed" sensors ($A1_{MIX}$ and

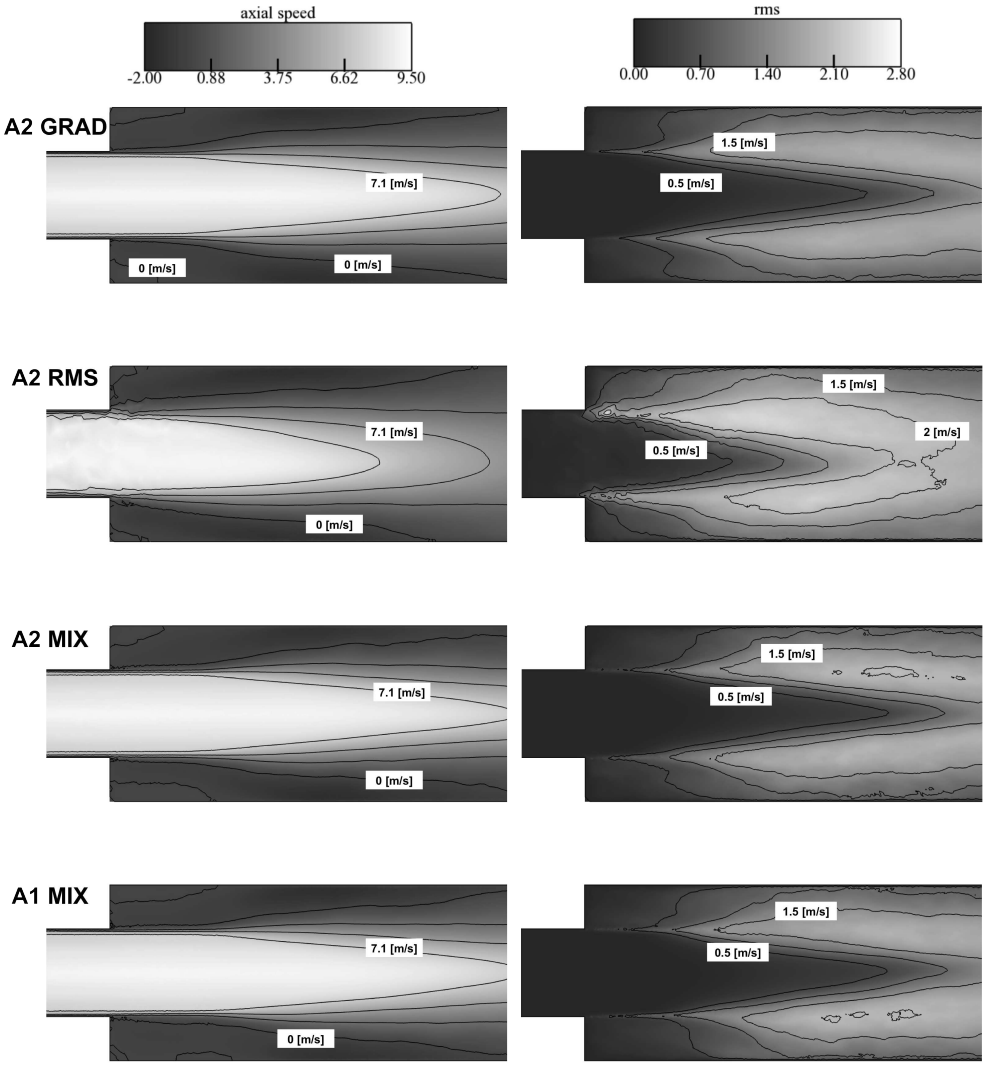

Figure 7.15: Meshes of table 7.4

$A2_{MIX}$) show a good comparison with experimental data, a prediction similar to LES H3 but with an efficiency which is 50% higher. Sensors $A2_{GRAD}$ and $A2_{RMS}$ alone are not able to improve results. $A2_{GRAD}$ is too coarse downstream where the turbulent structures generated in the shear layer reach the centerline of the flow: a too coarse mesh at this location causes an underestimation of the jet top speed because of an excessive dissipation due to modeling ($\nu_t \propto \Delta^{\frac{4}{3}}$). $A2_{RMS}$ is too coarse before the expansion (Fig. 7.14), causing

the LES prediction to deteriorate rapidly. Note that the low resolution upstream of the expansion favors the growth of the shear layer instability (see Fig. 7.9) so that LES $A2_{RMS}$ compares better with experimental data at plane 4 for both mean and turbulence intensity (a phenomenon already experienced in section 7.2.1 for LES H1). As evident from Fig. 7.14, meshes $A1_{MIX}$ and $A2_{MIX}$ slightly differ, but they give similar results (Fig. 7.16-7.17). Such a phenomenon can be explained simply by the fact that none of the two meshes is optimal but both are close to it.

7.3.1 Pressure drop and LES quality

Improving the prediction of pressure losses in LES remains a significant issue. This section discusses the effects of mesh adaptation on pressure losses predictions.
Table 7.5 shows the characteristics of the flow field of the LES obtained with the adapted meshes. The comparison of table 7.5 and table 7.3 shows that in none of the adapted meshes neither the volume-time average value of the turbulent viscosity neither its maximum value diminish (see also Fig. 7.18(a)) with respect to LES of section 7.2.1. However, pressure drop[4] does not diminuish significantly in all LES compared to the homogeneous case. Pressure drop remains almost constant even though the zone where the adapted meshes are finer corresponds to regions where the mean SGS dissipation[5], $\epsilon =< \tau_{ij} S_{ij} >$, is higher (Fig. 7.19(a)).
The mean value of y^+ slightly improves in all LES, but an increase of the wall resolution seems to have little influence on pressure drop for this flow (as shown in table 7.3, LES H4 predicts a pressure drop 3.5% lower than H1 despite a 30% reduction of the mean y^+ in the domain).

mesh/LES name	Total pressure drop	y^+_{mean}	$\frac{\int_V <\frac{\nu_t}{\nu}> dV}{\int_V dV}$	$< max(\frac{\nu_t}{\nu}) >$	Pope criterion Eq.(4.1)
H2	39.6 [Pa]	8.1	3.0	87.1	0.63
$A2_{GRAD}$	39.1[Pa]	6.9	6.0	133	0.56
$A2_{RMS}$	38.5[Pa]	10.6	3.7	110	0.59
$A2_{MIX}$	39.1[Pa]	7.2	4.3	89	0.57
$A1_{MIX}$	38.9[Pa]	6.9	4.2	101	0.58
H4	38.8 [Pa]	4.4	0.82	33.3	0.79

Table 7.5: Total pressure ($P_{TOT} = P + \frac{1}{2} u_{ii}^2$) drop, surface averaged y_+, time-volume averaged turbulent viscosity (normalized by laminar viscosity), time averaged of the max turbulent viscosity (normalized by laminar viscosity), time-volume averaged Pope criterion.

The volume averaged Pope criterion of all adapted LES of table 7.5 gets worse compared to the homogeneous meshes. For instance LES $A2_{MIX}$ is able to give a comparison against experimental data as good as LES H3 but its Pope criterion is 13% lower. The low values of the Pope criterion (compare Figs. 7.13-7.19(b)) are consistent with the high values of turbulent viscosity in the domain.

[4]Note that $\Delta P/P$, as usually pressure drop is presented, is in the order of 0.04% ($\Delta P/P \approx 40/101300 = 4 \times 10^{-4}$), therefore it is preferred to present results in terms of ΔP simply.

[5]Note that ϵ is evaluated in real time and then averaged.

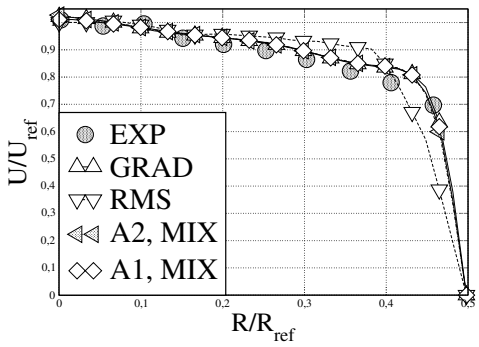

(a) Mean axial velocity profile at plane 2

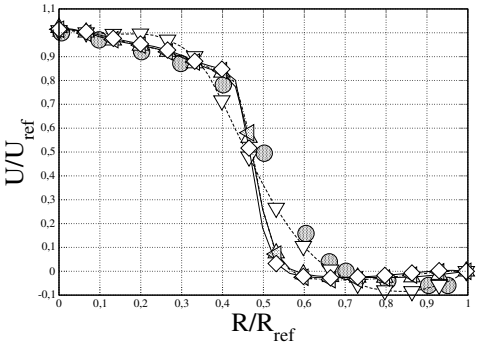

(b) Mean axial velocity profile at plane 4

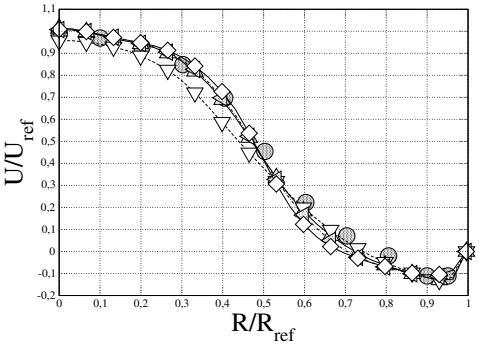

(c) Mean axial velocity profile at plane 5

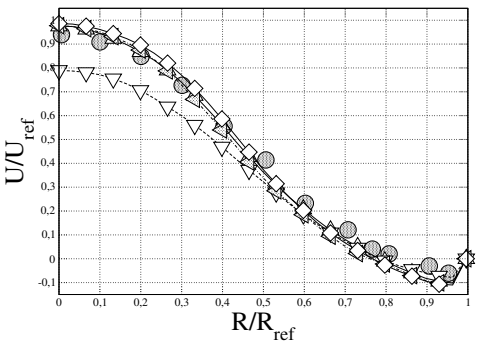

(d) Mean axial velocity profile at plane 6

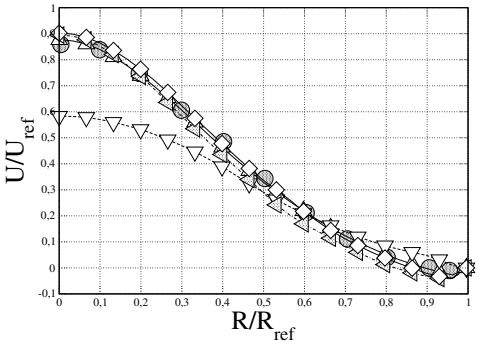

(e) Mean axial velocity profile at plane 7

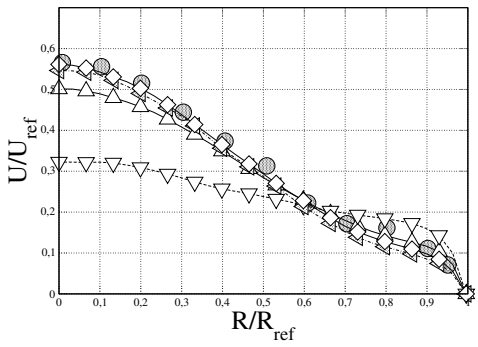

(f) Mean axial velocity profile at plane 8

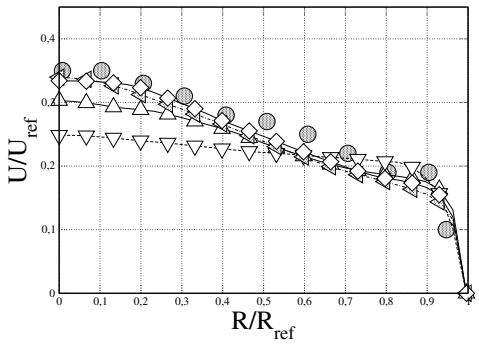

(g) Mean axial velocity profile at plane 9

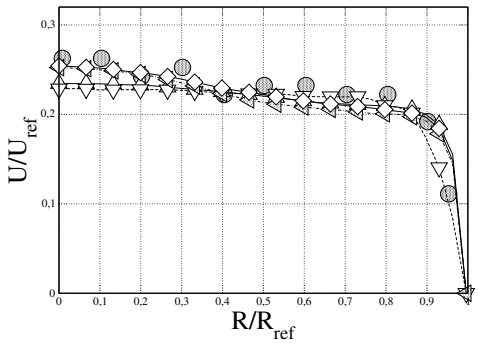

(h) Mean axial velocity profile at plane 10

Figure 7.16: Mean axial velocity profiles at the measurement planes of Fig. 7.2 for simulations of table 7.4.

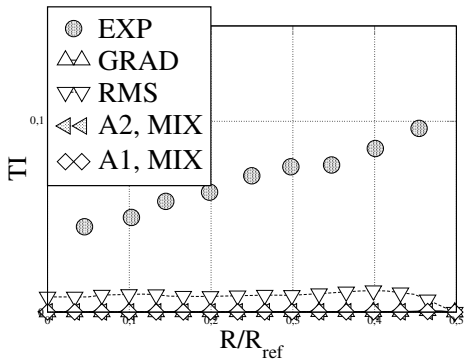

(a) TI axial velocity at plane 2

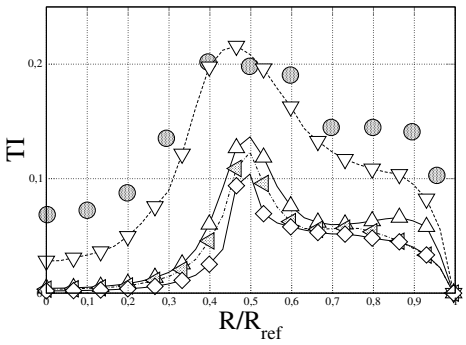

(b) TI axial velocity profile at plane 4

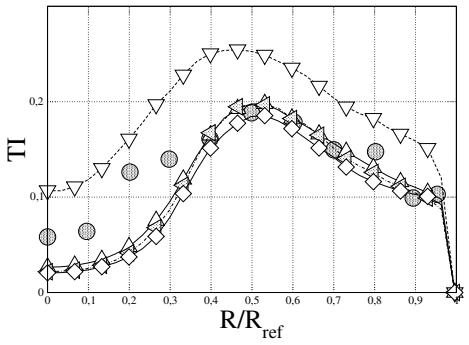

(c) TI axial velocity profile at plane 5

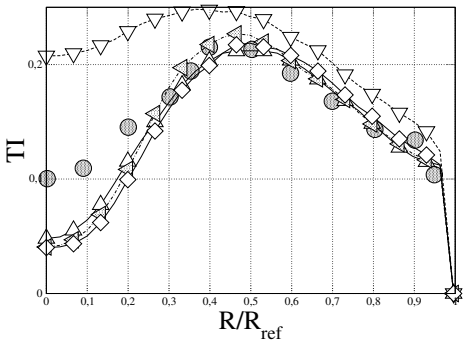

(d) TI axial velocity profile at plane 6

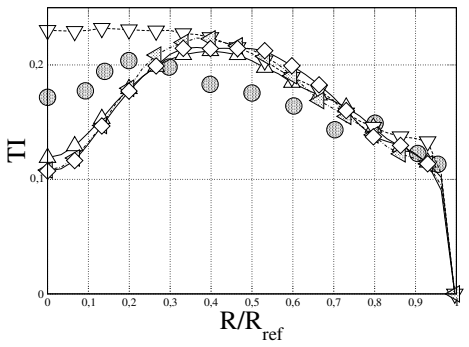

(e) TI axial velocity profile at plane 7

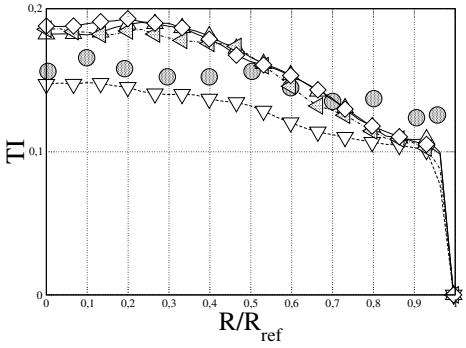

(f) TI axial velocity profile at plane 8

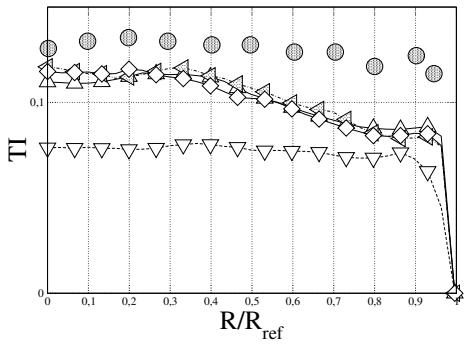

(g) TI axial velocity profile at plane 9

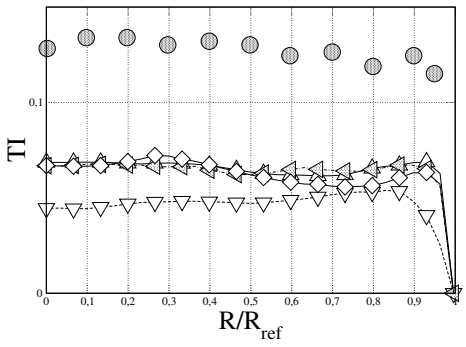

(h) TI axial velocity profile at plane 10

Figure 7.17: TI axial velocity ($TI = \frac{u_{RMS}}{u_{ref}} = \frac{u_{RMS}}{8.92[m/s]}$) at the measurement planes of Fig. 7.2 for simulations of table 7.4.

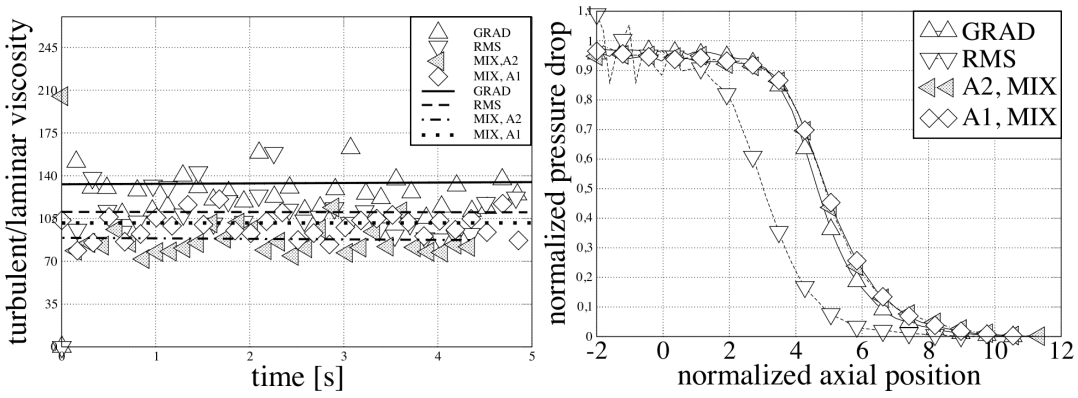

(a) (b)

Figure 7.18: (a) Time evolution of the maximum ratio of laminar over turbulent viscosity (lines are regression curves). (b) Total pressure drop against streamwise position for LES of table 7.4.

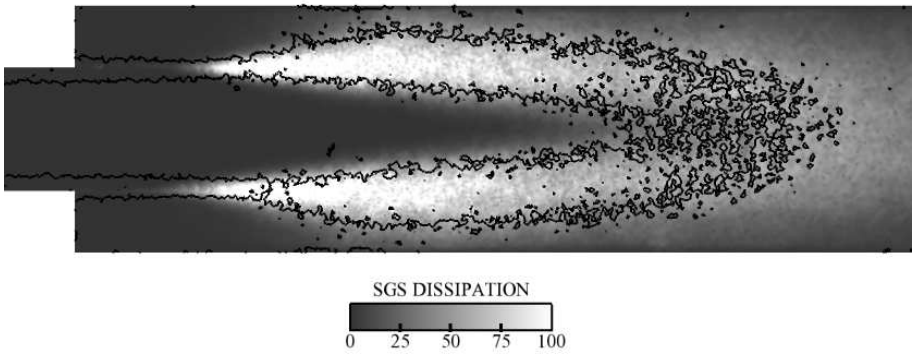

(a) SGS dissipation for LES $A2_{MIX}$

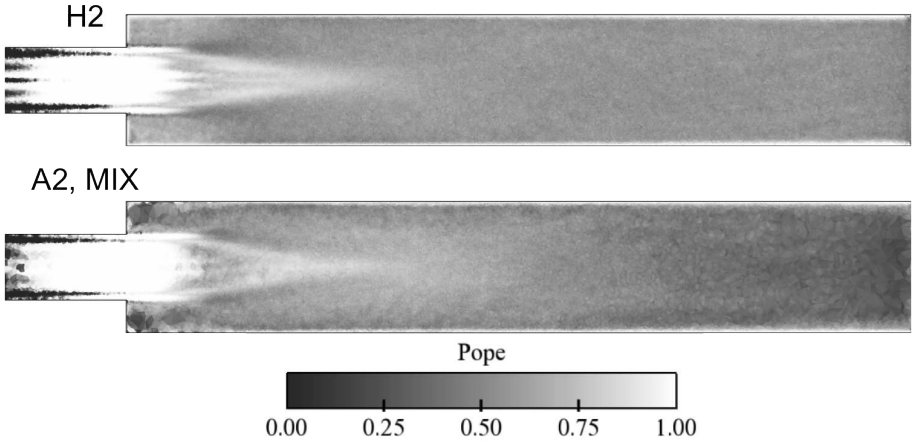

(b) Pope criterion of LES $A2_{MIX}$

Figure 7.19: Flow properties of LES $A2_{MIX}$ of table 7.4.

7.3.2 Why adaptation works

The comparison of Figs. 7.8-7.16 reveals that solutions on meshes adapted using the "MIX" sensor show a better match with experimental data than results obtained on an homogeneous mesh such as LES H2 (results are directly compared in Fig. 7.20). This improvement is obtained despite the fact that none of the common estimates used to evaluate LES quality improves after adaptation (such as the Pope criterion [89][6] or the ratio of turbulent over laminar viscosity, compare tables 7.3-7.5).

This phenomenon can be explained as follows. Mesh $A2_{MIX}$ (as well as $A1_{MIX}$ which

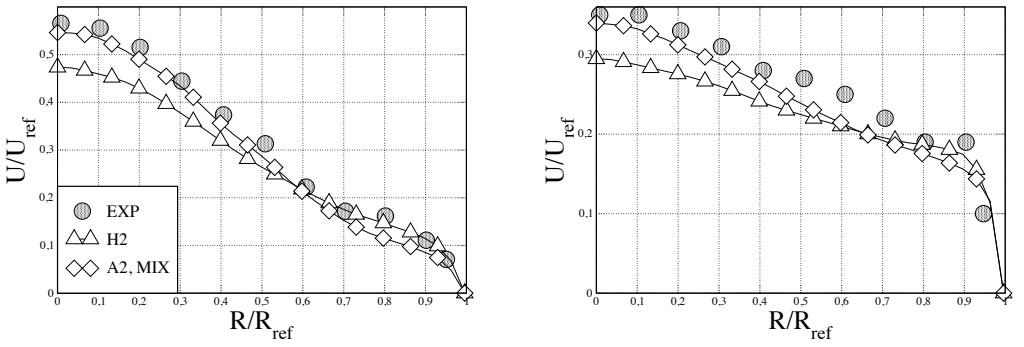

(a) Mean axial velocity profile at plane 8

(b) Mean axial velocity profile at plane 9

Figure 7.20: Comparison of LES H2 of table 7.2 and $A2_{MIX}$ of table 7.2. Adaptation ($A2_{MIX}$) improves results keeping constant the simulation efficiency.

gives similar results) are refined in the shear layer and, downstream, along the centerline of the flow (Fig. 7.14). At the same locations turbulent activity is more intense (Fig. 7.15-7.17). The zones where the grid is finer overlap with the zones where most of the eddies are located (Fig. 7.21). Most of the mesh resolution of meshes $A2_{MIX}$ and $A1_{MIX}$ is therefore targeted to resolve turbulence. Fig. 7.22 shows how different the resolved turbulence fields of LES $A2_{MIX}$ and $A1_{MIX}$ are with respect to H2. Fig. 7.22 shows a volume averaged Probability Density Function (PDF) of the Q criterion for some of the LES analyzed in this chapter. This PDF is obtained as follows. The interval $[0, Q_{MAX}], Q_{MAX} = 3 \times 10^6$ is divided in 100 sub-intervals $Q(1), Q(2), ..., Q(100)$. For each sub-interval "j" the number of nodes having a $Q \in [Q(j), Q(j+1)[$ is evaluated and weighted by the nodal volume. The weighting factor is motivated by the fact that homogeneous and non-homogeneous meshes are compared. Formally:

$$PDF_j(\%) = \sum_{i|Q(i)\in[Q(j),Q(j+1)[} \left(\frac{V_i}{V_{tot}}\right) \times 100, \tag{7.8}$$

where $PDF_j(\%)$ is the PDF of Q to be in the interval $[Q(j), Q(j+1)[$, V_i is the volume at the node "i" while,

$$V_{TOT} = \sum_{i|Q(i)\in[0,Q_{MAX}[} V_i, \tag{7.9}$$

[6]Note that the Pope criterion improves in the refined regions.

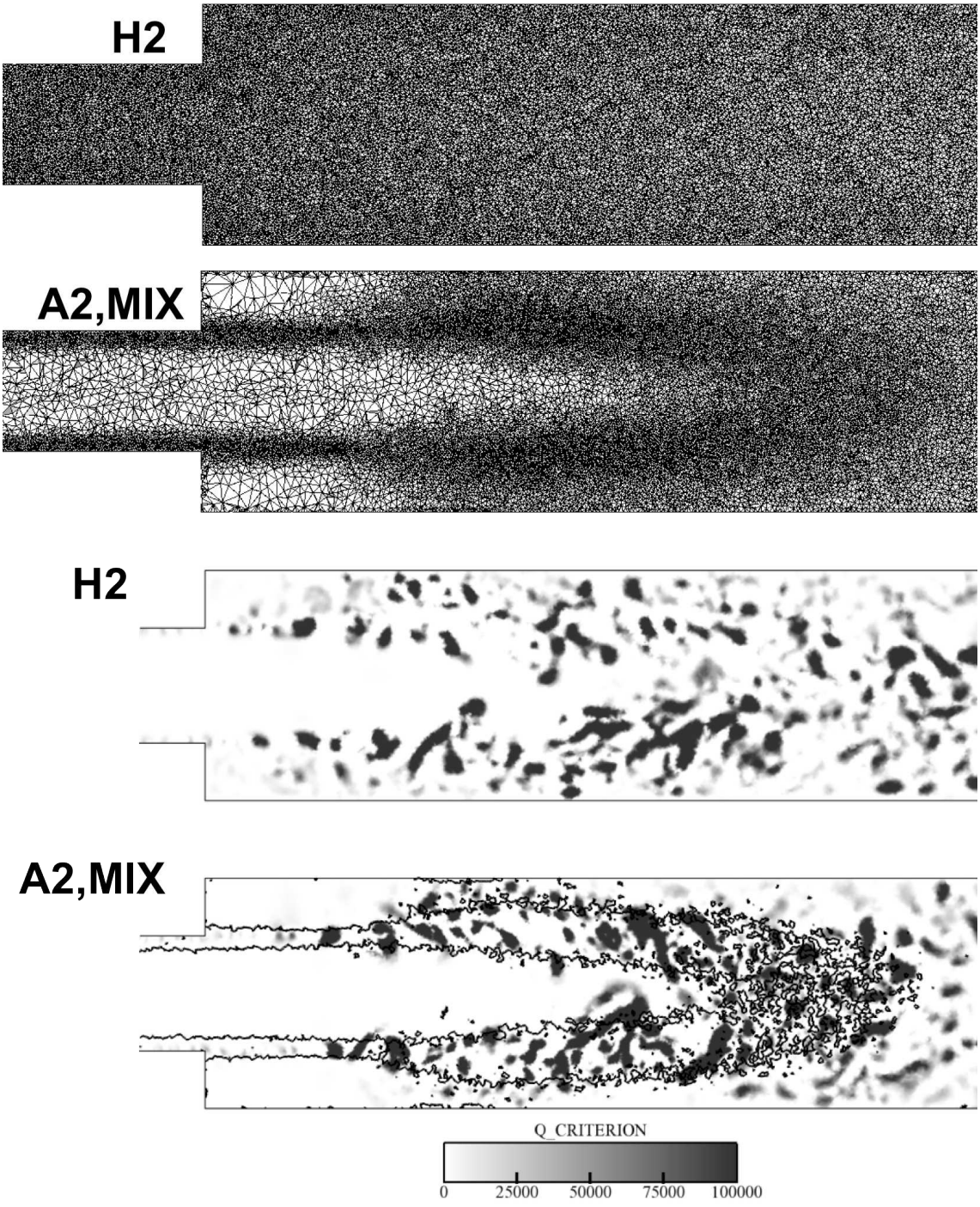

Figure 7.21: Mesh H2 and A2 and Q criterion (Eq.(7.1)) of the correspondent LES. In the bottom figure, the line represents the isovolume ($V = 0.4[mm^3] \approx 0.7^3[mm^3]$) and it envelops the zone where the grid is finer.

is the volume of of all the nodes with a Q criterion in the range $[0, Q_{MAX}]$ (the normalization condition). $PDF_j(\%)$ can be transformed easily in the portion of the whole domain volume occupied by eddies with an "intensity" $Q = (Q(j) + Q(j+1))/2$ by substituting

V_{TOT} with the total volume of the domain in Eq.(7.8).
As evident from Fig. 7.22 the PDF (Eq.(7.8)) of LES A2$_{MIX}$ and A1$_{MIX}$ is the same of LES H3: turbulence is resolved similarly on these meshes and better than on meshes H2 or H1 and this is the reason why results improve after adaptation. This flow is dominated by the dynamics of the turbulent structures generated in the shear layer, convected downstream by the mean flow and diffused by their own chaotic behavior. Mesh resolution is increased (for meshes A2$_{MIX}$ and A1$_{MIX}$) exactly along the primary path of main vortical activity, reducing errors due to modeling and to numerics.

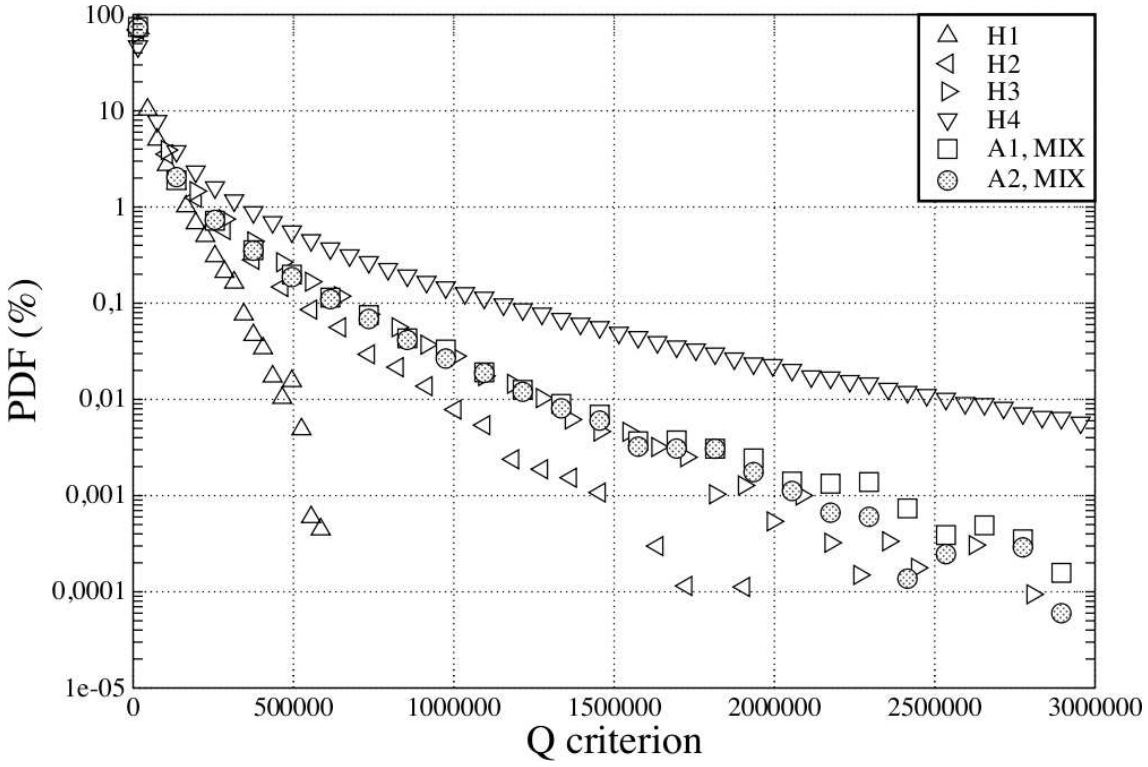

Figure 7.22: $PDF(\%)$ (Eq.(7.8)) of the Q criterion (Eq.(7.1)) for LES H1,H2,H3,H4 and A1$_{MIX}$ and A2$_{MIX}$.

Chapter 8

Test case B: the Dellenback experiment, swirled case

This chapter deals with the second adaptation test case. While in chapter 7 mesh adaptation was tested on the LES of the "axial" case of the Delleback experiment [17](a confined jet at high Reynolds number), here it is tested on the "swirled" case of the same experiment. As already mentioned in chapter 7 and as explained in the first part of this thesis (see Chapter 2), the introduction of a swirl velocity component strongly modifies the flow topology and the flow in the "axial" and "swirled" cases have little in common. The introduction of a swirl velocity component triggers a set of flow instabilities, such as the vortex breakdown or the PVC (described in detail in section 2.2.2) which are not present in the "axial" case of Chapter 7. The swirled case here tested corresponds to the condition of $Re = 30000$ and $S = 0.6$.

8.1 Numerical settings

The LES solver used here is YALES2. Boundary conditions used are those of chapter 7. Three B.C.s are used: an inlet ($2D_1$ upstream of the step expansion), an outlet at the end of the domain, and solid, adherent and adiabatic walls everywhere else.
Axial and tangential experimental velocity profiles are imposed at the inlet in a different manner. Both velocity profiles reproduce the experimental (normalized) curve at the first measurement plane multiplied by a characteristic speed[1]. The characteristic speed differs for the axial and tangential velocities. For the axial speed, it is $U^{ax}_{ref} = 10[m/s]$ which corresponds to a Reynolds number[2] of 30000. For the tangential speed, the characteristic velocity is $U^{tan}_{ref} = 8.2[m/s] \neq U^{ax}_{ref}$. This choice is motivated by the fact that, by choosing the same speed to re-dimentionalize the axial and the tangential velocity profiles (i.e. $U^{ax}_{ref} = U^{tan}_{ref}$) the swirl number (Eq.(2.2)) was off by 16% with respect to the experimental condition chosen[3] ($S = 0.7$ vs. $S = 0.6$). As in the axial case of chapter 7, no turbulence is

[1]The experimental curve is normalized by the jet top speed, i.e. profiles of U/U_{ref} are shown in Dellenback et al. [17].

[2]In Dellenback et al.[17] the Reynolds number is evaluated using "the average velocity in the upstream tube".

[3]This discrepancy is present also in the experimental data: by integrating numerically the experimental velocity profile the swirl number results 16% higher than the expected value of $S = 0.6$. This phenomenon

injected at the inlet. The effects of such an approximation are negligible since turbulence develops naturally because of the injected vorticity (the swirl velocity component) and because of the large coherent structures (such as the PVC) which trigger turbulence. Table 8.1 summarizes the B.C.s used.

BC NAME	IMPOSED PROPERTY	TARGET VALUE
inlet	EXP velocity profile	$U_{ref}^{ax} = 10[m/s]$, $U_{ref}^{tan} = 8.2[m/s]$
outlet	pressure	101300 $[Pa]$
walls	adherence, impermeability, adiabaticity	

Table 8.1: Imposed values for boundary conditions of the geometry of Fig. 8.2.

The geometry of the swirled case differs from the geometry of the axial case. An expansion is mounted at the end of the second, downstream, cylinder. This expansion was also present in the experimental settings (Fig. 8.1, the expansion is indicated with the letter K).

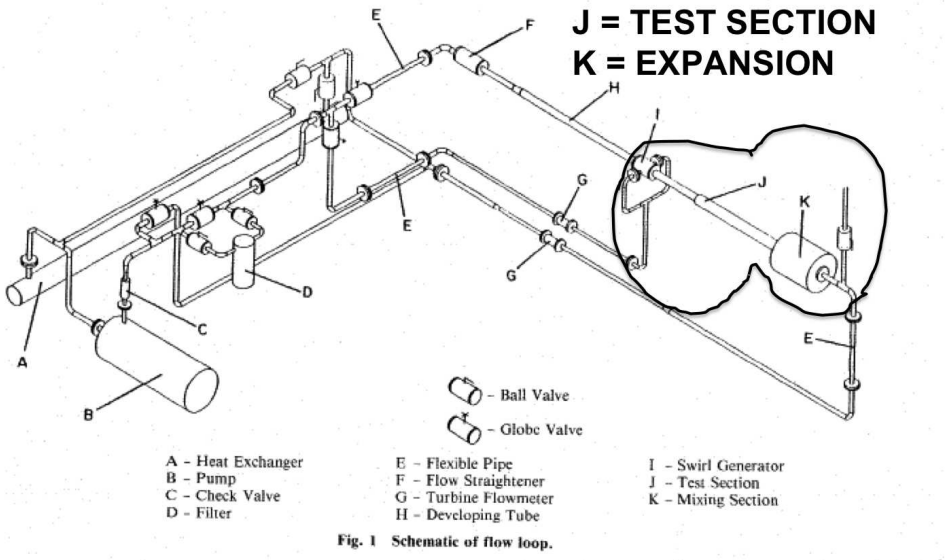

Figure 8.1: Arranged from Dellenback et al.[17]. Experimental settings: the test section "J" is the domain simulated in the axial case of chapter 7 while J and K are simulated here (see Fig. 8.2). Note that the swirler ("I" in figure) is not included in the domain.

This additional geometry (expansion K in Fig. 8.1 and Fig. 8.2) is required to be included in the simulation domain the flow downstream of the test section which interacts with the central recirculation zone (CRZ). As evident from Fig. 8.2 the central recirculation zone extends throughout the pipe and downstream inside the expansion K. LES prediction without the expansion K (i.e. using the same geometry of chapter 7 shown in Fig. 7.1) were bad and showed a trend opposite to what usually experienced: increasing the mesh resolution results got worse. This phenomenon is due to the convective outlet boundary

is likely to be related to fact that the experimental velocity profiles where acquired by post-processing the electronic paper were they are reported. Such method/measure is evidently subject to errors.

condition[85] used which is not suited to feed recirculation zones. The outlet is therefore pushed downstream and the flow is free to develop entering in the expansion "K". The geometry used for the swirled case (and the measurements planes used for the comparison LES-EXP data) is shown in Fig. 8.2.

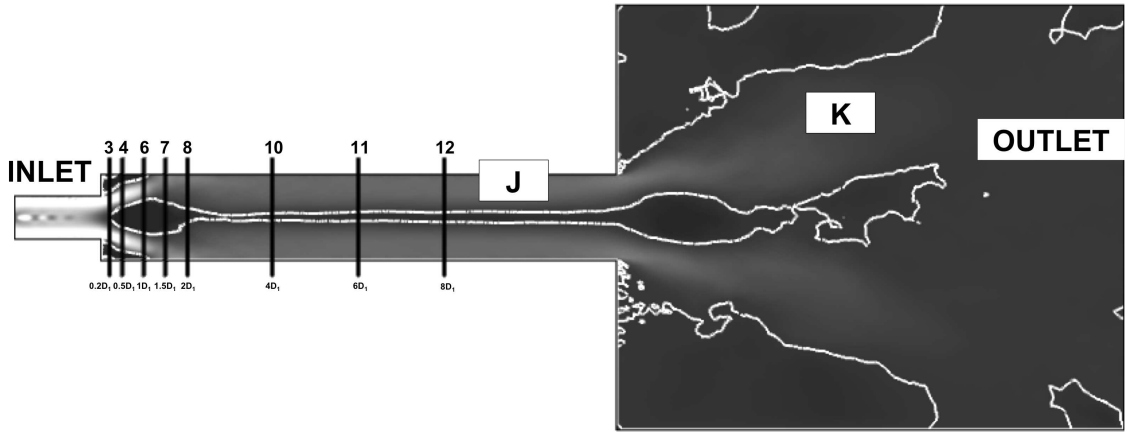

Figure 8.2: Measurement planes names (above) and axial position with respect to the first expansion for the swirled case of Dellenback[17]. The white line is zero mean axial velocity of LES H2, the picture is colored by the mean axial velocity to highlight the central recirculation zone. Measurements are taken at $x/D_1 = 0.2, 0.5, 1, 1.5, 2, 4, 6, 8$ (planes 3,4,5,6,7,8,10,11,12) downstream of the first expansion. J and K are the test section and the expansion of shown in Fig. 8.1, respectively.

The SGS model chosen for all LES of this chapter is $SIGMA$ [79] where the turbulent viscosity is proportional to the cube of the wall distance (see section 3.2.2). The SIGMA model is preferred to WALE since it does not generate turbulent viscosity in the case of a solid-body rotation. It is therefore more suited for this flow than WALE because experimental data shows that, the flow is in solid body rotation (along the centerline of the geometry) in most of the domain J. All simulations are initialized with a zero velocity flow.

8.2 Swirled case, homogeneous meshes

The swirled case corresponds to a confined jet at $Re = 30\ 000$ and $S = 0.6$. The set of basic LES and the characteristics of the meshes used are summarized in table 8.2. Results

mesh LES name	number of nodes	number of tetra	numerical efficiency Eq.(6.27)	Δ/η_K
H0	0.3M	1.5M	1	134
H1	0.6M	3.4M	0.513	106
H2	1.7M	10M	0.016	62

Table 8.2: Table of simulations. The numerical efficiency (Eq.(6.27)) is normalized by the efficiency of LES H0 while the average mesh size Δ is non-dimensionalized by the Kolmogorov length scale for a HIT at the same Reynolds number ($\eta_K = Re^{-\frac{3}{4}}\ D_1 = 2.24 \times 10^{-5}[m]$). The average mesh size (Δ) refers to the first two cylinders where measurements were taken (J in Fig. 8.1-8.2).

are compared with experimental data taken at 8 measurement positions (Fig. 8.2). Three different meshes are used for the basic LES (basic means without adaptation) ranging from mesh H0 to H2 (where "H" stands for homogeneous and the number for the refinement level). Names refer to meshes and simulations indifferently. As in chapter 7, results obtained with the homogeneous meshes are used as reference together with experimental data.
The flow field is highly unstable and perturbed by the presence of a Precessing Vortex Core (PVC). Fig. 8.3 shows the PVC (made evident by a low pressure iso-surface) and the instantaneous, velocity vectors. In swirled flows, the PVC is a small tornado that lies on the boundary of the reverse flow zone between the zero velocity and zero streamline [78].

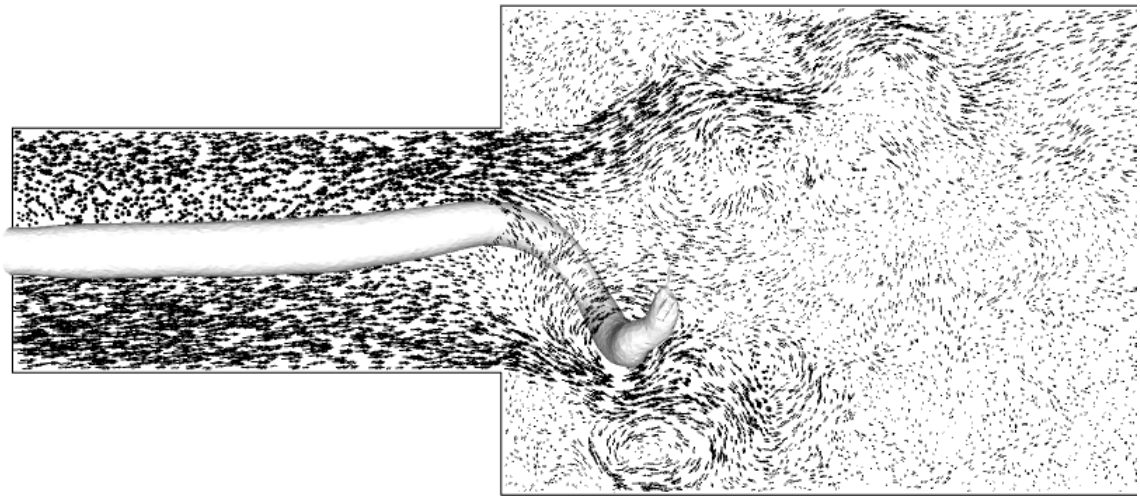

Figure 8.3: Snapshot of the instantaneous velocity field (vectors) of the Dellenback LES. The PVC is identified by pressure isosurfaces: the centrifugal force induced by the vortical motion balance the external pressure causing a local depression. Pressure isosurfaces are particularly suited to identify big vortices [58].

The flow field changes with homogeneous refinement. LES H0 and H1 show a very small CRZ (in Fig. 8.4 it is visualized by the zero axial velocity isoline) and a secondary recirculation zone inside the expansion K. On the contrary, the CRZ of LES H2 extends along the whole length of the pipe and merges with the secondary recirculation zone. However, Fig. 8.4 is misleading. The apparent continuity of the CRZ appears only in the mean field of LES H2, while looking at one snapshot (Fig. 8.5) is evident that the CRZ is somehow "intermittent" with the pockets of zero axial velocity (the black line along the centerline of the flow in Fig. 8.5) which are not connected (this has been verified using 3D isosurfaces of zero axial velocity).
Similarly, the mean tangential velocity field (Fig. 8.6) changes with homogeneous refinement, and LES H2 shows a higher tangential speed throughout the pipe.

The differences in the flow fields of LES of table 8.2 are made evident in Figs. 8.4-8.6. The velocity profiles in Figs. 8.7-8.8 show that predictions of LES H2 are better with respect to LES H0 or H1 in all planes and LES H2 gives a good comparison with experimental data. However, homogeneous refinement has a smaller effect in the swirled case than in the the axial case of Chapter 7 (compare with Fig. 7.8 which shows how homogeneous refinement can change LES results). Note that a variation of the swirl level introduced at the inlet could modify the velocity profiles significantly. However, the aim

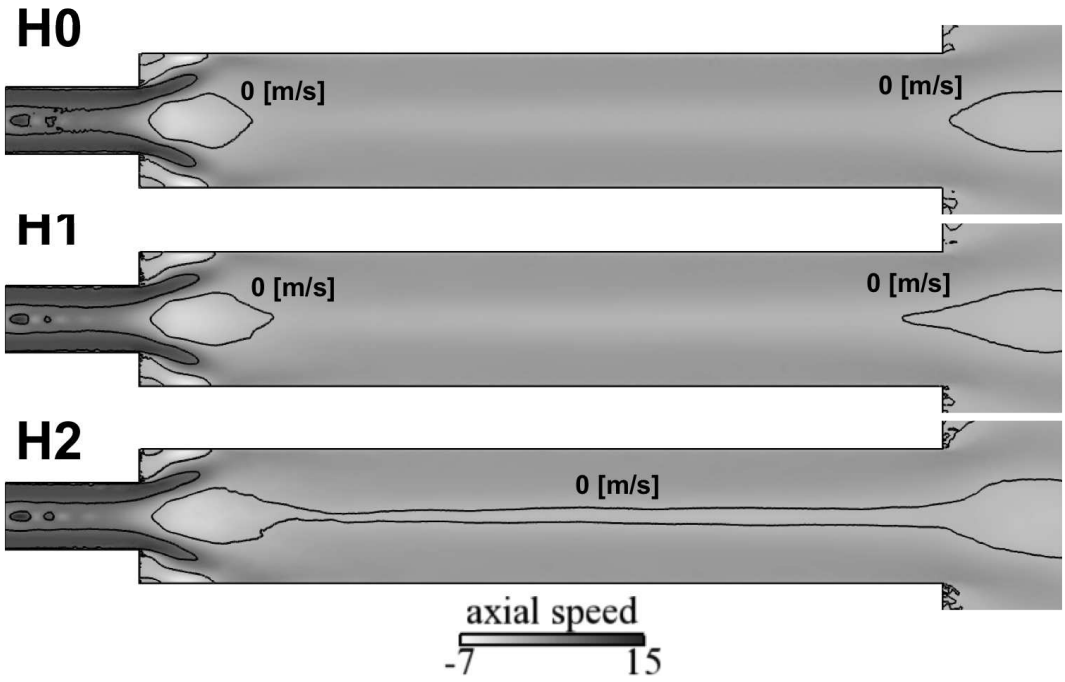

Figure 8.4: Mean axial velocity and axial velocity isolines for LES of table 8.2

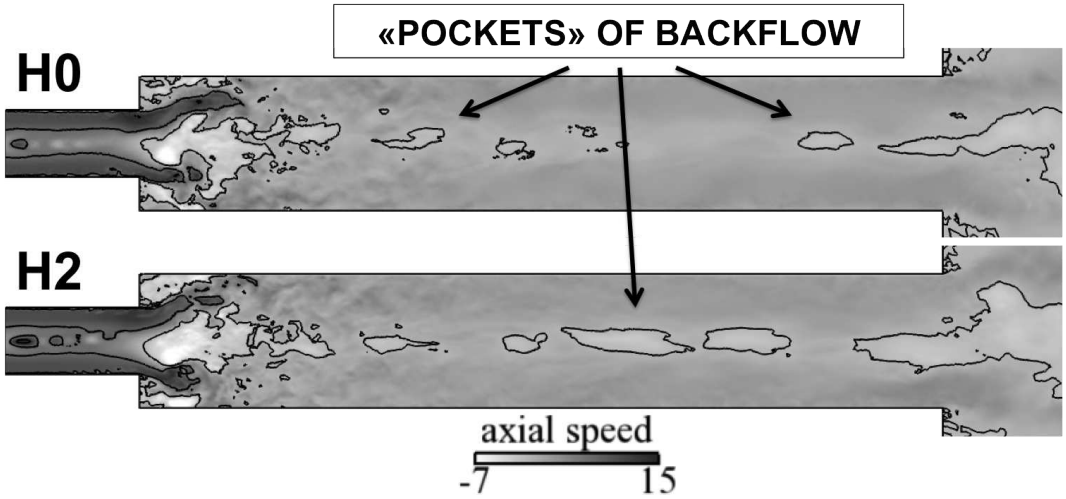

Figure 8.5: Snapshot of axial velocity and zero axial velocity isoline of LES H0 and H2 of table 8.2.

of these tests is not to reproduce experimental data by adjusting the swirl level, even though, as explained earlier, the amount of swirl in the flow is a source of uncertainty for this experiment.

The RMS fields of LES of table 8.2 appear very similar in Fig. 8.9, with a zone of higher RMS values after the first step expansion. These high RMS values are due to the PVC (Fig. 8.3). Similarly, the zone of higher axial velocity RMS along the centerline of the flow is linked to the "intermittency" of the "pockets" of backflow shown in Fig. 8.5. Only the zone downstream of the $1.4[m/s]$ isoline can be considered as "pure" turbulence.

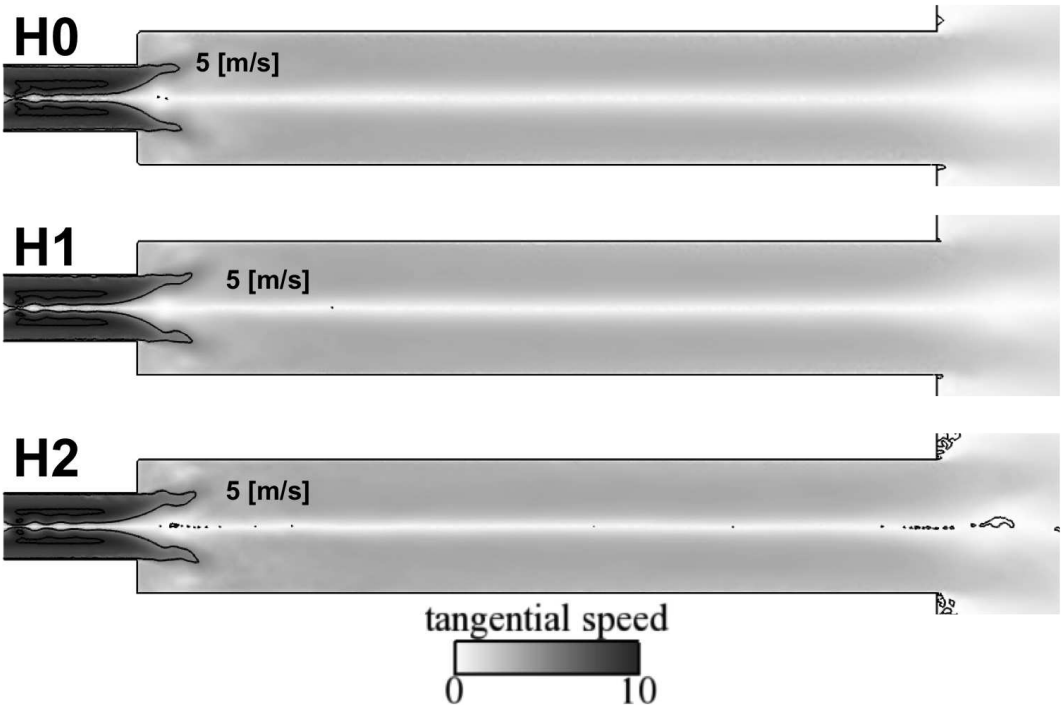

Figure 8.6: Mean tangential velocity and tangential velocity isolines for LES of table 8.2

Fig. 8.10 shows the RMS profiles at plane number 3 for LES of table 8.2: clearly not injecting turbulence at the inlet has a limited effect on the flow since all LES are able to reproduce the experimental trend. This phenomenon is linked to the fact that vorticity (i.e. tangential velocity) is injected in the domain and this helps turbulence to develop. All LES converge in terms of kinetic energy after a transient period of $\approx 0.6[s]$ (Fig. 8.11). After $\approx 0.6[s]$, kinetic energy then increases in time with a small drift because of the slow convergence of the flow in the downstream expansion whose time scale is significantly larger.

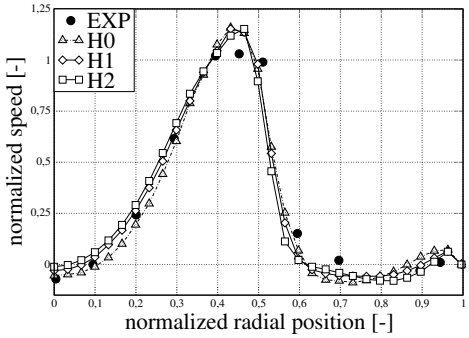

(a) Mean axial velocity profile at plane 3

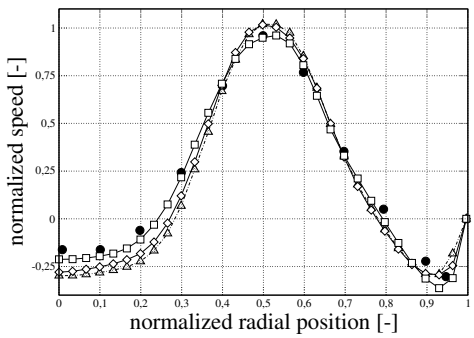

(b) Mean axial velocity profile at plane 4

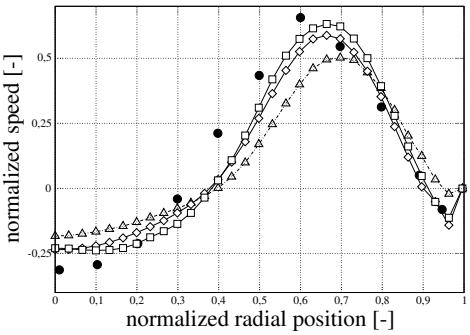

(c) Mean axial velocity profile at plane 6

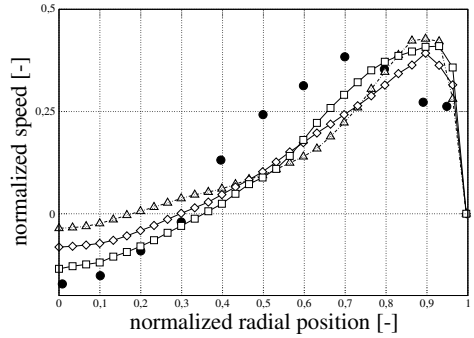

(d) Mean axial velocity profile at plane 7

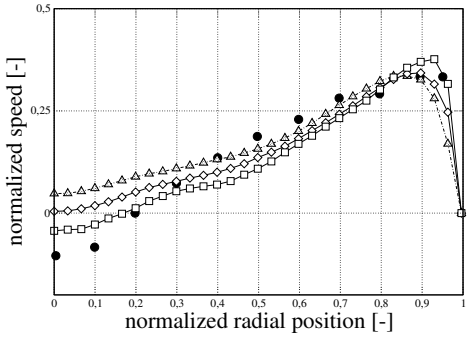

(e) Mean axial velocity profile at plane 8

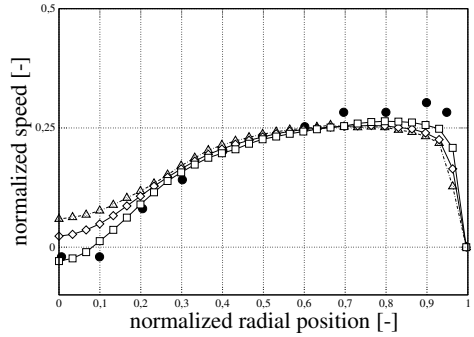

(f) Mean axial velocity profile at plane 10

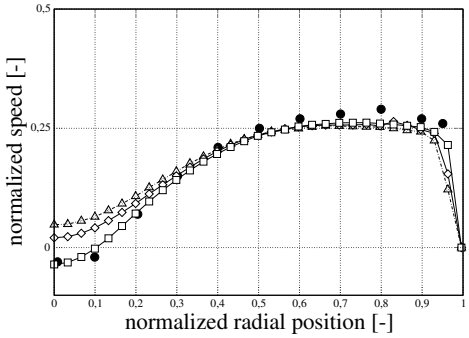

(g) Mean axial velocity profile at plane 11

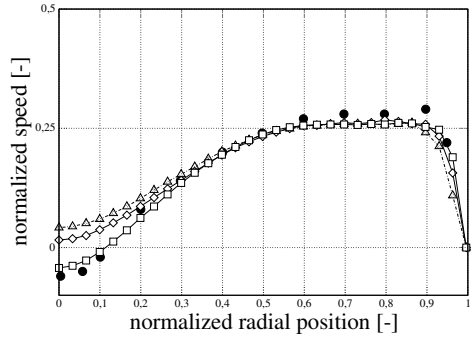

(h) Mean axial velocity profile at plane 12

Figure 8.7: Mean axial velocity profiles at the measurement planes of Fig. 8.2 for simulations of table 8.2.

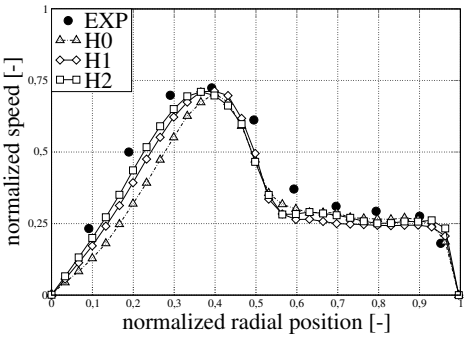

(a) Mean tangential velocity profile at plane 3

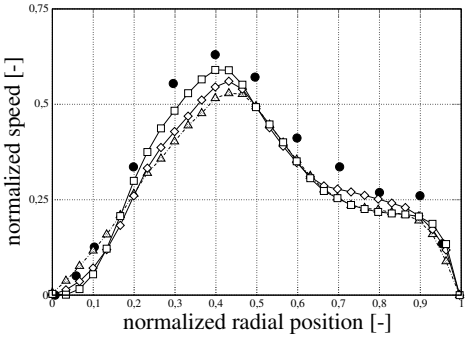

(b) Mean tangential velocity profile at plane 4

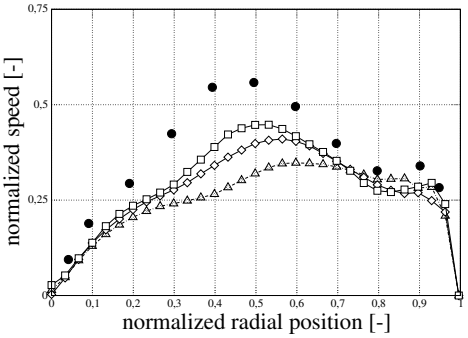

(c) Mean tangential velocity profile at plane 6

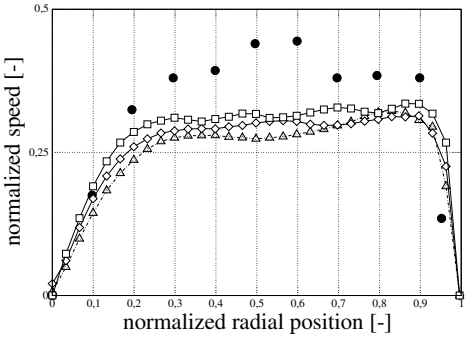

(d) Mean tangential velocity profile at plane 7

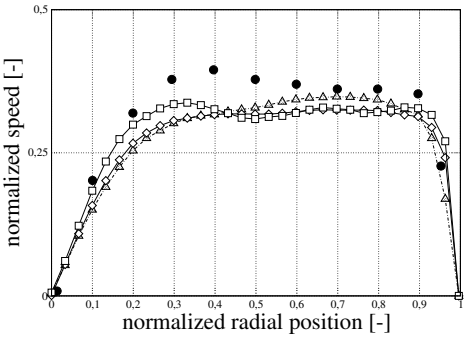

(e) Mean tangential velocity profile at plane 8

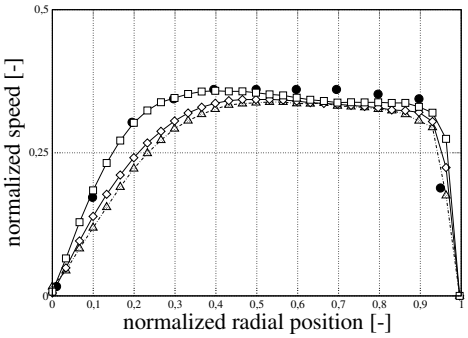

(f) Mean tangential velocity profile at plane 10

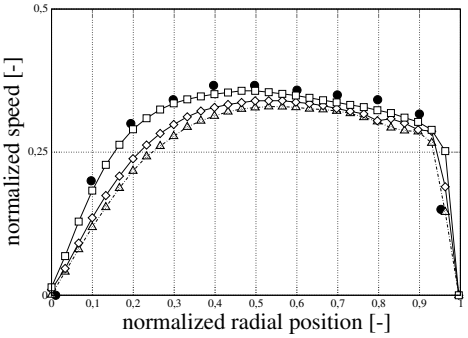

(g) Mean tangential velocity profile at plane 11

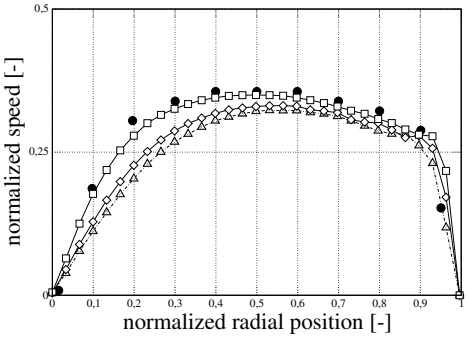

(h) Mean tangential velocity profile at plane 12

Figure 8.8: Mean tangential velocity profiles at measurement planes of Fig. 8.2 for simulations of table 8.2.

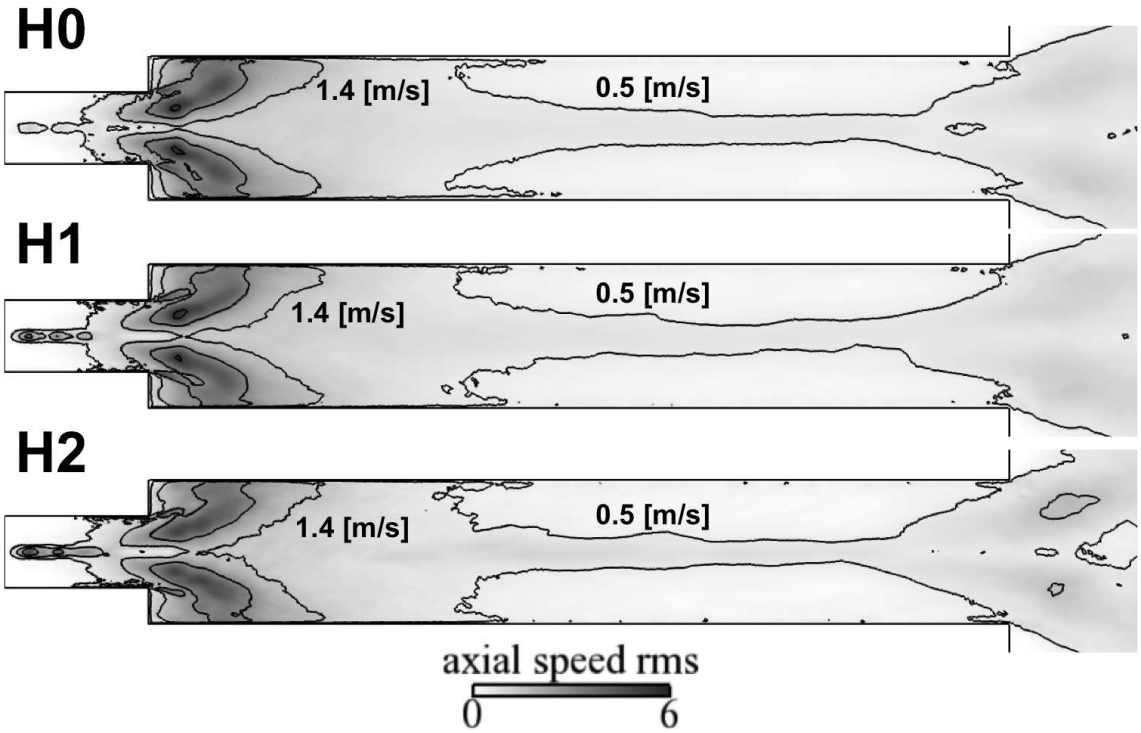

Figure 8.9: RMS of axial velocity for LES of table 8.2

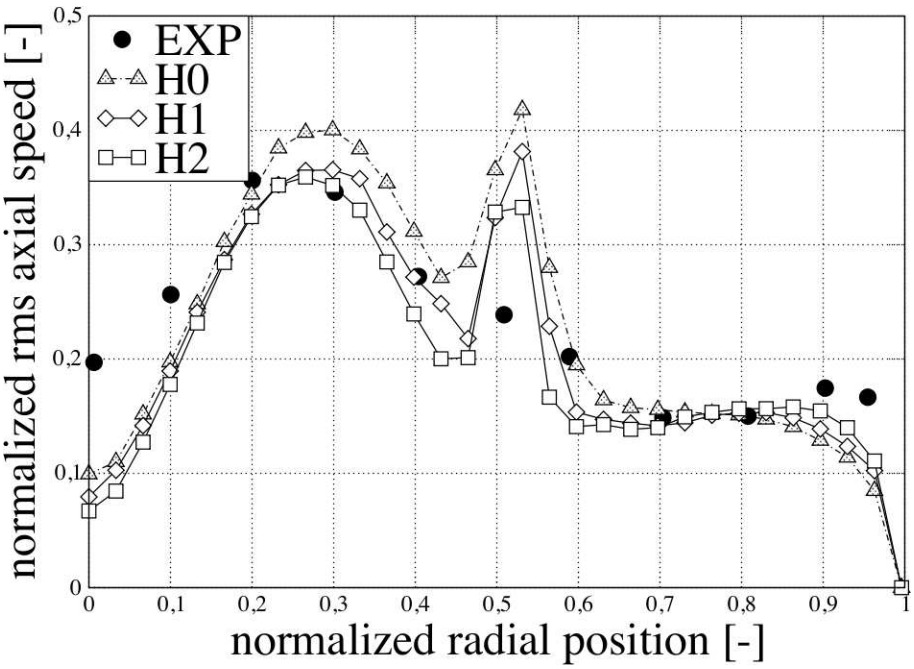

Figure 8.10: RMS axial velocity for LES of table 8.2 at plane 3 of Fig. 8.2.

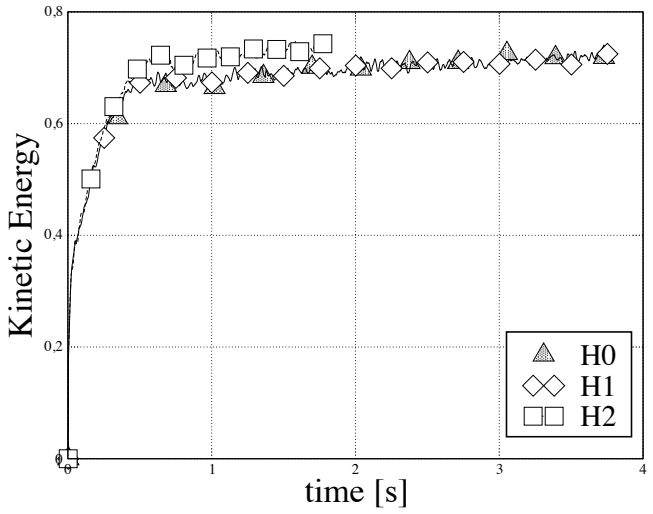

Figure 8.11: Time evolution of kinetic energy over the whole computational domain for LES of table 8.2.

8.3 Quality estimates for the homogeneous meshes

The quality of LES of table 8.2 is monitored via Pope's criterion (Eq. 4.1) and the amount of turbulent viscosity generated by the SGS model, both time and volume averaged, the mean value of the non-dimensional wall distance (y^+) for wall nodes, the cumulative PDF ($\int_a^\infty PDF(Q)dQ$) of the Q criterion (Eq. 7.1) as discussed in section 7.3.2. All these quantities are monitored in test section J (see Fig. 8.1-8.2) and summarized in table 8.3.

mesh/LES name	y^+_{mean}	$\frac{\int_V <\frac{\nu_t}{\nu}> dV}{\int_V dV}$	Pope criterion Eq.(4.1)	$Q_{cum} = \int_{10^5}^\infty PDF(Q)dQ$ (Fig. 8.14)
H0	22.4	5.6	0.60	13%
H1	16.8	3.7	0.65	16%
H2	15.4	2.0	0.72	21%

Table 8.3: Surface time-averaged y_+ and time-volume average of turbulent viscosity (normalized by laminar viscosity), time-volume average Pope criterion, cumulative probability of the Q criterion (as elucidated in section 7.3.2).

As for the axial case of chapter 7, turbulent viscosity[4] follows the theoretical curve of Eq.(7.7), see Fig. 8.12. Also, as expected, the mean value of y^+ diminishes as the mesh resolution is increased. Comparing table 7.3 with table 8.3 reveals that turbulent viscosity is significantly lower in the swirled case. This phenomenon can be related to the different SGS model used (WALE vs. SIGMA) and mainly to the fact that, in the swirled case, most of the energy is contained and transported by the largest organized flow structures which are almost inviscid (the tangential velocity profile does not change between plane 8 and 12, see Fig. 8.8).

[4]Only the volume averaged turbulent viscosity is monitored since the max value of such quantity was significantly high inside the expansion K, a zone that was not isotropically refined as the test section J.

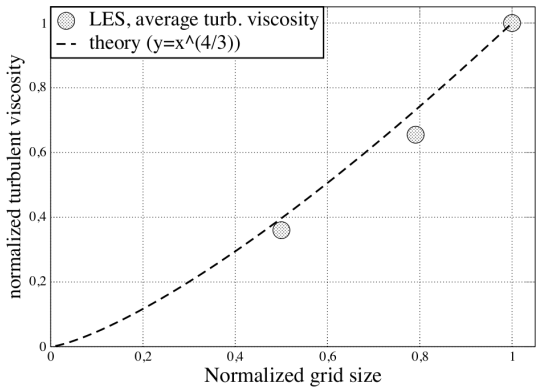

Figure 8.12: Normalized turbulent viscosity for LES of table 8.2 vs. theoretical curve (Eq.(7.7)).

Fig. 8.13 shows the $Q = 1 \times 10^6 [1/s^2]$ isosurface of the Q criterion for LES of table 8.2. The PVC in the upstream tube is distorted and destroyed soon downstream of the expansion giving birth to numerous smaller structures. The amount of small vortices increases with the mesh resolution (Fig. 8.13 and Fig. 8.14). These vortices are then convected downstream by the mean flow (Fig. 8.13 shows in transparence the Q criterion field). A measure of the different amount of small eddies is given in Fig. 8.14 which shows the PDF of the Q criterion (Eq.(7.8)) as discussed in section 7.3.2. Three informations can be extracted from Fig. 8.14. When the mesh resolution is increased:

- the amount of high frequency eddy cores augments since the cumulative probability,

$$Q_{cum} = \int_a^\infty PDF(Q) dQ, \tag{8.1}$$

  increases (see table 8.3), "a" $= 10^5 [1/s^2]$ in Eq.(8.1) is chosen arbitrarily. Note that Q_{cum} includes also the PVC;

- The highest frequency present in the flow increases.

- The slope of the PDF changes. This phenomenon is likely to be the effect of filtering on the spectrum of turbulent kinetic energy, see Pope [89], which affects the transfer of energy from the larger to the smaller scales (a similar trend can be observed in Fig. 7.22 also).

Finally, Pope's criterion (Eq. 4.1) shows the expected trend, increasing with mesh refinement (see table 8.3). Pope's criterion remains below the arbitrary value of 0.8 set by Pope [89] for all LES. The fields of Pope's criterion for LES of table 8.2 are shown in Fig. 8.15.

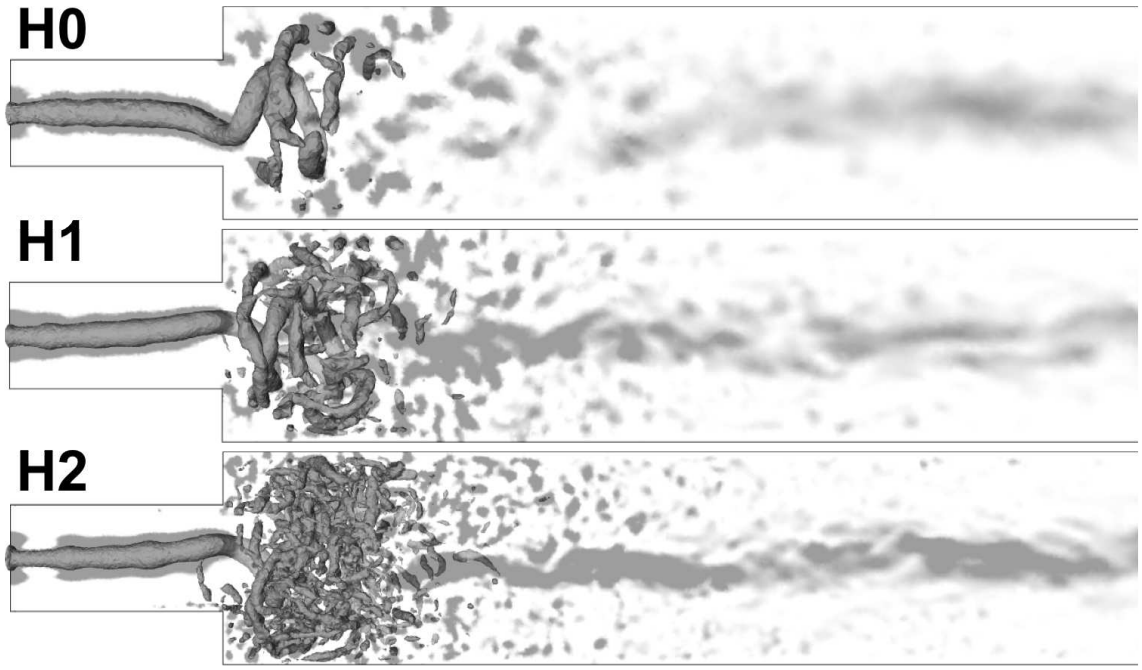

Figure 8.13: Snapshots of Q criterion for simulations of table 8.2. The field of the Q criterion (black dots are zones at $Q > 1 \times 10^6$) is made transparent to make visible the 3D structure of the PVC and of the smaller eddies

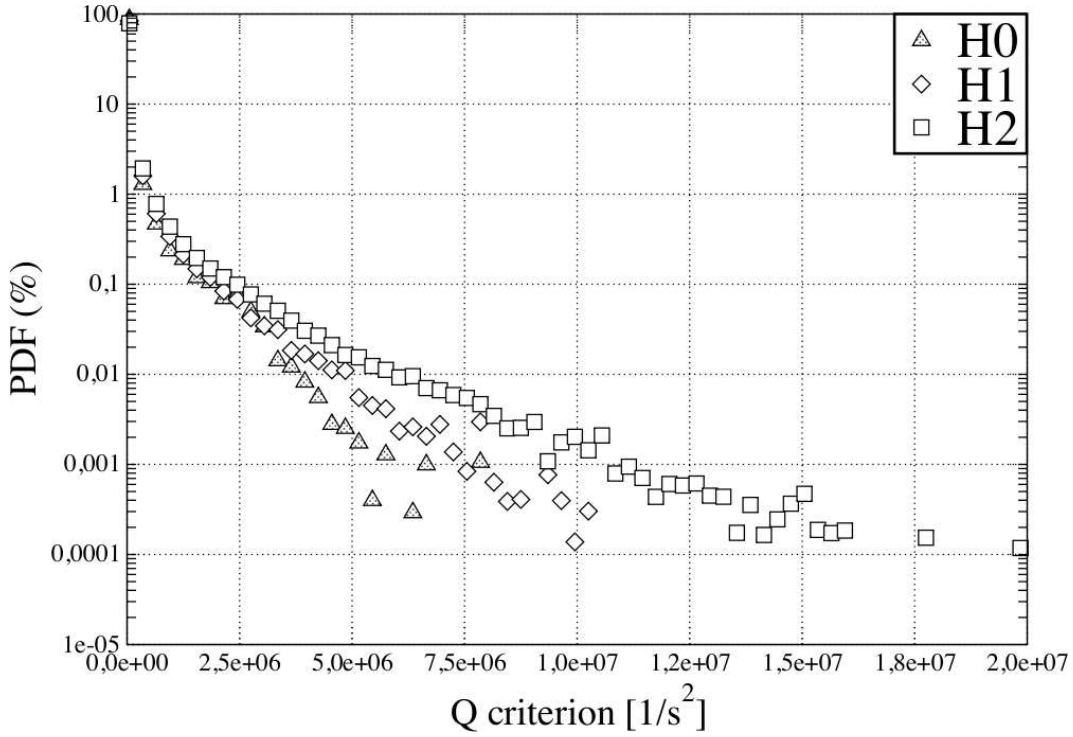

Figure 8.14: $PDF(\%)$ (Eq.(7.8)) of the Q criterion (Eq.(7.1)) for LES H1,H2,H3,H4 and $\mathrm{A1}_{MIX}$ and $\mathrm{A2}_{MIX}$.

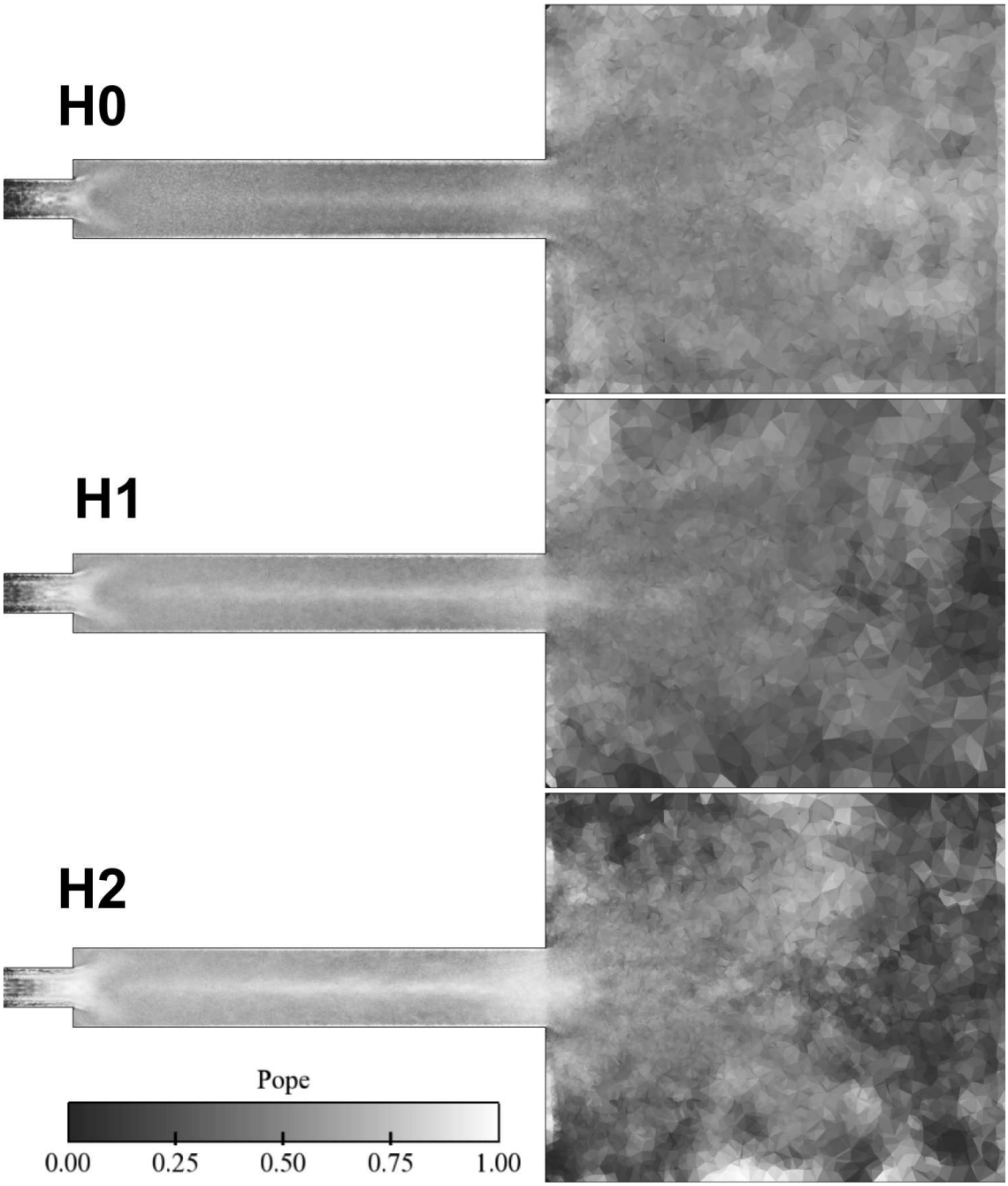

Figure 8.15: Pope criterion (Eq. 4.1) for simulations table 8.2.

8.4 Adapted meshes

Mesh adaptation is now tested using the two sensors which were able to improve LES results in chapter 7 ("GRAD" and "MIX"), plus a third sensor based on turbulent viscosity. The "GRAD" sensor is based on the mean velocity gradient tensor (see section 6.1.2). The MIX sensor (here named "MIX_{RMS}") is the intersection of the "GRAD" sensor and of a sensor based on a flow property Φ (see section 6.1.1) where $\Phi = RMS = (u_{ii}^2)^{\frac{1}{2}}$. Similarly, the third sensor (here named "MIX_{ν_T}") is obtained as the intersection of the "GRAD" sensor and a sensor based on a flow property Φ, where $\Phi = \nu_T$ (see section 6.1.1).
Meshes are adapted using the solution of LES H2 of table 8.2 and are named as the sensors used to generate them, i.e. "GRAD", MIX_{RMS} and MIX_{ν_T}. Meshes and LES are summarized in table 8.4.

mesh/LES name	number of nodes	number of tetra	numerical efficiency (normalized by H0)	Δ/η_K
GRAD	0.6M	3.1M	0.33	≈ 100
MIX_{RMS}	0.6M	3.3M	0.37	≈ 100
MIX_{ν_T}	0.6M	3.5M	0.45	≈ 100

Table 8.4: Table of simulations performed for mesh adaptation.

Figs. 8.16 and 8.17 show the adapted meshes of table 8.4 and mesh H1 of table 8.2 as a comparison. Mesh *GRAD* is refined:

- close to the walls,
- in the internal and external shear layer between the central recirculation zone and the corner recirculation zone,
- along the centerline of the flow because of the radial gradient of axial and tangential velocity.

Meshes MIX_{RMS} and MIX_{ν_T} are obviously refined at the same locations of mesh "*GRAD*" and in the zones where the flow criterion used (the RMS of the flow speed or the modeled turbulence respectively) is higher.
Note that for this flow the zone where the RMS of the jet velocity is higher corresponds to the location of the PVC and it is not directly connected to turbulence as in chapter 7. For this reason a sensor based on turbulent viscosity (MIX_{ν_T}) was tested.
As for the axial case of chapter 7, the minimum cell size was set to the one used in LES H1 in order to keep the numerical efficiency constant while the levels of gradation (see section 6.2.3) is set as 1.3[5]. Even if the minimum cell size was similar for all meshes of table 8.4, it was not possible to control the simulation time step with an accuracy sufficient to get the same numerical efficiency. However LES MIX_{RMS} and MIX_{ν_T} have approximately the same efficiency as LES H1.

[5]Value commonly used at CERFACS and also in Chapter 7

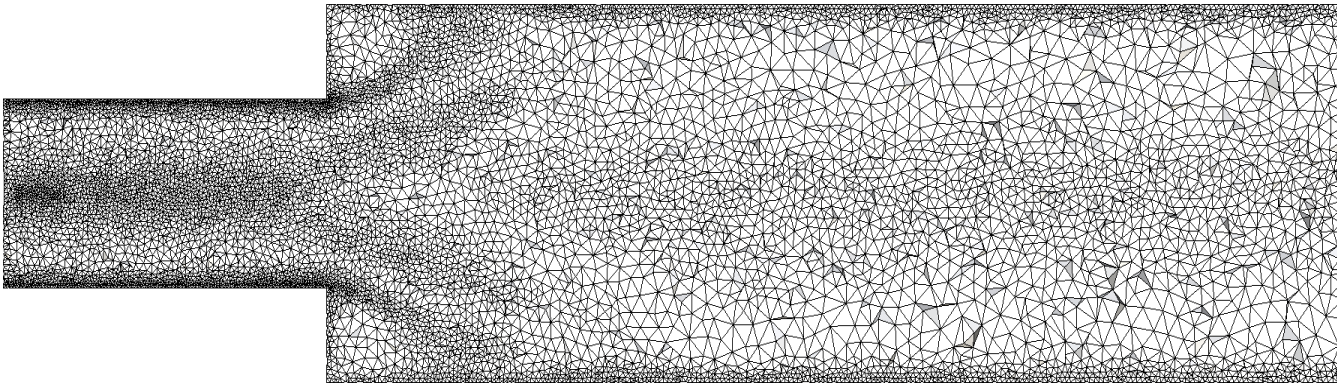

(a) *GRAD*

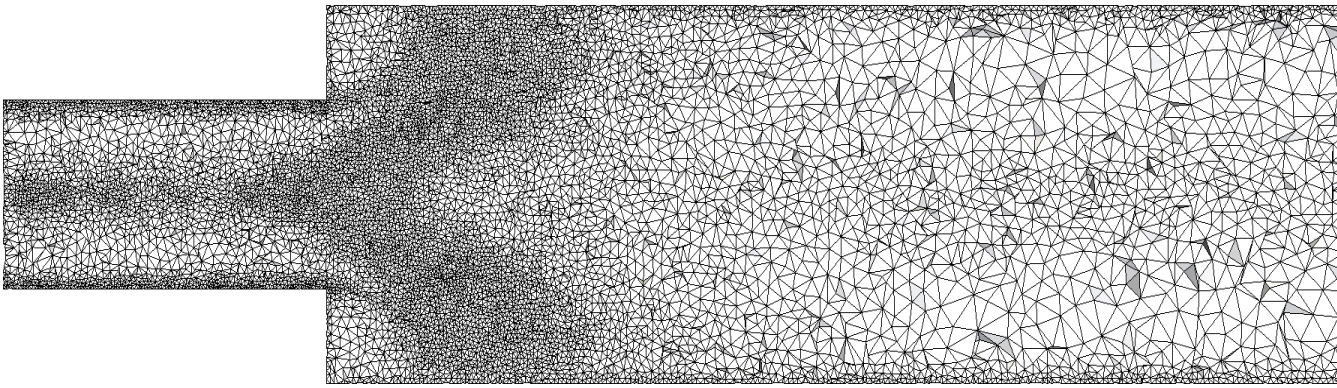

(b) MIX_{RMS}

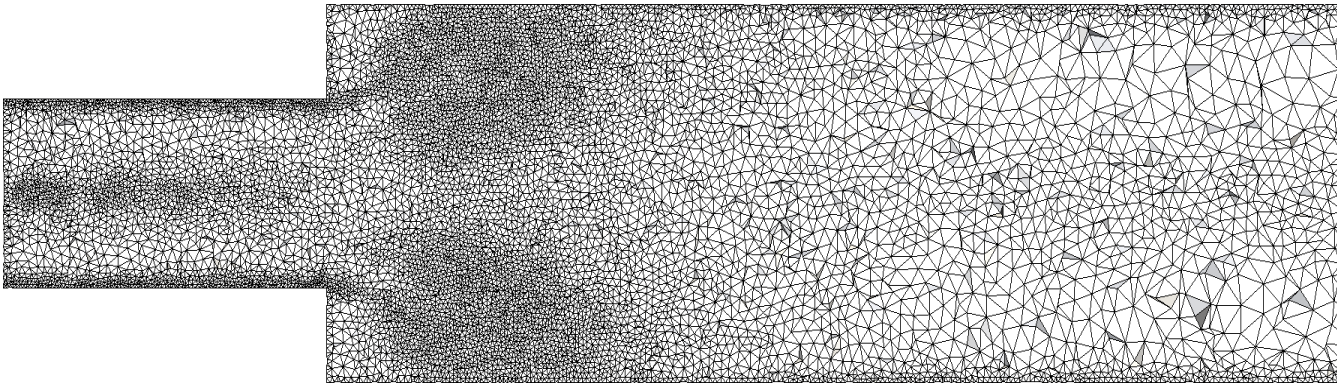

(c) MIX_{ν_T}

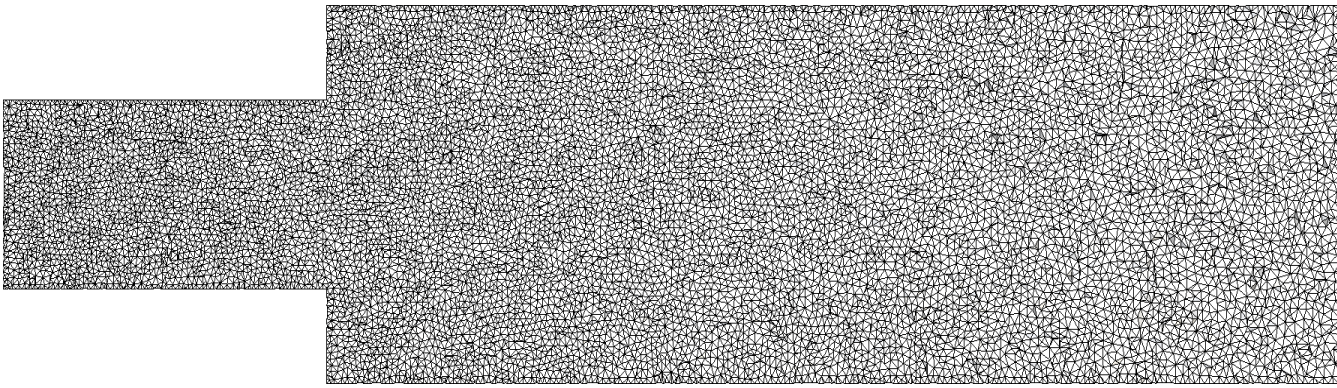

(d) H1

Figure 8.16: Meshes of table 8.4 and mesh H1 of table 8.2 as reference.

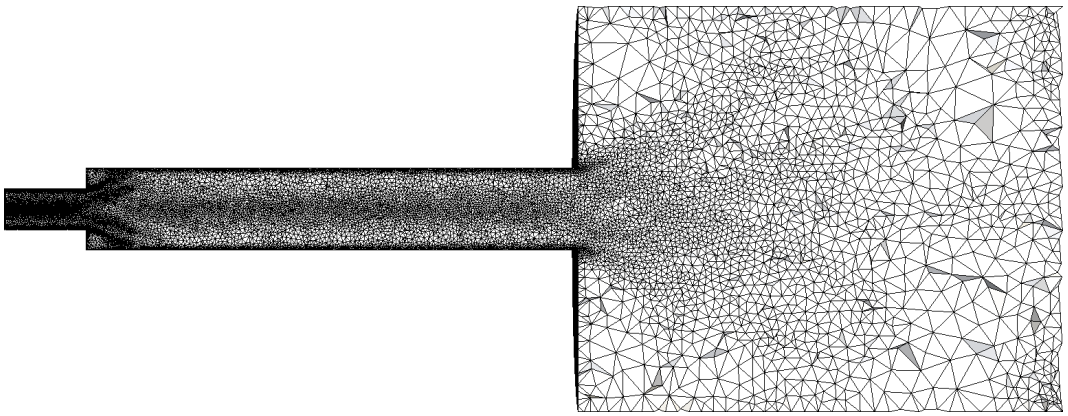

(a) *GRAD*

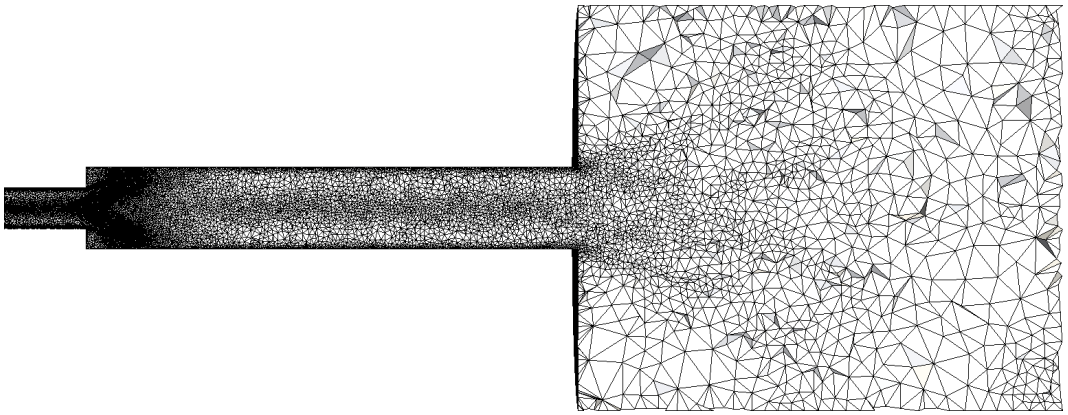

(b) MIX_{RMS}

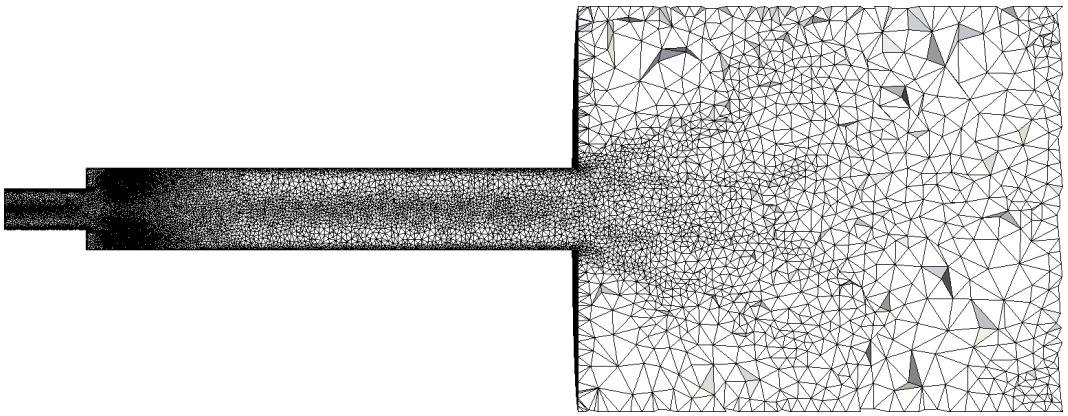

(c) MIX_{ν_T}

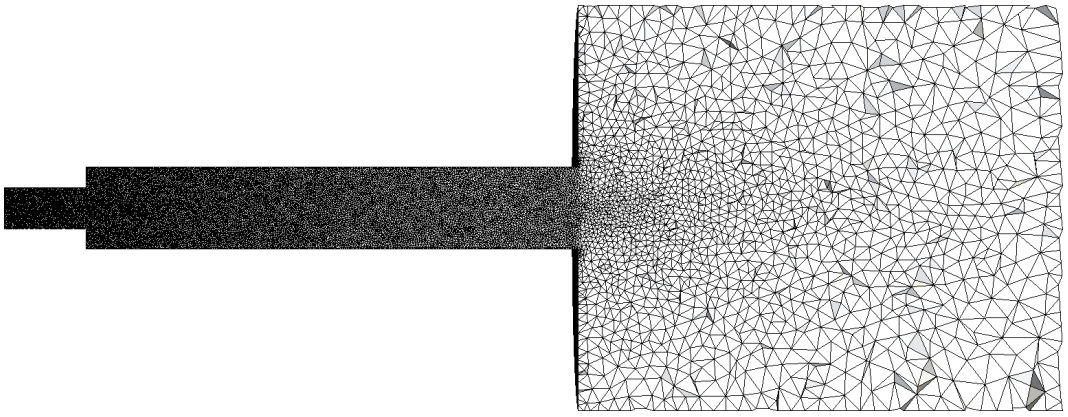

(d) H1

Figure 8.17: Meshes of table 8.4 and mesh H1 of table 8.2 as reference.

All adapted meshes are refined in the junction between the test section J and the expansion K (see Fig. 8.2 and Fig. 8.17) while they are all coarsened with respect to H1 in the remaining part of the expansion K. In this zone (inside the expansion K and far from the junction with the test section) turbulent viscosity was extremely high because of the large mesh size. Here, the element size for mesh MIX_{ν_T} was limited by evaluating the sensor $\Phi = \nu_t$ only inside the test section J while fixing the mesh size in the expansion K as a fraction of the cylinder diameter.

8.5 Flow field and simulations quality

The flow field changes after adaptation. The length of the central recirculation zone augments in all adapted meshes/LES compared to the LES on H1 (compare Fig. 8.19 and Fig. 8.4). The CRZ gets closer to LES H2 (which is significantly more expensive numerically). Results get closer to experimental data at all planes (Fig. 8.20-8.21). Globally, results improve with adaptation.
As shown in Chapter 7, despite a better comparison with experimental data in terms of velocity profiles, not all quality measures improve. Comparing table 8.3 with table 8.5, shows that Pope's criterion (Eq. 4.1) and the mean value of turbulent viscosity inside the test section J get worse for all adapted meshes. On the other hand, the time and surface

mesh/LES name	y^+_{mean}	$\frac{\int_V <\frac{\nu_t}{\nu}> dV}{\int_V dV}$	Pope criterion Eq. 4.1	$Q_{cum} = \int_{10^5}^{\infty} PDF(Q)dQ$ of Fig. 8.14
$GRAD$	12.5	6.6	0.57	12%
MIX_{RMS}	13.6	6.8	0.51	23%
MIX_{ν_T}	13.6	6.3	0.52	22%

Table 8.5: Surface time-averaged y_+ and time-volume average of turbulent viscosity (normalized by laminar viscosity), time average of the max value of turbulent viscosity (normalized by laminar viscosity), time-volume average Pope criterion.

averaged y^+ is improved in all adapted meshes with a value even smaller than LES H2. Lower y^+ values can have an effect on the axial velocity profiles: between all adapted meshes the one which shows the longer recirculation zone (at $r = 0$) is also the one which predicts the best match with experimental data in the boundary layer (at $r \approx 2D_1$), see Fig. 8.20 at planes 8-10-11. Indeed, LES $GRAD$ matches experimental data perfectly at plane 8 close to the walls (Fig. 8.20(e)) while at the same plane it predicts the highest backflow speed. Similarly, at plane 10, it predicts the highest speed between all adapted meshes at $r \approx 2D_1$ and it reproduces the central backflow better. This observation suggests to test the effects of a wall refinement only, by increasing the resolution close to the wall in the second cylinder of the tet section J. Mesh H1 was refined at the walls but keeping the overall number of nodes constant. However, with this new mesh, despite the fact that the mean y^+ was reduced to 13.9 with respect to 16.8 of LES H1 (more precisely in the second, larger cylinder went from 16.1 in H1 to 11.8 in the wall-refined H1) there was no appreciable effect on the velocity profiles.
By looking at the Q criterion (Fig. 8.22), at its PDF obtained from one snapshot (Fig. 8.23,

Eq.(7.8)) and at its cumulative probability (Eq.(8.1)), the best quality LES are MIX^{RMS} and MIX^{ν_t} with a quality level similar to LES H2. On the contrary, these quantities get worse for LES *GRAD*.
While in the axial case of Chapter 7 it was easy to identify the reason why adaptation improved results, in the swirled case studied here it is very difficult to understand the jet dynamics and their interactions. The presence of a swirl velocity component increase the complexity of the flow significantly, which is particularly unstable because of the presence of a very large PVC. Such a condition, a large PVC which impacts the whole flow, is very far from the flow of the aeronautical swirler shown in the first part of this manuscript in which the PVC is confined into a small portion of the domain (see section 4.6.2).
The swirled case can therefore be considered as a very peculiar jet being very far from the common configurations and flows studied at CERFACS and the difficulties encountered are linked to the well-known complexity of swirl flows.

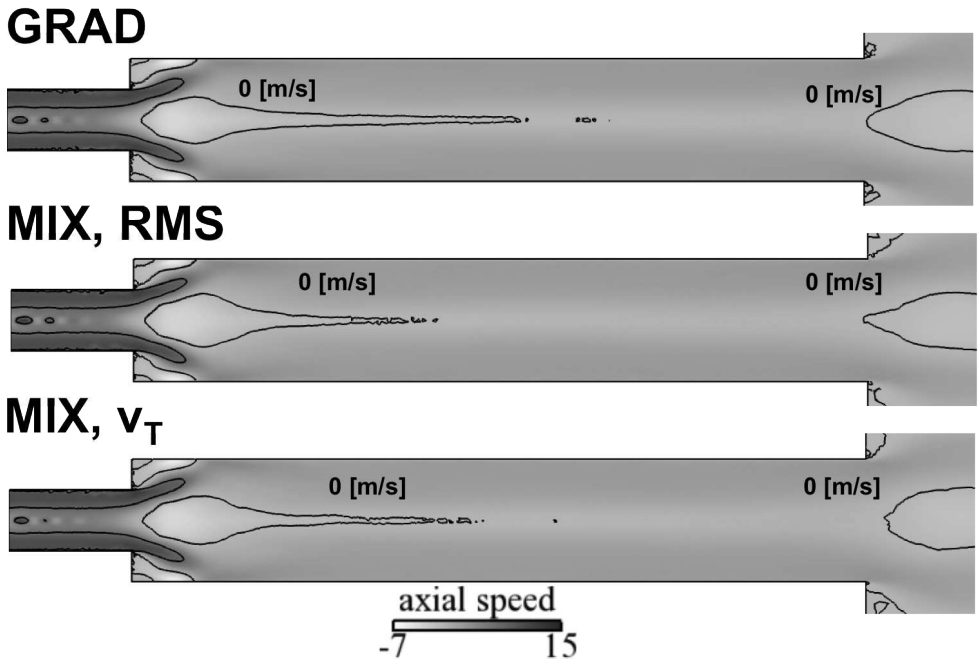

Figure 8.18: Mean axial velocity and axial velocity isolines for LES of table 8.4.

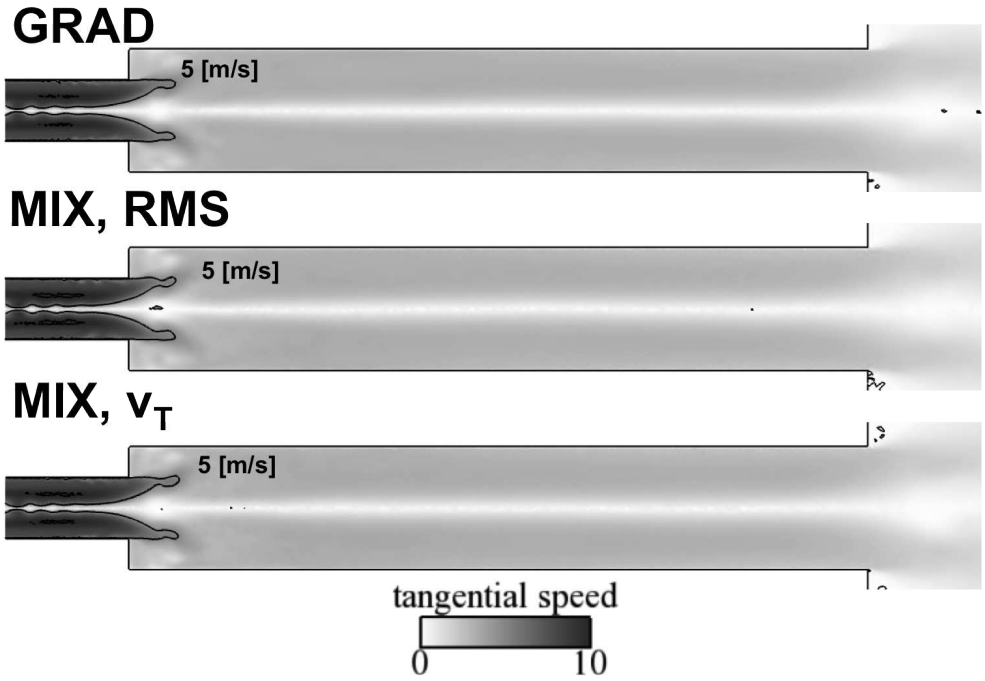

Figure 8.19: Mean axial velocity and axial velocity isolines for LES of table 8.4.

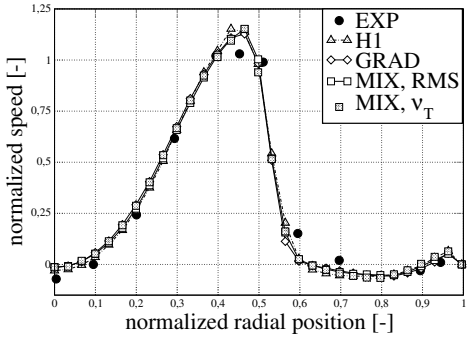

(a) Mean axial velocity profile at plane 3

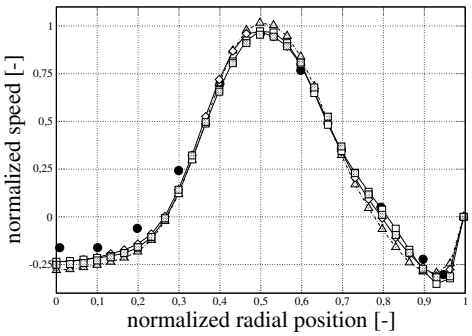

(b) Mean axial velocity profile at plane 4

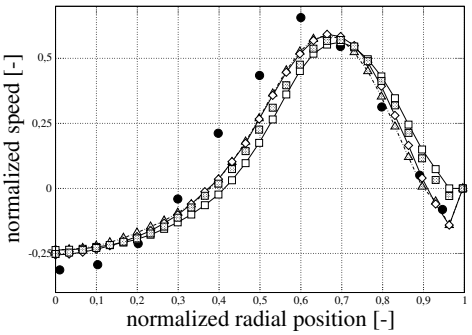

(c) Mean axial velocity profile at plane 6

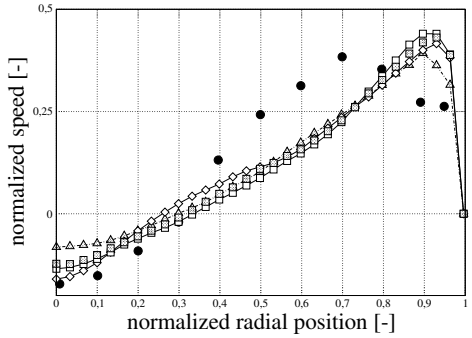

(d) Mean axial velocity profile at plane 7

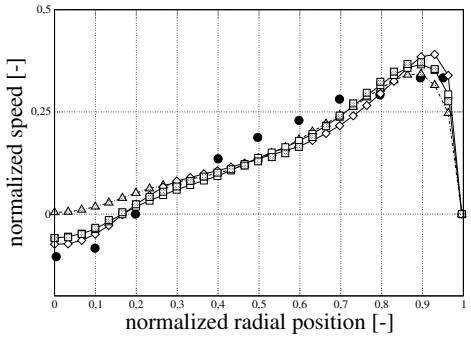

(e) Mean axial velocity profile at plane 8

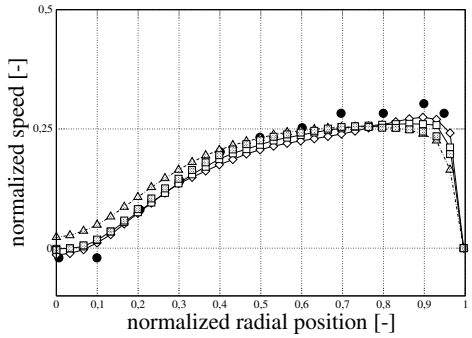

(f) Mean axial velocity profile at plane 10

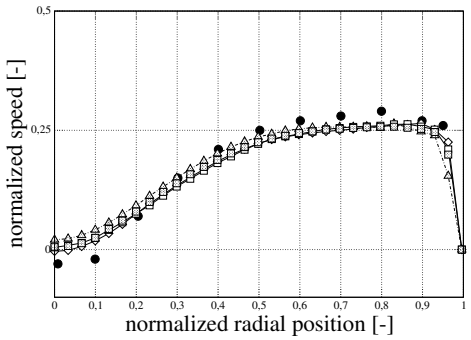

(g) Mean axial velocity profile at plane 11

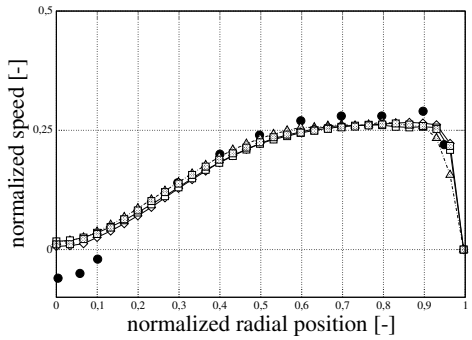

(h) Mean axial velocity profile at plane 12

Figure 8.20: Mean axial velocity profiles at the measurement planes of Fig. 8.2 for simulations of table 8.4.

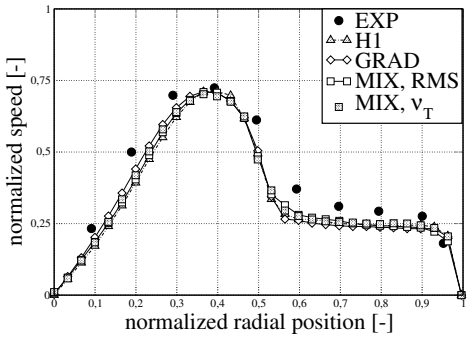

(a) Mean tangential velocity profile at plane 3

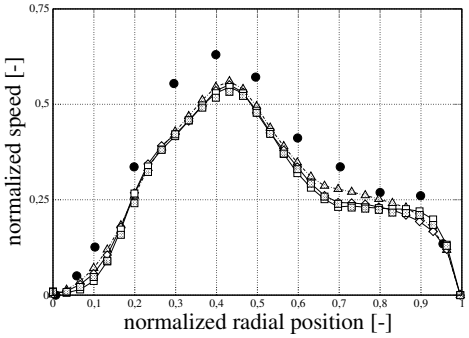

(b) Mean tangential velocity profile at plane 4

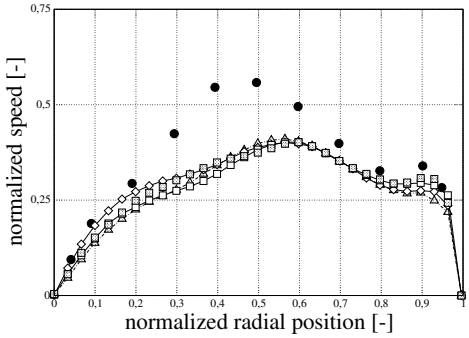

(c) Mean tangential velocity profile at plane 6

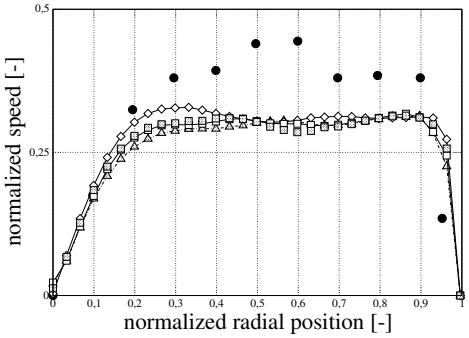

(d) Mean tangential velocity profile at plane 7

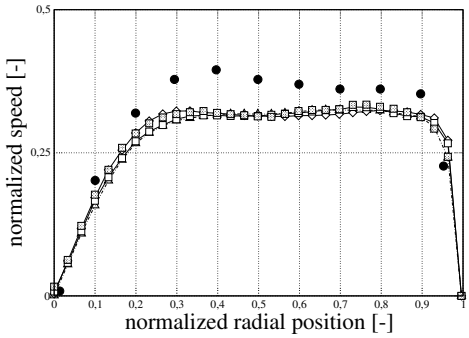

(e) Mean tangential velocity profile at plane 8

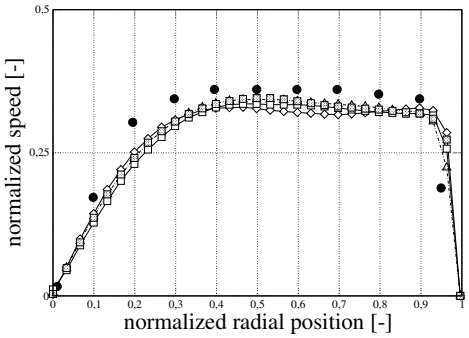

(f) Mean tangential velocity profile at plane 10

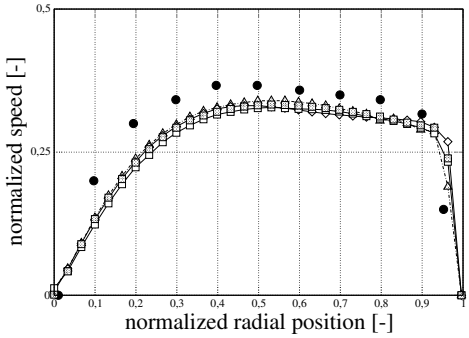

(g) Mean tangential velocity profile at plane 11

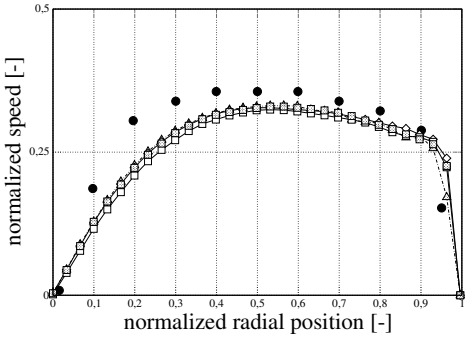

(h) Mean tangential velocity profile at plane 12

Figure 8.21: Mean tangential velocity profiles at measurement planes of Fig. 8.2 for simulations of table 8.4.

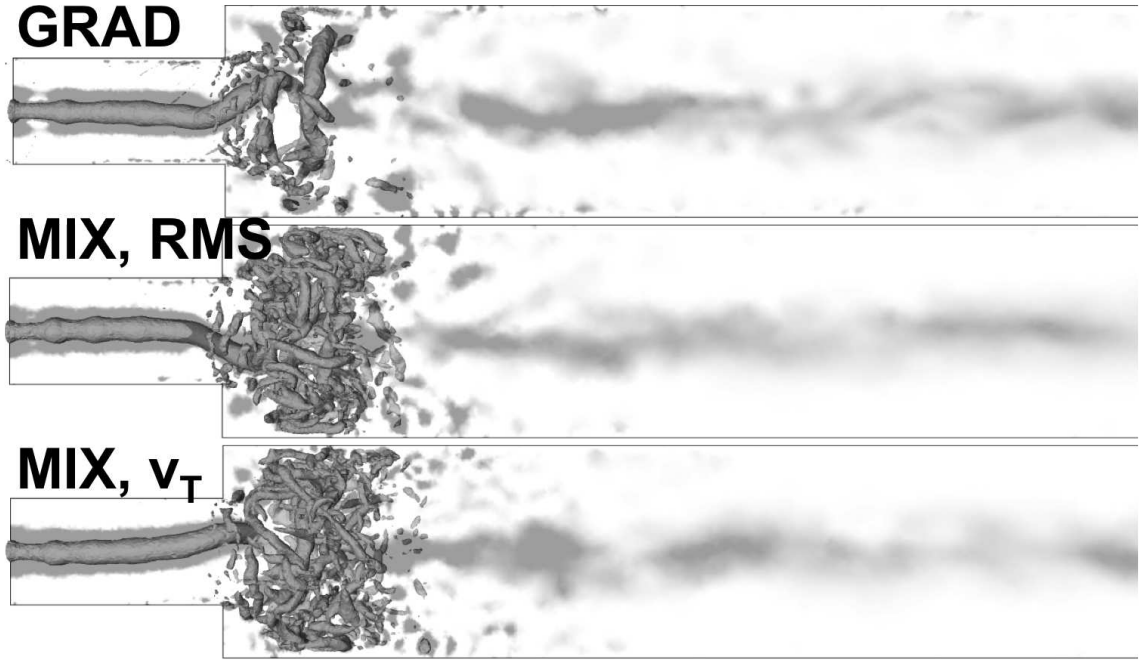

Figure 8.22: Snapshots of Q criterion for simulations of table 8.4. The field of the Q criterion (black dots are zones at $Q > 1 \times 10^6$) is made transparent to make visible the 3D structure of the PVC and of the smaller eddies

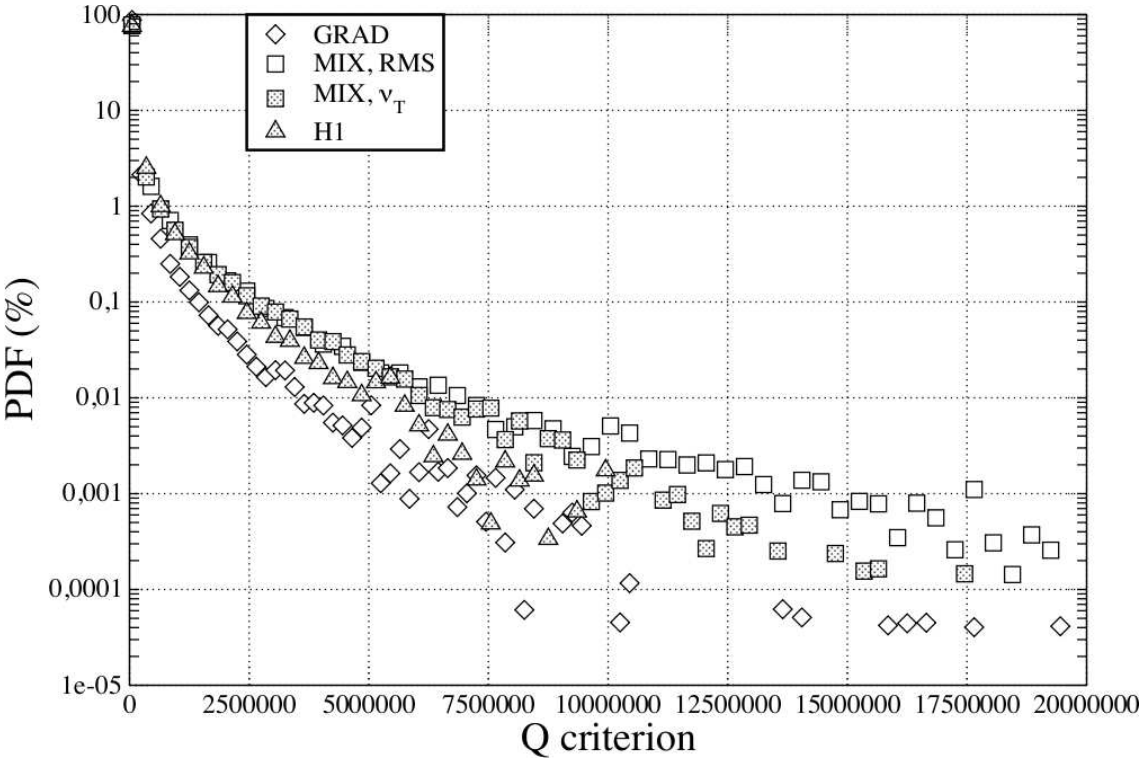

Figure 8.23: $PDF(\%)$ (Eq.(7.8)) of the Q criterion (Eq.(7.1)) for LES of table 8.4 and H1 of table 8.2.

Chapter 9

Test case C: industrial configuration

This final chapter deals with the application of mesh adaptation (described in chapters 5-8) to the industrial configuration studied in the first part of this thesis. This chapter bridges the two parts that compose this manuscript. Here, mesh adaptation is tested on the fixed swirler configuration (left in Fig. 2.1) studied in chapter 3. For the fixed swirler case, it was proven that the mesh has a significant influence on LES results because of its impacts on turbulent viscosity (Eq.(3.6)) and because of the numerical noise induced by a locally under-resolved flow. These effects, whose magnitude depends on the particular SGS model used, are able to modify the flow speed locally and these local modifications bring about a global flow bifurcation because of critical conditions[1]. However, two issues remain open from chapter 3:

1. results did not match experimental data perfectly, both in terms of the jet opening half-angle and of the length of the recirculation zone (Fig. 3.20) even when an optimized mesh[2] was employed and despite the fact that LES predicted the same flow state (Axial Jet, see chapters 3-4) of the experiment[3];

2. pressure drop was over-predicted compared to experimental data ranging from a at least +66% to a at most +160%, depending on the SGS model used (Fig. 3.22).

The challenge of mesh adaptation here is therefore to improve comparison with experimental data in terms of velocity profiles and pressure drop predictions.
Most of the mesh related issues of chapter 3 came from the interaction wall resolution/SGS modeling. For instance, SGS modeling was proven to modify the amount of swirl in the flow and to cause a change in the flow topology (sections 3.4-3.5) while this phenomenon disappeared when mesh resolution was increased in the wakes of the radial swirler blades and inside the vane itself (see section 3.7).
Regarding pressure losses, results of Barre et. al [7] show that pressure drop error can be reduced from +105% to +52% with respect to experimental data by reducing the y^+ of wall elements from $O(60)$ to $O(15)$ (i.e. refining the mesh at the wall). This result can be

[1] This second statement was proven in chapter 4.
[2] Optimized based on fluid dynamics considerations, see section 3.7, Fig. 3.16 right.
[3] See section 2.2.3 and section 3.6

considered as "obvious" since dissipation for bounded flows is governed by the boundary layer physics and, since LES equations are consistent with the Navier-Stokes equations, a higher resolution in the boundary layer should improve results. Similarly, the scaling of turbulent viscosity with the distance to the solid boundary affects pressure drop.
Finally, as mentioned in the introduction, as soon as a swirler with multiple passages is used, any error on pressure losses will directly impact on the flow split between the passages, leading to significant flow variations.
For all these reasons, mesh adaptation is targeted toward wall resolution in order to study the effects of the error distribution between the different swirler vanes on the global flow field generated by the swirler.

9.1 Meshes and numerical settings

The metric field (see chapter 6) used for mesh adaptation in this chapter is based on y^+ (Eq. 3.1), the wall distance in wall units. This choice is motivated by the fact that wall resolution is of importance for flow split and pressure drop and because the use of any of the sensor field used in the previous Chapters would have required some ad-hoc adjustments. The reason is simple: while in Chapters 7-8 confined flows were simulated (as usually happens at CERFACS with gas turbines combustion chambers) the jet examined here blows in open atmosphere. Here, in the far field, all sensors previously tested (such as turbulent viscosity or resolved turbulent kinetic energy) are high because of the coarse mesh used[4].
On the other hand, a sensor based on the velocity gradient would cluster all nodes close to the swirler walls because of high shear present in this zone, obtaining a mesh similar to the one proposed in this chapter. However, while adapting the mesh based on y^+ is possible to choose how well we want to resolve the boundary layer (by adjusting the target y^+), choosing the velocity gradient, grid resolution would have been controlled by the constraint on minimum mesh size (the sensor generator would impose very small elements at the wall while the constraint on the minimum cell size would limit their size, see section 6.2.2).
A sensor based on y^+ helps to skip all these problems fast and allows to test directly the mesh adaptation on the industrial configuration studied in the first part of this manuscript. This approach is in line with the mesh adaptation strategy explored in this thesis: any category of flow (such as "round jets" of Chapter 7) has its own peculiarities and requires a targeted mesh adaptation method.
The metric field is built as follows:

$$M(\overline{x}) = \begin{pmatrix} \frac{1}{(h(\overline{x})s(\overline{x}))^2} & 0 & 0 \\ 0 & \frac{1}{(h(\overline{x})s(\overline{x}))^2} & 0 \\ 0 & 0 & \frac{1}{(h(\overline{x})s(\overline{x}))^2} \end{pmatrix} \tag{9.1}$$

where $M(\overline{x})$ is the local metric at a position $\overline{x} = (x_1, x_2, x_3)$, $h(\overline{x})$ is the local mesh size of the original mesh to be adapted, $s(\overline{x})$ is a scaling factor. The value of the scaling factor s

[4] A coarse mesh in this zone is justified by the fact that the flow in the open atmosphere has a limited effect on the jet dynamics compared to flow inside the swirler or at the nozzle, see Chapters 3-4

is evaluated as follows:

$$s(\overline{x}) = \begin{cases} \frac{y_T^+}{y^+} & \text{at the walls,} \\ 1 & \text{else,} \end{cases} \tag{9.2}$$

where y_T^+ is the desired target value of y^+ to obtain on the adapted mesh (in this case $y_T^+ = 11$, that is above the laminar sublayer).
The mesh size gradation (see section 6.2.3) is set to 1.2 in order to smooth the metric field which is by construction (Eq.(9.2)) discontinuous. The metric field built using Eq.(9.1-9.2) has the peculiarity to refine the grid only at the walls while interior cells are, in a first instance, left untouched ($s(\overline{x}) = 1$). However, since the number of nodes of the mesh is preserved, a wall-targeted refinement implies a coarsening in the bulk of the flow, therefore no element remains the same after adaptation.
The aim of this sensor field is to equidistribute the size of the wall elements in order to get an homogeneous mesh in terms of y^+. The adaptation criterion is very simple: if the local value of y^+ of flow computed on the original mesh is smaller than the target value y_T^+, the element will be enlarged ($s(\overline{x}) > 1$ so $h(\overline{x})s(\overline{x}) > h(\overline{x})$ in Eq.(9.1)), on the contrary it will be reduced ($s(\overline{x}) < 1$ so $h(\overline{x})s(\overline{x}) > h(\overline{x})$ in Eq.(9.1)).
Obviously, such a method requires a LES flow field to compute the local scaling factor $s(\overline{x})$. The mesh and flow field chosen as the initial grid and solution are the one of LES YALES-SIGMA of section 3.4 (the mesh is shown in Figs. 3.5(a) and 3.16, "basic"), which are the worst in terms of comparison with experimental data between all results of chapter 3.
The resulting adapted mesh (based on the metric field built using Eq.(9.1-9.2)) is shown in Fig. 9.1(a)-9.1(b) along with the "basic" mesh used for LES YALES-SIGMA. The adapted mesh (named ADAPTED simply) is refined mainly inside the radial swirler (where the value of y^+ is higher) and coarsened away from the wall.
As evident from Fig. 9.1(b), far from the solid boundaries, the "basic" and ADAPTED meshes are very similar. This is a consequence of the fact that, in these zones, elements of adapted mesh are by construction similar to the elements of the basic mesh ($s(\overline{x}) = 1$ in Eq.(9.2)). However, there, in the free jet, the ADAPTED mesh is clearly coarser than the "basic" mesh (Fig. 9.1(b)). This phenomenon is due to the fact that the overall number of nodes is kept constant (see section 6.2.4). Since the ADAPTED mesh is refined at the walls and, at the same time, the overall number of nodes is conserved, the ADAPTED mesh is coarsened away from the solid boundaries.
The number of nodes and elements of the ADAPTED mesh are 2269213 and 12888044 respectively, similar to the number of nodes/elements of meshes "basic" and "optimized" of Fig. 3.16. The boundary conditions used for the test performed in this chapter are the same as in chapter 3 (see Fig. 3.3 and table 3.1). The code used here is YALES2 and the SGS model is the Dynamic Smagorinsky model [29] (see section 3.2.2).

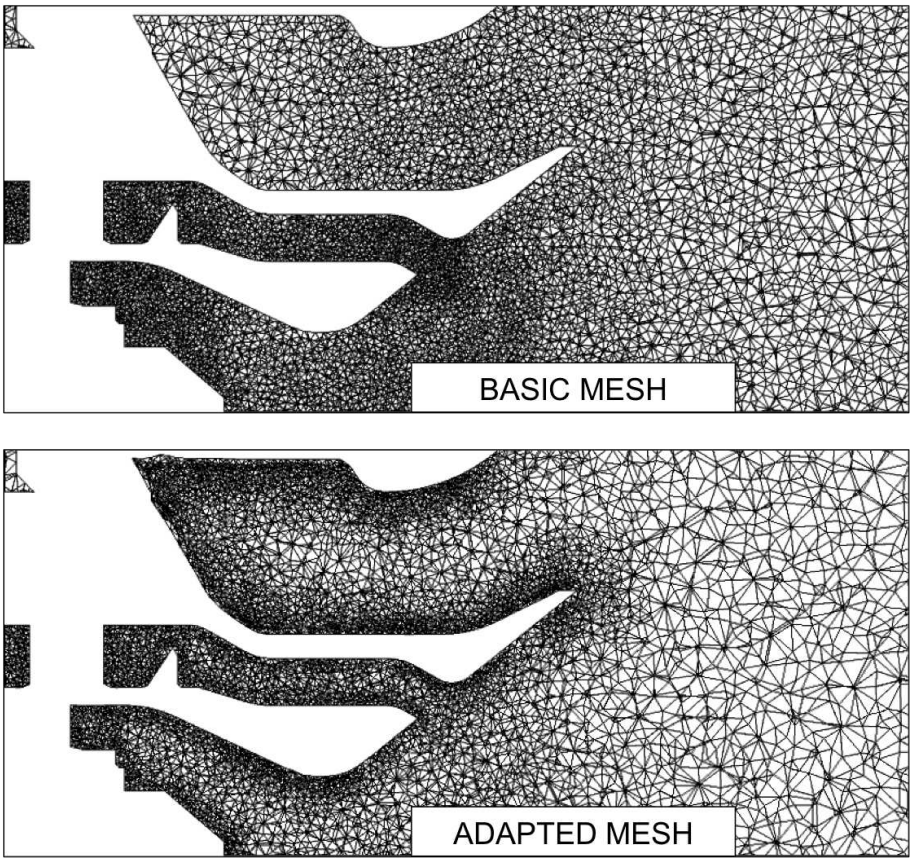

(a) Zoom inside the bowls

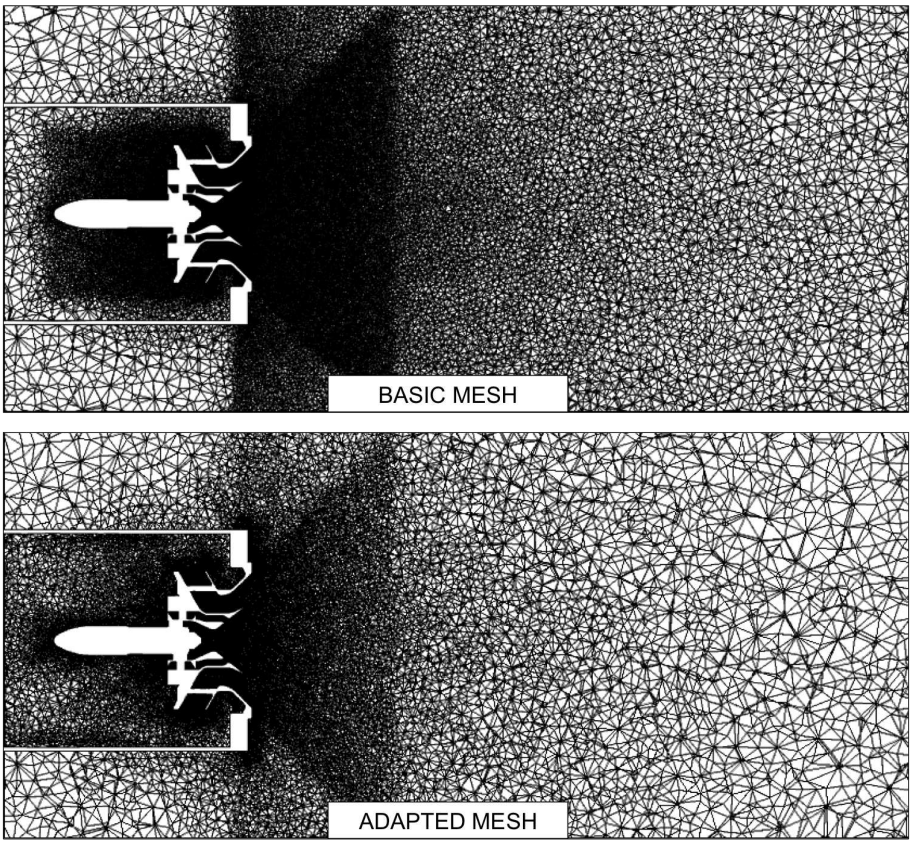

(b) Zoom out

Figure 9.1: "Basic" mesh vs. mesh ADAPTED using Eq.(9.1-9.2) and the flow field of LES YALES-SIGMA of section 3.4.

9.2 Flow field

The ADAPTED LES (the mesh and simulation are both named ADAPTED for simplicity) reaches convergence in terms of kinetic energy after $\approx 0.030[s]$. Kinetic energy is evaluated inside a box (see Fig. 4.11) big enough to fully contain the recirculation bubble of the Blasted vortex Breakdown state (which is the largest observed, see Chapters 3-4). This choice is motivated by the fact that to obtain the convergence of kinetic energy in the whole simulation domain requires an excessively long simulation time. For comparison, both kinetic energies (evaluated inside the "box" of Fig. 4.11 and in the whole simulation domain) are shown in Fig. 9.2: kinetic energy inside the box converges fast (as already experienced for LES of chapter 4) while in the whole chamber it keeps on increasing slowly.

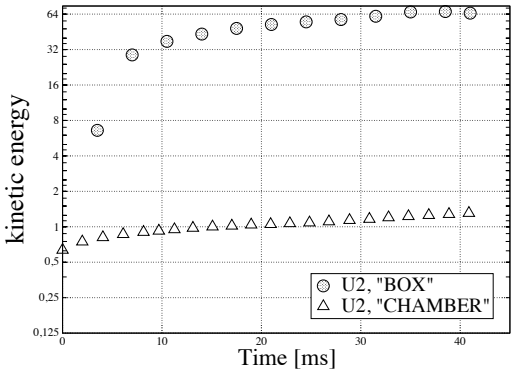

Figure 9.2: Instantaneous kinetic energy evolution for LES ADAPTED of table 9.1. Kinetic energy is evaluated inside the "box" of Fig. 4.11 and in the whole simulation domain. Logarithmic scale.

The flow field of LES ADAPTED is compared to the flow of LES of table 3.13, obtained with the optimized mesh of Fig. 3.16 (see section 3.7). The flow field of LES adapted is shown in Fig. 9.3 (together with results of LES YALES-SIGMA_O as comparison) while its characteristics, in terms of the three different jets swirl number/ratio (measured on surfaces S1, S2 and S3 of Fig. 3.6 as explained in section 3.3.1) are summarized in table 9.1.

LES name	S (eq. 2.2) inner/outer jet	S_r (eq. 2.3) radial jet	jet configuration
ADAPTED	0.12/ 0.47	0.76	AJ
YALES-SIGMA_O	0.12/0.58	0.74	AJ
YALES-DSMAG_O	0.12/0.4	0.72	AJ
AVBP-SIGMA_O	0.12/0.52	0.76	AJ

Table 9.1: Fluid dynamics characteristics of LES ADAPTED and of LES of table 3.13.

Under these fluid dynamics conditions (summarized in table 9.1), the flow obtained with the adapted mesh is in the AJ state (as evident from the size of the central recirculation zone shown in Fig. 9.4, the pressure and rms profiles shown in Fig. 9.5).
The first difference between LES ADAPTED and LES of table 3.13 (which are used as comparison) is the jet opening half-angle (see Fig. 3.7) which is significantly larger and is the largest obtained in the fixed swirler configuration (Fig. 2.1) for a jet in the AJ state.

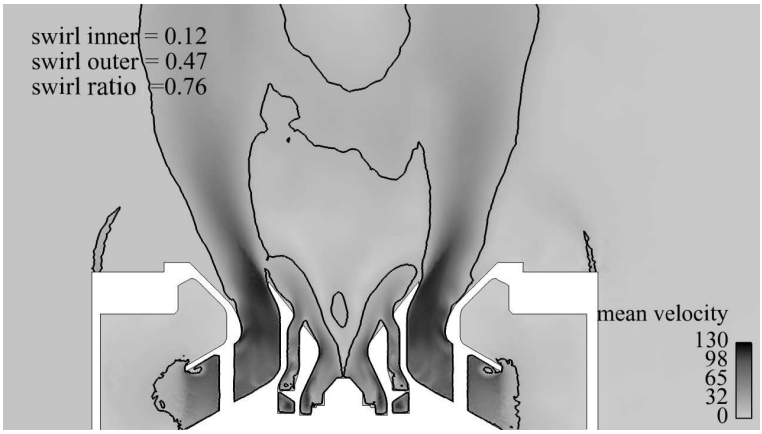

(a) ADAPTED

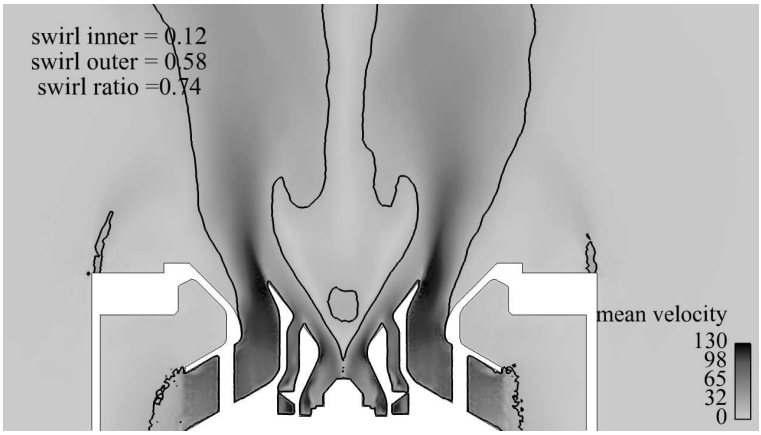

(b) YALES-SIGMA_O

Figure 9.3: Mean velocity for two of the LES of table 9.1.

Fig. 9.6 shows the jet opening half-angle for LES ADAPTED and for all LES of table 3.13: LES ADAPTED predicts a jet opening half-angle of 35[deg] very close to the experimental value of 34[deg] and similar to the result obtained with LES *basic* of section 4.5 obtained on a much finer mesh.
The second remarkable difference is the size of the Central Toroidal Recirculation Zone (CTRZ). As evident from Fig. 9.4 (where the CTRZ of LES YALES-SIGMA_O is shown as comparison) the CTRZ is significantly longer.
The different jet opening angles and the size of the CTRZ have a deep impact on the velocity profiles. Figs. 9.7-9.8-9.9 show the velocity profiles of all LES of table 3.13, of LES ADAPTED and compare them with the experimental velocity profiles. Results of LES ADAPTED show a significant improvement with respect to all LES obtained with the optimized mesh, showing a better comparison with experimental data at all planes and for all velocity components. Note that the size of the CTRZ is perfectly matched with the back-flow intensity (Fig. 9.9(a)).

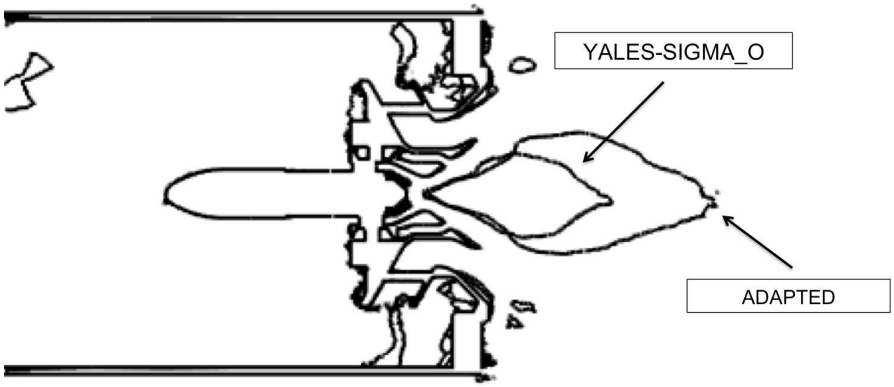

Figure 9.4: CTRZ for LES of ADAPTED of table 9.1 compared with LES YALES-SGIMA_O of table 3.13.

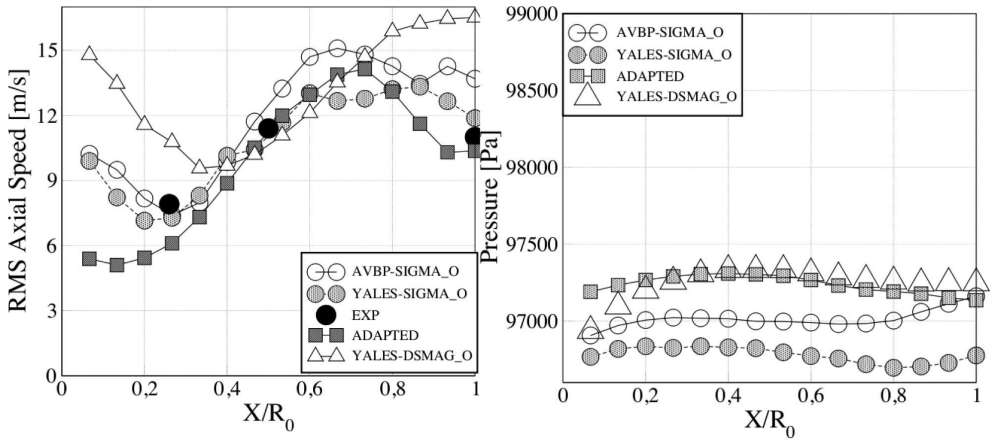

Figure 9.5: Axial velocity RMS and pressure distribution measured along the centerline of the geometry for simulations of table 3.13 and LES ADAPTED of table 9.1. Results are plotted against normalized axial distance (X/R_0) from the swirler ending plate. Experimental data are available only for RMS values.

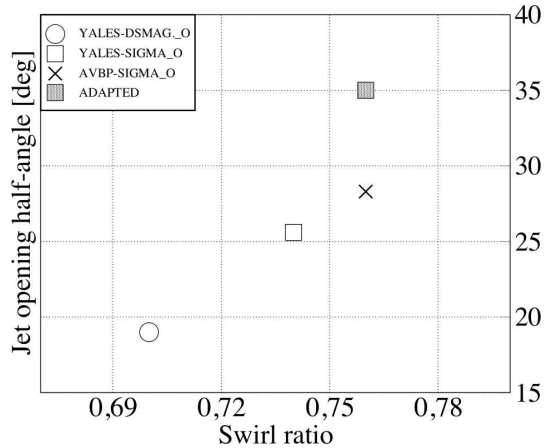

Figure 9.6: Jet opening half-angle (Fig.3.7) for simulations of table 3.13 and LES ADAPTED of table 9.1. Note that LES ADAPTED shows a jet opening half-angle of 35[deg] very close to the experimental data of 34[deg].

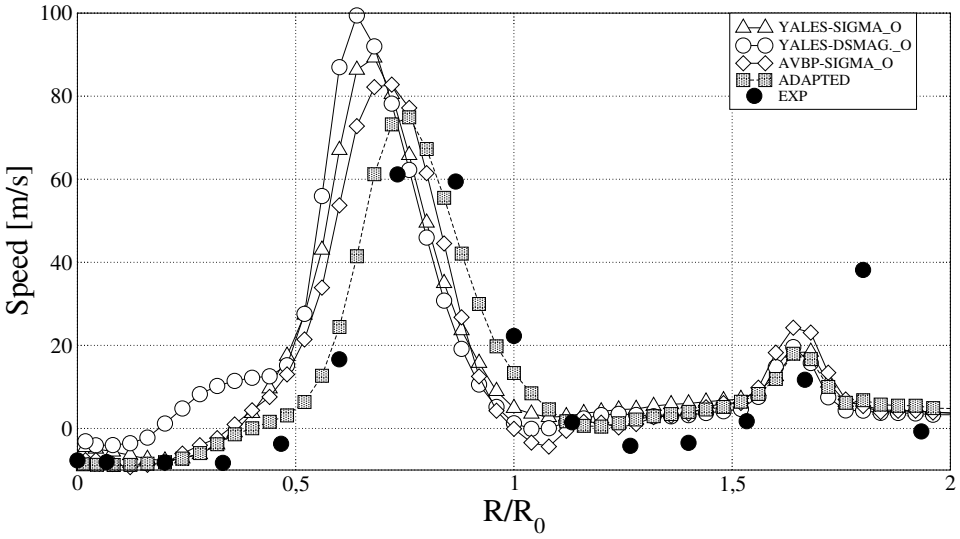

(a) Axial

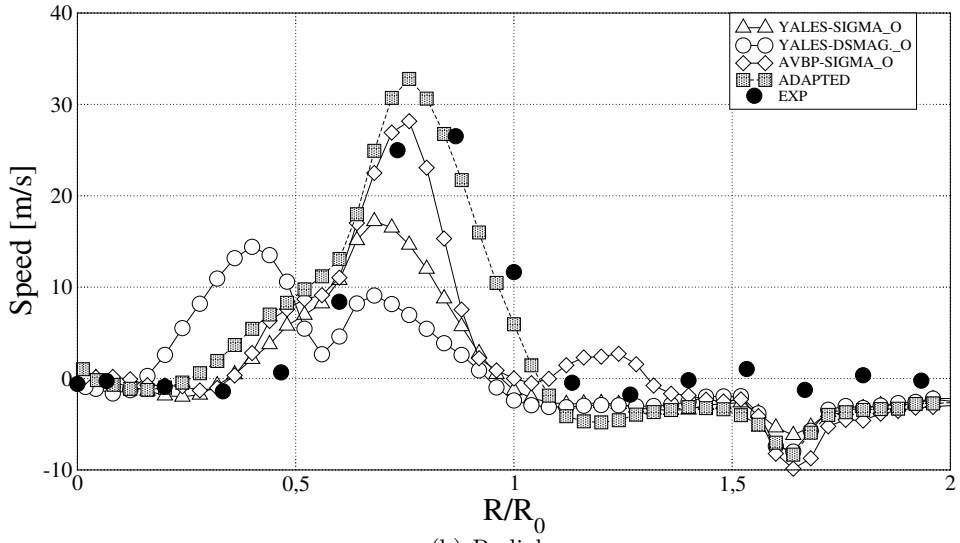

(b) Radial

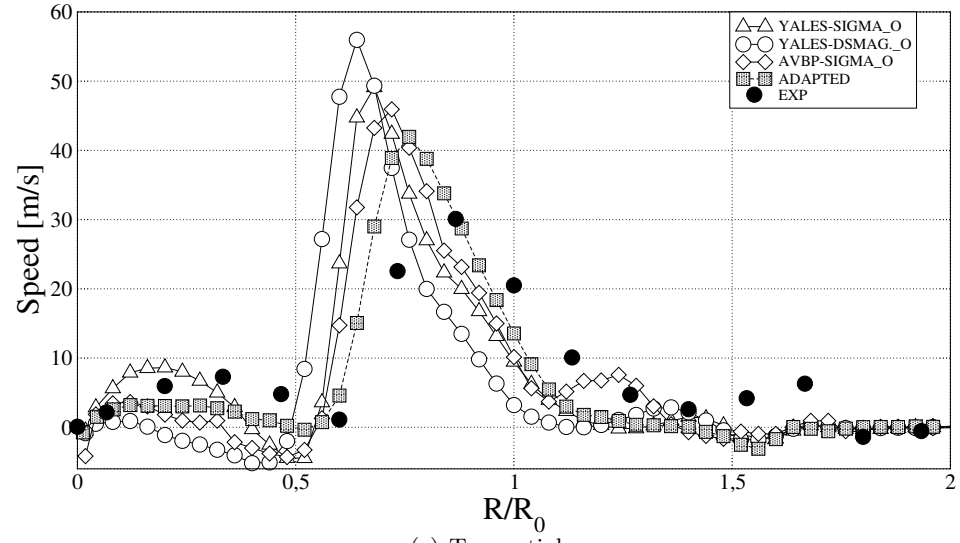

(c) Tangential

Figure 9.7: Velocity profiles of LES of table 3.13 and LES ADAPTED of table 9.1. 8mm plane, $R_0 = 30[mm]$.

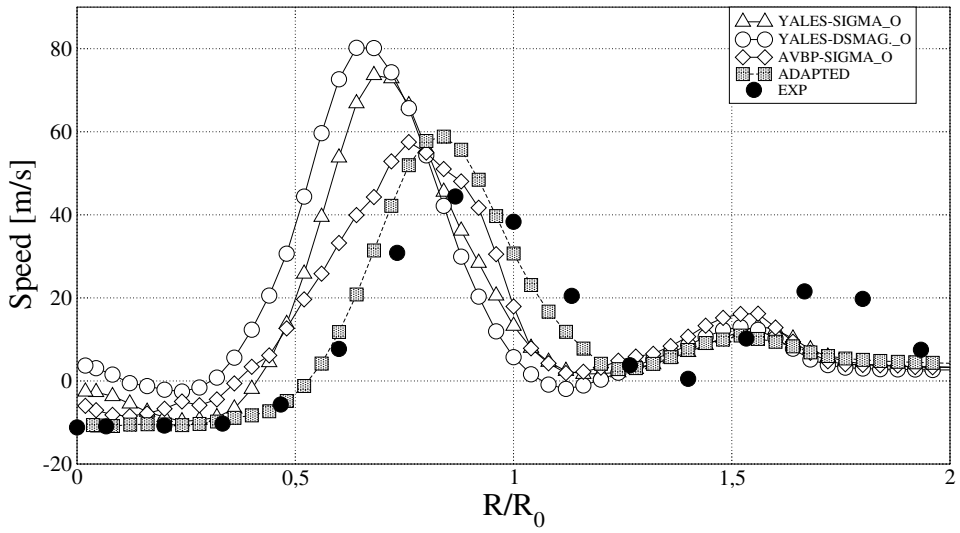

(a) Axial

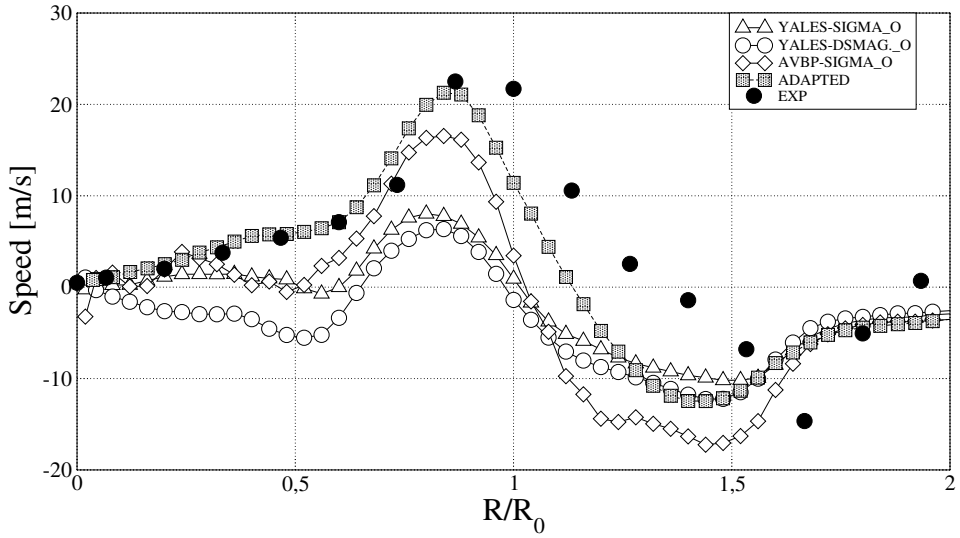

(b) Radial

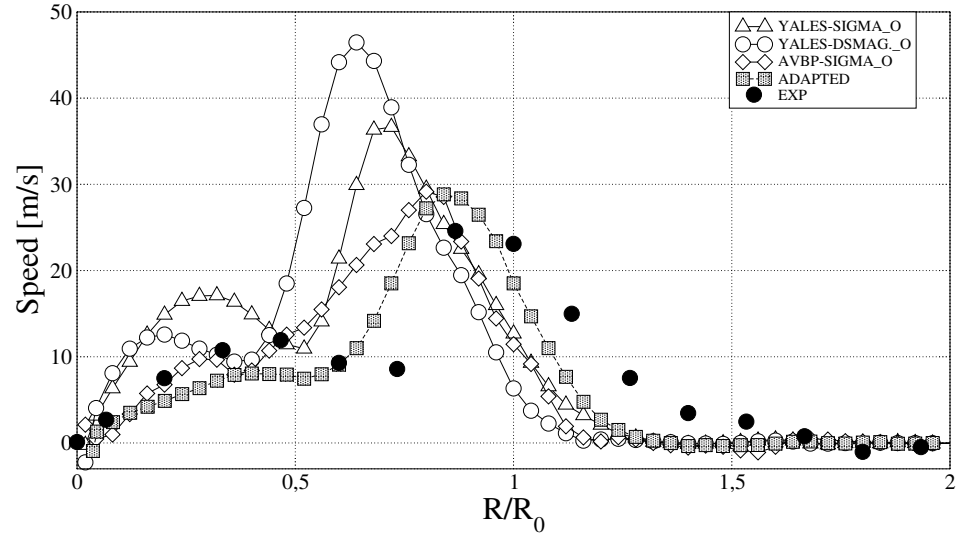

(c) Tangential

Figure 9.8: Velocity profiles of LES of table 3.13 and LES ADAPTED of table 9.1. 15mm plane, $R_0 = 30[mm]$.

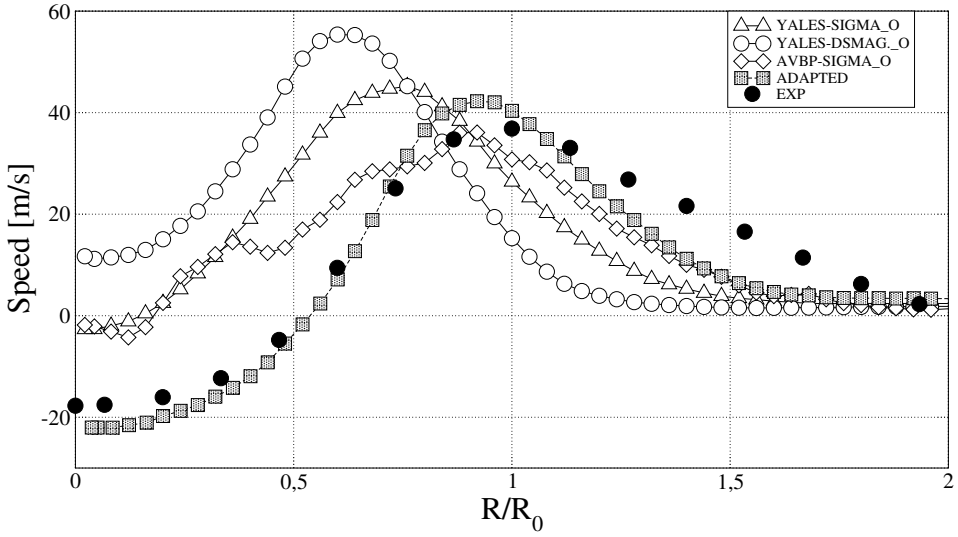

(a) Axial

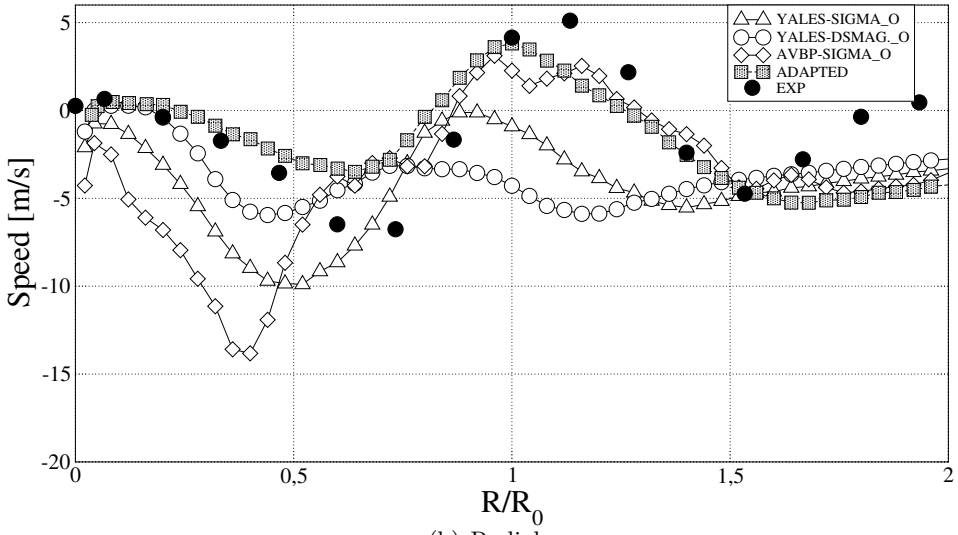

(b) Radial

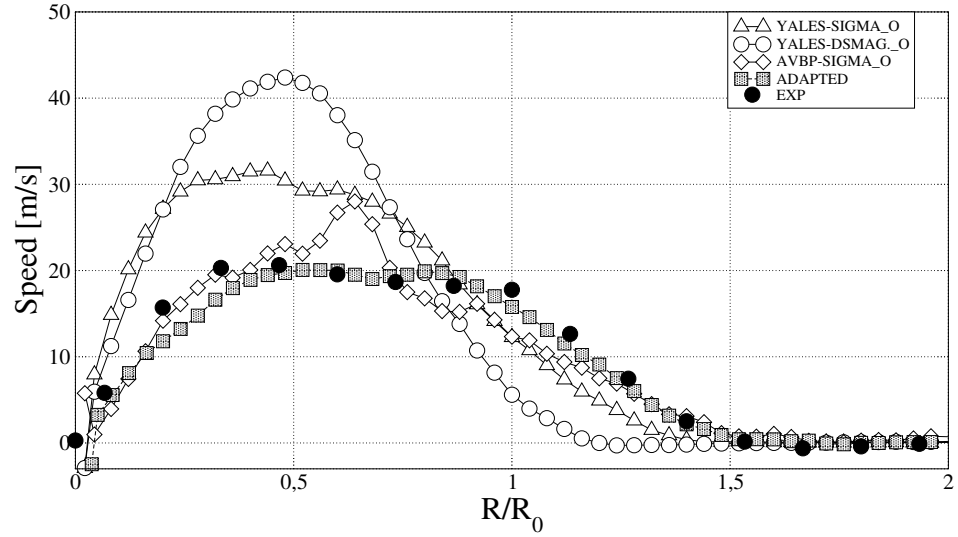

(c) Tangential

Figure 9.9: Velocity profiles of LES of table 3.13 and LES ADAPTED of table 9.1. 30mm plane, $R_0 = 30[mm]$.

9.3 Pressure drop and flow split

Flow split changes significantly after mesh adaptation: using the ADAPTED mesh, the mass flow rate through the radial stage increases while the mass flow rate through the axial stage decreases (it reduces by 17% with respect to YALES-DSMAG_O, see table 9.2) and differs significantly from permeability measurements.
Mesh adaptation causes a drastic reduction of the pressure drop (table 9.2). Note that table 9.2 compares pressure drop and flow split of LES that have the same SGS model (Dynamic Smagorinsky [29]), since, as proved by Fig. 3.22, pressure drop is mainly a function of the SGS modeling. Using adaptation, the error on pressure drop reduces from +120% of LES YALES-DSMAG_O to +70% with the adapted mesh, which still is a large error, but represents a net improvement.

Flow repartition and pressure drop				
	axial stage	radial stage	total mass flow	pressure drop
EXP	16.5 [g/s]	85.5 [g/s]	102 [g/s]	4800 [Pa]
ADAPTED	13.4 [g/s]	88.2 [g/s]	101.6 [g/s]	8205 [Pa]
YALES-DSMAG_O	15.9 [g/s]	86.1 [g/s]	102.0 [g/s]	10657 [Pa]

Table 9.2: Flow repartition and pressure drop for LES ADAPTED of table 9.1. Note that flow split is significantly different from the experimental value obtained from permeability measurements. However, the accuracy of permeability measurement is questionable.

In order to study the effects of modeling on pressure drop, the SGS model was switched from Dynamic Smagorinsky to SIGMA in the converged flow of LES ADAPTED. Results obtained with this new simulation, labelled ADAPTED_S, are summarized in table 9.3.
As expected, using the SIGMA SGS model, pressure drop reduces to 6826 [Pa] equivalent to an error of +42 % with respect to experimental data and which is significantly lower than LES YALES-SIGMA_O or AVBP-SIGMA_O (+80 %). Such an error on pressure losses is even lower than the one shown on Jaegle's [47] LES on a very similar injector and with a dedicated wall function (+54%).

Flow repartition and pressure drop				
	axial stage	radial stage	total mass flow	pressure drop
EXP	16.5 [g/s]	85.5 [g/s]	102 [g/s]	4800 [Pa]
ADAPTED_S	13.5 [g/s]	88.0 [g/s]	101.5 [g/s]	6826 [Pa]
YALES-SIGMA_O	15 [g/s]	87 [g/s]	102.0 [g/s]	8535 [Pa]
AVBP-SIGMA_O	15.7 [g/s]	85.8 [g/s]	101.5 [g/s]	8647 [Pa]

Table 9.3: Flow repartition and pressure drop for LES ADAPTED_S and LES of table 9.1.

From the analysis of tables 9.2-9.3 it can be argued that the improvements on pressure drop are likely to be linked to a different flow split in the axial and radial stages. This flow split change is due to an equirepartition of the error made at the walls. Fig. 9.10 shows the Probability Density Function (PDF) of the y^+ in the computational domain for LES ADAPTED and LES YALES-SIGMA (which was used for building the sensor field). Using a mesh adapted based on a target value of y^+, this quantity becomes homogeneous in the different stages of the swirler (the Root Mean Square of this quantity reduces almost

by 50%, from 13 in LES YALES-SIGMA to 6.8 with the adapted mesh).
However also the mean y^+ value reduces (from 27 in LES YALES-SIGMA to 18 with the adapted mesh) and it is therefore impossible to verify if pressure drop prediction improves because of a lower y^+ or because of a change in flow split related to a more homogeneous y^+ in the different passages.

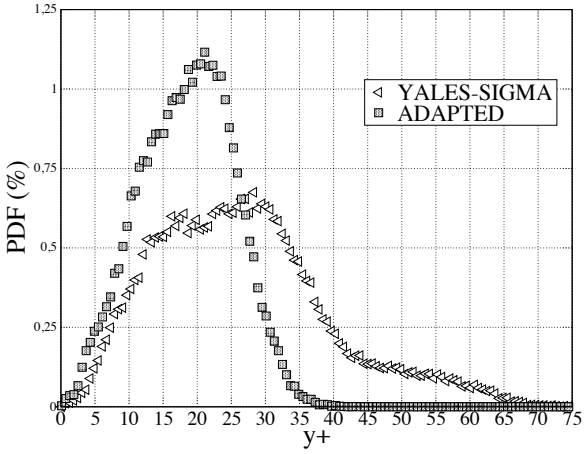

Figure 9.10: PDF of mean y^+ for LES ADAPTED and LES YALES-SIGMA (which was used for building the sensor field). Using adaptation the y^+ becomes more homogeneous in the domain (the RMS value of this quantity reduces from 13 in LES YALES-SIGMA to 6.8 with the ADAPTED mesh) while its mean value reduces from 27 in LES YALES-SIGMA to 18 with the ADAPTED mesh (close to the imposed value of 11). This causes a net improvement of pressure drop prediction and a different flow split.

In order to clarify this issue, a second adapted mesh was generated in which the target y^+ (y_T^+ in Eq.(9.2)) was fixed to be twice larger in the radial swirler than everywhere else in the domain. Fig. 9.12 shows this mesh, labelled ADAPTED_NH (Non-Homogeneous), which is clearly coarser than the adapted mesh inside the radial swirler. The LES performed with this mesh, using the Dynamic Smagorinsky model, predicts a flow split similar to all LES of Chapter 3 (see also tables 9.2-9.3) and a pressure drop error of +100% with respect to experimental data (see table 9.4). It was impossible to repeat the same test with SIGMA since the flow bifurcated to the BB state (the swirl ratio of the radial jet increased to 0.81 causing a bifurcation of the flow to the BB state as experienced in Chapter 3).

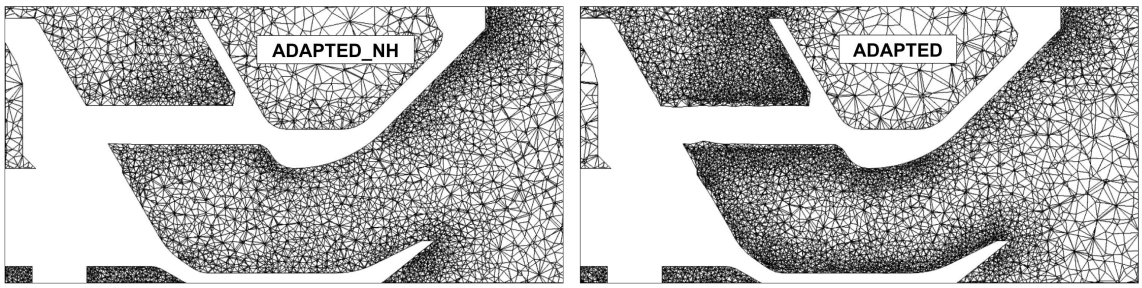

Figure 9.11:

LES ADAPTED_NH is characterized by a net reduction of the mean y^+ with respect

Flow repartition and pressure drop				
	axial stage	radial stage	total mass flow	pressure drop
EXP	16.5 [g/s]	85.5 [g/s]	102 [g/s]	4800 [Pa]
ADAPTED_NH	15.2 [g/s]	86.1 [g/s]	101.2 [g/s]	9618 [Pa]

Table 9.4: Flow repartition and pressure drop for LES ADAPTED_NH.

to LES YALES-SIGMA (-26%) and by an RMS,

$$y^+_{RMS} = \sqrt{< (y^+)^2 > - (< y^+ >)^2}, \tag{9.3}$$

which remains equal to 50% of the mean y^+, see table 9.5 and Fig. 9.12. This result was expected since the mesh resolution mesh ADAPTED_NH was imposed to be different in the radial stage.
Despite the fact that the mean y^+ of LES ADAPTED_NH is similar to LES ADAPTED, see table 9.5, its RMS remains substantially higher causing a different flow split which is negatively-affecting pressure drop predictions and confirming the hypothesis made (namely that flow split has a deep influence on pressure losses for this configuration).

Flow repartition and pressure drop		
	$< y^+ >$	$y^+_{RMS}(Eq.(9.3))$
YALES-SIGMA	27	13
ADAPTED	18	6.8
ADAPTED_NH	20	10.2

Table 9.5: Mean and RMS y^+ for LES YALES-SIGMA, ADAPTED and ADAPTED_NH which is built to have a different y^+ in the radial stage.

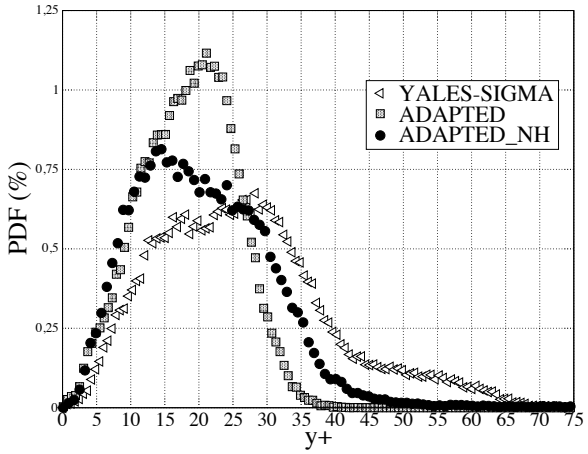

Figure 9.12: PDF of mean y^+ for LES YALES-SIGMA, ADAPTED and ADAPTED_NH which is built to have a different y^+ in the radial stage.

9.4 Conclusions

The LES results of this chapter have shown that mesh adaptation can improve comparison with experimental data both in terms of the flow velocity profiles (Fig. 9.7-9.8-9.9) and in terms of pressure drop (tables 9.3-9.3). Such improvements are linked to a different flow split in the axial and radial stages.
This flow split change is due to an equirepartition of the error made at the walls. What can be argued from these results is that, together with the absolute error on wall friction due to an insufficient resolution, what is of importance for this configuration is the relative repartition of the error in the different stages.
This idea is coherent with the basic hydraulic concept which suggests that, in the presence of multiple passages (as in this case, multiple stages), pressure drop is governed by pressure losses on the smallest one in a non-trivial way because of the self-adjustment of the flow. For LES, it seems that pressure drop and flow split dynamics are governed by the less resolved passage and that an equirepartition of the error made causes a drastic improvement of predictions (see tables 9.2-9.3).
Such improvements (in terms of velocity profiles and pressure drop) come at no numerical cost, see table 9.6. On the contrary, the numerical efficiency (Eq.(6.27)) of LES ADAPTED increases by more than 10% since the mesh is refined in the boundary layer where the flow speed is low so that mesh refinement has no effect on the simulation time step. Obviously, this is not the case when a compressible code is used since the time step is determined by the speed of sound which is approximately constant in this case. However, when the adapted mesh (Fig. 9.1(a)-9.1(b)) was tested in AVBP, the reduction of the simulation efficiency was of $O(50\%)$ due to the very fine elements generated at the walls. Such an increase of numerical cost can be considered as affordable.

LES name	Numerical Efficiency (Eq.(6.27))
YALES-DSMAG._O	1
YALES-SIGMA_O	1.09
ADAPTED	1.13

Table 9.6: Numerical efficiency for LES ADAPTED and LES of table 3.13 performed using the incompressible solver YALES2. The numerical efficiency of LES YALES-DSMAG._O is used as normalization condition.

Chapter 10

Conclusions

This thesis has shown that LES of confined swirling flows can be more difficult than most classical flows because swirling flows are characterized by bifurcations [10, 32] and various instabilities (Chapter 2).
The jet studied here, generated by an aeronautical swirler blowing in open atmosphere (Chapter 3), resulted to be very sensitive to numerical settings: a change of SGS modeling or grid resolution triggered a large bifurcation. Two totally different flow states (shown side by side in Fig. 10.1) appeared as a function of the numerical settings.

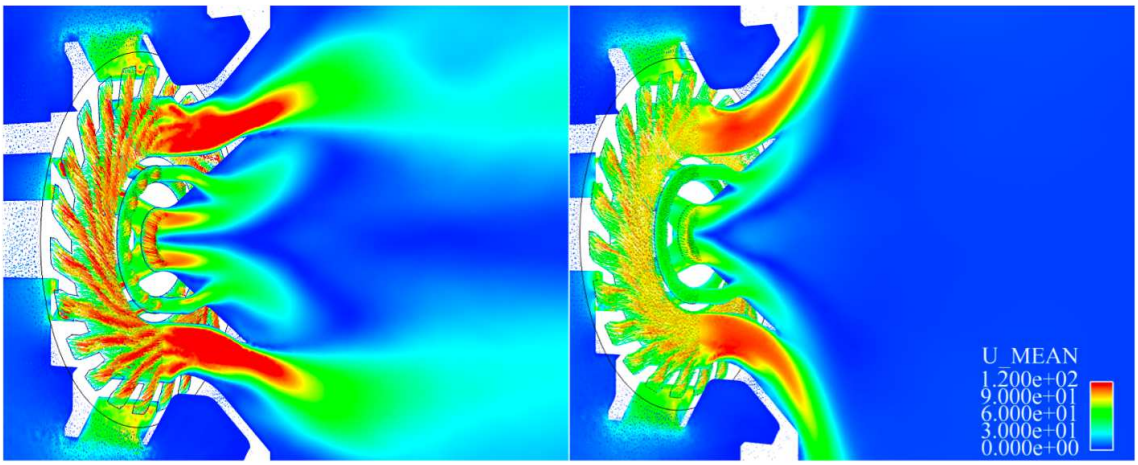

Figure 10.1: Left, simulation YALES-DSMAG representative of the AJ state, right radial jet of simulation YALES-SIGMA, representative of the BB state.

These flow states are:

- a "free Axial Jet" (AJ, Fig. 10.1 left), in which the central vortex core is not influenced by the presence of confinement and behaves like a free swirling jet.
- A "Blasted Breakdown jet" (BB, Fig. 10.1 right), in which the central vortex core has disappeared (or "blasted").

From the analysis of results of Chapter 3 (shown in Fig. 3.21 where they are all cast in the same graph) it appeared that all BB states were obtained for a swirl ratio of the radial jet of $S_r = 0.8 - 0.82$ while all AJ states appeared for smaller values. This suggested that

the critical parameter for the AJ-BB bifurcation was the swirl level.
However, this hypothesis could not be verified in the geometry used in Chapter 3 (Fig. 2.1 left) since too many flow properties (such as the swirl level of the axial stage jets, flow split, pressure drop) changed at once with numerical settings.
To clarify this issue a modified swirler geometry ("adjustable swirler" in Fig. 2.1) was tested in Chapter 4. The geometry simplification allowed to change the swirl level easily and to decouple the dynamics of each jet from the others while keeping all numerical parameters constant: this modified set-up allowed to study bifurcation in a controlled environment.
Results of this second numerical experiment, performed with a high-fidelity LES, confirm that the critical parameter of the system is the swirl level of the radial jet: between $0.75 < S_r < 0.84$ (Fig. 4.27) the flow is bistable and therefore the jet studied in Chapter 3 was very close to a bifurcation threshold. Because of these critical conditions, the change in numerical settings tested in Chapter 3 was able to modify the swirl level just enough to trigger the AJ-BB transition.
LES of Chapter 4 also verified the presence of hysteresis (Fig. 4.27) between the two flow states. These phenomena (bifurcation and hysteresis) were already reported in the experimental literature on confined swirl flows (Chedaille et al. [46], Beer and Chigier [8], Vanierschot et al. [105]) and commonly associated with the Coanda effect.

10.1 Mesh adaptation

The dependency of the swirl level on numerical settings experienced in Chapter 3 was caused by the mesh. Mesh resolution determines the portion of turbulent structures explicitly resolved, turbulent viscosity (Eq.(3.6)) and the level of numerical noise induced by a locally under-resolved flow (see section 3.8.3 and Appendix A).
Such effects, whose magnitude depends on the interaction with the SGS model used, were sufficient to induce a global bifurcation in the flow studied in Chapter 3, a phenomenon which disappeared when mesh resolution was increased at a particular location (see section 3.7). Grid resolution (coupled with SGS modeling) also affected pressure losses (Fig. 3.22).
Even though the mesh is definitely of primary importance for these flows, there is no standard way to do it and its preparation is often made more or less arbitrarily. The quality of the mesh, and so of LES, depends on the experience (or lack of it) of who is preparing the grid. For these reasons,

- because of the importance of the mesh in LES and in particular for the jet studied here,
- because of the lack of a standard way to prepare a LES-suited grid,

the second part of this thesis was focused on mesh adaptation, that is the ability of manipulating a grid based on a set of criteria. Mesh adaptation (presented in Chapters 5-6) was based on a computed solution (which is also known as *a posteriori* adaptation) coupled with simple, empirical criteria.
The LES solver used in this second part was YALES2, an incompressible code (CORIA), and the mesh adapation tool was MMG3D (INRIA).

Mesh adaptation was first tested on the confined round jet of Dellenback et al. [17], in the purely axial case (Chapter 7) and the swirled case (Chapter 8).
For the axial case (Chapter 7), mesh adaptation improved the simulation of turbulence (quantified by Fig. 7.22) by targeting the mesh refinement exactly along the primary path of main vortical activity. In this flow mainly governed by the dynamics of the turbulent structures generated in the shear layer, mesh adaptation improved significantly the quality of the comparison with experimental data with respect to LES performed on homogeneous meshes.
Similarly, mesh adaptation improved LES predictions in the swirled case of Chapter 8. However, while in the axial case (Chapter 7) it was easy to identify why adaptation improved results, in the swirled case (Chapter 8) it was difficult to understand the impact of adaptation on the jet dynamics.
After the preliminary tests on the canonical flow of Dellenback, mesh adaptation was tested on the industrial configuration studied in the first part of this thesis, bridging the two parts that compose this manuscript (Chapter 9). These tests were motivated by the will of resolving the issues discussed in Chapter 3, namely:

1. the insufficient comparison with experimental data, even where the experimental flow state was predicted,

2. the large error on pressure drop predictions.

Mesh adaptation was targeted to master the grid resolution near the walls: while it is obvious that a wall-resolved mesh will improve the prediction of pressure drop for a single passage swirler, the impact of an uniform (or on the contrary nonuniform) y^+ (the wall distance in wall units, Eq. 3.1) in a multiple passages swirler is unknown. Mesh adaptation was used to generate an uniform y^+ in the simulation domain by adjusting the element size close to the solid boundary while all the human-made meshes used in the first part of the thesis were highly nonuniform in this respect.
Results of Chapter 9 demonstrates that y^+ uniformity along the walls surface can significantly improve comparison with experimental data both in terms of the flow velocity profiles (Fig. 9.7-9.8-9.9) and in terms of pressure drop (tables 9.3-9.3).
They also show that the relative repartition of the error made in the boundary layer in the different stages is of importance, since, together with the overall absolute error made on wall friction and on concentrated pressure losses, it was proven to affect pressure drop predictions.
All improvements obtained with mesh adaptation (shown in Chapter 7-8-9) came at no numerical cost increase: simply re-distributing grid resolution can positively affect the LES outcome.
This work can be considered as one of the first efforts in applying mesh adaptation to LES of industrial configuration. Establishing a mesh adaptation framework is mandatory to achieve, in the next future, standardization and optimization of such an important procedure.
Note that the best simulation of the jet of Fig. 10.1 was obtained using mesh adaptation.

Appendix A

Effects of turbulent viscosity in the LOTAR fixed swirler case

This appendix discusses the effects of turbulent viscosity in the LOTAR fixed swirler case presented in chapter 3.
From tables 3.7 & 3.12 is evident that, for the LOTAR fixed swirler case, the AJ state is characterized by a lower swirl ratio ($S_r \approx 0.7$) in the radial jet while the BB state is characterized by an higher swirl ratio ($S_r \approx 0.81$) in the radial jet. This variation of the swirl ratio can be justified only by an *effective geometry* variation due to SGS modeling. Because of the eddy viscosity hypotheses, turbulent viscosity in AVBP and YALES2 is proportional to the strain rate tensor per the turbulent viscosity generated by the SGS model, see section 3.2.2. The level of strain rate inside the swirler is high at the solid boundaries, because of the no slip condition coupled with an insufficient wall resolution. The Dynamic Smagorinsky model generates high levels of turbulent viscosity at the solid boundary while the SIGMA model is built to generate low turbulent viscosity levels. The outcome is that the Dynamic Smagorinky simulations show multiple spots of high turbulent diffusion which damp the flow momentum and that are seen by the flow as obstacles, with the stream lines flowing around them. Even if the mesh is not modified, the flow sees a different section depending on the SGS model used. An example of how a spot of high turbulent diffusion can modify the flow is shown in Fig. A.1: the presence of this obstacle-like zone helps the jet to detach, while its absence make it stick to the wall[1]. In Fig. A.2 are shown the velocity vectors and the field of turbulent viscosity in the radial swirler for LES YALES-DSMAG and YALES-SIGMA.

These two phenomena, high turbulent diffusion and the modification of the effective geometry, have a deep impact in a particular zone: the radial swirler bowl. Here, at the exit of the vane passsages, all the jets coming from the swirler passages merge. In a distance of O(1mm), the velocity magnitude varies from $100[m/s]$ in the core of one jet, to zero, because of the solid boundary, and again to $100[m/s]$ because of the neighbouring jet, Fig. A.3. Note that, considering a boundary layer at a streamwise position $x = 0.01[m]$ (the length of the swirler vane) and a freestream velocity $U_0 = 100[m/s]$, the boundary

[1]It can be argued that the detachment dynamics of the central jet can be related to the swirl number (Eq.(2.2)) of the outermost axial jet, which is ≤ 0.43 for all the detached cases while it is ≥ 0.58 for all the attached ones. Chapter 4 shows how an attached central jet can be obtained with a swirl ≤ 0.43, and that its dynamics are not linked to the swirl number.

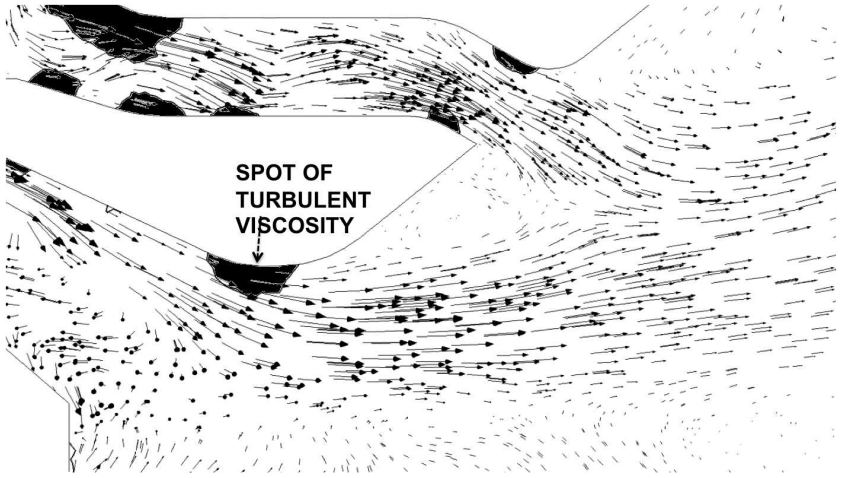

(a) YALES-DSMAG.

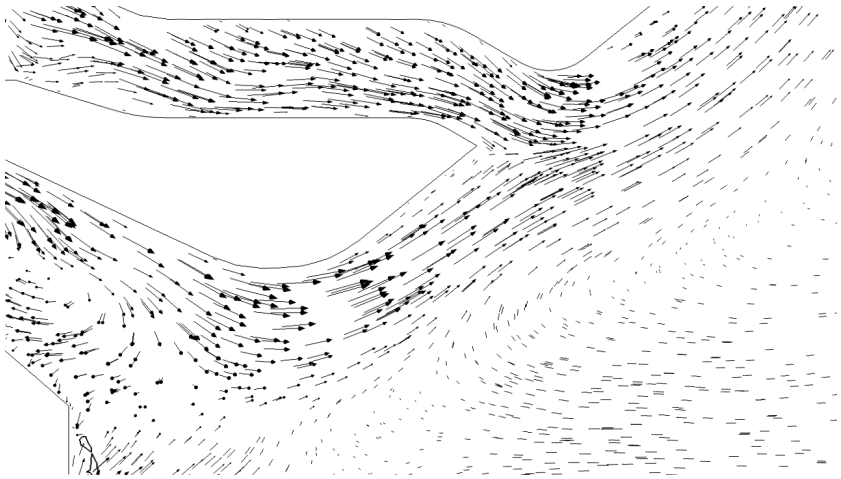

(b) YALES-SIGMA

Figure A.1: Central jet detachment, (a) detached vs. (b) attached. Vector field is the mean flow velocity, the black spot of time averaged turbulent viscosity (corresponding to a $\mu_t/\mu \geq 100$) acts as an obstacle and induces the flow separation.

layer thickness (the distance from the wall at which the mean flow speed reaches 99% the free stream speed, U_0) is $\approx 0.4[mm]$. Considering that the geometric length scales of the flow are of the same order of magnitude, it is now evident why numerous difficulties have been encountered during the simulation this particular area of the flow field.

Because of the large velocity gradient, numerical errors in this region can be large and affect the solution, for instance introducing an additional, un-physical, turbulence to the flow field. Turbulent viscosity generated by the SGS model interacts with the velocity field, causing a damping effect on the turbulence generated by the jet-to-jet interaction (natural or numerically generated), Fig. A.4. The overall effect is a modification of the mean velocity profile with a consequent variation of the swirl ratio of the jet depending on the turbulent viscosity level. The same phenomenon is happening in the outer and inner axial jets, where each jet is separated from its neighbour by a O(1mm) wall. While for

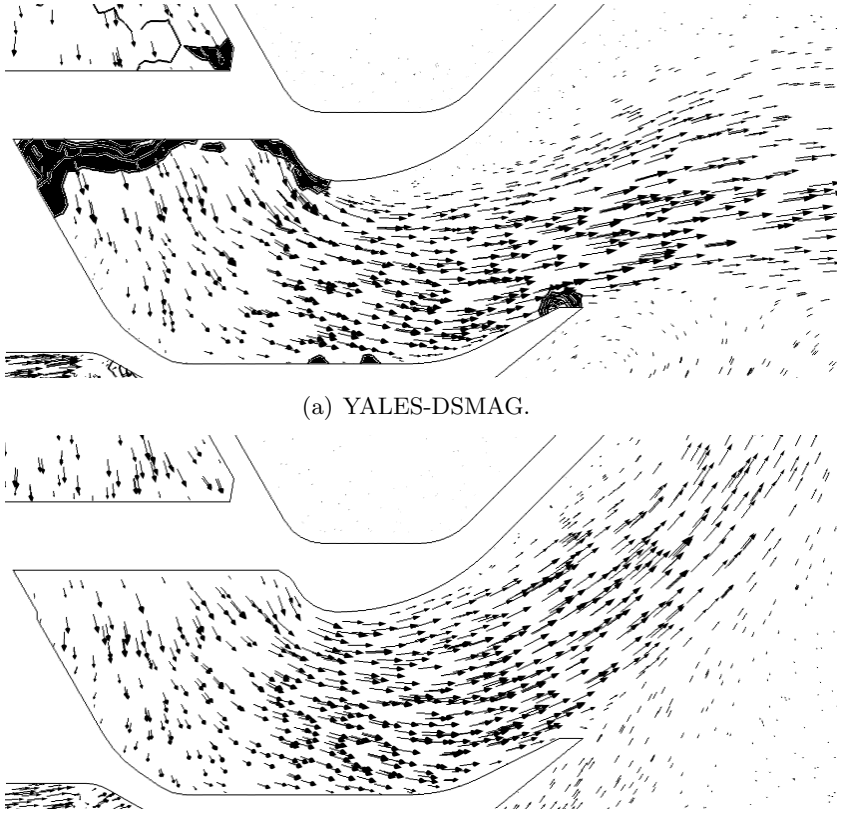

(a) YALES-DSMAG.

(b) YALES-SIGMA

Figure A.2: Turbulent viscosity and velocity vectors inside the radial swirler and inside the diffuser.

the outer axial jet a strong variation of the swirl number is experienced switching from Dynamic Smagorinsky to SIGMA, for the inner jet it is not and all simulations give a measured swirl in the inner axial jet of $S \approx 0.11 - 0.12$.

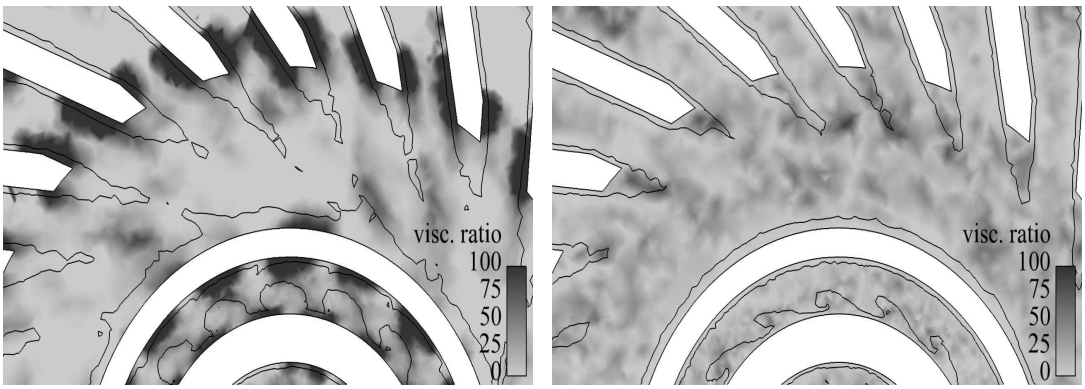

(a) YALES-DSMAG. (b) YALES-SIGMA

Figure A.3: Multiple jets in the LOTAR simulation. Turbulent over laminar viscosity field in the radial swirler vane, line corresponds to $50[m/s]$ velocity magnitude.

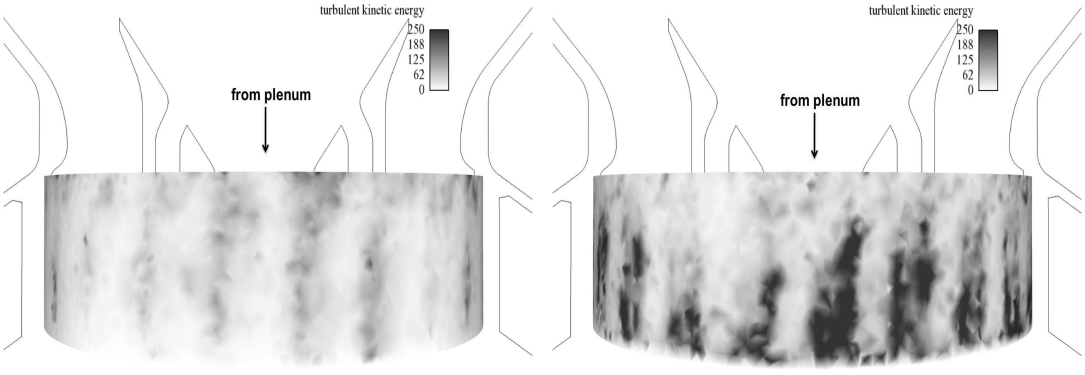

(a) YALES-DSMAG (b) YALES-SIGMA

Figure A.4: Turbulent kinetic energy. The level of resolved turbulence is higher in LES YALES-SIGMA.

Appendix B

Coflow effects on the LOTAR adjustable swirler case

This appendix shows the effects of the coflow speed on the flow structures (and in general of the far field conditions) on the LOTAR adjustable swirler case of chapter 4. Its objective is to verify that the small velocity added in the coflow (Fig. 3.3) has a very limited effect on the results.
For this type of flow (a confined swirling jet) the jet dynamics are mainly governed by the swirler-diffuser geometry and the far field has only a secondary effect on the flow configuration. As shown in Vanierschot et al. [107] it is possible to achieve drastic change in the jet pattern (causing instantaneous transitions such as AJ-WJ or WJ-BB) by modifying the flow field at the injector nozzle and this way activating/deactivating the flow structures generated between the jet outer shear layer and the solid walls. Focusing on LES, this last simulation, named *coflow*, has the same characteristics of simulation high of table 4.1 but it has an higher coflow speed of $10[m/s]$ equivalent to 13% of the jet speed. Data are collected after a period of $50[ms]$, time needed by the coflow jet to reach and overtake the injector ($0.37[m]$ downstream of the coflow B.C. shown in Fig. 3.3). As evident from Fig. B.1, the coflow speed has a reduced influence on the flow direction and the jet remains attached to the side walls of the injector (Fig. B.2) in the BB state. Despite the fact that the size of the recirculation zone (Fig. B.3) is smaller, the jet topology is unaltered as evident from the turbulence intensity and pressure fields (Fig. B.4). Finally, the whole flow field of LES *high* and *coflow* are compared in Fig. B.5.

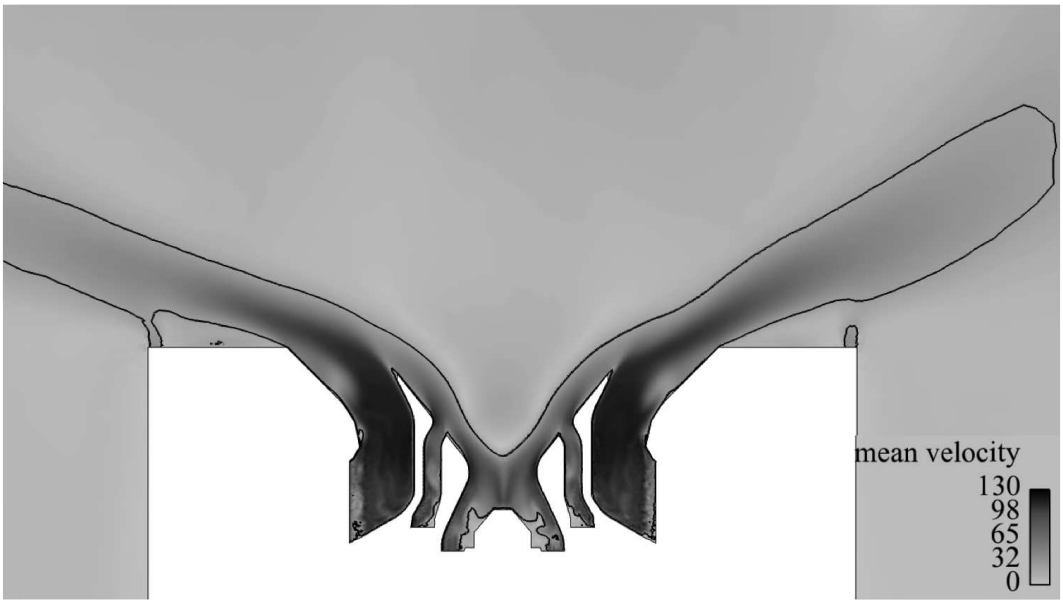

Figure B.1: Flow field and velocity isoline ($U = 20[m/s]$) of simulations *coflow*. The jet opening half-angle is slightly smaller than LES *high* of table 4.5 (Fig. 4.12).

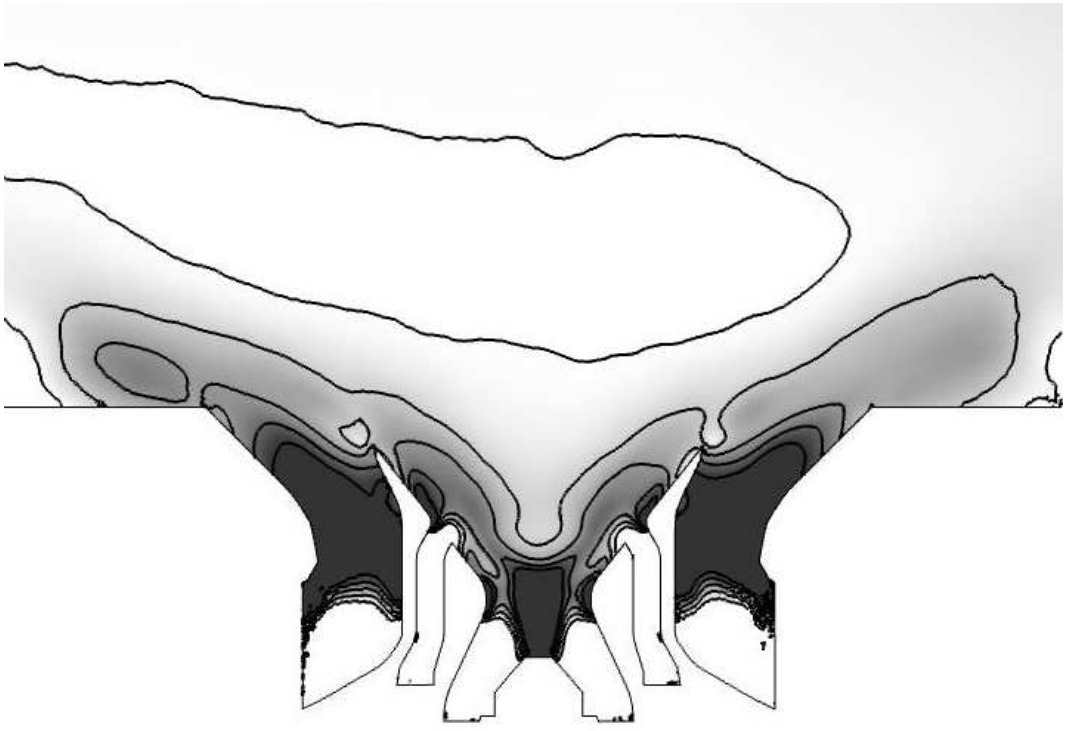

Figure B.2: Pressure field of the *coflow* LES studied here (legend is the same of Fig. 4.15d). A pressure gradient from the side-walls toward the core of the CTRZ is still present as in LES *high* of table 4.5.

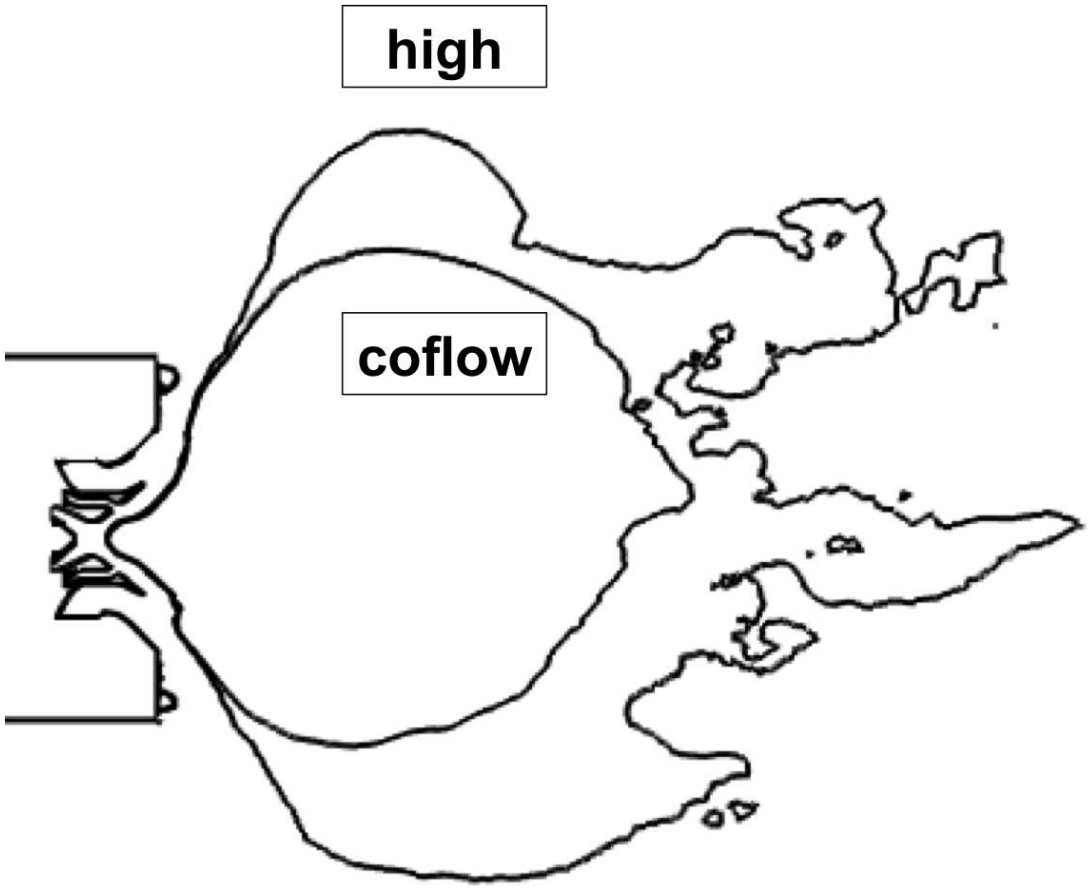

Figure B.3: Comparison of the recirculation bubbles of LES *high* of table 4.5 and *coflow* studied here. Despite the reduction of the size of the CTRZ for LES *coflow*, the flow topology is unaltered with a CTRZ that is equally expanding in the radial and axial directions.

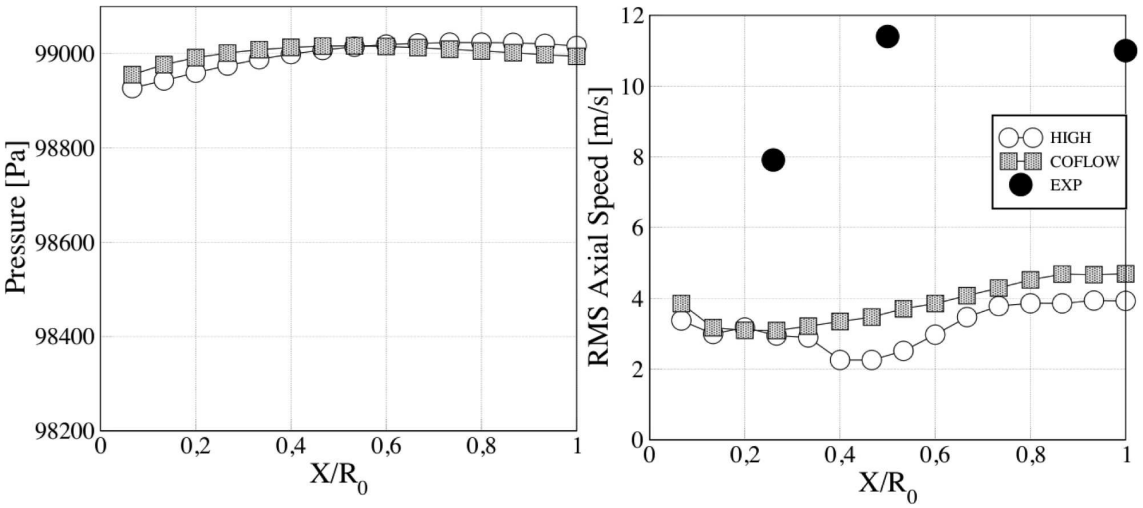

Figure B.4: Axial velocity RMS and pressure distribution measured along the centerline of the geometry. Results are plotted against normalized axial distance (X/R_0) from the swirler ending plate for simulations *high* of table 4.5 and *coflow*.

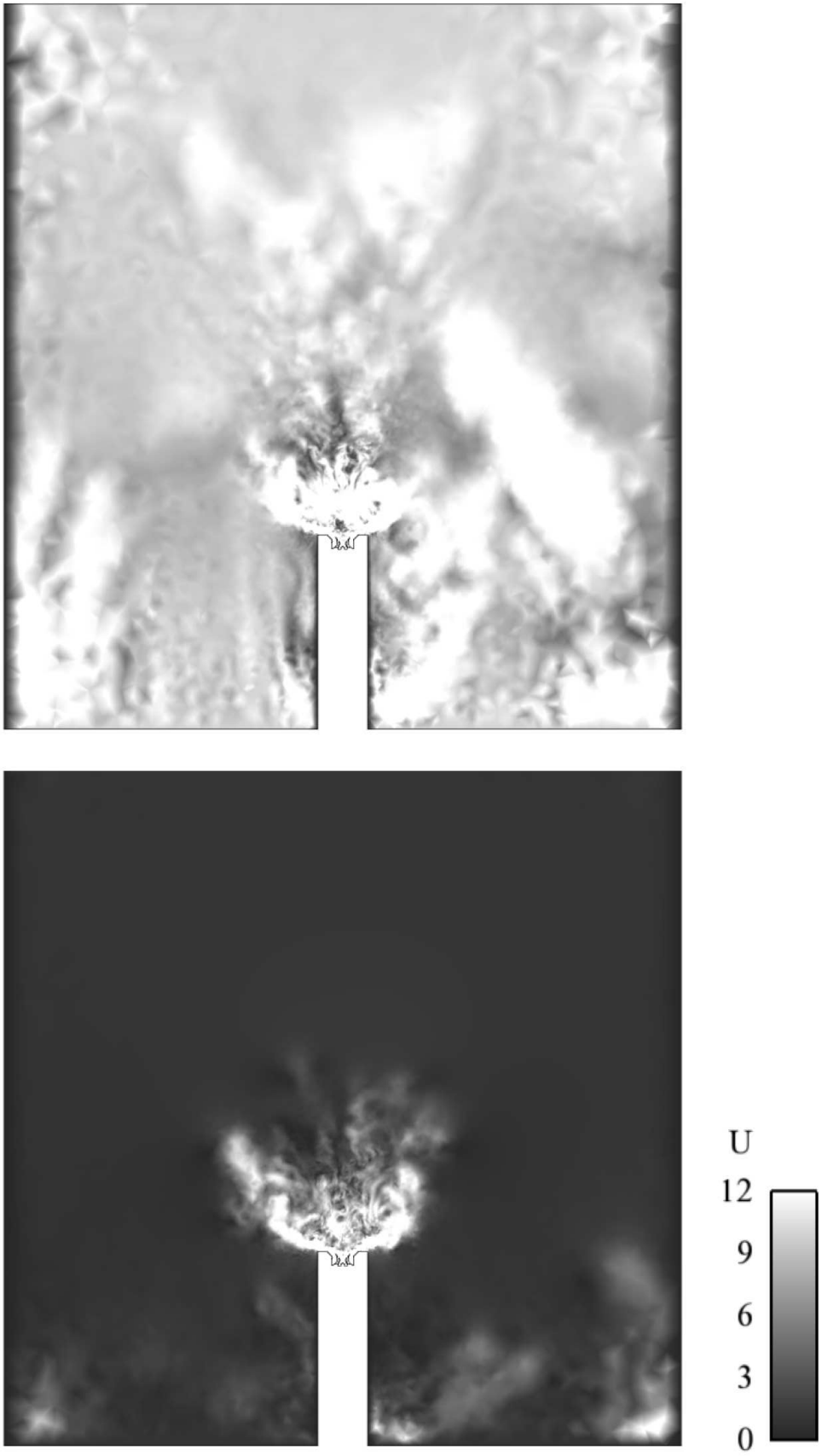

Figure B.5: Far field of simulations *high* of table 4.5 and *coflow*. The higher coflow speed is evident from the instantaneous velocity magnitude field.

Appendix C

Effects of turbulence injection for the "axial" case of Delenback

This appendix shows the effect of turbulence injection for the "axial" case of Dellenback experiment shown in Chapter 7. Turbulence is injected at the inlet of the domain (Fig. 7.1). The amount of turbulence necessary to match experimental data is dependent on the particular mesh and/or LES solver and settings used. For instance, a too coarse mesh or a too dissipative numerical scheme can nullify the effects of turbulence injection by damping it just downstream the injection position. Therefore, this test is performed for one of the simulations/meshes of table 7.2 only and turbulence intensity is adjusted to match experimental data. The mesh chosen (numerical settings do not change for LES of table 7.2) is LES H3 and it is named here $H3_{TJ}$, where the subscript TJ stands for turbulence injection. Turbulence injected has an intensity $TI = u'/U = 0.043$ and a characteristic lenght scale of $10[mm] \approx \frac{1}{5}D_1$.
Results are shown in Fig. C.1 where the velocity profiles of LES $H3_{TJ}$ are compared with the velocity profiles of LES H1, H2 and H3 of table 7.2 and experimental data at the 8 measurement planes of Fig. 7.2.
Fig. C.1 shows that the injection of turbulence allows to better match experimental data at plane 1 and at plane 4 (with the same accuracy of LES H1) without being particularly detrimental for the flow speed at the downstream planes. It is also verifies the assumption of section 7.2.1, namely that results of LES H1 showed the best comparison with experimental data at plane 4 thanks to wall-generated numerical noise. This noise affects the growth rate of the shear layer instability, modifying the flow speed. Finally, Fig. C.2 shows how deep (comparing its negligible effects on the mean velocity profiles shown in Fig. C.1) is the influence of turbulence injection on RMS values.

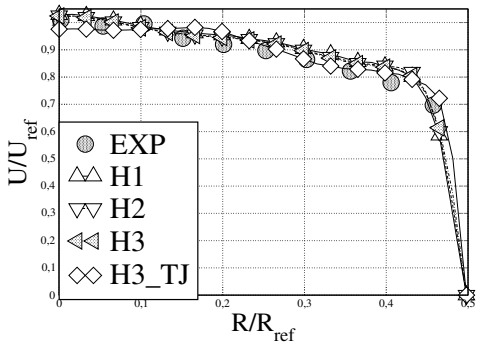

(a) Mean axial velocity profile at plane 2

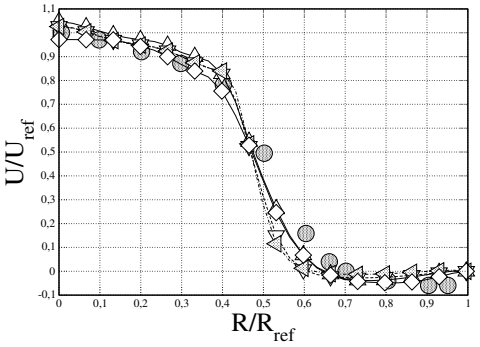

(b) Mean axial velocity profile at plane 4

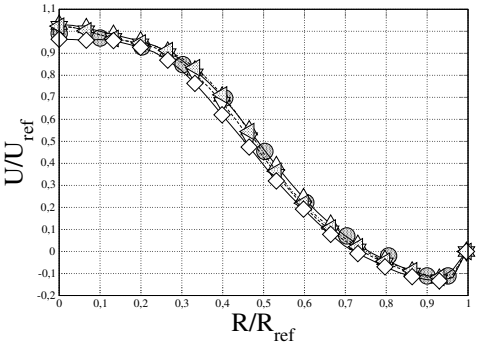

(c) Mean axial velocity profile at plane 5

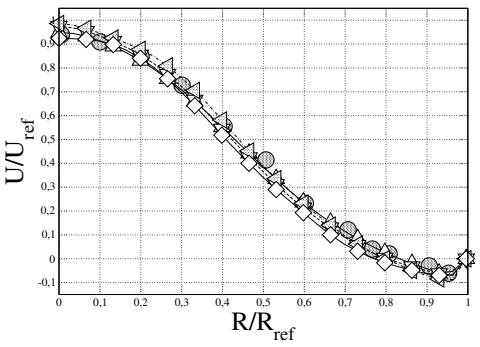

(d) Mean axial velocity profile at plane 6

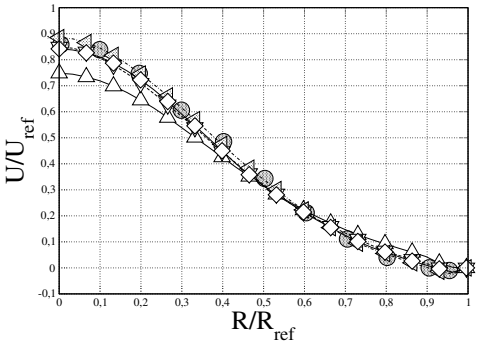

(e) Mean axial velocity profile at plane 7

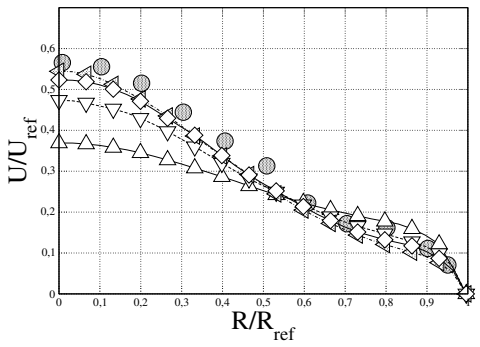

(f) Mean axial velocity profile at plane 8

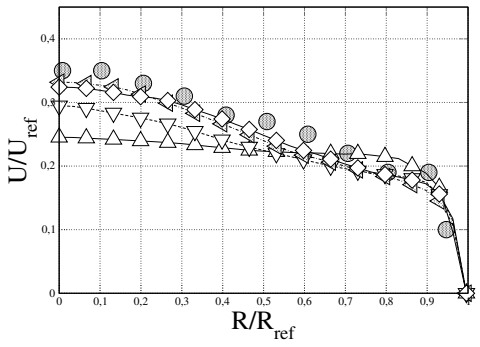

(g) Mean axial velocity profile at plane 9

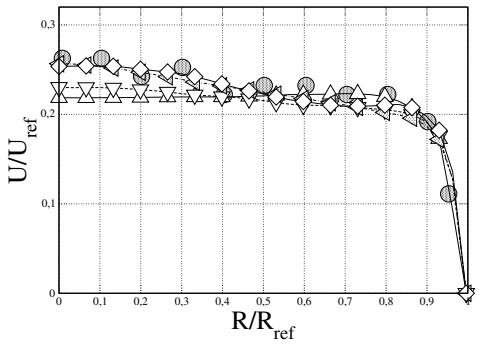

(h) Mean axial velocity profile at plane 10

Figure C.1: Mean axial velocity profiles at the measurement planes of Fig. 7.2 for simulations H1, H2, H3 of table 7.2 and LES H3$_{TJ}$ (TJ stands for turbulence injection).

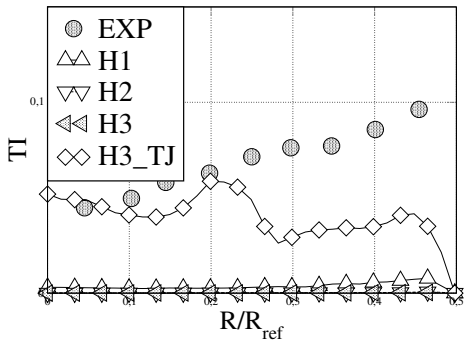

(a) TI axial velocity at plane 2

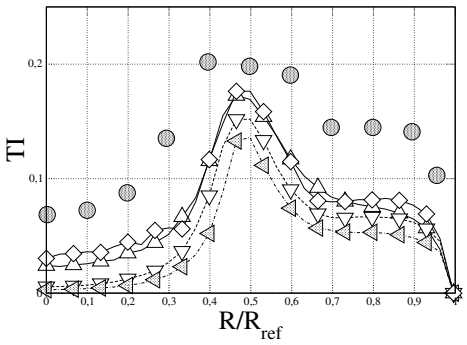

(b) TI axial profile at plane 4

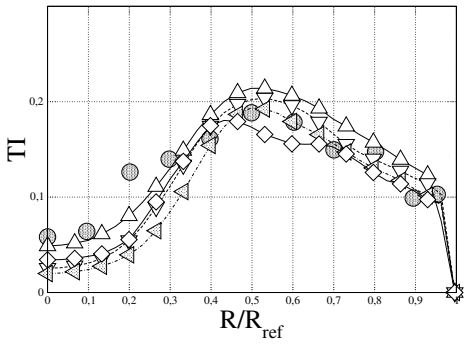

(c) TI axial profile at plane 5

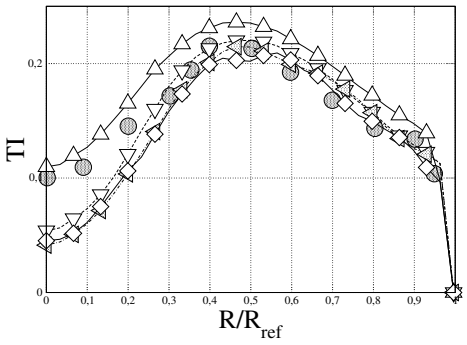

(d) TI axial profile at plane 6

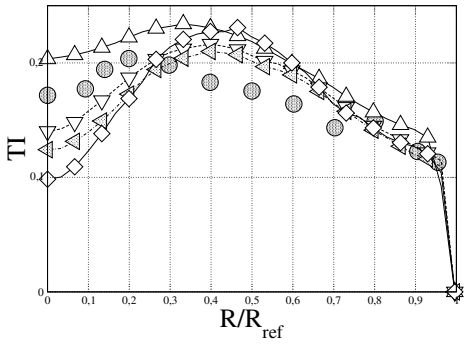

(e) TI axial profile at plane 7

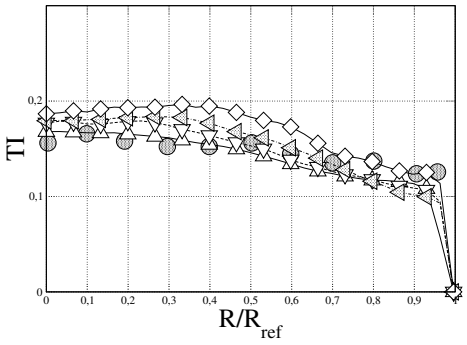

(f) TI axial profile at plane 8

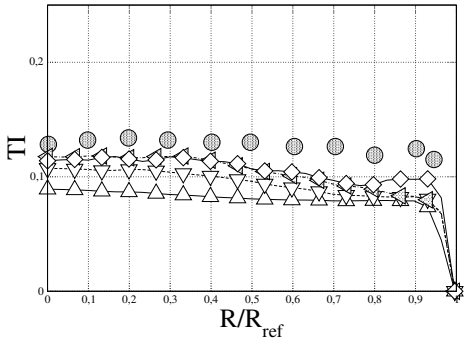

(g) TI axial profile at plane 9

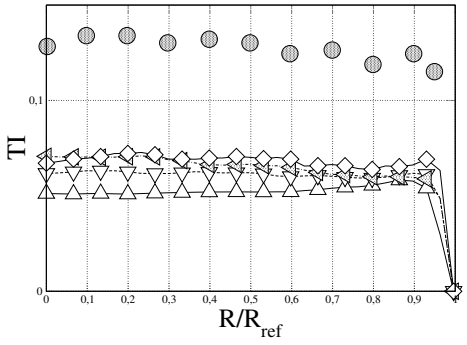

(h) TI axial profile at plane 10

Figure C.2: TI axial profiles ($TI = \frac{u_{RMS}}{u_{ref}} = \frac{u_{RMS}}{8.92[m/s]}$) at the measurement planes of Fig. 7.2 for simulations H1, H2, H3 of table 7.2 and LES H3$_{TJ}$ (TJ stands for turbulence injection).

Appendix D

Comparison of the flow states of LOTAR and Vanierschot

In this appendix, the two flow topologies of LOTAR shown in chapters 3 and 4, the "Axial Jet" (AJ) and the "Blasted Breakdown jet"(BB), are compared with the same flow states of the experimental study of Vanierschot and Van Den Bulck [105]. The comparison is carried on in terms of pressure deficit and turbulence intensity.
Fig. D.1 shows the ratio of the mean, axial, turbulent kinetic energy normalized by the jet kinetic energy U^2 for the LOTAR and Vanierschot's cases [105]. Despite the large geometric discrepancies between the two configurations, normalized turbulence levels are similar in both flows when the same flow state is compared.
Corcerning the pressure deficit (Eq.(2.9)), in both cases the BB state is characterized by a zero pressure deficit, while the AJ states is characterized by a $P_D \approx 1.5$ for Vanierschot's case and $P_D \approx 0.4$ for LOTAR. Note that it was not possible to generate a graph similar to Fig. D.1 for the pressure deficit because of the lack of similar data for Vanierschot's case.

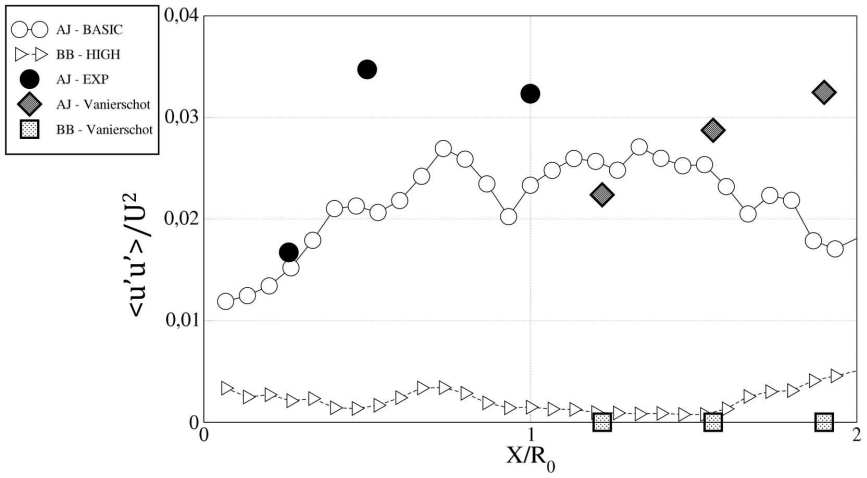

Figure D.1: Comparison of LOTAR LES *basic* and *high* and experimental data (EXP) of Chapter 4 with Vanierschot's results [105] for the AJ and BB states. Normalization conditions for LOTAR are $U = 61.17[m/s]$ and $R_0 = 30[mm]$.

Bibliography

[1] Flying above the clouds. *The Economist*, 2011.

[2] 17th International Meshing Roundtable. *Anisotropic Delaunay mesh adaptation for unsteady simulations*, 1997.

[3] F. Alauzet, P.J. Frey, P.L. George, and B. Mohammadi. 3d transient fixed point mesh adaptation for time-dependent problems: Application to cfd simulations. *Journal of Computational Physics*, 222(2):592 – 623, 2007.

[4] Frédéric Alauzet and Pascal J. Frey. Estimateur d'erreur géométrique et métriques anisotropes pour l'adaptation de maillage. Partie I : aspects théoriques. Rapport de recherche RR-4759, INRIA, 2003.

[5] S. V. Apte, K. Mahesh, M. Gorokhovski, and P. Moin. Stochastic modeling of atomizing spray in a complex swirl injector using large eddy simulation. *Proc. Combust. Inst.*, 32:2257–2266, 2009.

[6] AVBP. Avbp code: www.cerfacs.fr/cfd/avbp_code.php and www.cerfacs.fr/cfd/cfdpublications.html.

[7] D. Barre, M. Kraushaar, G. Staffelbach, V. Moureau, and L.Y.M. Gicquel. Compressible and incompressible les of a swirl experimental burner. In *3rd INCA Colloquim*, 2011.

[8] J. M. Beer and N. A. Chigier. *Combustion aerodynamics*. Krieger, Malabar, Florida, 1983.

[9] T. Brooke Benjamin. Theory of the vortex breakdown phenomenon. *Journal of Fluid Mechanics*, 14:593–629, 11 1962.

[10] P. Billant, J.-M. Chomaz, and P. Huerre. Experimental study of vortex breakdown in swirling jets. *J. Fluid Mech.*, 376:183–219, 1998.

[11] M. Boileau, S. Pascaud, E. Riber, B. Cuenot, L.Y.M. Gicquel, T. Poinsot, and M. Cazalens. Investigation of two-fluid methods for Large Eddy Simulation of spray combustion in Gas Turbines. *Flow, Turb. and Combustion*, 80(3):291–321, 2008.

[12] S. T. Bose, P. Moin, and D. You. Grid-independent large-eddy simulation using explicit filtering. *Phys. Fluids*, 22(10):105103, October 2010.

[13] John J. Cassidy and Henry T. Falvey. Observations of unsteady flow arising after vortex breakdown. *Journal of Fluid Mechanics*, 41(04):727–736, 1970.

[14] Jean Cea. *Approximation variationnelle des problèmes aux limites.* PhD thesis, 1964.

[15] D. R. Chapman and G. D. Kuhn. The limiting behaviour of turbulence near a wall. *J. Fluid Mech.*, 170:265–292, 1986.

[16] Fotini Katopodes Chow and Parviz Moin. A further study of numerical errors in large-eddy simulations. *Journal of Computational Physics*, 184(2):366 – 380, 2003.

[17] P. Dellenback, D. Metzger, and G. Neitzel. Measurement in turbulent swirling flows through an abrupt axisymmetric expansion. *AIAA Journal*, 13(4):669–681, 1988.

[18] Cecile Dobrzynski. *Adaptation de Maillage anisotrope 3D et application a l'aerothermique des batiments.* PhD thesis, Universite Pierre et Marie Curie, Paris VI, 2005.

[19] Cecile Dobrzynski. *MMG3D manual.* INRIA, 2010.

[20] J Dombard, T Poinsot, V Moureau, N Savary, G Staffelbach, and V Bodoc. Experimental and numerical study of the influence of small geometrical modifications on the dynamics of swirling flows. In *CTR, Proceedings of the Summer Program 2012.*

[21] E.Bank. Mesh smoothing using a posteriori error estimates. *SIAM Journal on Numerical Analysis*, Vol. 34(No. 3):pp. 979–997, Jun., 1997.

[22] M.P. Escudier and J.J. Keller. Vortex breakdown: a two stage transition. Technical report, Brown Boveri Research center Baden (Switzerland), 1983.

[23] J. H. Faler and S. Leibovich. Disrupted states of vortex flow and vortex breakdown. *Phys. Fluids*, 20:1395–1400, 1977.

[24] L. Freitag, M. Jones, and P. Plassmann. An efficient parallel algorithm for mesh smoothing. In *Proceedings of the 4th International Meshing Roundtable, Sandia National Laboratories*, 1995.

[25] P.J. Frey and F. Alauzet. Anisotropic mesh adaptation for cfd computations. *Computer Methods in Applied Mechanics and Engineering*, 194(48–49):5068 – 5082, 2005.

[26] Isaac Fried. Condition of finite element matrices generated from nonuniform meshes. 1972.

[27] J. Frøhlich, C. P. Mellen, W. Rodi, L. Temmerman, and M. A. Leschziner. Highly resolved large-eddy simulation of separated flow in a channel with streamwise periodic constrictions. *J. Fluid Mech.*, 526:19–66, 2005.

[28] M. García-Villalba, J. Fröhlich, and W. Rodi. Identification and analysis of coherent structures in the near field of a turbulent unconfined annular swirling jet using large eddy simulation. *Phys. Fluids*, 18, 2006.

[29] M. Germano, U. Piomelli, P. Moin, and W. Cabot. A dynamic subgrid-scale eddy viscosity model. *Phys. Fluids*, 3(7):1760–1765, 1991.

[30] B. J. Geurts and J.Fröhlich. A framework for predicting accuracy limitations in large-eddy simulation. *Phys. Fluids*, 14, 2002.

[31] S. Ghosal. An analysis of numerical errors in large eddy simulations of turbulence. *J. Comput. Phys.*, 125:187 – 206, 1996.

[32] A. K. Gupta, D. G. Lilley, and N. Syred. *Swirl flows*. Abacus Press, 1984.

[33] Wagdi G. Habashi, Julien Dompierrea, Yves Bourgaulta, Djaffar Ait-Ali-Yahiaa, Michel Fortin, and Marie-Gabrielle Vallet. Anisotropic mesh adaptation: towards user-independent, mesh-independent and solver-independent cfd. part i: general principles. *Int. J. Numer. Meth. Fluids*, 32:725–744, 2000.

[34] M. G. Hall. Vortex breakdown. *Ann. Rev. Fluid Mech*, 4:195–217, 1972.

[35] M.G. Hall. The structure of concentrated vortex cores. *Progress in Aerospace Sciences*, 7(53-110), 1966.

[36] G. Hannebique, P. Sierra, E. Riber, and B. Cuenot. Large Eddy Simulation of reactive two-phase flow in aeronautical multipoint burner. In *7th Mediterranean Combustion Symposium - September 11-15*, Chia Laguna, Cagliari, Sardinia, Italy, 2011.

[37] Claudia Hertel and Jochen Fröhlich. Error reduction in les via adaptive moving grids. In Maria Vittoria Salvetti, Bernard Geurts, Johan Meyers, and Pierre Sagaut, editors, *Quality and Reliability of Large-Eddy Simulations II*, volume 16 of *ERCOFTAC Series*, pages 309–318. Springer Netherlands, 2011.

[38] J. Hoffman. computation of mean drag for bluff body problems using adaptive DNS/LES. *SIAM Journal on Scientific Computing*, 27(1):184–207, 2005.

[39] J. Hoffman and C. Johnson. A new approach to computational turbulence modeling. *Computer Methods in Applied Mechanics and Engineering*, 195(23–24):2865 – 2880, 2006.

[40] P. G. Huang and G. N. Coleman. Van driest transformation and compressible wall-bounded flows. *AIAA Journal*, 32(10):2110–2113, 1994.

[41] Weizhang Huang. Variational mesh adaptation: Isotropy and equidistribution. *Journal of Computational Physics*, (174):903–924, 2001.

[42] Y. Huang, S. Wang, and V. Yang. Systematic analysis of lean-premixed swirl-stabilized combustion. *AIAA Journal*, 44(724-740), 2006.

[43] Ying Huang and Vigor Yang. Dynamics and stability of lean-premixed swirl-stabilized combustion. *Progress in Energy and Combustion Science*, 35(4):293 – 364, 2009.

[44] J. C. R. Hunt, A. A. Wray, and P. Moin. Eddies, streams, and convergence zones in turbulent flows. In *Proc. of the Summer Program*, pages 193–208. Center for Turbulence Research, NASA Ames/Stanford Univ., 1988.

[45] A. K. Aziz I. Babuska. On the angle condition in the finite element method. *SIAM J. NUMER. ANAL.*, 13(2), April 1976.

[46] A.K. Chesters J. Chedaille, W. Leuckel. Aerodynamic studies carried out on turbulent jets by the international flame research. *Journal of the institute of Fuel*, 39(311):506–521, 1966.

[47] F. Jaegle. *LES of two-phase flow in aero-engines*. PhD thesis, Université de Toulouse - Ecole doctorale MEGeP, CERFACS - CFD Team, Toulouse, December 2009.

[48] F. Jaegle, J.-M. Senoner, M. Garcia, F. Bismes, R. Lecourt, B. Cuenot, and T. Poinsot. Lagrangian and eulerian simulations of evaporating fuel spray in an aeronautical multipoint injector. *Proc. Combust. Inst.*, 33:2099–2107, 2011.

[49] J. Jimenez. On why dynamic subgrid-scale models work. Technical report, 1995.

[50] J. Jiménez. Turbulence and vortex dynamics. Technical Report Ecole Polytechnique, 2004.

[51] J. Jiménez and R. D. Moser. Large-eddy simulations: where are we and what can we expect? *AIAA Journal*, 23(4):605–612, April 2000.

[52] Won-Wook Kim and Saadat Syed. Large-eddy simulation needs for gas-turbine combustor design. (0331), 2004.

[53] Markus Klein, Johan Meyers, and Bernard J. Geurts. Assessment of les quality measures using the error landscape approach. In Johan Meyers, Bernard J. Geurts, and Pierre Sagaut, editors, *Quality and Reliability of Large-Eddy Simulations*, volume 12 of *ERCOFTAC Series*, pages 131–142. Springer Netherlands, 2008.

[54] A. N. Kolmogorov. The local structure of turbulence in incompressible viscous fluid for very large reynolds numbers. *C. R. Acad. Sci., USSR*, 30:301, 1941.

[55] Matthias Krausaar. *Application of the compressible and low-Mach number approaches to Large-Eddy Simulation of turbulent flows in aero-engines.* PhD thesis, CERFACS, 2011.

[56] A. G. Kravchenko and P. Moin. On the effect of numerical errors in large eddy simulations of turbulent flows. *J. Comput. Phys.*, 131(2):310–322, March 1997.

[57] Y.A. Kuznetsov. *Elements of Applied Bifurcation Theory.* Springer, 1998.

[58] E. Lamballais and J.P. Bonnet. DNS/LES data processing and its relation with experiment, February 2003. ISSN 0377-8312 VKI Lectures Series 2003-03 "Post-processing of experimental and numerical data ISSN 0377-8312.

[59] N. C. Lambourne and D. W. Bryer. The bursting of leading-edge vortices: Some observations and discussions of the phenomenon. Technical Report R. & M, Aeronautical Research Council (G.B.), 1961.

[60] H. Liang and T. Maxworthy. An experimental investigation of swirling jets. *Journal of Fluid Mechanics*, 525:115–159, 1 2005.

[61] T. Loiseleux, J. M. Chomaz, and P. Huerre. The effect of swirl on jets and wakes: Linear instability of the rankine vortex with axial flow. *Physics of Fluids*, 10(5):1120–1134, 1998.

[62] Adrien Loseille and Frédéric Alauzet. Continuous Mesh Model and Well-Posed Continuous Interpolation Error Estimation, 2009. Rapport de recherche INRIA.

[63] Adrien Loseille, Alain Dervieux, Pascal Frey, and Frederic Alauzet. Achievement of global second-order mesh convergence for discontinuous flows with adapted unstructured meshes. In *18th AIAA computatonal Fluid Dynamics Conference*, 2007.

[64] O. Lucca-Negro and T. O'Doherty. Vortex breakdown: a review. *Prog. Energy Comb. Sci.*, 27:431–481, 2001.

[65] D. Lucor, J. Meyers, and P. Sagaut. Sensitivity analysis of large-eddy simulations to subgrid-scale-model parametric uncertainty using polynomial chaos. *Journal of Fluid Mechanics*, 585:255–279, 2007.

[66] T. S. Lund. The use of explicit filters in large eddy simulation. *Computers and Mathematics with Applications*, 46(4):603–616, August 2003.

[67] K. Mahesh, G. Constantinescu, and P. Moin. A numerical method for large-eddy simulation in complex geometries. *J. Comput. Phys.*, 197(1):215–240, 2004.

[68] C. Martin, L. Benoit, Y. Sommerer, F. Nicoud, and T. Poinsot. Les and acoustic analysis of combustion instability in a staged turbulent swirled combustor. *AIAA Journal*, 44(4):741–750, 2006.

[69] Carl Ollivier-Gooch M.Batford, Lori A. Freitag. Computational study of the effect of unstructured mesh quality on solution efficiency.

[70] C. Meneveau and J. Katz. Scale-invariance and turbulence models for large eddy simulation. *Ann. Rev. Fluid Mech*, 32:1–32, 2000.

[71] J. Meyers, B.J. Geurts, and P. Sagaut. A computational error-assessment of central finite-volume discretizations in large-eddy simulation using a smagorinsky model. *Journal of Computational Physics*, 227(1):156 – 173, 2007.

[72] Johan Meyers and Pierre Sagaut. Is plane-channel flow a friendly case for the testing of large-eddy simulation subgrid-scale models? *Physics of Fluids*, 19(4):048105, 2007.

[73] R. Mittal and P. Moin. Suitability of upwind-biased finite difference schemes for large-eddy simulation of turbulent flows. *AIAA Journal*, 35:1415–1417, 1997.

[74] P. Moin and S. V. Apte. Large-eddy simulation of realistic gas turbine combustors. *AIAA Journal*, 44(4):698–708, 2006.

[75] Stèphane Moreau. Private conversation, September 2013.

[76] V. Moureau, P. Domingo, and L. Vervisch. From large-eddy simulation to direct numerical simulation of a lean premixed swirl flame: Filtered laminar flame-pdf modeling. *Combust. Flame*, in press, 2011.

[77] V. Moureau, G. Lartigue, Y. Sommerer, C. Angelberger, O. Colin, and T. Poinsot. Numerical methods for unsteady compressible multi-component reacting flows on fixed and moving grids. *J. Comput. Phys.*, 202(2):710–736, 2005.

[78] JM Beer N Syred. Vortex core precession in high swirl flows. In *The second International JSME Symposium on Fluid Machinery and Fluidics, Tokyo*, volume 2, pages 111–120. JSME, 1972.

[79] F. Nicoud and F. Ducros. Subgrid-scale stress modelling based on the square of the velocity gradient. *Flow, Turb. and Combustion*, 62(3):183–200, 1999.

[80] Franck Nicoud, Hubert Baya Toda, Olivier Cabrit, Sanjeeb Bose, and Jungil Lee. Using singular values to build a subgrid-scale model for large eddy simulations. *Phys. Fluids*, 23, 2011.

[81] K Oberleithner, S Terhaar, L Rukes, and C O Paschereit. Why non-uniform density suppresses the precessing vortex core. In *Proceedings of ASME Turbo Expo 2013*.

[82] F. Bismes-F. Simon P. Gajan, J. Apeloig. Kiai deliverable d2.3.1: Experimental characterization of the injector. 2011.

[83] P. Palies. *Dynamique et instabilies de combustion de flammes swirlees*. Phd thesis, Ecole Centrale Paris, 2010.

[84] Noma Park and Krishnan Mahesh. Analysis of numerical errors in large eddy simulation using statistical closure theory. *Journal of Computational Physics*, 222(1):194 – 216, 2007.

[85] P.; Reynolds W.C. Pauley, L.L.; Moin. The structure of two-dimensional separation. *J. Fluid Mech.*, 1990.

[86] U. Piomelli, W. H. Cabot, P. Moin, and S. Lee. Subgrid-scale backscatter in turbulent and transitional flows. *Phys. FluidsA*, 3(7):1766–1771, July 1991.

[87] T. Poinsot and S. Lele. Boundary conditions for direct simulations of compressible viscous flows. *J. Comput. Phys.*, 101(1):104–129, 1992.

[88] T. Poinsot and D. Veynante. *Theoretical and Numerical Combustion*. R.T. Edwards, 2nd edition, 2005.

[89] S. B. Pope. *Turbulent flows*. Cambridge University Press, 2000.

[90] S. B. Pope. Ten questions concerning the large-eddy simulation of turbulent flows. *New Journal of Physics*, 6:35, 2004.

[91] S. Roux, G. Lartigue, T. Poinsot, U. Meier, and C. Bérat. Studies of mean and unsteady flow in a swirled combustor using experiments, acoustic analysis and large eddy simulations. *Combust. Flame*, 141:40–54, 2005.

[92] M. Rudgyard. Integrated preprocessing tools for unstructured parallel cfd applications. Technical Report TR/CFD/95/08, CERFACS, 1995.

[93] M. Rudgyard, T. Schoenfeld, R. Struijs, G. Audemar, and P. Leyland. A modular approach for computational fluid dynamics. Technical Report TR/CFD/95/07, CERFACS, 1995.

[94] P. Sagaut. *Large eddy simulation for incompressible flows*. Springer, 2002.

[95] M. Sanjosé, E. Riber, L. Gicquel, B. Cuenot, and T. Poinsot. Large Eddy Simulation of a two-phase reacting flow in an experimental burner. In *ERCOFTAC Workshop - DLES7*, pages 251–263, Trieste, Italy, September 2008.

[96] T. Sarpkaya. On stationary and travelling vortex breakdowns. *J. Fluid Mech.*, 45:545–559, 1971.

[97] A. Scotti, C. Meneveau, and M. Fatica. Generalized smagorinski model for anisotropic grids. *Phys. Fluids*, 9(6):1856–1858, 1997.

[98] A. Scotti, C. Meneveau, and D. K. Lilly. Generalized smagorinski model for anisotropic grids. *Phys. Fluids*, 5(9):2306–2308, 1993.

[99] L. Selle, L. Benoit, T. Poinsot, F. Nicoud, and W. Krebs. Joint use of compressible large-eddy simulation and helmoltz solvers for the analysis of rotating modes in an industrial swirled burner. *Combust. Flame*, 145(1-2):194–205, 2006.

[100] L. Selle, G. Lartigue, T. Poinsot, R. Koch, K.-U. Schildmacher, W. Krebs, B. Prade, P. Kaufmann, and D. Veynante. Compressible large-eddy simulation of turbulent combustion in complex geometry on unstructured meshes. *Combust. Flame*, 137(4):489–505, 2004.

[101] Jean-Mathieu Senoner. *Simulation aux Grandes Échelles de l'écoulement diphasique dans un brûleur aéronautique par une approche Euler-Lagrange*. PhD thesis, CERFACS, 2010.

[102] N. Syred. A review of oscillation mechanims and the role of the precessing vortex core in swirl combustion systems. *Prog. Energy Comb. Sci.*, 32(2):93–161, 2006.

[103] L. Thobois, G. Rymer, and T. Souleres. Large-eddy simulation in IC engine geometries. *SAE*, (2004-01-1854), 2004.

[104] L. Thobois, G. Rymer, T. Souleres, T. Poinsot, and B. Van den Heuvel. Large-eddy simulation for the prediction of aerodynamics in IC engine. *Int. J. Vehicle Des.*, 39(4):368–382, 2005.

[105] M. Vanierschot and E. Van den Bulck. Hysteresis in flow patterns in annular swirling jets. *Experimental Thermal and Fluid Science*, 31(6):513 – 524, 2007.

[106] M. Vanierschot and E. Van den Bulck. Influence of the nozzle geometry on the hysteresis of annular swirling jets. *Combustion Science and Technology*, 179(8):1451–1466, 2007.

[107] M. Vanierschot, T. Persoons, and E. Van den Bulck. A new method for annular jet control based on cross-flow injection. *Physics of Fluids*, 21(2):25103–25112, 2009.

[108] M. Vanierschot and E. Van den Bulck. Computation of a drastic flow pattern change in an annular swirling jet caused by a small decrease in inlet swirl. *International Journal for Numerical Methods in Fluids*, 59(5):577–592, 2009.

[109] Shanwu Wang, Shih-Yang Hsieh, and Vigor Yang. Unsteady flow evolution in swirl injector with radial entry. i. stationary conditions. *Physics of Fluids*, 17(4):045106, 2005.

[110] Shanwu Wang and Vigor Yang. Unsteady flow evolution in swirl injectors with radial entry. ii. external excitations. *Physics of Fluids*, 17(4):045107, 2005.

[111] Shanwu Wang, Vigor Yang, George Hsiao, Shih-Yang Hsieh, and Hukam C. Mongia. Large-eddy simulations of gas-turbine swirl injector flow dynamics. *J. Fluid Mech.*, 583:99–122, 2007.

[112] R. Wille and H. Fernholz. Report on the first european mechanics colloquium, on the coanda effect. *Journal of Fluid Mechanics*, 23(04):801–819, 1965.

Appendix E

Paper accepted for publication (October 2013) in "Computers and Fluids".

LES of bifurcation and hysteresis in confined annular swirling flows

Mario Falese[1]

Centre Europeen de Recherche et de Formation Avancee en Calcul Scientifique (CERFACS), 31057 Toulouse, France.

L.Y.M. Gicquel

Centre Europeen de Recherche et de Formation Avancee en Calcul Scientifique (CERFACS), 31057 Toulouse, France.

Thierry Poinsot

Institut de Mecanique des Fluides de Toulouse (IMFT), 31100 Toulouse, France.

Abstract

This paper presents a LES based study of two swirling confined jet configurations corresponding to an aeronautical injection system. The objectives are to demonstrate that LES codes become sensitive to numerical parameters (grid, SGS model) in such cases and that this is due to the fact that these flows are close to bifurcating conditions because of the presence of swirl and confinement walls. To demonstrate this, in the first configuration ('full swirler'), the swirler/plenum ensemble is computed while only the swirler without plenum is computed in the second ('adjustable swirler'): this simplification allows to vary swirl continuously and explore bifurcation diagrams

[1]Corresponding author, falese@cerfacs.fr, tel. +330561193109.

where the control parameter is the mean swirl number. These numerical results are compared to a similar study performed experimentally by Vanierschot and Van Den Bulck [1]. They confirm that certain confined swirling flows are intrinsically submitted to bifurcations. In the context of LES this leads to a large sensitivity of the simulation results to numerical parameters, a property which is not observed in most other non swirling or non confined situations.
Keywords: LES, swirl flows, bifurcation, hysteresis, numerical simulations, swirling jets, aeronautical injector

---

Nomenclature

D_0	=	jet characteristic diameter $[m]$
R_0	=	jet characteristic radius $[m]$
U_0	=	jet characteristic speed $[m/s]$
x, X	=	axial position $[m]$
r, R	=	radial position $[m]$
S	=	swirl number $[-]$
u_a	=	axial velocity $[m/s]$
u_θ	=	tangential velocity $[m/s]$
u_r	=	radial velocity $[m/s]$
U	=	jet velocity $[m/s]$
ρ	=	density $[kg/m^3]$
Δ	=	grid size $[m]$
T	=	temperature $[K]$
P	=	pressure $[kg/s^2/m]$
P_{atm}	=	atmospheric pressure $[kg/s^2/m]$
P_D	=	normalized subpressure $[-]$
y^+	=	nondimensional wall distance $[-]$
$Pope$	=	Pope criterion [2] $[-]$
k_{res}	=	resolved, turbulent kinetic energy $[m^2/s^2]$
k_{sgs}	=	SGS, turbulent kinetic energy $[m^2/s^2]$
ν_t	=	turbulent viscosity $[m^2/s]$
C_m	=	SGS model constant $[-]$
C_M	=	constant $[-]$
$\tilde{u}$	=	filtered velocity $[m/s]$
$D_m(\tilde{u})$	=	differential operator $[1/s]$

1. Introduction

The objectives of this work are (1) to study bifurcation in confined swirling flows, typically swirlers used in combustion system, (2) to indicate specific aspects of LES methods to which careful attention must be paid for a successful simulation of an industrial swirling flow. Swirling jets are essential elements of many combustion chambers and lead to complex flows which control the fuel atomization, the shape of the recirculating zone produced in front of the swirler and ultimately a large part of the engine performances. Experimentalists know that bifurcation is a common feature in many swirling flows where multiple instabilities take place [3]. The most common of them is vortex breakdown [4, 5], which occurs when reverse flow takes place along the jet axis [6] because of the adverse pressure gradient induced by the conservation of circulation and the jet expansion [4], as first proposed by Hall [7]. Seven different types of vortex breakdown have been identified depending on the swirl and Reynolds number [3] but there are numerous parameters ranges for which "two forms (or more) can exist and transform spontaneously into each other" [5]. Swirl intensity is one of the parameters controlling transition between flow states and its effects will be analyzed here using LES, focusing the investigation on an aeronautical swirl injector. Two geometries are analyzed in this paper; in the first, named full swirler, the plenum (located upstream of the injector) and the swirler passages are included in the simulation domain (Fig. C.1). Results of the full swirler case show that LES can bifurcate depending on the grid resolution inside the radial swirler, under

the same inflow conditions. This property is observed exactly in the same manner for the two LES codes used here: AVBP [8, 9] & YALES2 [10] (a compressible and an incompressible LES solver respectively).

In the second geometry, named adjustable swirler (Fig. C.1), the simulation domain, extracted from the full geometry of the full swirler case, starts downstream of the swirler vanes. The three counter-rotating swirlers, which together form the swirl injector, are replaced by a set of boundary conditions (B.C.s) in order to vary the swirl intensity as desired. This modification allows to transform the original, swirl injector into an adjustable swirl device which can be used to change swirl over a wide range and to explore the resulting flow topologies. The jet states generated in the adjustable swirler case show common, peculiar, properties with the experimental results of Vanierschot and Van Den Bulck [1]. Even if the exact limits of the different states and the hysteresis patterns differ (as a consequence of the different geometries), both the present LES of an aeronautical swirler and the simpler configuration of Vanierschot et al. [1], exhibit similar bifurcations controlled by the swirl level and induced by the presence of confinement walls. This suggests that LES of confined swirling flows can be difficult because of their natural sensitivity to small swirl level variations: in the real world, this sensitivity leads to bifurcations and hysteresis mechanisms; in LES, it explains why simulation results of swirling flows are very sensitive to small details of the numerical setup (mesh, SGS model, boundary conditions) and require much more attention. Section 2 first recalls evidences of bifurcation in

swirling flows obtained experimentally and presents a jet states classification based on flow properties. Section 3 describes the swirler investigated using LES here in the full swirler case and presents the effects of bifurcation observed for this flow. The source of these bifurcations is identified in section 4, where the adjustable swirler is computed and a bifurcation diagram depending on the swirl number is constructed. Results of section 4 shows that LES is sensitive to numerical parameters in the full swirler case because the jet has a swirl number corresponding to an hysteresis zone, which is captured in the adjustable swirler LES.

2. Bifurcation in confined swirling flows: experimental evidence.

This section discusses flow states which can appear in confined swirling flows because of the proximity of solid boundaries. Above a critical swirl strength, confinement walls alter the expansion angle of the jet, which can attach to the sidewalls and behave like a radial jet, a phenomenon similar to the Coanda effect [12]. The critical swirl number at which this transition takes place is dependent on the nozzle geometry as several phenomena such as separation of the jet, Coanda effect and jet expansion angle all play a role. In Chedaille et al. [13], three different swirling jet configurations appear depending on the nozzle opening angle or on the expansion rate of the divergent nozzle. Similar jet configurations and recirculation zones are reported by Beer and Chigier [14], in a qualitative manner and more recently by Vanierschot and Van Den Bulck [1]. The experiment of Vanierschot et

al. [1], provides a quantitative analysis of a flow with variable swirl and it will be used as a reference example to classify flow states. Vanierschot et al. [1], investigate the influence of swirl on an annular jet with a stepped-conical expansion ($Re = 11000$), identifying four, distinct flow states.

The first two states identified by Vanierschot et al. [1], are named here, "Un-broken axial jet" (UJ) and "free Axial Jet" (AJ) (Fig.C.2). UJ states are obtained when $S < 0.4$ while AJ states appear for $S \geq 0.4$, where the swirl number S is defined by:

$$S = \frac{\int_A \rho u_a u_\theta r dA}{R_0 \int_A \rho u_a u_a dA}. \tag{1}$$

At $S = 0.4$, vortex breakdown takes place in this configuration. The transition between the "Axial Jet" and the "Weak axial Jet" (WJ), as named here, and the transition between the WJ and the "Blasted Breakdown jet" (BB), as named here, take place as follows (Fig. C.3).

First, increasing the swirl number up, from state AJ, to the second critical threshold of $S = 0.6$, the flow bifurcates to the WJ state. The AJ-WJ transition is the result of the attachment of the jet to the side walls of the nozzle (Fig.C.2) which causes a widening of the expansion angle of the jet and the creation of a "corner recirculation zone" between the jet and the diffuser walls [15]. This bifurcation is characterized by an abrupt expansion of the Central Toroidal Recirculation Zone (CTRZ) which doubles its diameter (Fig. C.2). At the same time, the azimuthal velocity, the sub-pressure in the CTRZ and turbulence levels, decrease. Because of hysteresis, the WJ state

remains stable even when swirl is decreased back to values which are lower than the transition point AJ-WJ ($S = 0.6$). At $S = 0.5$ (transition WJ-BB), the jet "attaches to the horizontal wall of the infinite expansion and a purely radial jet is formed" [1], a phenomenon also known as the Coanda effect. A third bifurcation takes place: the recirculation zone widens even more (its "eye" has disappeared from Fig. C.2); sub-pressure, tangential velocity and turbulent kinetic energy drop to zero close to the flow centerline (where the vortex breakdown, in the WJ state, is located). The characteristics of the three flow states of interest for the current study are summarized in table C.1: after each transition (AJ-WJ-BB) CTRZ expands, tangential velocity and subpressure (which are inter-related) diminish, turbulence intensity reduces. For a swirl number of 0.3, for example, two very different states (UJ and BB) can be obtained (Fig. C.3).

Bifurcation and hysteresis described in [1] are the result of a variety of mechanisms (jet expansion angle related to the swirl level, jet attachment to the nozzle walls, dynamics of the corner recirculation zone [15]) which are configuration dependent.

3. LES of an aeronautical swirl injector: full swirler case.

The first part of the present work focuses on mesh effects on LES of an industrial swirling flow, a configuration more complex than the Vanierschot geometry [1]. To make sure that conclusions are not code dependent, two completely different LES solvers have been tested: AVBP [8, 9] &

YALES2 [10], a compressible and an incompressible LES solver respectively, whose characteristics are recalled in Appendix B at the end of this paper. The configuration corresponds to an aeronautical liquid fuel injector which has been experimentally investigated at ONERA (Office National d'Etudes et Recherches Aerospatiales) in the framework of the European project KIAI (Knowledge for Ignition Acoustics and Instabilities). It consists of "a pilot injection system (Fig. C.4) surrounded by two counter-rotating axial swirlers and a multipoint injection system, surrounded by a radial swirler" [11]. Experimental measurements were taken in open atmosphere at 99000$[Pa]$ and $270K$. The injector was fed with air. The mass flow rate studied here is 138$[g/s]$, introduced via an upstream plenum; the pressure drop corresponding to these conditions is 4800$[Pa]$. Two passages connect the plenum to the open atmosphere: the swirler, which is explicitly resolved in LES; a cooling film at the periphery of the injector, which is reproduced using a boundary condition (Fig. C.4).

The swirler is fed by the plenum inlet shown in Fig. C.4, while the amount of mass flow rate evacuated by the cooling film is obtained from the permeability measurements of ONERA. The Reynolds number of the jet is 75000, considering a jet speed $U_0 = O(75)[m/s]$, a characteristic length scale (size of the annular flow passage) of $O(10)[mm]$ and a kinematic viscosity of $O(10^{-5})[m^2/s]$. The swirl number is measured before jets merge into common structures (Fig. C.5). Note that the swirl number of the radial swirler jet, evaluated on surface S3 of Fig. C.5B, is simply a measure of the

angular momentum introduced into the flow by the radial jet for a given mass flow rate, since radial velocity is used in Eq.(1) instead of axial velocity. In order to mimic open atmosphere, the swirler is placed inside a cylindrical box ("far field" in Fig. C.4) with a diameter and a streamwise elongation of 24 & 25 swirler diameters respectively ($25D_0 = 1.5[m]$) (Fig. C.4). Here, another set of boundary conditions is set up: the simulation outlet, with an imposed pressure of $99000[Pa]$; an inlet coflow with an imposed velocity of $1[m/s]$ (1.3% of U_0); solid walls at the periphery of the box. In the current analysis, the zone upstream of the injector is included (Fig. C.4) and the largest flow structures generated by the jet in the cylindrical box are explicitly resolved. To test the effects of the coflow, a simulation was performed imposing a higher streamwise velocity ($10[m/s]$) for simulation high of section 4: the jet is not modified, confirming, as shown in [16], that the coflow speed has no major influence on the flow structure. Finally, all solid boundaries present in the full swirler configuration are imposed as adherent, impermeable, adiabatic walls (table C.2). Imposed boundary values are the same in both codes (AVBP [8, 9] & YALES2 [10]).

Two meshes are used for the full swirler case, named basic & optimized grids in Fig. C.6: they contain 14081708 & 15873485 tetrahedra respectively. The basic & optimized grids have the same resolution except in the radial swirler (Fig. C.7). The optimized grid was generated from the analysis of the characteristics of the radial jet (Fig. C.5) in the basic grid. The radial jet showed a variation of O(10%) of the swirl level changing the SGS model (these

results are not shown here) which suggested a localized mesh refinement in this zone, inside the radial swirler.

Four simulations are performed in the full swirler case (table C.3) each of them initialized using a zero velocity flow field. Results show that the two LES codes behave similarly and that both predict results which depend on the grid: with the optimized grid, an axial jet (AJ) in which the flow detaches from the nozzle and is mainly axially oriented (Fig. C.8, right); with the basic grid, a Blasted Breakdown jet (BB), with the jet following the geometric curvature of the device (Fig. C.8, left). Note that the detachment/attachment dynamics of the jet from the nozzle walls are crucial to predict the flow state and require a fine grid resolution to be properly simulated.

As in [1], the AJ state is characterized by a recirculation zone smaller than one injector diameter and a high tangential velocity (Fig. C.9), a high level of turbulent activity and a high subpressure ($P_D \approx 0.56$) close to the injector orifice (Fig. C.10). On the contrary, the BB state is characterized by a wider recirculation zone and by (inside the CTRZ) a zero tangential velocity, a negligible turbulent activity and sub-pressure (Fig. C.9-C.10).

Obviously, both AJ and BB states can appear as a function of the local grid resolution, basic vs. optimized grid see Fig. C.7, in the results of both LES codes, AVBP [8, 9] & YALES2 [10]. The differences between the two codes are visualized in Fig. C.8, and quantified in terms of the velocity profiles in Fig. C.9. They are negligible compared to the bifurcation induced by the local grid resolution. Experimental data fit quite well the velocity profiles and

RMS distribution of the AJ state (Fig. C.9 and C.10) while results associated to the BB state are clearly very different from the experimental data. LES captures two flow states here (AJ and BB) while the experiment is showing only an AJ state.

An interesting observation in table C.3 is that state BB is obtained in both codes for a swirl number of $S = 0.8 - 0.82$ (measured on section S3 of Fig C.5), while state AJ is obtained for a smaller swirl ≈ 0.76. This suggests a possible explanation for the sensitivity of the flow to the grid: on the optimized grid the flow field computation leads to a smaller swirl number of the radial jet (downstream of the swirler vanes) and this change leads to an AJ state. This explanation makes sense only if a small variation of swirl can trigger a large jet re-configuration, something that is possible only if the flow conditions are close to critical.

The dependency of the swirl number of the radial jet on the mesh resolution inside the radial swirler (i.e. using the basic or the optimized mesh of Fig. C.6) can be explained as follows. The swirl number measured inside each of the vanes of the radial swirler (measured $3[mm]$ upstream of surface S3 of Fig. C.5, before the vanes converge and generate a single flow) is $S = 0.71$ for all simulations of table C.3: here the swirl number is fully determined by the geometry of the flow passage. Only downstream, on surface S3 (Fig. C.5) where all vanes merge, the swirl number does change depending on the mesh used.

Here (see Fig. C.11 where the mean flow of LES YALES-OPT and YALES-

BASIC on surface S3 are shown), the flow speed varies from $100[m/s]$ in the core of one jet, to zero, because of the solid boundary, and again to $100[m/s]$ because of the neighboring jet, in less than $5[mm]$. This large velocity gradient is challenging for LES: while the optimized mesh is sufficiently refined to simulate this configuration (see Fig. C.11 bottom where the mean flow looks regular and the backflow behind each swirler vane is distinct from the main stream), the basic mesh is not (see Fig. C.11 top and Fig. C.12). As a consequence, mesh resolution affects the mean velocity profile causing the swirl number of the jet to differ when the optimized mesh is replaced with the basic mesh.

Additional results (not shown here) show that a similar bifurcation (AJ-BB), appears in the LES with the basic mesh when the SGS model is changed, replacing SIGMA [17], with Dynamic Smagorinsky [18], for instance: two flow states appear above and below the supposed critical value of $S = 0.77 - 0.79$, on both codes (AVBP [8, 9] & YALES2 [10]). The SIGMA model causes a high swirl level in the radial jet and a consequent BB state, while the Dynamic Smagorisnky model causes a low swirl level in the radial jet and an AJ state. The dependency on SGS model is due to the different amount of turbulent viscosity generated by the two models: SIGMA generates less turbulent viscosity than the Dynamic Smagorinsky model in the wakes of the radial swirler vanes. The turbulent viscosity generated by the SGS model interacts with the velocity field, damping the turbulence generated by the jet-to-jet interaction shown for instance in Fig. C.12. The overall effect is

a modification of the mean velocity profile (determined by the amount of resolved turbulence which spreads momentum toward the different jet directions) so a variation of the swirl number which now depends on the turbulent viscosity level.

To clarify the dependency of the jet state to the amount of swirl of the flow, a modified swirler geometry is tested in LES (section 4) where the simplification of the geometry allows to change swirl levels easily while keeping all numerical parameters constant.

4. LES of an aeronautical swirl injector with adjustable swirl: adjustable swirler case

This part is dedicated to the verification of the hypothesis presented in section 3, namely that the swirled flow studied in section 3 is close to critical conditions and that swirl is the main control parameter. The mesh and the numerical settings (all simulations are performed with YALES2 [10]) are kept constant while the inlet conditions are varied in order to explore various swirl levels. To be able to modify the level of swirl, the original set up is modified and LES are conducted on a simpler geometry (Fig. C.13): the three swirlers, which determine the amount of swirl in the flow, and the upstream plenum are removed and replaced by inlets patches with adjustable swirl (Fig. C.13). As a result, the original swirl injector is transformed into an adjustable swirl device.

A similar methodology was used in [19] by imposing constant velocities at the swirler inlet. Here, the tangential velocity component of the "radial"

B.C. (Fig. C.13) will also be varied in order to modify swirl. The cylindrical box used to mimic open atmosphere is the same as in the full geometry case while the mesh characteristics are shown in Appendix A. Since the domain is smaller, the mesh used for the adjustable swirler case is significantly finer and tests (not shown here) prove that results do not depend on the mesh for this case.

Two simulations are tested where the radial jet swirl number is varied. The swirl introduced by the inner and outer jets are kept constant ($S = 0.12$ and $S = 0.4$ respectively). The first simulation (basic) uses a swirl number of the radial jet similar to simulation AVBP-OPT or YALES-OPT; the second (high), uses a swirl number 10% higher ($S = 0.84$). Each simulation is initialized using a zero-velocity flow field. The characteristics of these two simulations are summarized in table C.4, while their flow fields and CTRZs are shown in Fig. C.14.

The flow configuration of the basic case is characterized by a CTRZ smaller than one injector diameter (Fig. C.14), a high tangential velocity (Fig. C.15), a high sub-pressure ($P_D \approx 0.44$) and high turbulence intensity inside the CTRZ (Fig. C.16). On the contrary, the flow configuration of the high case is characterized by a CTRZ which is several injector diameters wide (Fig. C.14), a strong reduction of tangential velocity inside the CTRZ (Fig. C.15) and a reduced sub-pressure ($P_D \approx 0$) as well as a negligible turbulence intensity inside the CTRZ (Fig. C.16). The jet of basic LES is therefore in the AJ state while the jet of the high case is in the BB state: an

increase of 10% of the swirl number of the radial swirler jet (from $S = 0.75$ to $S = 0.84$) is enough to induce a bifurcation of the flow from AJ to BB states.

Note also that the flows in the full swirler case (Fig. C.9 and C.10) are similar to the flows in the adjustable swirler case (Fig. C.15 and C.16), showing that replacing the full swirler computation by an equivalent set of boundary conditions has a limited impact on the flow organization, as long as both jets are in the same state (AJ or BB).

Various phenomena control the flow topology: the jet separation from the smooth curved walls of the nozzle/diffuser (Fig. C.17), the jet attachment to the side walls (Fig. C.18), the jet expansion angle due to swirl and the presence/absence of a central coherent vortex core. The jet of the basic LES computation separates more upstream and reattaches more downstream in the nozzle than the jet of the high LES case (Fig. C.17). Similarly, it detaches from the side walls earlier than the jet of LES high (Fig. C.18). How the jet separation affects the formation of a central coherent vortex core and how swirl (that is the control parameter of the system as a whole) plays a role in each of these phenomena is difficult to estimate for such complex flows and was left for further studies. However, it is important to underline that to capture all these phenomena a very fine mesh LES is required: the swirl level of the jet can be strongly affected by a poor grid at the end of the swirler vanes (as shown in section 3 of this paper) and the detachment dynamics of the jet from the nozzle walls can be very sensitive to wall friction (which is

strongly dependent on the grid resolution).

In order to verify if hysteresis is present, a second set of tests is performed by changing continuously the swirl number of the radial jet while the amount of swirl of the remaining co-axial jets is kept constant at $S = 0.12$ and $S = -0.4$ respectively. LES are cast in two groups named path A & B. Path A begins with LES basic and the following simulation is obtained by increasing the swirl number of the radial swirler jet. Path B begins with LES high and the following simulations are obtained by decreasing the swirl number of the radial swirler jet except for the final simulation ($P3\_D$) in which the swirl level is brought back to LES basic ($S = 0.75$). The investigation is limited to the range $0.6 < S < 0.84$, around the working condition of $S \approx 0.75$, which is of interest for the present study and which is sufficient to close the hysteresis loop. Paths A & B are summarized in table C.5, while the swirler transition map is shown in Fig. C.19. The swirler bifurcation diagram (Fig. C.19) differs from the Vanierschot et al. one (Fig. C.3): this does not come as surprise since each transition map is dependent on the particular flow and geometry examined (as made evident in Vanierschot and Van Den Bulck [20], who analyzed the influence of the nozzle geometry on the bifurcation diagram of their original experiment [1], presented in section 2).

LES along path A are characterized by multiple bifurcations. At a swirl number of the radial swirler jet of 0.84 (simulation P1_U) the jet bifurcates from AJ to a flow state very similar to the "Weak axial Jet" (WJ) state described in section 2. Differently from the Vanierschot's experiment [1], this

flow state is unstable and transitory: after a period of $0.05[s]$ the flow bifurcates to the BB state. Transitions change pressure and turbulence intensity distributions (Fig. C.20) as well as the shape of the CTRZ (Fig. C.21) which expands both radially and axially after each bifurcation.

Viceversa, a decrease of the swirl number of the radial swirler jet from the value of 0.84 triggers a transition in LES of path B only at $S = 0.60$ (simulation $P2\_D$): at this swirl level the jet detaches from the external side walls and bifurcates back to the AJ state (Fig. C.21-C.22).

The adjustable swirler case results, summarized in Fig. C.19, show that the aeronautical swirler flow field with a swirl number of the radial jet close to 0.8 is close to multiple bifurcations (AJ-WJ, WJ-BB, BB-AJ) around the nominal working conditions. Two stable flow states (AJ-BB) can appear as a function of the swirl level of the jet and the initial conditions. Note that results of Fig. C.19 can not be validated experimentally since any change of swirl level would require a total change of the swirler geometry. However, they prove that, for fixed numerical settings, the jet is very sensitive to small variations of the fluid dynamics conditions.

Results obtained in the adjustable swirler case are consistent with results of the full swirler configuration. They show that the swirl number of the radial jet of the full swirler case $(0.74 - 0.82)$ is very close to the bifurcation threshold obtained in the adjustable swirler case: between $0.75 < S < 0.84$, the flow is bistable. LES senses this property and becomes sensitive to multiple parameters such as grid refinement or SGS model. As a result, characteriz-

ing swirling flows using LES can become difficult when the flow is in such conditions.

5. Conclusions

The present work has shown that LES of industrial swirling jets can be an extremely difficult task since small flow modifications can trigger large flow re-configurations near critical flow conditions. In the case examined here, the main parameter controlling the flow state is the swirl level of the radial jet. Bifurcations occur when swirl is changed by modifying inlet conditions or when it is changed by a modification of the LES grid or SGS model. This hypothesis was verified using a high-fidelity LES to simulate an adjustable swirl device capable of changing the amount of swirl in the flow. These bifurcations, which appeared to be due to uncontrollable errors in LES, were reproduced in a controlled environment where swirl was varied continuously. Two flow states were obtained and characterized based on the strength of the central, coherent, turbulent, vortex core associated with vortex breakdown. They are: a "free Axial Jet" (AJ) in which the central vortex core is not (or only weakly, like in simulation basic of section 4) influenced by the presence of confinement and behaves like a free swirling jet; a "Blasted Breakdown jet" (BB), in which the central vortex core, made evident by high tangential velocity and turbulence intensity, has disappeared (or "blasted"). A third flow state, a "Weak axial Jet" (WJ) in which the central vortex core is weaker because of a jet expansion angle higher than the one of a free Axial Jet under

the same amount of swirl, appeared as an unstable, transient state with the flow bifurcating either to the AJ or to the BB state for long simulation times. Flow states show similar properties in LOTAR and in the reference case of Vanierschot et al. [1] and appear to be the result of the combination of swirl intensity and jet separation/attachment to the diverging nozzle and side walls.

A second useful consideration is that, because of hysteresis, a change in simulation parameters should be accompanied by a re-initialization of the flow field. More generally, LES for swirled flows with combustion are also very likely to exhibit bifurcating behaviors. Since combustion can act as a triggering mechanism for bifurcations and instabilities, LES codes used to study turbulent swirled confined flames should be expected to exhibit a sensitivity to numerical "detail" (similarly to what shown in this paper) which is much larger than what has been observed in non swirling free flames and might raise significant difficulties.

Appendix A. Mesh and LES quality.

The mesh used for the adjustable swirler case of section 4 is shown in Fig. C.23-C.24. The mesh is fully tetrahedral and composed by 30 millions elements. The cell size gradation (variation of the cell size in neighbor elements) has been limited to 1.6. The smallest cells are located at the solid boundaries where a minimum cell size of $50[\mu m]$ is imposed, while, inside the swirler, elements size varies between $300[\mu m]$ and $400[\mu m]$ (Fig. C.23). The mesh is then smoothly coarsened away from the swirler (Fig. C.24).

LES quality is assured by monitoring multiple sensors: the wall distance nondimensionalized by the boundary layer thickness, the y^+ values, the ratio between laminar and turbulent viscosity and the Pope criterion [2] (ratio of resolved turbulent kinetic energy to resolved plus SGS turbulent kinetic energy, Eq. (A.1)). In the adjustable swirler case, the values of y^+ (evaluated at the cell baricentrum) are below 10 everywhere except downstream of the swirler vanes because of the high jet velocity (Fig. C.25) while in the full swirler case they are higher (Fig. C.26).

The ratio of turbulent to laminar viscosity is low (Fig. C.27 right and Fig. C.28 up), while the Pope criterion [2]:

$$Pope = \frac{k_{res}}{k_{res} + k_{sgs}}, \tag{A.1}$$

is everywhere higher than 0.9 in the proximity of the swirler and equal to 1 inside the well resolved jet (Fig. C.27 left and Fig. C.28 down). Resolved turbulence, k_{res}, is evaluated as $\frac{1}{2}\sum_{i=1}^{3}(u_i'^2)$ where u_i' is the Reynolds decom-

position of the velocity component u_i. Subgrid scale turbulence is evaluated as [21]:

$$k_{sgs} = (\frac{\nu_t}{C_M \Delta})^2 \tag{A.2}$$

where $C_M = 0.069$ and Δ is estimated as the cubic root of the elements volume.

Appendix B. LES solvers & settings.

All simulations of the present work are performed using the compressible LES solver named AVBP [8, 9] and the incompressible LES solver named YALES2 [10]. AVBP is a finite-volume/elements solver, cell-vertex (i.e. variables are stored at nodes while conservation laws are integrated inside the elements). YALES2 is a finite-volume solver, vertex centered (equations are solved at the element vertex), 4th-order accurate in space. The numerical scheme chosen for time advancement is Lax Wendroff for AVBP while is TRK4 [22], for YALES2. TRK4 (or TFV4A) is a fourth order time integration scheme providing a large region of stability (in terms of the Courant-Friedrichs-Lewy, CFL, number) which gives the possibility to adjust the incorporated numerical diffusion [22]. The CFL number chosen for the current study is 0.9 for YALES2 and 0.7 (acoustic CFL number) for AVBP. Both solvers use classical LES models. For example, turbulent viscosity is expressed as:

$$\nu_{SGS} = (C_m \Delta)^2 D_m(\tilde{u}), \tag{B.1}$$

so that ν_{SGS} is proportional to the square of the grid size per an ad-hoc coefficient multiplied a "differential operator associated with the model" $D_m(\tilde{u})$ [17]. The SGS model chosen for the current study is SIGMA [17], whose differential operator (i.e. turbulent viscosity coefficient) "goes to zero in near-wall regions in order to mimic the turbulence damping due to the no-slip condition" [17] (turbulent stress should decay as "the distance to the solid boundary to the third power" [17, 23]) and vanishes in the case of a flow in solid rotation and in the case of a pure shear. These properties are of importance since the flow under examination in the present study is both confined and swirled.

Acknowledgments

The authors thank Dr. G. Staffelbach and Dr. O. Vermorel for maintaining and supporting the LES code AVBP and Dr. V. Moureau for maintaining and supporting the LES code YALES2. The support of the Marie Curie program MYPLANET (contract PITN-GA-2008-210781) is gratefully acknowledged.

References

[1] M. Vanierschot and E. Van den Bulck. Hysteresis in flow patterns in annular swirling jets. *Experimental Thermal and Fluid Science*, Vol. 31, N. 6, pp.513-524, 2007. doi: 10.1016/j.expthermflusci.2006.06.001

[2] Pope, S.B. Turbulent Flows. *Cambridge Press*. ISBN:9780521598866

[3] J. H. Faler and S. Leibovich Disrupted states of vortex flow and vortex breakdown. *Physics of Fluids*, Vol. 20, N. 9, pp. 1385-1400, 1977. doi:10.1063/1.862033

[4] P. Billant and J.-M. Chomaz and P. Huerre. Experimental Study of Vortex Breakdown in Swirling Jets. *Journal of Fluid Mechanics*, Vol. 376, pp.183-219, 1998. doi:10.1017/S0022112098002870

[5] O Lucca-Negro and T O'Doherty Vortex breakdown: a review. *Progress in Energy and Combustion Science*, Vol. 27, pp.431 - 481, 2001. doi:10.1016/S0360-1285(00)00022-8

[6] Cassidy,John J. and Falvey,Henry T. Observations of unsteady flow arising after vortex breakdown. *Journal of Fluid Mechanics*, Vol. 41, N.4, pp. 727-736, 1970. doi:10.1017/S0022112070000873

[7] M.G. Hall The structure of concentrated vortex cores. *Progress in Aerospace Sciences*, Vol. 7, pp. 53 - 110, 1966. doi:10.1016/0376-0421(66)90006-6

[8] M. Rudgyard and T. Schoenfeld and R. Struijs and G. Audemar and P. Leyland. A Modular Approach for Computational Fluid Dynamics. *CERFACS report*, 1995.

[9] M. Rudgyard. Integrated Preprocessing Tools for Unstructured Parallel CFD Applications. *CERFACS report*, 1995.

[10] Moureau, V.; Domingo, P.; Vervisch, L. Design of a massively parallel CFD code for complex geometries. *Comptes Rendus Mecanique*, Vol. 339, N. 2-3, pp.141-148, 2011. doi: 10.1016/j.crme.2010.12.001

[11] F. Bismes, F. Simon, P. Gajan, J. Apeloig. Experimental characterization of the injector. *Kiai deliverable d2.3.1*, 2011

[12] A. K. Gupta and D. G. Lilley and N. Syred. Swirl flows. *Abacus Press*, 1984.

[13] J Chedaille, W Leuckel, AK Chesters Aerodynamic studies carried out on turbulent jets by the international flame research. *Journal of the institute of Fuel*, Vol. 39, N. 311, pp. 506-521, 1966.

[14] J. M. Beer and N. A. Chigier Combustion aerodynamics. *Krieger*, 1983.

[15] M. Vanierschot, T. Persoons, E. Van den Bulck.M. A new method for annular jet control based on cross-flow injection. *Physics of Fluids*, Vol. 21, N. 2, 2009. doi: 10.1063/1.3037343

[16] M. García-Villalba, J. Fröhlich, and W. Rodi. Identification and analysis of coherent structures in the near field of a turbulent unconfined annular swirling jet using large eddy simulation. *Physics of Fluids*, Vol. 18, N. 5, 2006. doi: 10.1063/1.2202648

[17] Nicoud, F.; Baya Toda, H; Cabrit, O.; Bose, S.; Lee, J. Using singular values to build a subgrid-scale model for large eddy simulations. *Physics of Fluids*, Vol. 23, N. 8, 2011. doi: 10.1063/1.3623274

[18] Massimo Germano and Ugo Piomelli and Parviz Moin and William H. Cabot. A dynamic subgrid-scale eddy viscosity model. *Physics of Fluids*, Vol. 3, N. 7, pp. 1760-1765, 1991. doi:10.1063/1.857955

[19] S. Wang, V. Yang, G. Hsiao, S.Y. Hsieh and H. C. Mongia. Large-eddy simulations of gas-turbine swirl injector flow dynamics. *Journal of Fluid Mechanics*, Vol. 583, pp 99-122, 2007. doi:10.1017/S0022112007006155

[20] M. Vanierschot and E. Van den Bulck. Influence of the nozzle geometry on the hysteresis of annular swirling jets. *Combustion Science and Technology*, Vol. 179, N. 8, pp.1451-1466, 2007. doi: 10.1080/00102200601147856

[21] P. Sagaut Large eddy simulation for incompressible flows. *Springer*.

[22] Kraushaar, M. Application of the compressible and low-Mach number approaches to Large-Eddy Simulation of turbulent flows in aero-engines. *Phd. Thesis, CERFACS.*

[23] Chapman,Dean R. and Kuhn,Gary D. The limiting behaviour of turbulence near a wall. *Journal of Fluid Mechanics*, Vol. 170, pp. 265-292, 1986. doi:10.1017/S0022112086000885

Appendix C. Tables & figures

flow state	CTRZ size	normalized subpressure	CTRZ tangential velocity	CTRZ Reynolds stresses
AJ	$R_v < 0.5$	$1.4 < P_D < 0.8$	high	high
WJ	$0.5 < R_v < 1$	$P_D < 0.4$	moderate	moderate
BB	$R_v >> 1$	$P_D = 0$	zero	zero

Table C.1: Summary of the characteristics of the three different states (AJ-WJ-BB) documented in [1] after vortex breakdown. R_v indicates the approximate radial position of the "eye" of the CTRZ while P_D is the subpressure normalized by the jet kinetic energy, $P_D = \frac{P_{atm}-P}{0.5\rho U_0^2}$.

SWIRLER B.C.s (Fig. C.4)		
B.C. name	imposed property	target value
cooling film	mass flow - T	30.3 $[g/s]$ - 270K
plenum inlet	mass flow - T	102.12 $[g/s]$ - 270K
FAR FIELD B.C.s (Fig. C.4)		
B.C. name	imposed property	target value
coflow	speed - T	1 $[m/s]$ - 270K
outlet	pressure	99000 $[Pa]$
walls	adherence, impermeability, adiabaticity	

Table C.2: Imposed boundary values for LES of the full swirler case.

LES name	S, **Eq.(1) inner axial jet**	S, **Eq.(1) outer axial jet**	S, **Eq.(1) radial swirler jet**	**flow state**
AVBP-BASIC	0.12	-0.60	0.82	BB
YALES-BASIC	0.12	-0.58	0.80	BB
AVBP-OPT	0.12	-0.61	0.76	AJ
YALES-OPT	0.12	-0.58	0.74	AJ

Table C.3: Summary of the characteristics of the full swirler case simulations of Fig. C.8. Simulation names indicate the code (AVBP [8, 9] or YALES2[10]) and the grid (basic vs. optimized, OPT) used.

LES name	S (eq. 1) inner/outer jet	S (eq. 1) radial jet	jet configuration
basic	0.12/ -0.4	0.75	AJ
high	0.12/ -0.4	0.84	BB

Table C.4: First set of LES of the adjustable swirler case.

LES name	S (eq. 1) radial jet	initial condition	jet configuration
P1_U	0.84	basic	WJ $\rightarrow$ BB
P1_D	0.75	high	BB
P2_D	0.60	P1_D	AJ
P3_D	0.75	P2_D	AJ

Table C.5: Characteristics of LES of Path A & B.

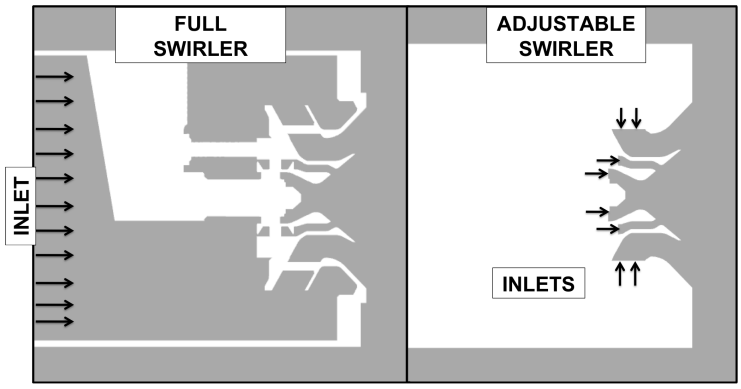

Figure C.1: Full and adjustable swirler configurations. Arrows represent inlet boundary conditions.

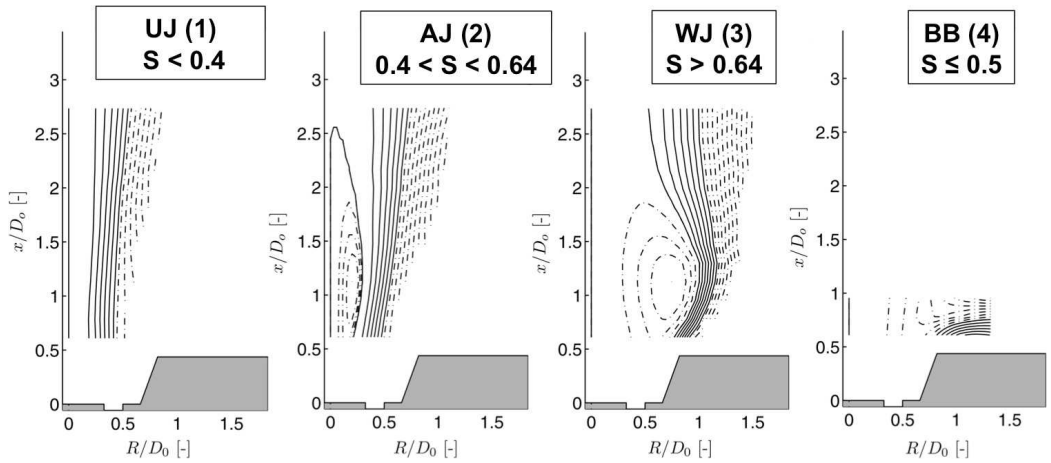

Figure C.2: Experimental results of Vanierschot and Van Den Bulck, [1]: streamlines for four different flow states. Solid lines correspond to the jet boundaries and dashed-dotted lines are recirculation zones. Swirl number exact values are from left to right: $S = 0.335, 0.56, 0.69, 0.5$. The flow states named here UJ, AJ, WJ and BB were originally named [1]: "closed jet flow", "open jet low swirl flow", "open jet high swirl flow" and "Coanda jet flow" respectively.

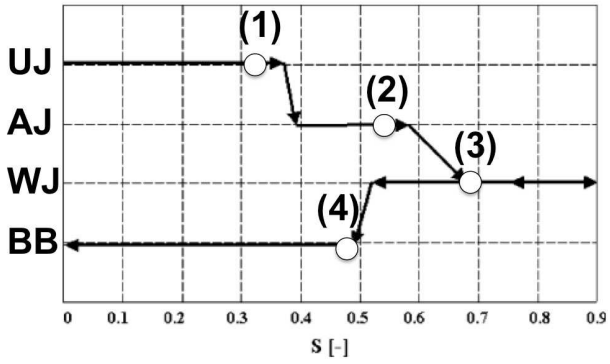

Figure C.3: Transition map of Vanierschot and Van Den Bulck, [1]. The different flow states are plotted against the swirl number S. The four states of Fig. C.2 (1 to 4) are added on the diagram.

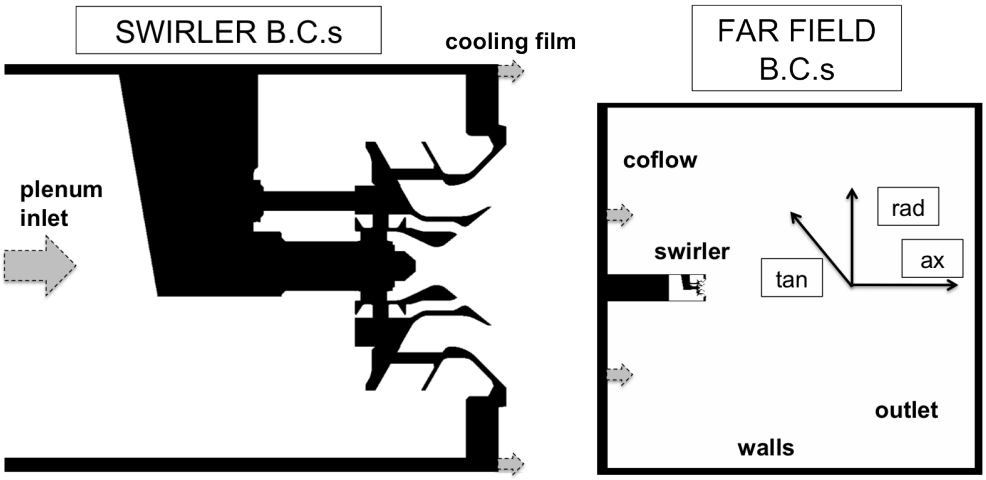

Figure C.4: Aeronautical swirler boundary conditions for the full swirler case. Arrows indicates inlets. The right picture specifies the flow directions (ax = axial, rad = radial and tan = tangential) in cylindrical coordinates, where the axial direction corresponds to the axis of symmetry of the cylindrical box used to mimic open atmosphere.

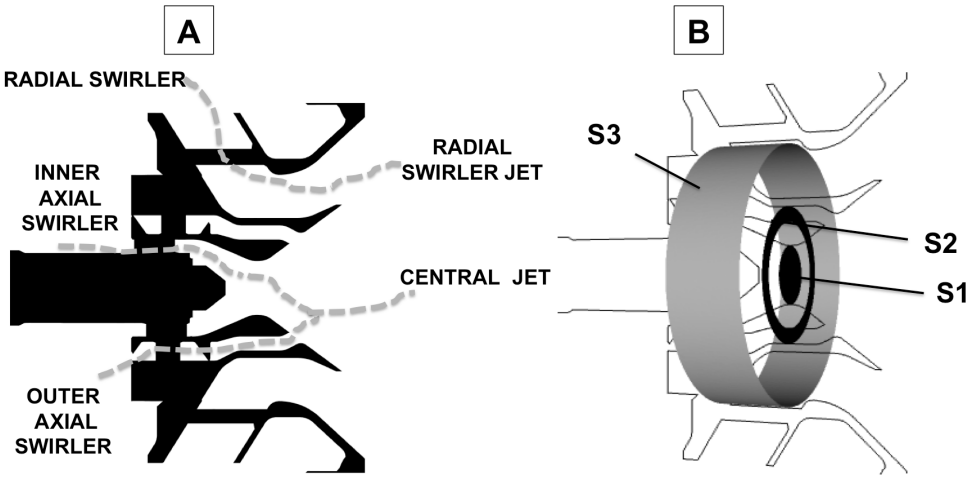

Figure C.5: full swirler case. **A**: swirler passages and jets. **B**: Measurement surfaces for the swirl numbers Eq.(1). $S1$ and $S2$ are the measurement surfaces for the two co-axial jets. $S3$ for the radial jet.

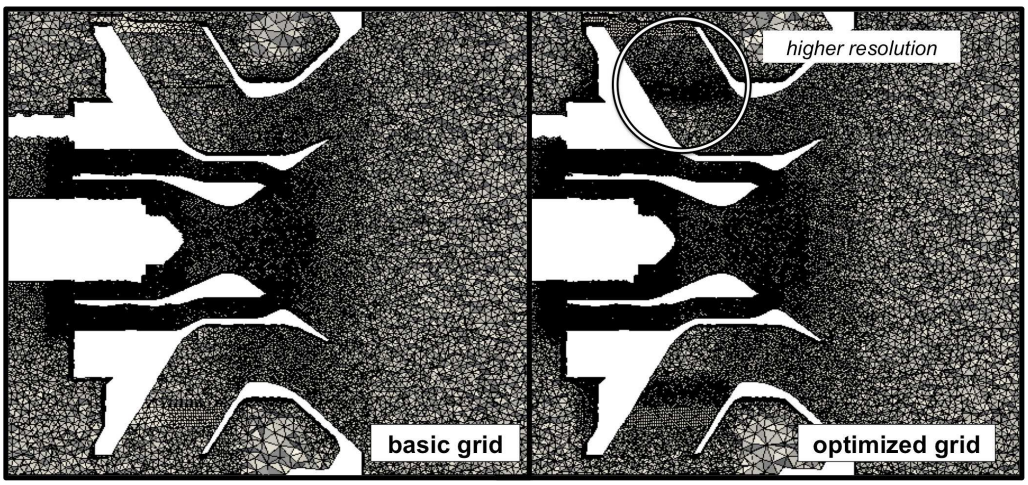

Figure C.6: full swirler case, basic and optimized grids.

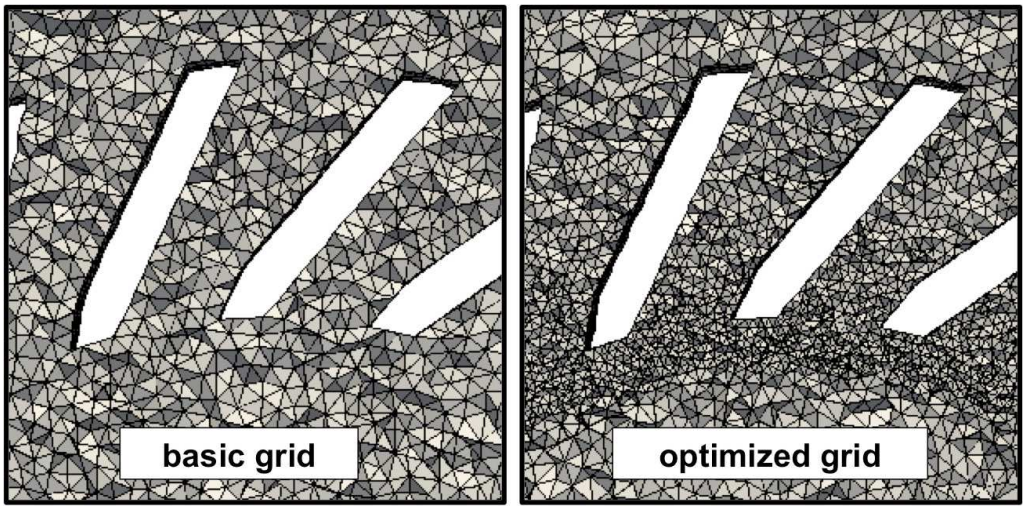

Figure C.7: full swirler case, basic and optimized grids, zoom at the radial swirler.

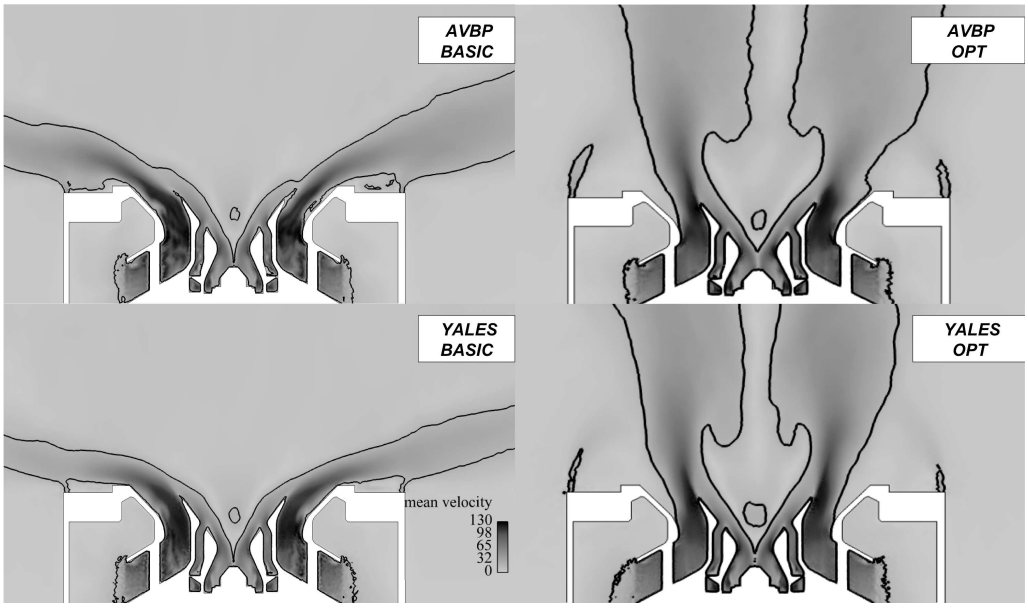

Figure C.8: Flow fields of the full swirler case LES of table C.3. The jet bifurcates in both codes (AVBP [8, 9] & YALES2 [10]) depending on the grid used (basic vs. optimized grid, Fig. C.6 and Fig. C.7). In black, iso-velocity line ($U = 20[m/s]$).

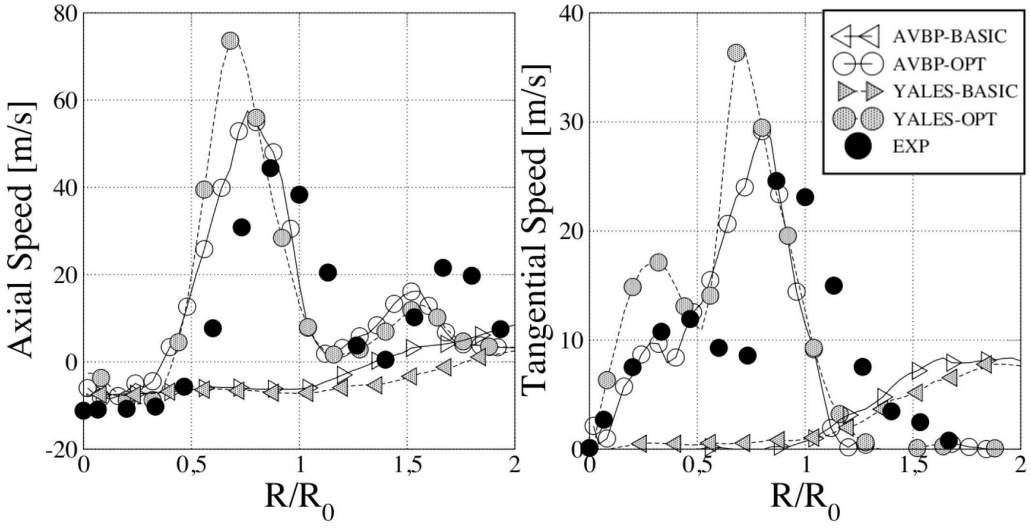

Figure C.9: Flow velocities plotted against normalized radial positions (R/R_0) of LES of the full swirler case, table C.3. Measurement are taken $0.5R_0$ downstream of the swirler ending plate.

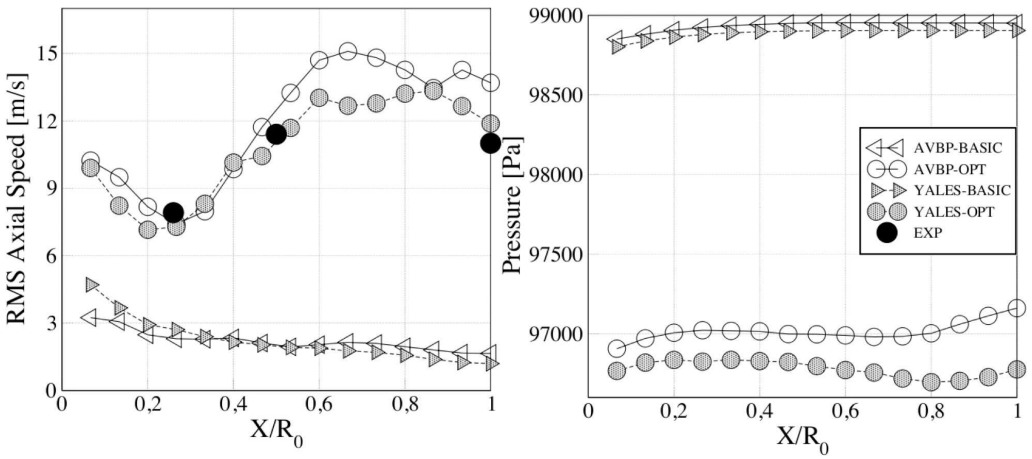

Figure C.10: Axial velocity RMS and pressure distribution measured along the centerline of the geometry. Results are plotted against normalized axial distance (X/R_0) from the swirler ending plate, for the full swirler case simulations, table C.3. Experimental data are available only for RMS values.

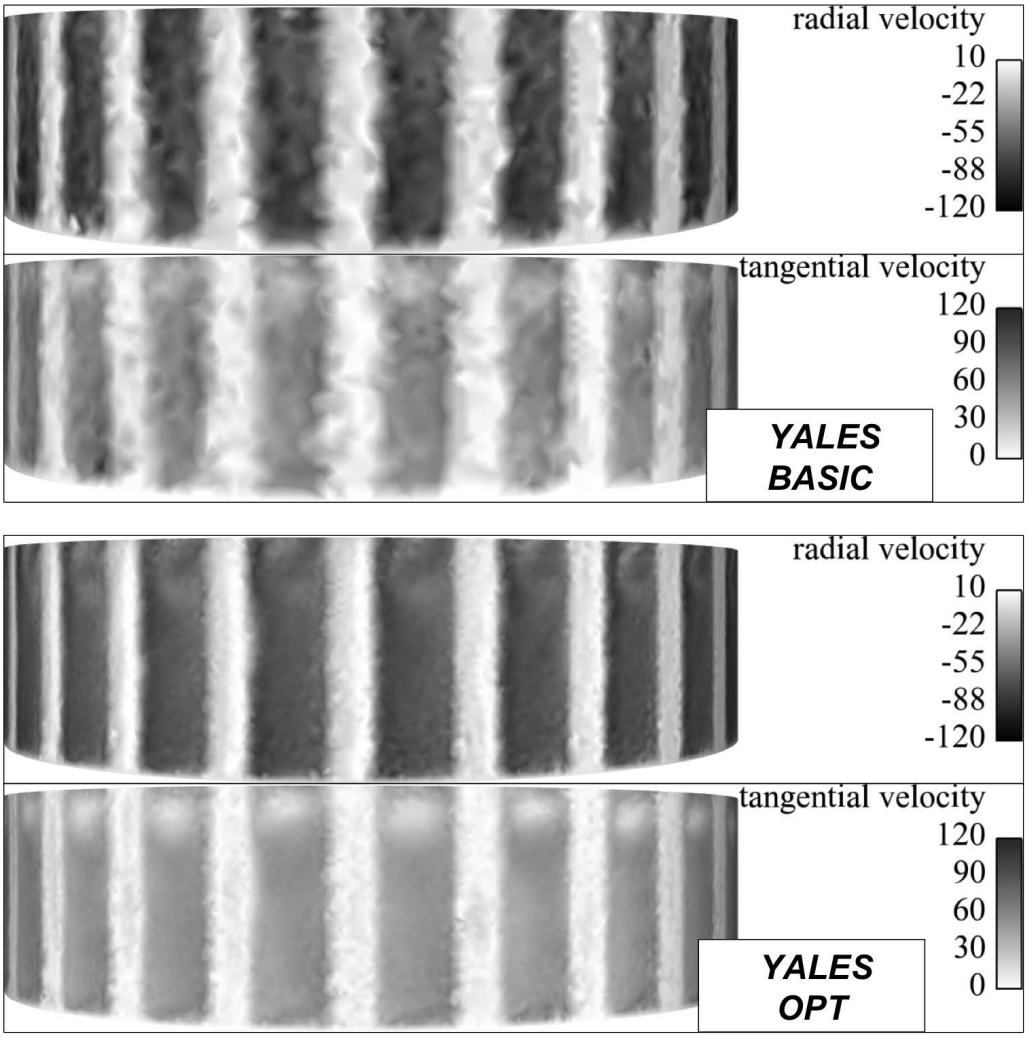

Figure C.11: Mean radial and tangential velocities ([m/s]) on surface S3 (Fig. C.5) for LES YALES-BASIC and YALES-OPT of table C.3. The mean flow speed is more irregular on the basic grid (top) than on the optimized grid (bottom) because of the different grid resolution in this zone.

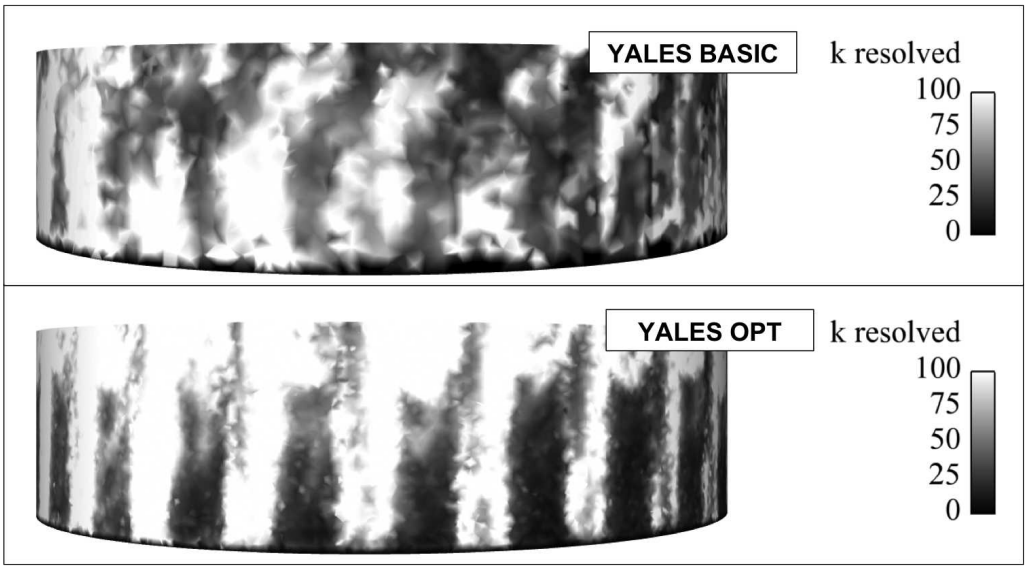

Figure C.12: Resolved turbulent kinetic energy for LES YALES-BASIC and YALES-OPT of table C.3.

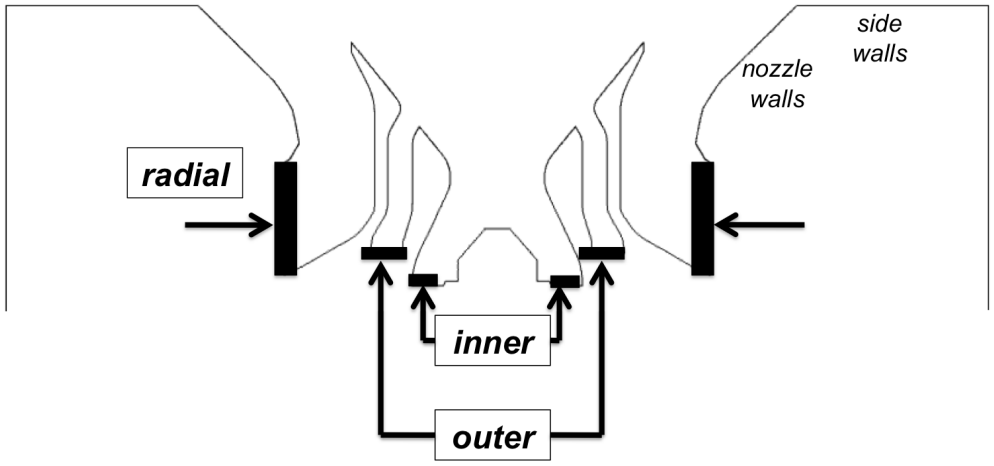

Figure C.13: Domain of the adjustable swirler case and boundary conditions.

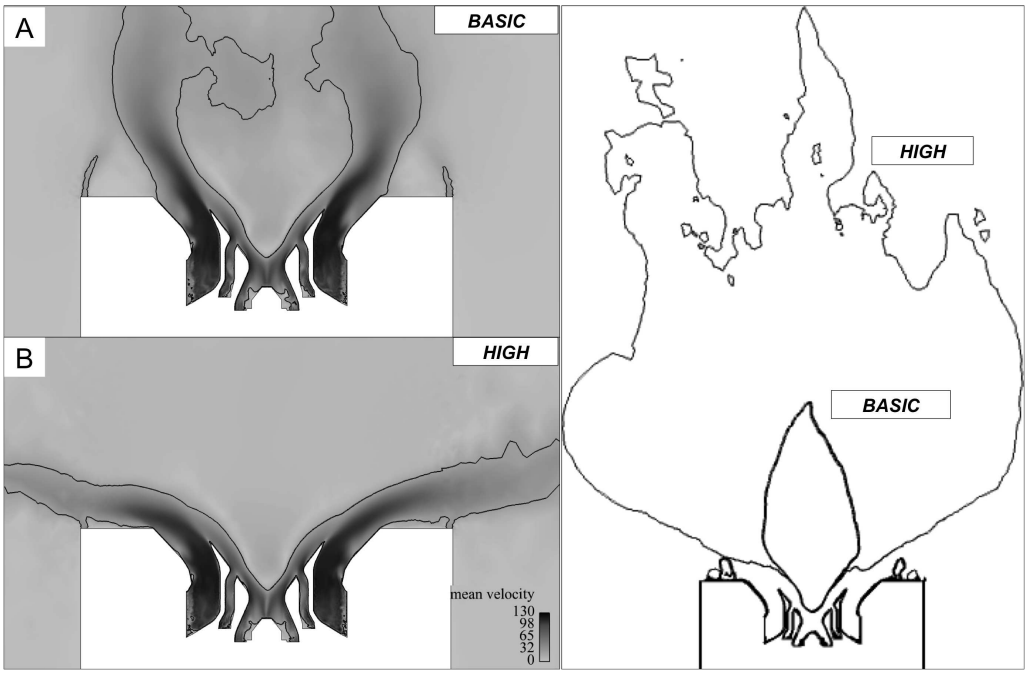

Figure C.14: A-B: flow fields and velocity isoline ($U = 20[m/s]$) of simulations basic and high of table C.4. CTRZs lines (zero axial velocity isoline) of these simulations are plotted in the right picture.

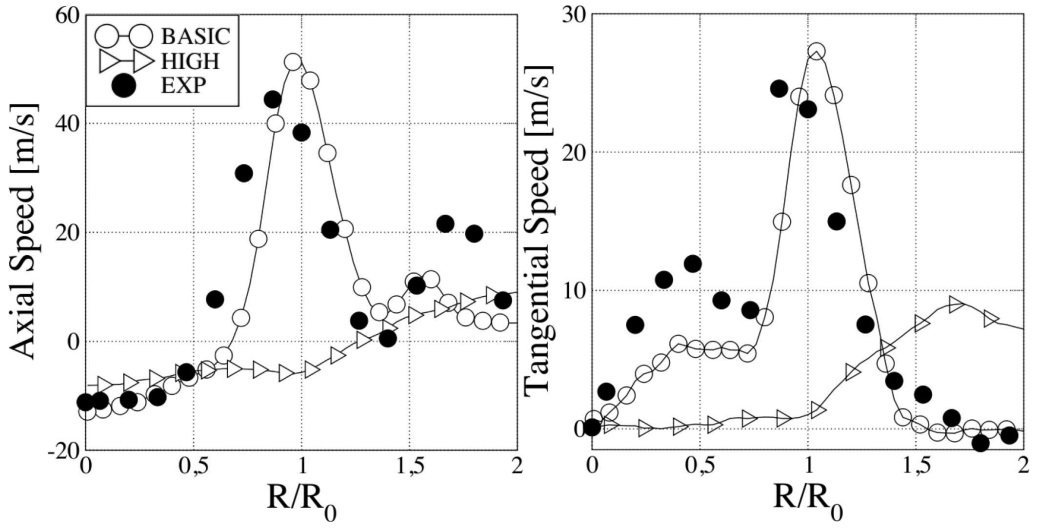

Figure C.15: Flow velocities plotted against normalized radial positions for simulations basic and high of table C.4. Measurement are taken $0.5R_0$ downstream of the swirler ending plate.

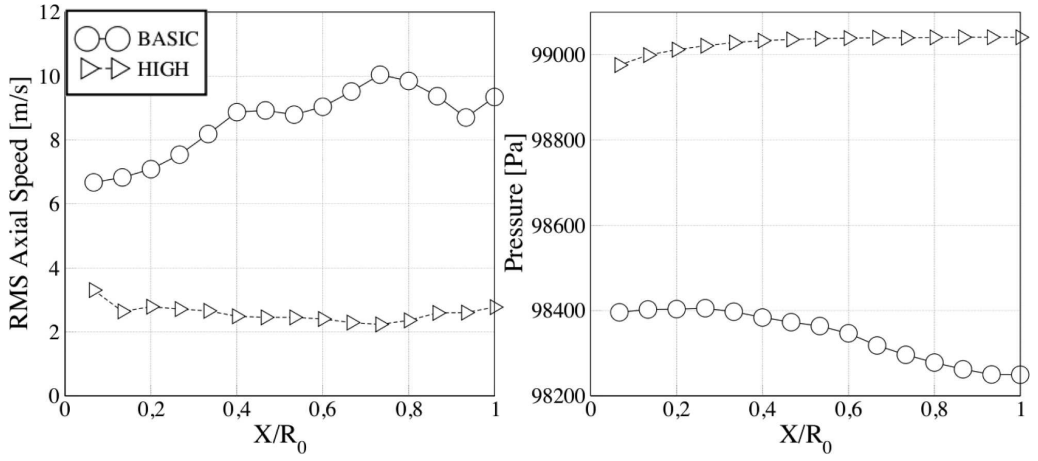

Figure C.16: Axial velocity RMS and pressure distribution measured along the centerline of the geometry. Results are plotted against normalized axial distance (X/R_0) from the swirler ending plate for simulations basic and high of table C.4.

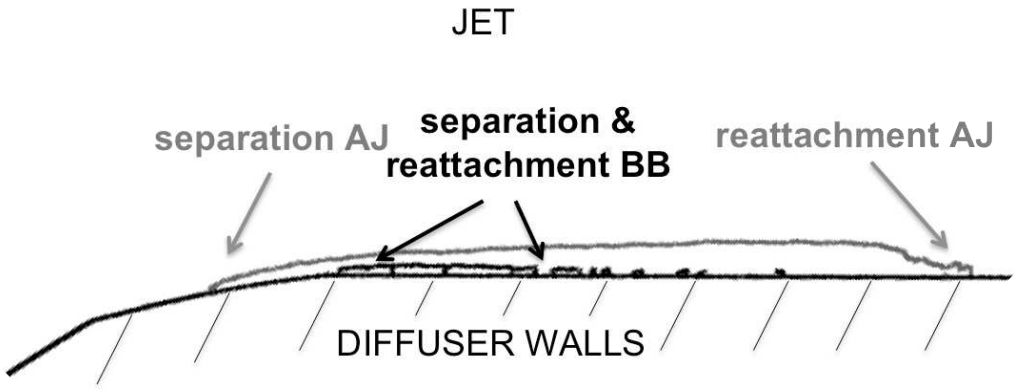

Figure C.17: Jet separation and reattachment inside the nozzle for LES of table C.4. The jet dynamics are made evident by the zero velocity isoline in the streamwise direction. Grey line, LES basic in the AJ state, Black line, LES high in the BB state.

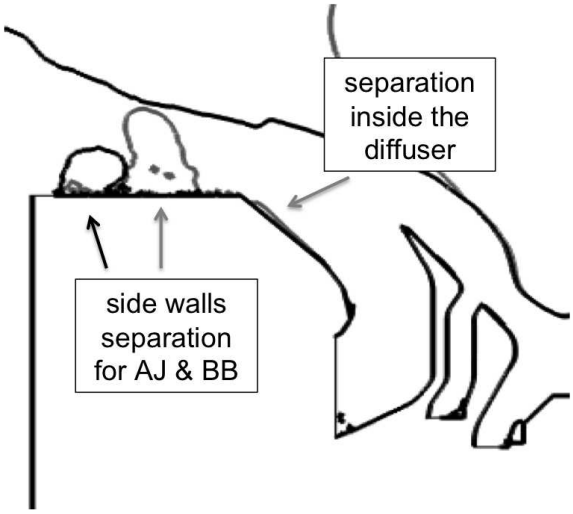

Figure C.18: Jet separation and reattachment to the side walls for LES of table C.4. The jet dynamics are made evident by the zero velocity isoline in the streamwise direction. Grey line, LES basic in the AJ state, Black line, LES high in the BB state.

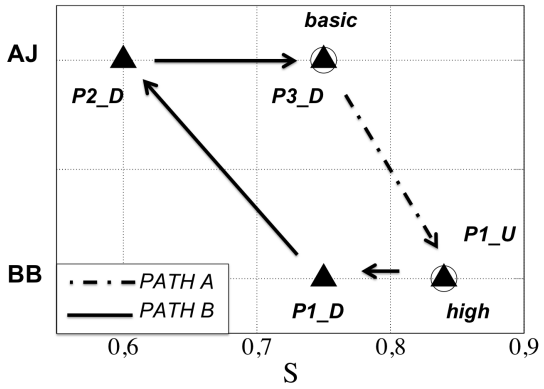

Figure C.19: Transition map of the aeronautical swirler, adjustable swirler case. Circles are LES of path A (which starts with LES basic) while black triangles are LES of path B (which starts with LES high). The hysteresis loop is closed.

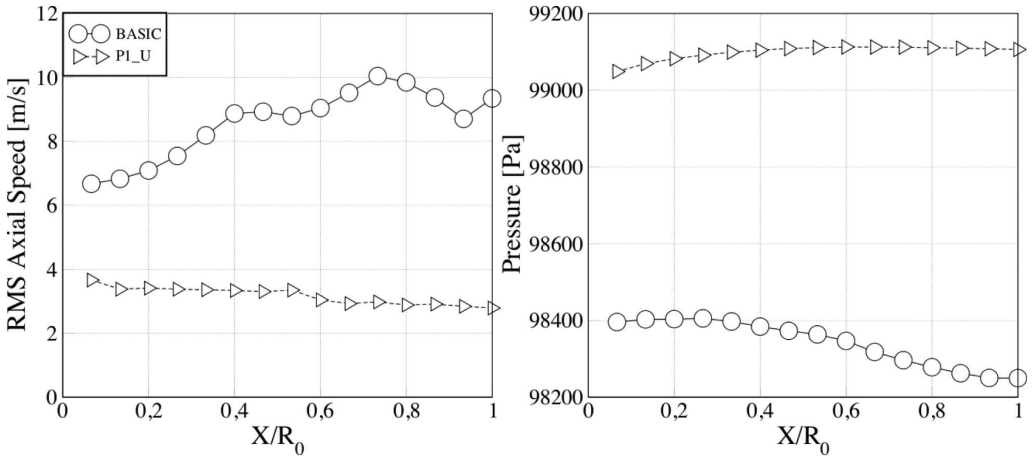

Figure C.20: Axial velocity RMS and pressure distribution measured along the centerline of the geometry. Results are plotted against normalized axial distance (X/R_0) from the swirler ending plate, for simulations of path A, table C.5.

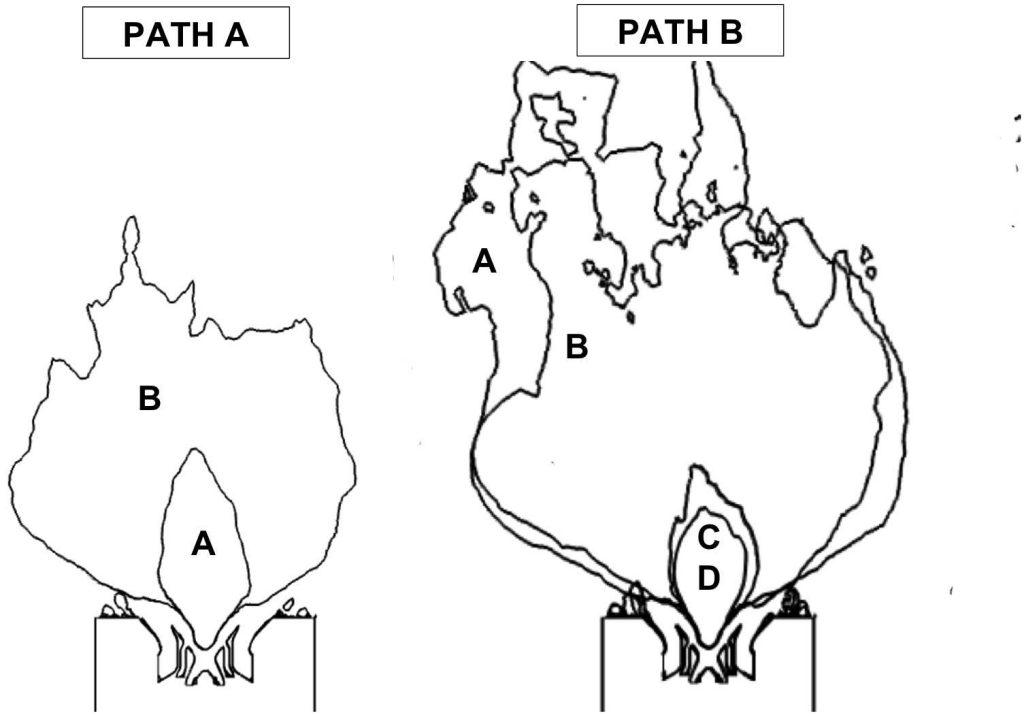

Figure C.21: Path A: CTRZs of LES basic (A), $P1\_U$ (B). Path B: CTRZs of LES high (A), $P1\_D$ (B), $P2\_D$ (C), $P3\_D$ (D).

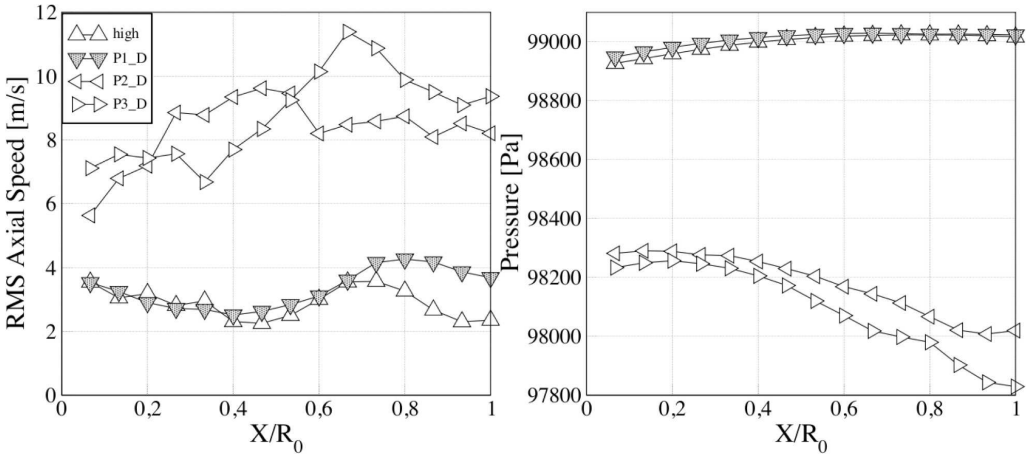

Figure C.22: Axial velocity RMS and pressure distribution measured along the centerline of the geometry. Results are plotted against normalized axial distance (X/R_0) from the swirler ending plate, for simulations of path B, table C.5.

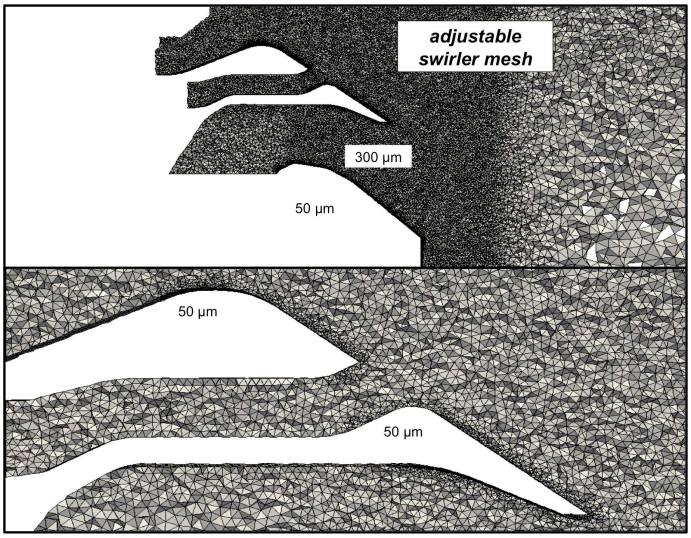

Figure C.23: Adjustable swirler case mesh, zoom at the swirler.

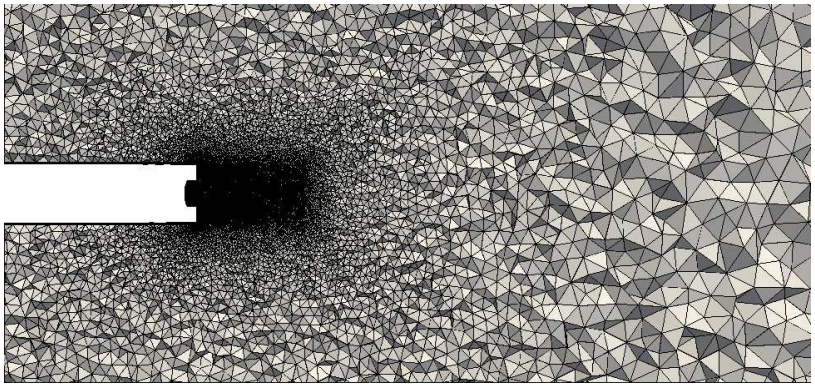

Figure C.24: Adjustable swirler case mesh, far field.

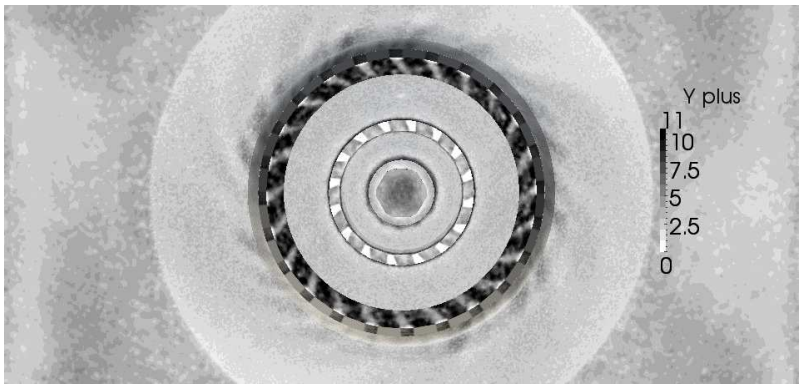

Figure C.25: Mean y^+ values for LES basic of section 4. The swirler surface is seen from the open atmosphere.

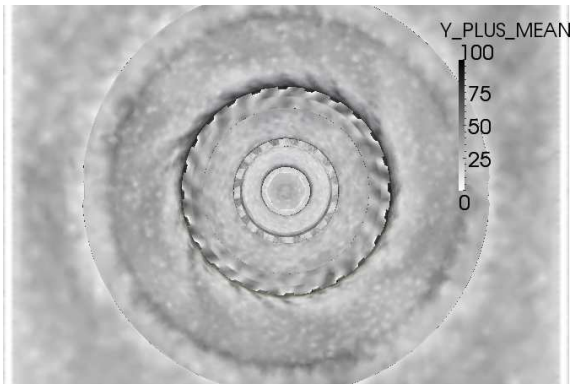

Figure C.26: Mean y^+ values for LES YALES-OPT of section 3. The swirler surface is seen from the open atmosphere.

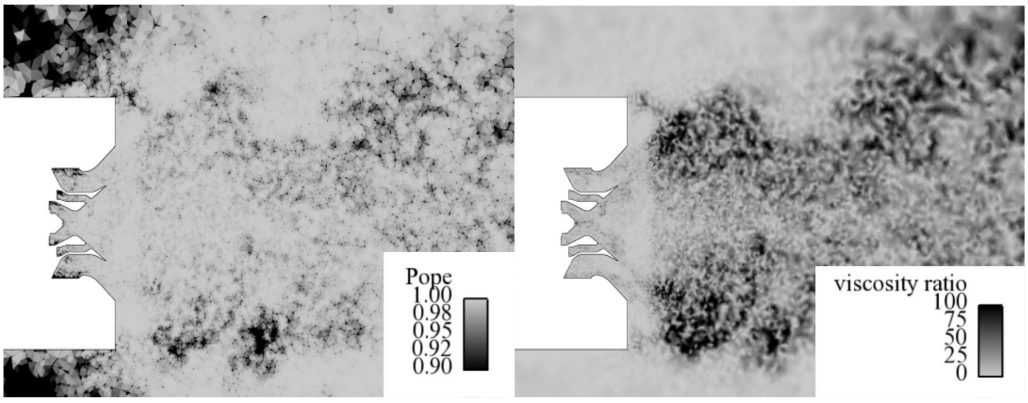

Figure C.27: Snapshots of ratio of turbulent over laminar viscosity and Pope criterion, Eq. (A.1), for LES basic of section 4.

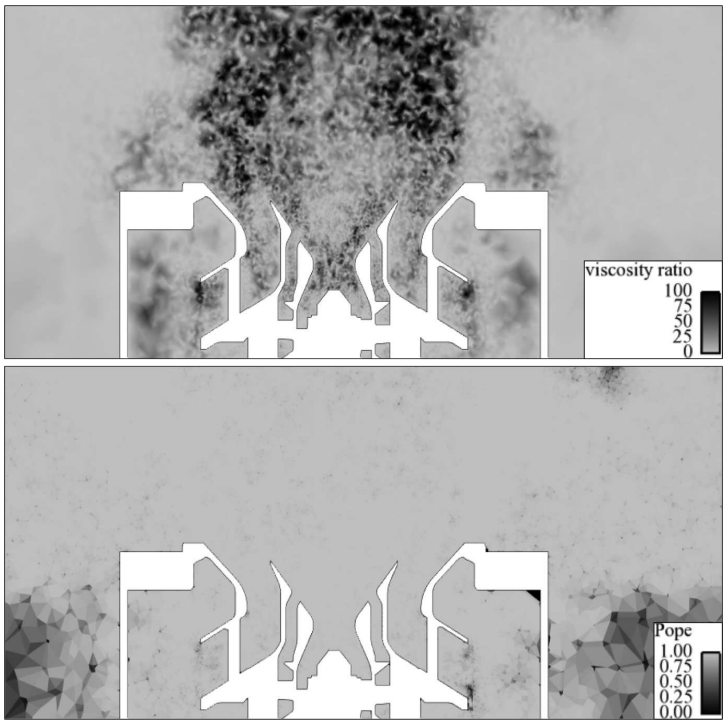

Figure C.28: Snapshots of ratio of turbulent over laminar viscosity and Pope criterion, Eq. (A.1), for LES YALES-OPT of section 3.